STUDY OF RESIDUAL STRESSES AROUND COLD-EXPANDED HOLES

By

Khurram Amjad

A THESIS

Submitted to

The University of Liverpool

And

National Tsing Hua University

in accordance with the requirements of both the Institutions for the degree of

DOCTOR OF PHILOSOPHY

February 2018

ABSTRACT

Split sleeve cold expansion is one of the most widely used methods in the aerospace industry to enhance the fatigue performance of fastener holes in airframe structures. The initial motivation, which led to this research programme, was to develop an understanding of the behaviour of fatigue cracks emanating from cold-expanded holes, with a particular emphasis on the influence of these cracks on the surrounding compressive residual stresses. There are two strands of the research presented in this thesis: first being related to the study of hole deformation resulting from split sleeve cold expansion; and the second one focused on the fatigue behaviour of cracks emanating from cold-expanded holes.

The strain fields developed from cold expansion were measured using stereoscopic digital image correlation (DIC) technique in aluminium specimens of two different thicknesses giving thickness to hole diameter ratio of 0.25 and 1. The capability of DIC in providing full-field strain data was exploited to determine the shape and size of the plastic zones developed from cold expansion. The results showed that the existing split sleeve cold expansion process is not as effective in creating an axisymmetric compressive residual elastic stress zone around the fastener holes in thin as it is in the thick specimens. The thin specimens used in this investigation were equivalent in thickness to sheet material commonly used in an aircraft fuselage or wing skins and the results indicate that there is a need to review the use of cold expansion process using a split sleeve and mandrel for holes in thin sheets.

A simple approach utilising DIC was presented to analyse the strain fields resulting from cold expansion in stacked specimens. The results showed that stacking offers some improvement in the cold expansion of thin sheet components. They also demonstrated the workability of this approach which can be applied effectively to analyse cold expansion of fastener holes associated with a real joint configuration in an airframe.

The propagation of fatigue cracks initiating from the cold-expanded holes was investigated by employing the thermoelastic stress analysis (TSA) technique and

their influence on the surrounding residual stresses was determined using synchrotron x-ray diffraction (SXRD) technique. A long-standing ambiguity in the literature regarding the potential relaxation of beneficial compressive residual stresses, as a result of fatigue crack propagation, was addressed; and it was established, from TSA and SXRD results, that the formation or propagation of a fatigue crack does not cause any significant relaxation of these residual stresses. The results also clearly identify the loading conditions under which the residual stresses are expected to relax. This information is important in improving the theoretical models for fatigue life assessment of cold-expanded holes. The results should also be useful for the engineers in the aerospace industry to realise the full potential of the cold expansion process and to utilise it more effectively in the manufacturing of airframes leading to improved fatigue endurance under different loading conditions.

中文摘要 **(Abstract in Chinese)**

為了增強機體結構中緊固件孔的疲勞特性，開縫襯套擴孔是一個目前廣泛應用於航太工業中之技術。本研究觀察在結構件於擴孔後，周圍產生的壓縮殘餘應力引起疲勞行為產生的裂紋。為了探討擴孔後所產生之疲勞裂紋行為，並且同時探討裂紋周圍之殘留應力，本研究主要探討的有兩方向：一為探討擴孔後之變形行為，二為擴孔後之裂紋疲勞行為。

應變分析採用立體數位影像相關（Digital Image Correlation, DIC）法量測 0.25 與 1 的兩種厚度/孔洞直徑比的鋁合金於擴孔後之應變變化，經 DIC 法量測能獲得擴孔後所產生塑性區域的全域形變與擴孔後的孔徑形狀與尺寸。結果顯示傳統開縫襯套擴孔法並無法有效的在厚壁與薄壁緊固件孔周圍產生軸對稱的壓縮殘餘應力，而實驗之薄壁試片採用與飛行器之機身與機翼蒙皮相同厚度，因此需要重新檢視傳統開縫襯套擴孔法之作業程序。

本論文以利用 DIC 法分析多層板試片於擴孔後之全域應變，由實驗結果可得知使用多層板之結構確實可改善結構。因此，本論文建立一可有效分析機體結構中之緊固件孔與鉚釘固定連結後結構強度之判斷方法。此外，利用熱彈應力（Thermoelastic Stress Analysis, TSA）方法探討構件於擴孔後孔邊

之疲勞裂紋成長；同步輻射 X 光繞射（Synchrotron X-ray Diffraction, SXRD）技術分析裂紋周圍之殘留應力。

長久以來許多文獻探討如何利用降低壓縮殘留應力抑制疲勞裂紋成長有著不同之論點，本論文為了探討此問題利用 TSA 與 SXRD 進行量測並探討疲勞裂紋成長與殘留應力間之關係，但由實驗結果可得知疲勞裂紋之形成與成長並無明顯之關聯性。實驗結果可觀察到構件受力條件與殘留應力有效降低之關係，由此對於建立一準確之理論模型為非常之重要。因此，本論文提出的方法與實驗結果有利於航太工業提供一精準分析與量測擴孔製程後之技術，並於製造機體時有效判斷最佳之加工狀態以提高構件之疲勞耐久性。

To Khatija and My Parents

ACKNOWLEDGEMENTS

I am very grateful to my supervisors, Professor Eann Patterson of the University of Liverpool (UoL) and Professor Wei-Chung Wang of the National Tsing Hua University (NTHU) for their guidance and feedback throughout my research project. This thesis would not have been possible without their continued encouragement and support. I am indebted to Prof. Patterson for his time and effort in helping me progress during the first three years of my PhD at UoL. I would like to express my gratitude to Prof. Wang and all his students at NTHU for being unimaginably supportive and kind during my stay in Taiwan.

I gratefully acknowledge the technical support provided by Jijimon Mathew and Dave Atkinson throughout my PhD studies. I want to thank Dr. David Asquith at Sheffield Hallam University and Dr. Chris Sebastian of the UoL for helping me plan and perform x-ray diffraction experiments at European Synchrotron Radiation Facility in France, which were integral to my research. I would also like to thank Grace and Chun Yi in the College of Nuclear Science at NTHU for providing training to operate the scanning electron microscope. Finally, I am grateful to Tzu Yu Kuo and Bo Yu Chen for translating my thesis abstract in Chinese.

TABLE OF CONTENTS

LIST OF TABLES

LIST OF FIGURES

1 INTRODUCTION

Thousands of holes for bolts and rivets are required for the assembly of aircraft structures. These holes act as stress concentrators and are a potential source of fatigue crack initiation[1]. It is a routine practice in the aerospace industry to perform cold expansion on such holes to enhance the fatigue endurance of both new and existing airframes. Cold expansion can be referred to as any process which causes expansion of the hole beyond the yield strength of the material to induce compressive residual stresses. The word 'cold' is used to indicate that the hole is plastically expanded at room temperature. An overview of various types of cold expansion methods has been provided by Champoux[2]. These methods can be characterised into either low or high interference processes. Traditionally, the low interference processes, which include roller burnishing, ballizing and coining, have been used for sizing of holes and their influence on fatigue performance is not well-established[2]. The most common high interference processes include mandrelizing, split mandrel, split sleeve and solid sleeve cold expansion[2]. These methods are essentially similar in their operation as they all involve the passage of an oversized mandrel through a hole to cause plastic deformation. The mandrel taper effectively translates the axial motion of the mandrel into a radial expansion of the hole; however, at higher expansion levels, some plastic displacement along the axial direction is inevitable which is termed as 'surface upset'[3]. Recently, a novel cold expansion tool has been developed by Maximov et al[4] which claims to minimize surface upset by ensuring axisymmetric radial expansion of the holes.

Despite the existence of several cold expansion processes and recent developments in the cold expansion tooling, the split sleeve cold expansion remains one of the most extensively used processes in the aerospace industry, and therefore, was selected to be studied in this research. It was invented by The Boeing Company in 1969 and further developed and marketed by the Fatigue Technology Incorporated (FTI), Seattle, USA[5]. This process involves passing a hardened steel mandrel with an oversized head through an initially undersized hole to plastically expand it. Upon removal of the mandrel, the elastic material surrounding the plastically deformed material causes a spring-back effect, which creates a ring of residual compressive hoop stresses around the cold-expanded hole. The process utilises an internally lubricated, 0.2-0.25 mm thick stainless steel sleeve, with a split in it, which resides on the mandrel shank. A schematic of the split sleeve cold expansion process is shown in Figure 1.1. The main purpose of this sleeve is to allow the cold expansion process to be carried out without access to the other side of the component; however, it also avoids direct contact of the mandrel head with the internal surface of the hole, which minimises distortion of the hole during the expansion process. The mandrel entry and exit faces refer to the surfaces of a component from which the mandrel enters or leaves the component, respectively, during the cold expansion process. The amount of expansion or interference (I_o) is a function of initial hole diameter, oversized mandrel head diameter and the split sleeve thickness, which can be calculated using the following equation:

$$I_o = \frac{D_m + 2t_s - D_o}{D_o} \qquad 1.1$$

where D_o and D_m are the initial hole and the oversized mandrel head diameters respectively and t_s is the thickness of the split sleeve respectively.

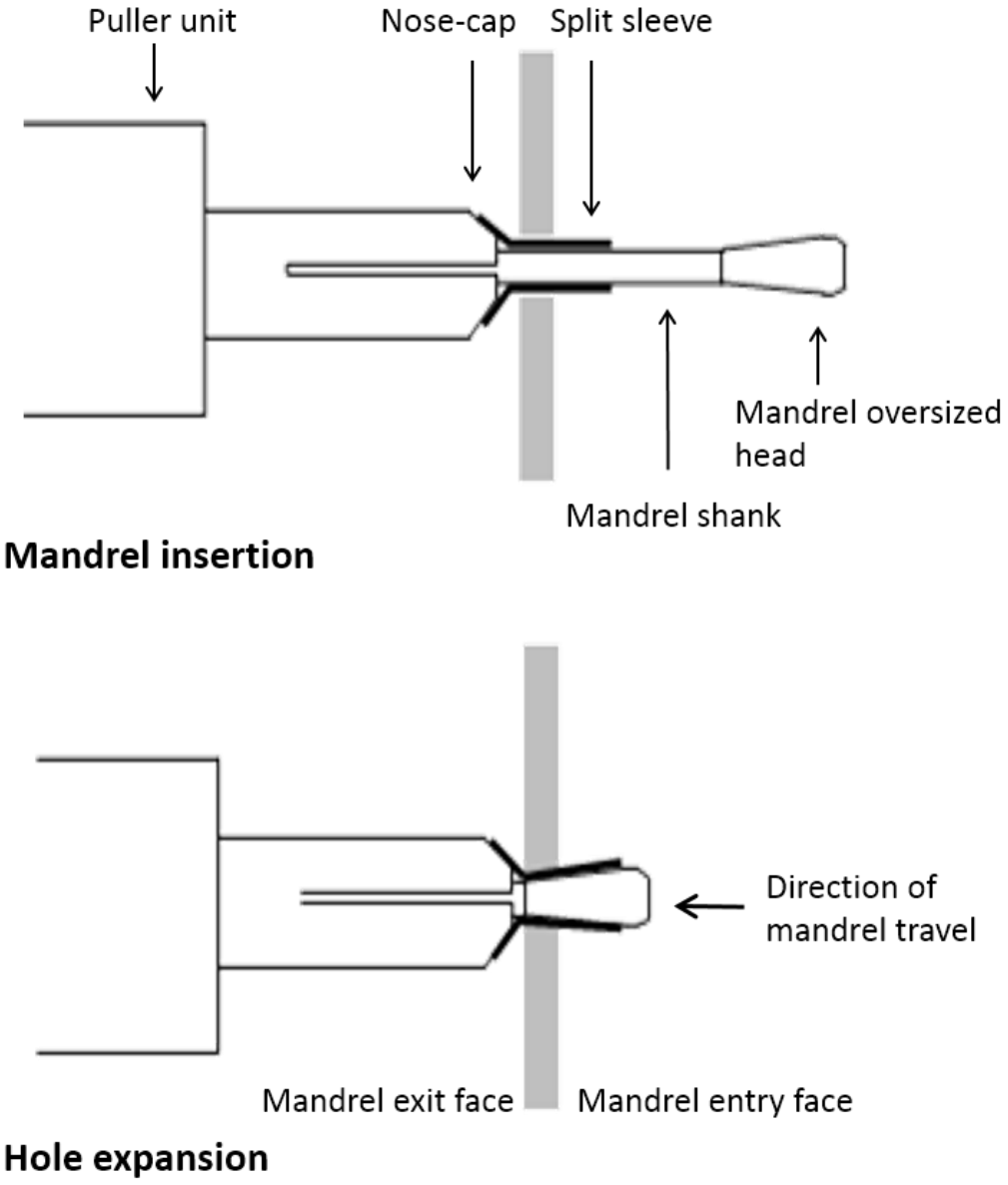

Figure 1.1 The schematic diagram for split sleeve cold expansion process.

1.1 Motivation for research

This research is motivated by the previous work carried out by Backman, as part of his doctoral thesis[6], on the analysis of cold expansion and riveting operations in monolithic aluminium and fibre metal laminate materials. It addresses some of the

research questions put forward in Backman's doctoral thesis as the possible avenues for future research.

It has been noticed in many earlier investigations[7-13] that cold expansion results in a non-uniform residual stress field through the thickness of the component due to different geometric constraints at the mandrel entry and exit faces of the component, which plays a limiting role in the fatigue performance of cold-expanded holes. The role of component thickness in the effectiveness of the cold expansion process in developing a highly compressive residual stress field is not well-established as there has been limited research[14-16] which focused explicitly on this aspect of the cold expansion process. The dominating factor in this context appears to be the component thickness to hole diameter ratio, t/D_o, where t and D_o are the component thickness and the initial hole diameter respectively. FTI[5], who are the manufacturers of the split sleeve cold expansion tools, support the cold expansion of holes as small as $t/D_o = 0.2$. However, a discussion with some sectors of the aerospace industry implied that, at these small t/D_o ratios, the components are usually stacked during cold expansion to ensure that the t/D_o ratio, resulting from combined thickness of the stack, is at least 1, for a more consistent outcome. Therefore, one of the broad objectives, envisaged at the start of this research, was to establish the role of t/D_o ratio in the effectiveness of cold expansion process for both the monolithic and stacked components.

In general, there is a consensus in the literature that the cold expansion process is substantially effective in enhancing the fatigue life of fastener holes. This improvement in fatigue performance is believed to be solely due to the

compressive residual stress field, developed by cold expansion, whose magnitude close to the hole edge approaches the yield stress of the material. Despite the presence of such high compressive residual stresses, fatigue cracks do appear occasionally from the fastener holes, during service life of the component. This indicates a need for an investigation to identify the circumstances under which cracks originate from the cold-expanded holes. There seems to be a lack of understanding in the literature regarding the mechanism of fatigue crack propagation through a highly compressive residual stress field, in particular, on the role of these compressive residual stresses in shielding the crack from the influence of external applied loads. Thus, one of the major stimuli for this research was to develop an understanding of the fatigue behaviour of cracks emanating from cold-expanded holes and their influence on the surrounding residual stress field, which should lead to better predictive capability for the fatigue life of such holes.

1.2 Thesis outline

The following chapters in this thesis start with a brief overview of the chapter and conclude with a summary highlighting the main findings of the chapter. This thesis consists of ten chapters in total which are as follows:

Chapter 1: Introduction

This chapter provides overview of the cold expansion process and describes the factors which motivated the research presented in this thesis.

Chapter 2: Literature review

A detailed review of the existing body of literature on various aspects of the cold expansion process has been presented in this chapter. The literature review was aimed at identifying the knowledge gaps where original contributions were required. The aims and objectives of this research which followed directly from the identified knowledge gaps are reported in this chapter.

Chapter 3: Background

This chapter describes the three main measurement techniques utilised in this research i.e. digital image correlation (DIC), thermoelastic stress analysis (TSA) and synchrotron x-ray diffraction (SXRD). The reasons for the choice of these techniques for achieving specific objectives of this research are also discussed in this chapter.

Chapter 4: Material, Specimen and Experimental procedures

This chapter provides details of the material and the specimen geometry employed in this research. The procedure for performing cold expansion of holes and the experimental setups for the three measurement techniques i.e. DIC, TSA and SXRD utilised in this research are also described in this chapter.

Chapter 5: Cold expansion in single specimens

This chapter reports the results of the DIC experiments which were performed to analyse the hole deformation resulting from cold expansion in single aluminium specimens. The effect of specimen thickness on the effectiveness of the cold expansion process in creating an axisymmetric compressive residual stress zone has been analysed in this chapter.

Chapter 6: Cold expansion in stacked specimens

This chapter shows the results of the DIC experiments which were aimed at investigating the cold expansion of holes in stacked aluminium specimens. The improvement in the axisymmetry of the compressive residual stress zone caused by stacking is discussed in this chapter.

Chapter 7: Analysis of fatigue cracks emanating from cold-expanded holes

This chapter presents the results obtained from first half of the experimental study on the fatigue performance of cold-expanded holes which focused on developing understanding of the behaviour of fatigue crack propagation utilising TSA. The fractographic analysis performed to qualitatively determine the influence of the residual stresses induced by cold expansion on fatigue crack initiation is also reported in this chapter.

Chapter 8: Residual elastic stresses around cold-expanded holes

This chapter presents the results obtained from second half of the experimental study on the fatigue performance of cold-expanded holes which focused on determining the influence of fatigue cracks on the beneficial compressive residual stresses developed from cold expansion using SXRD.

Chapter 9: Discussion

This chapter discusses the findings of the two major experimental studies carried out in this research; first being related to the study of hole deformation resulting from cold expansion, which is reported in Chapters 5 & 6, and the second one about the fatigue performance of cold-expanded holes, which is presented in Chapters 7 & 8.

Chapter 10: Conclusions

This chapter highlights the key contributions of the research presented in this thesis. It also includes a section on recommendations for future work on the subject of cold expansion.

2 LITERATURE REVIEW

A detailed review of the previously published literature on cold expansion is presented in this section which was aimed at attaining an in-depth knowledge of this subject area as well as identifying the knowledge gaps where original research contributions were required. Various aspects of cold expansion have been studied extensively over the past four decades because of its importance in the design of lighter aircraft structures with enhanced structural integrity. The research conducted so far on this subject can be categorised into two broad categories: residual strains developed by the cold expansion process and the fatigue performance of cold-expanded holes.

2.1 Residual strains developed by cold expansion process

The experimental techniques that have been used to study the development of residual strains during cold expansion process can be categorised on the basis of the strain measured, that is, total residual strain or elastic residual strain. In both cases, 'residual' indicates that the strain remains locked into the material after the cold expansion process. The residual elastic strain arises from the elastic spring-back of the material around the plastic region and is typically measured non-destructively using diffraction techniques[9, 10, 17, 18] or destructively using the Sachs method[8, 16, 17, 19]. The residual stresses can be determined directly from the measured residual elastic strains using Hooke's law. The total residual strain, on the other hand, is the combination of the residual elastic and plastic strains resulting from elastic-plastic loading during mandrel insertion and the unloading when the mandrel is removed. The magnitude of residual stresses cannot be

obtained directly from the total residual strains; however, their interpretation can reveal meaningful information about the mechanics of hole deformation during cold expansion process.

2.1.1 Total residual strain measurements

Moiré was one of the earliest full-field strain measurement techniques used to measure total residual strains resulting from cold expansion[20, 21]. Cloud[20] used moiré photography to produce strain maps for various degrees of cold expansion. The cold expansion process investigated in his work utilised a solid sleeve to expand the hole which remained in place after hole expansion. Link and Sanford[21] studied the split sleeve cold expansion process using moiré interferometry. They measured radial displacements along a line at 90^{o} around the hole circumference from the sleeve split position, for various degrees of cold expansion, on both the mandrel entry and exit faces. The radial displacements were differentiated with respect to the radial length to calculate radial strains. Link and Sanford[21] reported a difference in the radial strain profiles on the mandrel entry and exit faces, which indicated the three-dimensional (3D) nature of the cold expansion process. Another full-field strain measurement technique used to study the cold expansion process is the grid method[22-24]. Ball and Lowry[24] used the grid method to measure total residual strains in both hoop and radial directions on the mandrel entry and exit faces of a 6.35 mm thick aluminium specimen as a result of a 5% cold expansion using a split sleeve. They also reported a slight difference between the magnitude of the measured strain values on the mandrel entry and exit faces. The difference was more significant for the radial strains than for the hoop strains.

More recently, Backman and his co-workers[25, 26] used the digital image correlation method to measure total residual strains resulting from split sleeve cold expansion. They investigated the effect of hole-to-free-edge distance on the hoop strains around cold-expanded holes. It was reported that as the hole-to-free-edge distance decreased, hoop strains increased exponentially. This implies that, for the hole located very close to the free edge, there is not enough material at the edge to provide adequate constraint to the plastic deformation resulting from hole expansion and generate a spring-back effect, thereby, reducing the effectiveness of cold expansion. The strains around cold-expanded holes have also been measured using strain gauges[27-29]. However, strain gauges measure an average strain over their finite gauge length which makes them unsuitable for resolving strains near the hole edge, where the strain gradients are very high.

2.1.2 Extent of plastic deformation resulting from cold expansion

The size of the plastic zone developed around the cold-expanded hole is an indication of the effectiveness of cold expansion process. The development of a larger plastic zone during hole expansion results in a higher spring-back force from the elastic material surrounding the plastically deformed material, thus creating a more compressive residual elastic stress field. Some of the experimental investigations focused specifically on determining the extent of the elastic-plastic boundary after cold expansion either by measuring the total residual strains[27, 28, 30] or the out-of-plane deformation around the hole[27, 31, 32]. In all these investigations, the radius of elastic-plastic boundary, r_p was determined using an underlying assumption that in the elastic domain ($r \geq r_p$), the radial and tangential stresses can be defined by the theoretical solution for a hole expansion by a

uniform pressure in an infinite plate, under a state of plane stress, as dictated by the following equations[27]:

$$\sigma_r = -\frac{\sigma_y}{\sqrt{3}}\left(\frac{r_p}{r}\right)^2 \qquad 2.1(a)$$

$$\sigma_t = \frac{\sigma_y}{\sqrt{3}}\left(\frac{r_p}{r}\right)^2 \qquad 2.1(b)$$

where σ_r and σ_t are the radial and tangential stress components respectively and σ_y and r are the yield stress and the radial distance from hole centre, respectively. Since the radial and tangential stresses are equal in magnitude and opposite in sign, the strain in the out-of-plane direction (ε_z), defined by the following equation for the case of plane stress, will be zero in the elastic domain[31]:

$$\varepsilon_z = -v\frac{\sigma_r + \sigma_t}{E} \qquad 2.2$$

where E and v are the Young's modulus and Poisson's ratio respectively.

Therefore, the radius of elastic-plastic boundary were estimated in these investigations either by locating where the magnitudes of radial and tangential strains were equal[27, 28, 30] or where the out-of-plane displacements were zero[27, 31, 32].

Poolsuk and Sharpe[27] determined r_p by measuring both the total residual strains and the out-of-plane displacements around a hole, in aluminium specimens of 6.35 and 3.18 mm thicknesses. In this investigation, the holes were expanded utilising the solid sleeve cold expansion process. The degree of expansion or interference used, ranged from 3 - 4.6 %. Their results showed a slight increase in the values of r_p with increasing degree of interference. Overall, the r_p values were

found to be higher for the thick specimens in comparison to the thin ones. Sanford and Link[31] estimated the location of the elastic-plastic boundary by measuring the out-of-plane displacements using holographic interferometry on the mandrel entry face of a 6.35 mm thick aluminium specimen. They utilised the split sleeve cold expansion process for expanding the holes and investigated the expansion levels ranging from 4 - 9.6 %. They demonstrated that, at expansion levels higher than 5 %, the out-of-plane plastic flow restricts further plastic deformation in the radial direction. Hence, the radius of the elastic-plastic boundary does not increase proportionally with expansion. The values for r_p determined by Sanford and Link[31] were found to be higher than those determined by Poolsuk and Sharpe[27], for the same expansion levels. This indicates that the split sleeve is more effective than the solid sleeve in translating the axial motion of the mandrel into radial expansion by minimising the out-of-plane plastic deformation close to the hole edge.

2.1.3 Residual elastic strain measurements

One of the earliest measurements of residual elastic stresses around cold-expanded holes were performed by Cannon et al[33]. They used the sectioning technique by employing strain gauges to determine residual elastic hoop stresses around rail end bolt holes, which were cold-expanded by split sleeve cold expansion process. They reported almost linear residual hoop stress distributions along the transverse centre line of the hole, indicating poor spatial resolution of the sectioning method.

Hermann and his co-workers[16, 17, 34] used the destructive Sachs method to measure the residual elastic stress distributions around holes in aluminium specimens of thicknesses ranging from 1.6 - 19 mm. They used an “in-house” developed

expansion tool, based on a roller burnishing (RB) operation, to perform cold expansion. One of the primary focuses of their work was to compare their RB method with the FTI's split sleeve cold expansion. Their results showed that the radius of the elastic-plastic boundary created by the RB method is significantly smaller in comparison with the one generated by split-sleeve cold expansion, which resulted in lower magnitude of compressive residual stresses. The poor performance of their RB process was attributed to the excessive out-of-plane plastic flow of the material at the hole edge during cold expansion. Sachs method was also utilised extensively by Özdemir and his co-workers[8, 35, 36] to study through-thickness variation of residual elastic stresses in 5 mm thick aluminium specimens. On the other hand, Stefanescu et al employed both the laboratory[9, 37-39] and synchrotron[18] x-ray diffraction techniques to analyse surface and through-thickness distributions of residual elastic stresses in specimens similar to the ones used by Özdemir and his co-workers[8, 35, 36]. A comparison between the three-dimensional residual hoop stress fields, determined by Stefanescu et al[37] and Özdemir and Edwards[36], around a 4 % cold-expanded hole is shown in Figure 2.1. The two plots show similar residual stress profiles and a significant through-thickness variation in the residual stresses can be noticed in both of these plots as well.

Several researchers[7-13] performed residual stress measurements to demonstrate that the magnitude of the compressive residual stresses, developed by cold expansion, are lower on the mandrel entry face compared to the exit face. This phenomenon plays a limiting role in the fatigue performance of cold expanded holes as the crack initiates preferentially from the mandrel entry face[40-46]. Forgues

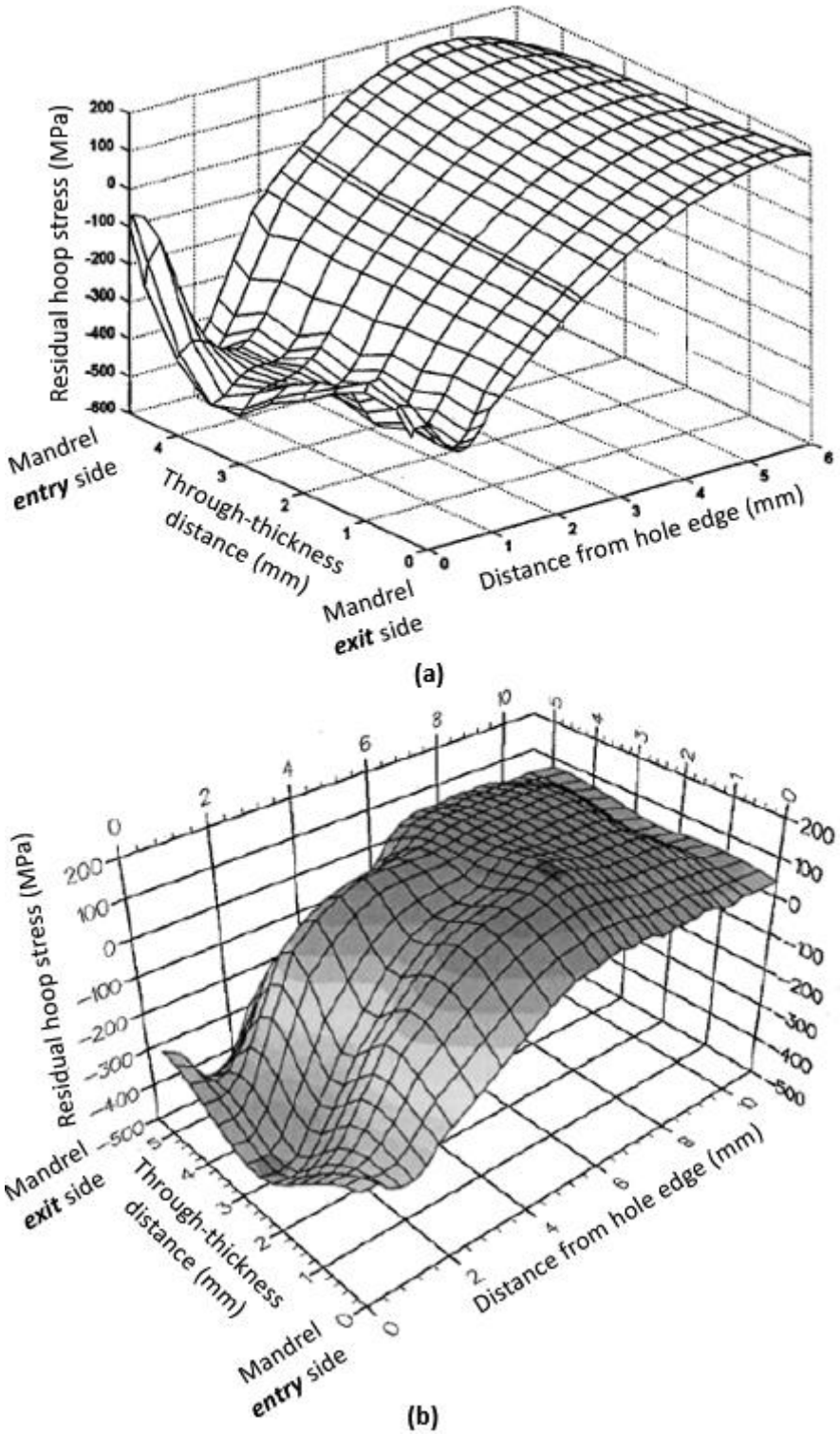

Figure 2.1 Three-dimensional residual hoop stress distribution around 4% cold-expanded hole in a 5 mm thick aluminium specimen, determined using (a) Sachs method[36] and (b) combination of x-ray and neutron based diffraction[37].

et al[47] suggested that the radial displacements at the hole edge, during cold expansion, are the largest on the mandrel exit face due to the material volume

being pushed towards this face by the mandrel. This results in a relatively larger spring-back effect, thereby causing more compressive residual stresses on the exit face in comparison with the entry face. Another plausible explanation for this phenomenon, presented by Babu et al[48], is the difference in constraint conditions between the mandrel entry and exit faces.

A simple approach to resolve the issue of through-thickness variation in the residual stresses is to repeat the cold expansion process by reversing the mandrel direction so that the component face which was the mandrel entry face in the first cold expansion becomes the exit face in the second one[9, 49, 50]. Stefanescu[9] performed residual stress measurements on holes, which were cold-expanded twice in the opposite directions, to demonstrate that the difference between the residual stresses on the mandrel entry and exit faces was significantly reduced, which resulted in an overall improvement in the fatigue performance. Despite this approach being straight-forward in creating uniform residual stresses through the thickness of the component can not be applied to structures for which only one face is accessible.

2.1.4 Theoretical solutions for cold expansion

A significant amount of theoretical work[51-57] has also been carried out in the past to develop closed form solutions to estimate the total residual strains and residual elastic strains developed around cold-expanded holes. All closed form solutions are based on the assumption of a circular disc with an inner radius being subjected to a uniform pressure. The analytical solutions can be classified according to whether an assumption of plane stress or plane strain is made. An early plane

strain model was presented by Rich and Impellizzeri[53] in 1977 who assumed elastic-perfectly plastic loading of a thick plate of finite width with elastic unloading. Subsequently, Wang[54] developed a plane strain model of a thick finite-width plate with elastic non-linear strain hardening for both the loading and the unloading that included the Baushinger effect[58].

Interest in plane strain models has declined because observations from experiment showed that out-of-plane deformations were significant. Most plane stress models are based on the work of Hsu and Forman[52] in the 1970s who assumed a hole was being expanded in a thin infinite-wide plate of material represented by an elastic non-linear strain-hardening model with elastic behaviour on unloading. In the 1990s, Ball[56] extended this model by assuming elastic non-linear strain hardening with the Baushinger effect present during spring-back. Wanlin[55] made the same change to modelling of the spring-back behaviour but considered a plate of finite width; however, in 2005, Zhang et al[57] recast the model by Wanlin[55] to include an explicit solution of the unloading step. This model takes into account the elastic-plastic loading upon mandrel insertion and also addresses the development of a reverse yielding zone around the hole edge, due to the spring-back effect, upon mandrel removal.

2.1.5 Computational modelling of cold expansion process

Owing to the complicated mechanics of hole deformation during cold expansion process, many investigations[7, 11-14, 43, 44, 59-67] have utilised finite element (FE) modelling to study the generation of residual stresses during cold expansion. The schematic presented in Figure 2.2 shows different strategies used by researchers to model the cold expansion process in two dimensions (2D). The simplest 2D FE

model in the XZ plane, developed by Priest et al[7], involved axisymmetric expansion of the hole by a uniform radial displacement through the plate thickness (see Figure 2.2c). The predicted residual hoop stresses at the hole edge were found to be less compressive on the surface compared to the mid-plane of a plate. This residual stress gradient through the plate thickness was attributed to the progressive change in the deformation state from plane strain at the mid plane to the plane stress on the surface.

Poussard et al[59] compared the model, developed by Priest et al[7], with a 2D FE model in the XY plane (see Figure 2b). In this model, the hole was expanded by employing axisymmetric radial displacement and considering both the plane stress and the plane strain conditions. It was reported that the plane stress and plane strain assumptions are inadequate in approximating the three-dimensional residual stress field. Kang et al[62] extended the 2D FE model of Priest et al[7] in three dimensions, where the hole expansion was modelled by axisymmetric radial displacement which was uniform through the plate thickness. The results obtained from their model reaffirmed the conclusions drawn by Priest et al[7] that the through-thickness variation in residual stresses exists, which is symmetric about the mid-plane and can be attributed to the change in stress state across the plate thickness.

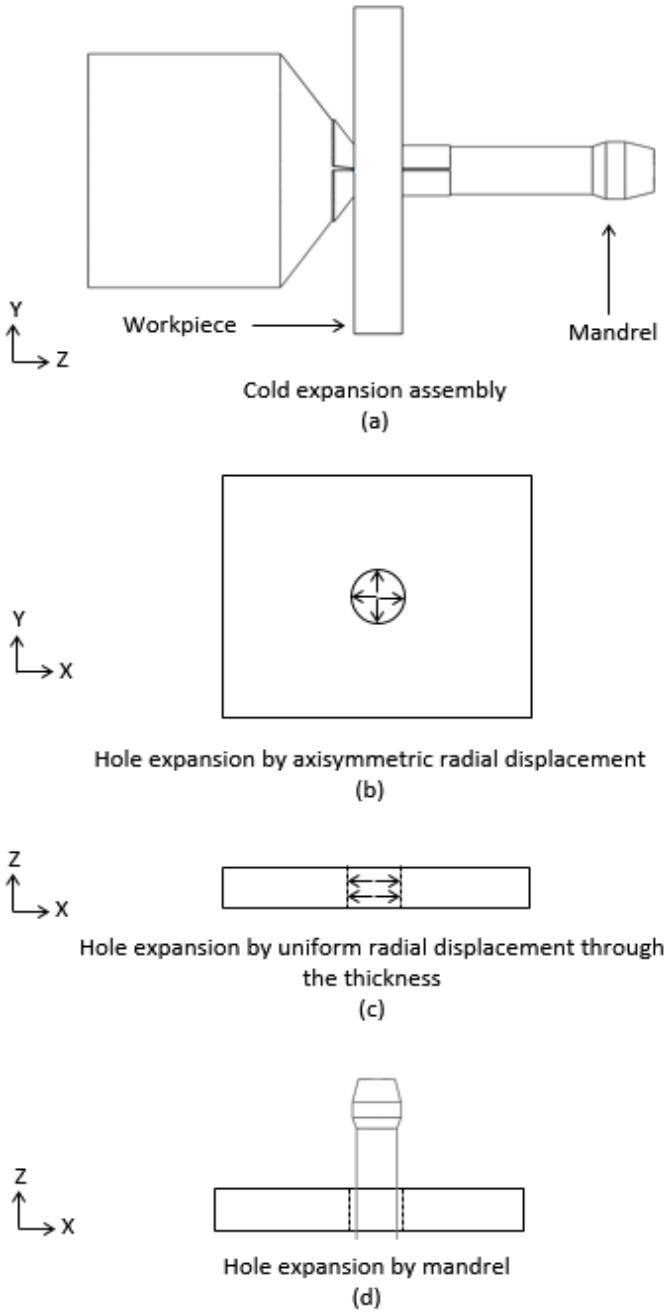

Figure 2.2 Schematic showing (a) cold expansion assembly and (b-d) different strategies used for finite element modelling of the cold expansion process in two dimensions.

As mentioned in an earlier section, in the actual cold expansion process, the mandrel pull results in the material at the hole edge being pushed towards the mandrel exit face. This causes a through-thickness gradient in the residual stress field which is not symmetric about the mid-plane and is not caused solely by the variation in the stress state across the plate thickness. Therefore, an accurate

prediction of the asymmetric residual stress field resulting from the actual cold expansion process cannot be made by an FE model which assumes hole expansion by a uniform through-thickness radial displacement. A few studies[11, 60, 63] have modelled the cold expansion process in 2D by expanding the hole using a mandrel as shown in Figure 2d. This modelling strategy is computationally inexpensive in comparison to 3D models and is capable of making reasonable prediction of the asymmetric residual stress field.

With reference to the 3D FE models involving hole expansion by a mandrel, many investigations[11, 14, 43, 63, 65] were able to capture the asymmetric residual stress field through the plate thickness. It was also reported in these investigations that the magnitude of residual compressive stress at the hole edge was lower on the mandrel entry face compared to the exit face, which is generally consistent with the experimental observations[7-13]. Few researchers had considered the presence of continuous[12, 63, 67] or split[13, 14, 65] sleeve between the mandrel and the internal hole edge in their 3D FE models, whilst, many[43, 44, 61] have ignored it under an assumption that its sole purpose is to limit the out-of-plane deformation at the hole edge and that it marginally influences the generation of the residual stress field. The FE simulations[14, 65] which involved the split sleeve have demonstrated the generation of a non-axisymmetric residual stress field around the hole and a significant discontinuity in the residual stresses at the location of split position where a ridge is created due to the gap between the two edges of the split. The creation of the ridge is also referred to as “pip” in the literature.

Most of the cold expansion simulations considered aluminium as their plate material and modelled it as an elastic non-linear strain hardening material with the Baushinger effect present during spring-back. This material model is referred to as the kinematic hardening model which is in contrast to the isotropic hardening model which does not include the Baushinger effect. The kinematic hardening model was found to be the most suitable for accurately predicting the residual stresses close to the hole edge which are affected significantly by the reverse yielding during the spring-back effect. There seems to be an ambiguity in the literature about the effect of friction between the contacts on the residual stresses. Some authors[13, 63, 66] have reported the frictional coefficient to be an insignificant parameter, whereas, a few[44, 65, 67] have demonstrated that its influence is localised close to the hole edge and is more significant on the mandrel entry face in comparison to the exit face.

This overview of the literature on computational modelling of the cold expansion process has revealed that the complexity of the FE models has increased substantially over the years. The recent FE models of split sleeve cold expansion take into account all the components and interactions involved in the actual cold expansion process and are capable of not only predicting the 3D residual stress distribution but also the out-of-plane deformation around the cold-expanded holes with reasonable accuracy[13].

2.2 Fatigue performance of cold-expanded holes

In some of the earliest investigations[68-70], the effectiveness of the cold expansion process in improving the fatigue performance of fastener holes was judged

predominantly by determining the increase in fatigue life of the specimens which contained a cold-expanded hole in comparison to the ones with an un-expanded hole. The foundation work for the fatigue assessment of various types of cold expansion and interference fit fastener systems was laid by Petrak and Stewart[68]. With reference to the cold expansion process, they investigated two systems i.e. split sleeve and solid sleeve by performing uniaxial fatigue tests on the specimens fabricated from a 6.35 mm thick aluminium plate. They reported that both the processes are significantly effective in improving the fatigue life of open hole specimens. Their results also implied that the creation of a ridge at the split position, during cold expansion by the split sleeve, does not have any adverse effect on the fatigue performance, as both the cold expansion processes produced comparable fatigue results. In other words, the statistical scatter in the fatigue results was bigger than the effect of the "pip".

Beaver et al[69] investigated the influence of two of the key variables involved in the split sleeve cold expansion process on the fatigue behaviour of open hole specimens i.e. the orientation of the split sleeve, and post cold expansion reaming for the removal of the surface upset close to the cold-expanded hole edge. Statistical analysis was performed on the data obtained from a series of fatigue tests and it was found that these factors do not have any significant adverse effect on the fatigue performance. The robustness of the split sleeve cold expansion, as demonstrated by Beaver et al[69], was likely to be one of the primary reasons for the widespread acceptance of this technique in the aerospace industry.

Beaver et al[69] was probably the first one to report in the open literature about the initiation of a fatigue crack at the hole edge from the mandrel entry face in the open cold-expanded holes resulting in a non-uniform crack front through the thickness of the specimen. Later, many studies[40-46], involving fractographic observations of the fatigue surface, proved this finding by reporting a significant difference in the extent of fatigue cracks at the mandrel entry face and the exit face. It was highlighted in these studies[40-46] that the primary crack tends to initiate at the hole edge from the entry face and propagates with a quarter-elliptical crack front. This characteristic behaviour of fatigue crack initiation from the mandrel entry face is primarily due to the lower magnitude of the compressive residual hoop stresses on this face in comparison to the exit face; a well-established fact confirmed by both experimental measurements[7-13] and FE model predictions[11, 14, 43, 63, 65] of the through-thickness residual stress distribution developed by the cold expansion process.

2.2.1 Stress intensity factors of cracks emanating from cold-expanded holes

Many investigations[24, 40, 71-77] used a more quantitative approach to analyse the fatigue performance of cold-expanded holes by determining the effective stress intensity factors (K_{eff}) for cracks emanating from such holes. In some of these investigations[24, 73, 75, 77], the calculated K_{eff} values were used to predict fatigue crack growth rates or the fatigue life as well, using the empirical relations similar to Paris' law[78], which relate the range of effective stress intensity factor (ΔK_{eff}) to the crack growth rate (da/dN). The conventional approach for determining K_{eff} for a crack propagating though a residual stress field involves linear superposition of

the stress intensity factors associated with the initial residual stress distribution, K_{res} and the applied mechanical loads, K_{app}. Most of the researchers[24, 71-73, 77] evaluated K_{res} using a weight function or Green's function approach, which is based on the work of Buckner[79] and Rice[80], to determine K_{eff}. However, a few researchers[76, 81, 82] performed FE analysis to predict K_{eff} for cracks emanating from cold-expanded holes.

Grandt[71] made one of the earliest predictions of K_{eff} which took into account the initial residual stress distribution, modelled as a crack face pressure, using a weight function approach. Their results showed a significant reduction in the effective stress intensity factors at the crack tip, due to the highly compressive nature of the residual stresses, which provided a qualitative explanation for the increased fatigue life of cracks originating from cold-expanded holes. Chandawanich and Sharpe[72] determined ΔK_{eff} experimentally, from the measured crack growth rates, by employing an empirical [ΔK_{eff} - da/dN] relation and also from the crack opening displacements measured using a laser-based interferometric system. The experimental results were compared with the theoretical predictions which were found to be in good agreement for cracks longer than 1 mm. The theoretical values for ΔK_{eff} were calculated in this work by taking into account the residual stress distribution, determined from the Hsu and Forman model[52], using a weight function approach. Later, Su et al[40] highlighted that the reason for poor agreement between the experimental and theoretical values of K_{eff} for cracks smaller than 1 mm, in the study by Chandawanich and Sharpe[72], was due to the overestimation of residual stress close to the hole edge by the Hsu and Forman model[52]. Su et al[40],

therefore, proposed a simplified residual stress model aimed at providing more realistic predictions of ΔK_{eff} for small cracks.

Theoretical predictions of fatigue lives for cracks originating from cold-expanded holes were made by Cathey and Grandt[73] as well as by Ball and Lowry[24], which showed a reasonable agreement with the experimental results. Their fatigue life predictions were based on the calculation of $\Delta K_{eff,}$ using a weight function approach, and the subsequent use of evaluated ΔK_{eff} in the empirical [ΔK_{eff} - da/dN] relation, which was then integrated with respect to the crack length. Pavier and his co-workers[76, 83] determined K_{eff} using a J-integral approach by carrying out an FE analysis. In their FE model, the residual stress field resulting from cold expansion was first quantified and the applied loads were then superimposed following the introduction of a crack in their simulation. They reported that weight function approaches provided non-conservative estimates of K_{eff} in comparison to their FE results.

Almost all the studies about the analytical or numerical predictions of K_{eff} for cracks emanating from cold-expanded holes have considered the initial state of the residual stress distribution, which was developed by the cold expansion process prior to fatigue loading. It was, therefore, intrinsically assumed that this initial residual stress distribution does not change with initiation or propagation of a fatigue crack. However, several researchers[72, 75, 76, 84] have highlighted that the residual stresses could potentially redistribute as the crack grows. The issue of residual stress redistribution is discussed in more detail in the next section. Stefanescu et al[77] defined the residual stress profile along the crack line as a

function of crack length in their theoretical calculations of K_{eff}. Their results showed that taking into account the variation in the residual stress distribution due to fatigue crack growth improves the accuracy of the K_{eff} prediction. This indicates that a reliable fatigue life prediction depends significantly on an accurate determination of the initial residual stress distribution along the crack line and its potential redistribution with crack growth should also be considered.

Another pertinent issue, which had been the focus of discussion in the literature, is whether cold expansion is effective in enhancing the fatigue life by delaying the fatigue crack initiation or by retarding the crack growth rate of a fatigue crack. The results reported by Chandawanich and Sharpe[72] shows that cold expansion improves the fatigue life by retarding the crack growth rate and has negligible influence on the fatigue crack initiation life, which was defined as the number of cycles to grow a crack of 0.1 mm. Chao and Xiulin[41] focused more thoroughly on the influence of cold expansion on the fatigue crack initiation and reported that cold expansion does improve the resistance to fatigue crack initiation, which was defined as the number of cycles to grow a crack of 0.25 mm. Lacarac et al[85] analysed the influence of maximum applied stress and the stress ratio on the growth rates for cracks emanating from cold-expanded holes and concluded that cold expansion is significantly effective in retarding the growth rate for cracks longer than 1 mm. Corroborating the results of Lacarac et al[85], Zhang and Wang[42] demonstrated that the cold expansion enhances the fatigue life primarily by substantially reducing the growth rate of cracks in the range of 0.5 - 1.5 mm. More recently, Backman[6] extensively studied the fatigue behaviour of cold-expanded holes in GLARE (Glass Laminate Aluminium Reinforced Epoxy). His overall

conclusions were that cold expansion was minimally effective in reducing the growth rate of short cracks of the order of 1 mm; which, according to Lacarac et al[85], is also true for cold-expanded holes in monolithic aluminium specimens. There seems to be a lack of agreement about the impact of cold expansion on the initiation and development of fatigue cracks in the early stage of fatigue process. However, it is clear that the compressive residual stress field induced by cold expansion is significantly effective in retarding the growth rate of cracks past the short crack regime.

2.2.2 Relaxation of residual stresses around cold-expanded holes

As mentioned earlier, effectiveness of the cold expansion process in enhancing the fatigue performance of fastener holes is well-established. However, compliance with the damage tolerance requirements of an airframe structure needs to be achieved without considering the beneficial effects of cold expansion[86]. One of the reasons for reluctance to account for these beneficial effects is the concern for potential redistribution of the compressive residual stresses imparted by cold expansion[87]. Despite significant relevance to the aerospace industry, few investigations[18, 33-35, 37, 38, 88-91] have focused on the potential redistribution or relaxation of these residual stresses resulting from either fatigue loading or due to the propagation of fatigue cracks from cold-expanded holes. Cannon and his co-workers[33] were probably the first to state that the application of large compressive loads can cause the relaxation of these compressive residual stresses. Stefanescu et al[37] later reaffirmed their conclusions by determining the residual stress relaxation close to the hole edge, resulting from compressive overloads, using a laboratory x-ray diffraction technique. It is, therefore, agreed upon that the

fatigue loads causing large-scale plastic deformation at the hole edge could significantly alter the initial residual stress distribution. Compressive loads are particularly detrimental in this context, because only a small magnitude load is required to cause the highly compressive residual stresses at the hole edge to exceed the yield stress.

Some researchers[18, 34, 35, 38, 88] have reported a relaxation or reduction in the residual stresses under fatigue loads which were not expected to cause large-scale plastic deformation at the hole edge. Herman and Moffat[34] utilised a destructive Sachs method to determine the relaxation at such fatigue loads in aluminium-lithium alloy specimens; though, no attempt was made to explain the cause of this relaxation. Özdemir and Edwards[35] used a similar Sachs technique to show a pronounced stress relaxation in 7075 aluminium specimens. The cause of this relaxation was reported to be the growth of short fatigue cracks from the hole edge, which were ultimately arrested as the residual stress distribution stabilised. Their results, therefore, indicate that the plastic zone associated with the crack tip could potentially affect the initial distribution of residual stresses. Stefanescu and his co-workers[18, 38] investigated the effect of a fatigue crack on the initial residual stress distribution in specimens, similar to those used by Özdemir and Edwards[35], using both laboratory and synchrotron x-ray diffraction techniques. In their work, a fatigue crack was grown from a 0.2 mm through-thickness electric discharge machined (EDM) notch at the edge of the hole. A relatively less-pronounced relaxation of residual stresses close to the hole edge was reported. This could be attributed to the presence of the notch because it both involves material removal with some associated plastic work and a geometric discontinuity in the hole

circumference that is significant enough to cause interruption of the load paths, and thus, redistribution of the residual stresses around its vicinity.

Lacarac et al[85] used a different approach to investigate the issue of residual stress relaxation by measuring the crack opening stress, σ_{op} at different crack lengths. The values for σ_{op} were found to be constant for all crack lengths. In a more recent investigation by Backman et al[92], crack opening displacements along the crack flanks were found to be constant across the residual compressive stress zone, which is in agreement with the results reported by Lacarac et al[85].The findings of these investigations, therefore, imply that the residual stress distribution does not necessarily relax as a result of fatigue crack propagation, which is contrary to the conclusions drawn by Özdemir and Edwards[35] and Stefanescu et al[18, 38]. This highlights an ambiguity in the literature about the loading conditions under which residual stresses are expected to relax significantly.

2.3 Identification of knowledge gaps

A comprehensive review of the literature regarding cold expansion has been carried out with the aim of identifying gaps in the existing body of knowledge about this subject, which need to be addressed. Various aspects of both the hole deformation, resulting from cold expansion, and the fatigue performance of cold-expanded holes have been researched extensively. It has been established that the split sleeve process, which is the most widely used process of performing cold expansion, induces a non-uniform residual stress field through the thickness of the component, which is also non-axisymmetric about the hole axis. A few studies[14-16] have focused, explicitly, on the influence of sheet thickness on the effectiveness

of the cold expansion process in developing a highly compressive residual stress field around the cold-expanded holes. The effect of sheet thickness has been analysed predominantly in the context of the stress state during hole deformation and it was concluded that with increasing sheet thickness, the state of stress changes from plane stress to plane strain, causing the resulting residual stresses to be slightly more compressive. It has also been suggested that the through-thickness residual stress distribution is more uniform in thin sheets in comparison to thick ones[13]. In the actual cold expansion process utilising a split sleeve, the axial movement of the mandrel causes an out-of-plane displacement close to the hole edge, not solely related to the plane stress condition on the surface, which limits the radial expansion of the hole. Moreover, the hole deformation is significantly influenced by the presence of the split sleeve as well. The mechanics of hole deformation involved in the split sleeve cold expansion process is, therefore, complicated and the above mentioned factors, which are interrelated, need to be thoroughly analysed in establishing the role of sheet thickness in the effectiveness of this process.

With regards to sheet thickness, a more appropriate factor which needs to be analysed is the sheet thickness to initial hole diameter ratio, t/D_o. A discussion with some sectors of the aerospace industry implied that the current practice is to stack thin sheet components together for simultaneous cold expansion to ensure that the t/D_o ratio, resulting from combined thickness of the stack, is at least 1, for a more consistent outcome. On the other hand, the most widely recognised manufacturer of the split sleeve cold expansion tools, FTI[5] supports the cold expansion of holes as small as $t/D_o = 0.2$. This highlights the need to investigate

the influence of t/D_o ratio on the effectiveness of cold expansion utilising a split sleeve, in developing a compressive residual stress field around the fastener holes, in both monolithic and stacked components.

The literature regarding the fatigue of cold-expanded holes clearly shows that cold expansion provides substantial improvements in fatigue life. Overall, there has been a consensus that the compressive residual stress field developed by cold expansion is significantly effective in shielding the crack from the service loads, thereby, reducing the magnitude of K_{eff} at the tip of a growing crack which, in turn, causes a substantial decrease in the crack growth rate. The theoretical models found in the literature can make reasonable fatigue life predictions for cracks emanating from cold-expanded holes, provided, the estimated residual stress distribution, considered in the model, adequately represents the actual distribution. What is less clear in the literature is the influence of fatigue crack propagation on the surrounding residual stresses. Some researchers[35, 38, 77] have reported significant relaxation or redistribution of the residual stresses as the fatigue crack grows which, according to them, must be taken into account for reliable fatigue life predictions; whilst, others[24, 73] have made accurate fatigue life predictions by ignoring any residual stress relaxation. It is, therefore, important to develop a clear understanding about the potential for and causes of any relaxation of these residual stresses.

2.4 Research objectives

The two primary aims of this research which followed directly from the identified knowledge gaps were: (1) to establish the role of sheet thickness in the

effectiveness of split sleeve cold expansion process in developing a compressive residual stress field around the cold-expanded hole in both single and stacked sheets and (2) to determine the influence of fatigue loading and propagation of a fatigue crack initiating from the cold-expanded hole edge on the surrounding beneficial compressive residual stresses. To achieve these aims, the following research objectives were laid out:

A. Measure the deformation fields developed as a result of split sleeve cold expansion in single specimens of two different thicknesses with t/D_0 ratios close to 0.2 and 1 for the thin and the thick specimens, respectively. Devise a methodology to interpret the measured deformation fields for the purpose of establishing the effect of sheet thickness on the effectiveness of cold expansion process in creating a compressive residual stress field around the cold-expanded hole.
B. Investigate the cold expansion of holes in stacked specimens by exploring the possibility of measuring deformation fields in the individual specimens of the stack. Implement the methodology developed for analysing cold expansion in single specimens to determine whether stacking improves the development of compressive residual stress field.
C. Experimentally study the fatigue behaviour of cracks emanating from cold-expanded holes to get meaningful insights into the mechanism of fatigue crack propagation through a highly compressive residual stress field and the interaction of the crack tip plastic zone of a growing crack with the surrounding residual stresses.

D. Measure residual elastic stresses, non-destructively, in both the un-cracked and the cracked cold-expanded hole specimens for evidence of any significant residual stress relaxation due to fatigue loading or propagation of a fatigue crack.

2.5 Research hypothesis

The plastic zone developed as a result of cold expansion can provide meaningful information about the effectiveness of the cold expansion process in creating an axisymmetric compressive residual stress zone around the cold-expanded hole. In the past, several researchers[27, 28, 30-32] attempted to measure the extent of plastic zone resulting from cold expansion. However, these measurements were discrete, and in most cases, the extent of plastic zone was determined along the radial line at 90° from the position of split in the sleeve. It was hypothesized that the evaluation of the shape and size of the plastic zone from the measured full-field strain data around the cold-expanded hole will be critical in establishing the role of t/D_o ratio in the effectiveness of the split sleeve cold expansion process in creating an axisymmetric compressive residual stress zone.

As mentioned in an earlier section, there has been a long-standing ambiguity in the literature about the influence of fatigue crack propagation on the beneficial compressive residual stresses. This ambiguity is partially due to the two different approaches employed by the researchers to develop fatigue cracks from the cold-expanded holes. In some studies, the cracks were grown from a notch installed at the cold-expanded hole edge[24, 38, 85], whilst in other investigations[35, 41, 72], the fatigue cracks were initiated naturally from the hole edge in the absence of any starter notch. There has been some evidence in the literature which suggests that

the crack grown from a notch is unable to produce the effect of a 'real' fatigue crack on the surrounding compressive residual stresses primarily because installing a notch involves material removal with some associated plastic deformation. It was, therefore, decided to develop understanding of the behaviour of fatigue cracks which initiate naturally from the cold-expanded holes.

2.6 Summary

A comprehensive review of the literature on cold expansion has been presented in this chapter. The first section provides an overview of the literature regarding the study of hole deformation resulting from cold expansion and the second section focuses on the research carried out so far about the fatigue performance of cold-expanded holes. The knowledge gaps in the existing body of literature on cold expansion has been discussed in the third section. It was identified from the literature review that the role of sheet thickness on the effectiveness of the cold expansion process in creating an axisymmetric compressive residual stress zone is not established. It was also revealed that there is an ambiguity in the literature about the influence of fatigue crack propagation on the beneficial compressive residual stresses around the cold-expanded holes. The research objectives which followed directly from the identified knowledge gaps have been listed in the fourth section. Finally, a research hypothesis has been presented in the fifth section which outlines an approach though out to tackle the objectives of this research.

3 BACKGROUND

This chapter provides background on the three main measurement techniques which were utilised in this research i.e. digital image correlation (DIC), thermoelastic stress analysis (TSA) and synchrotron x-ray diffraction (SXRD). Backman[6], as part of his PhD research, implemented the rational decision methodology, proposed by Olden and Patterson[93], to identify a suitable experimental mechanics technique to measure strains around fastener holes resulting from both the cold expansion and riveting process. It was concluded from the results of the rational decision process that DIC is the most suitable technique for performing strain measurements around fastener holes. The decision for selecting DIC in this research to measure surface deformation around holes, resulting from split sleeve cold expansion, in both monolithic and stacked aluminium specimens was, therefore, based on the conclusions from the rational decision process carried out by Backman[6].

DIC could also be potentially employed to study the fatigue cracks emanating from cold-expanded holes. The effective stress intensity factor range (ΔK_{eff}) of the fatigue crack tip is determined using DIC by first evaluating the minimum (K_{min}) and maximum (K_{max}) stress intensity factors. In cases where crack closure is present, K_{min} is not experienced by the crack tip at the minimum load, instead it is experienced at the instance during the loading cycle where the crack starts to open. Therefore, in order to determine K_{min}, a series of images needs to be acquired by the DIC setup during the loading cycle to be able to identify the instance where the crack faces start to separate. TSA, on the other hand, has the

advantage that it can determine ΔK_{eff} directly from the captured thermoelastic data representing the cyclic stress fields ahead of the fatigue crack. This is one of the primary reasons for employing TSA in this research to study the mechanism of fatigue crack propagation through a highly compressive residual stress field developed by cold expansion. The capability of TSA in directly determining ΔK_{eff} from the thermoelastic data is explained in more detail later in the chapter. One of the objectives of this research was to measure the residual stresses around cold-expanded holes. SXRD was used for this purpose because of its capability of performing non-destructive, high resolution, residual stress measurements in metallic components at much greater depths.

3.1 Digital image correlation

DIC is a non-contact optical technique used for full-field shape and deformation measurements. This technique is usually split into two levels of complexity: i.e. two-dimensional (2D) and three-dimensional (3D). 2D DIC involves a single digital camera and is capable of accurately measuring in-plane displacements on the object's surface, only if the surface can be considered flat and the loading does not cause significant out-of-plane motion of the object[94]. 3D DIC utilises the concepts of stereo-camera photogrammetry, and therefore, involves at least two digital cameras to obtain complete information about the location and orientation of the object's surface with respect to the reference camera of the stereo-vision setup. Hence, 3D DIC is capable of measuring surface topography and 3D displacements of a non-planar object's surface.

3.1.1 Two-dimensional digital image correlation

The equipment used in a 2D DIC setup includes a single digital camera and a LED light source for appropriate illumination of the object's surface over which the measurements needs to be performed. For accurate measurement of in-plane displacement, the object's surface needs to be planar and parallel to the sensor plane of the camera. Also, the deformation needs to be confined within the object's surface plane. The relative out-of-plane displacement of an object's surface with respect to the camera sensor plane can cause significant changes in magnification, which would introduce displacement gradients not related to surface deformation, thereby, corrupting the in-plane displacement measurements[94].

To perform displacement measurements, the image of the region of interest (ROI) is first captured prior to deformation, which is termed as the reference image. The subsequent images are then captured after applying the loads. The correlation between the reference and the subsequent (deformed) images is performed using a correlation algorithm based on image matching to obtain the full-field displacement data over the ROI. The predominant method of image correlation is subset based, in which, the reference image is discretised into small square regions called subsets. Each subset is matched onto the deformed image to determine the displacement vector (see Figure 3.1). For correlation algorithm to work effectively, the subsets should be statistically different from each other in terms of their grey-level intensity distribution. For this reason, the specimen surface is usually painted with high contrast, random black and white speckle pattern.

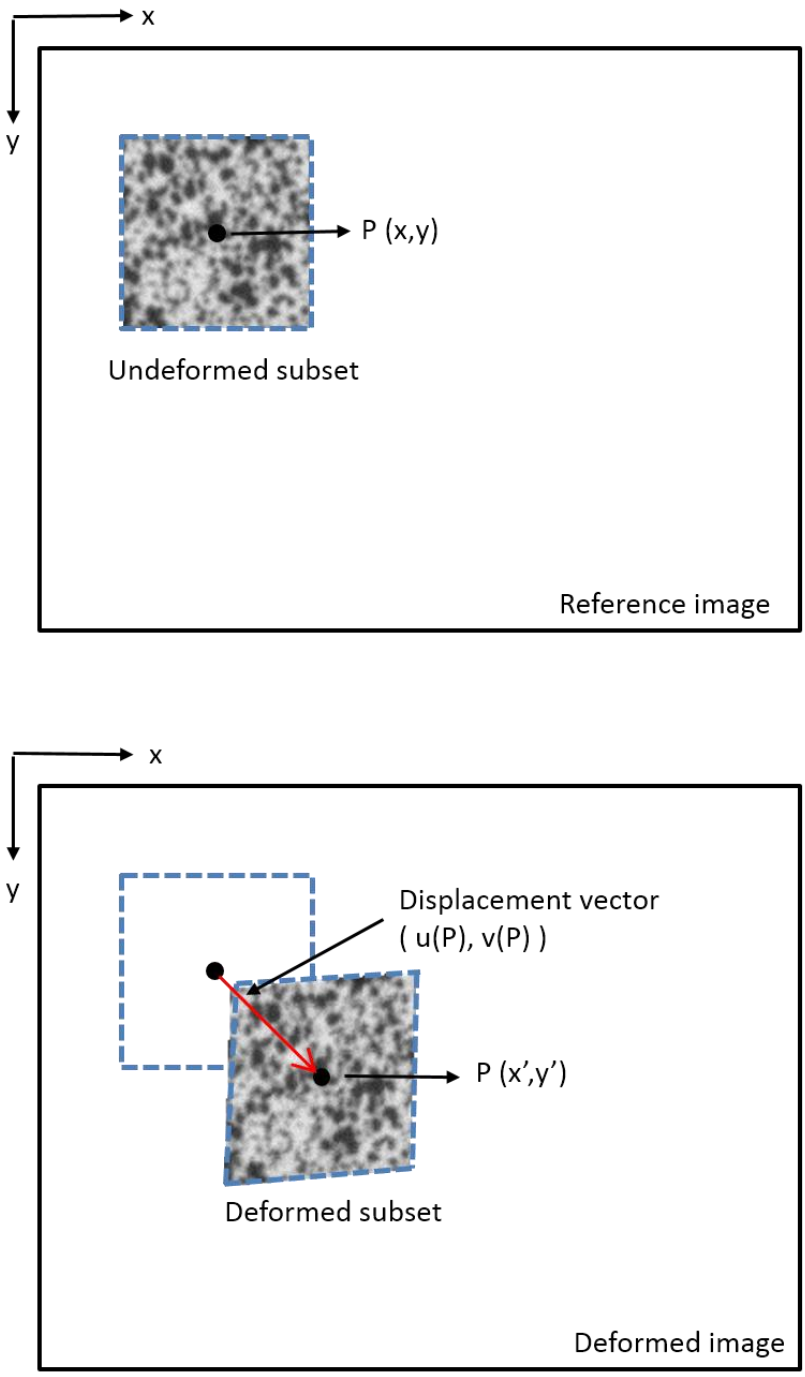

Figure 3.1 Schematic representing the undeformed subset in the reference image and the deformed subset in the deformed image. The difference in the positions of the undeformed and deformed subset centres yields the displacement vector.

A grayscale digital image is a numeric depiction of the matrix of pixels in which the numerical value at each pixel represents the light intensity information which ranges from 0 (black) to 255 (white) for an 8-bit image. In order to determine

displacements to a sub-pixel accuracy, the images need to be converted into continuous representation of intensity patterns, which is done using the interpolation algorithms. The most common scheme in this regard is bi-cubic spline fitting[95, 96]. Modern correlation software performs subset matching by not only locating the position of the undeformed subset of the reference image in the deformed image but also accounts for its distortion using higher order mathematical shape functions, which are then optimised using a cross-correlation function to obtain best estimates for the matched sub-set[96]. Once, the displacement data is obtained from the correlation process, it can be differentiated to evaluate strains.

3.1.2 Three-dimensional digital image correlation

As mentioned earlier, 2D DIC setups are limited to in-plane measurements of planar objects. These restrictions can be overcome by the use of a stereo-vision setup. The two camera stereo-vision setup typically used for 3D image correlation requires calibration to determine the imaging parameters of the cameras in the setup, referred to as the intrinsic parameters, as well as the extrinsic parameters which define the relative orientation and position of one camera with respect to the other one[94]. The calibration procedure is carried out by obtaining a series of images in different orientations of a grid pattern with known grid spacing, which is printed on a flat plate commonly referred to as “calibration target”. Attention needs to be paid during calibration to ensure that the grid pattern on the calibration target remains in the field-of-view and within the depth-of-field of both the cameras. The intrinsic and extrinsic parameters of the stereo-vision setup required for 3D position and displacement measurements are as follows:

- focal length (f) of each camera, which is defined as distance from the imaging lens to the camera sensor plane;
- Scale factors (λ_x , λ_y) which relate the sensor coordinates, in pixels, to the distance in the image plane;
- Coordinates for the image centre on the sensor plane (C_x , C_y) for each camera;
- Distortion coefficients (K) for each camera lens;
- Euler angles (θ_x, θ_y, θ_z) which define the orientation of one camera with respect to the other one; and
- Principal translations (t_x, t_y, t_z) which relate the position of one camera with respect to the other one.

To perform measurements, both the reference (undeformed) and the subsequent (deformed) images of the object's surface are simultaneously acquired by the two cameras of the stereo-vision setup. The correlation algorithm, which locates the reference image subsets in the deformed image, are common to both 2D and 3D DIC. The 3D profile of the object's surface is determined by identifying the subsets in the two images, acquired simultaneously by the two cameras of the stereo-vision setup, that correspond to the same position on the object's surface. The accuracy of a stereo-vision setup in measuring 3D displacements depends on many factors and the general estimates of the measurement errors are difficult to determine. The typical uncertainties reported by Sutton[97], which were derived from a wide range of experiments, are of the order of D/10,000 and Z/50,000 for the in-plane and the out-of-plane displacements, respectively, where D is the in-

plane dimension of the object's surface being imaged and Z is the approximate distance between the object surface and the camera sensor plane.

3.2 Thermoelastic stress analysis

TSA is a non-contact technique used for determining full-field stresses in real-time by measuring infinitesimally small temperature changes, associated with the time-varying deformation in a solid, by employing an infrared detector. An elastic solid subjected to tensile stress experiences a slight decrease in temperature, whereas, applied compressive stress results in a minute increase in temperature; this phenomenon is known as the thermoelastic effect. The theoretical basis for the thermoelastic effect was first proposed by Lord Kelvin in 1853 by relating the temperature change to the elastic deformation[98]. The detailed mathematical theory underpinning TSA can be found in a review by Pitarresi and Patterson[99]. The generalised form of the relation that relates the change in temperature of an elastic solid to its change in strain is as follows[99]:

$$\Delta T = \frac{T}{\rho c_\varepsilon} \sum \frac{\partial \sigma_{ij}}{\partial T} \Delta \varepsilon_{ij} + \frac{\delta q}{c_\varepsilon} \qquad 3.1$$

where ΔT is the temperature change, T is the absolute temperature, ρ is the density, c_ε is the specific heat capacity at constant strain, σ_{ij} and ε_{ij} are the stress and stain tensors, respectively, and δq is the heat transfer per unit mass. TSA is usually performed by loading the specimen cyclically, at a suitably high frequency to ensure adiabatic conditions, which allows the second term in Eq. 3.1 to be ignored[99]:

$$\Delta T = \frac{T}{\rho c_\varepsilon} \sum \frac{\partial \sigma_{ij}}{\partial T} \Delta \varepsilon_{ij} \qquad 3.2$$

Equation 3.2 is applicable for both isotropic and anisotropic solids with the assumptions that loading does not induce non-adiabatic effects and the thermal and elastic properties of the solid are independent of temperature variations. For an isotropic material in a state of plane stress, Eq. 3.2 can be simplified to[99]:

$$\Delta T = -\frac{\alpha T}{\rho c_\sigma} \Delta(\sigma_{11} + \sigma_{22}) \qquad 3.3$$

where α is the coefficient of linear thermal expansion and c_σ is the specific heat capacity at constant stress. The temperature variations are measured using an infrared detector in terms of the voltage output, S of the detector. Therefore, the working form of the relationship used for practical TSA is as follows[99]:

$$AS = \Delta(\sigma_{11} + \sigma_{22}) \qquad 3.4$$

where S is the output signal from the infrared detector, which corresponds to the thermoelastic effect, and A is the calibration factor, which is a function of both the material properties and the detector parameters. The calibration factor can be defined in terms of the material and detector parameters by the following equation[99]:

$$A = \frac{DRF\rho c_\sigma}{3eBT^3\alpha} \qquad 3.5$$

where D is the detector responsivity at a reference temperature (usually provided by the manufacturer), R is the correction factor used if the surface temperature is other than the reference temperature, F is the amplification parameter for analogue to digital output conversion, e is the surface emissivity and B is a constant dependent on the wavelength range of a detector. For quantitative stress

analysis, it is a common practice to paint the surface of a test specimen with a uniform thin coat of matt-black paint[100, 101]. Its purpose is to provide uniform, enhanced emissivity of the specimen surface to increase the photon flux[100, 101]. It also minimises the unwanted reflections of incident infrared radiation from the specimen surface which is not associated with the thermoelastic response. The calibration factor (A) can be determined, in a most reliable manner, experimentally by measuring the response from the surface of a calibration specimen, which is manufactured from the same material as the test specimen and has a paint coating, loading frequency and ambient conditions identical to the test specimen[100]. Typically, the geometry of the calibration specimen and the applied loads are such that its state of stress can be calculated theoretically or determined experimentally, fairly easily, by employing strain gauges.

The schematic of the TSA setup is shown in Figure 3.2. A signal processing unit, referred to as the lock-in analyser, is used to extract the voltage output signal (S), representing the thermoelastic response, from an inherently noisy detector output signal. This is done by correlating the reference signal at a loading frequency, usually obtained from either the function generator or a load transducer of the test machine, to the raw detector output signal. The resulting output signal, S is presented by a TSA software in the form of a vector, whose magnitude represents the thermoelastic response that is proportional to the temperature change and whose orientation represents the phase shift between the thermoelastic response and the reference signal. Under linear and adiabatic conditions, the thermoelastic response is in phase with the reference signal. The

phase shift can result from many factors such as low cyclic frequencies, high stress gradients, plastic deformation or even variation in paint thickness[100-102].

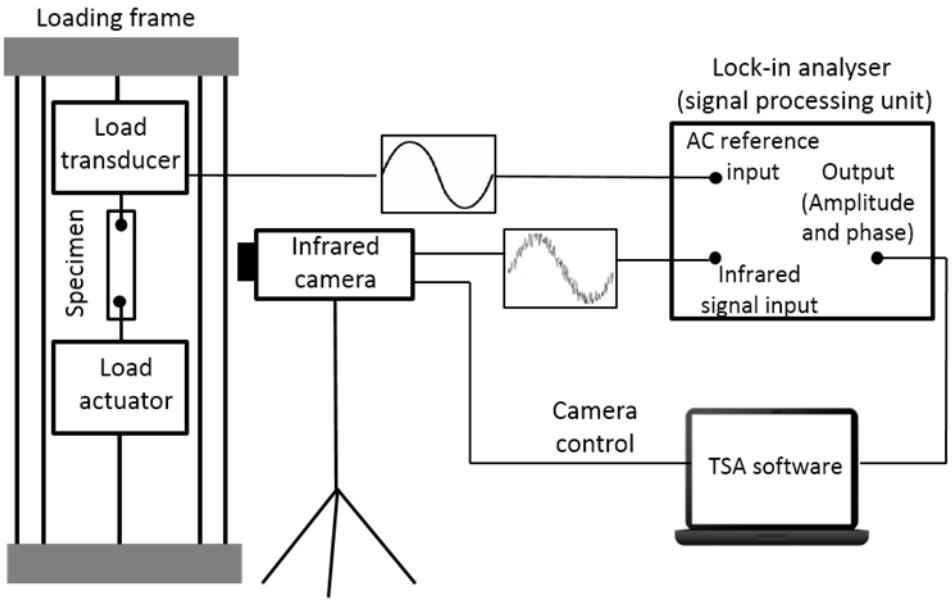

Figure 3.2 Schematic representing the typical arrangement of a TSA setup.

3.2.1 Quantitative analysis of fatigue cracks using TSA

One of the earliest commercially available infrared detector systems for stress measurement, SPATE (Stress Pattern Analysis by Thermal Emission) consists of a single infrared detector mounted with two independently motorised mirrors to perform a scan over specimen's surface in a point-by-point manner. This raster scanning approach, used by SPATE, takes a relatively long time to produce a thermoelastic image, which makes it unsuitable for obtaining high resolution, full-field stress data around the crack tip region because of the possibility of fatigue crack growth during data acquisition[103]. With the arrival of staring array infrared sensor systems, capable of acquiring data over the whole field-of-view within few seconds, TSA has become the ideal technique for monitoring fatigue crack growth and simultaneously performing full-field stress measurements around the tip of a growing crack.

Various methods, developed to experimentally determine the stress intensity factor range (ΔK) for fatigue cracks, from the thermoelastic data, have been reviewed comprehensively by Tomlinson and Olden[104]. In this research, methodology developed by Tomlinson et al[105], which was further improved and implemented in the software algorithm, FATCAT by Diaz et al[103], was used to evaluate the effective stress intensity factor range (ΔK_{eff}) for fatigue cracks emanating from cold-expanded holes. In this methodology, a mathematical model describing the distribution of the sum of principal stresses around the crack tip, which is based on Muskhelishvili's approach[106], is fitted to the thermoelastic data collected from the singularity dominated elastic zone around the crack tip. Tomlinson and Marsvania[107] used this methodology to determine ΔK for both mode I and mode II dominated mixed mode cracks to within 9% of the theoretical values. Diaz et al[103] utilised it to determine ΔK_{eff} for fatigue cracks under the influence of compressive residual stresses in welded steel plates. More recently, Patki and Patterson[108] used TSA to investigate the effect of plasticity-induced crack closure due to overloads on the fatigue crack growth and reported a significant reduction in ΔK_{eff} values in the region effected by the overload, which were determined using the method proposed by Tomlinson et al[105].

The investigations carried out by Diaz et al[103] and Patki and Patterson[108] demonstrated that the effect of both compressive residual stresses and crack closure on the stress intensity factor at a crack tip can be identified from the thermoelastic data. It was, therefore, hypothesized that TSA would be equally capable of identifying the influence of highly compressive residual stresses

developed by cold expansion on the fatigue cracks that originate from the cold-expanded holes.

3.3 Synchrotron x-ray diffraction for residual elastic strain measurement

Conventional x-ray methods, such as the traditional $\sin^2\psi$ technique[109] are well-established and are used extensively by engineers to get useful information, non-destructively, about the state of residual elastic stress in engineering components. However, only near-surface residual elastic strains can be resolved with conventional x-rays due to their limited penetration in the metals, which is of the order of few microns[110]. Modern synchrotron radiation sources are capable of providing a high intensity, coherent, x-ray beam with a small spot size and have great potential for engineers to make non-destructive, high resolution, residual elastic strain measurements in metallic components at much greater penetrations depths than was previously possible[110]. There are three main methods of residual elastic strain analysis utilising synchrotron x-rays: (1) using a monochromatic x-ray beam in a diffractometer configuration to determine the angle (2θ) of a diffracted beam, commonly known as the $\theta/2\theta$ scanning technique; (2) using a monochromatic beam in a transmission geometry with a two-dimensional detector; and, (3) using a polychromatic or white x-ray beam with an energy dispersive x-ray detector[110]. The schematics in Figure 3.3 represent the measurement geometries involved in the three methods mentioned above.

When a monochromatic x-ray beam is used, residual strains are typically determined from a single diffraction peak representing a particular grain

orientation, whereas in an energy dispersive diffraction method involving a polychromatic x-ray beam, the residual strains are determined from multiple diffraction peaks, thereby providing better representation of the macro scale residual strains present in the material. Despite superiority of the energy dispersive diffraction approach, the θ/2θ scanning technique, which utilises a monochromatic x-ray beam, is the most commonly used method by the researchers[111-117] owing to its simplicity and practicality. This method was chosen in this research primarily because the information about its experimental setup was readily available in the published literature which made it possible to design the required residual strain scanning experiments and apply for the monochromatic x-ray beam time at a synchrotron facility. The suitability of this method for measuring residual elastic strains around cold-expanded holes has been previously investigated by Stefanescu et al[18]. They compared their measurements from synchrotron x-ray source using this method with the ones obtained from neutron diffraction and conventional x-ray diffraction methods, which were found to be in good agreement[18].

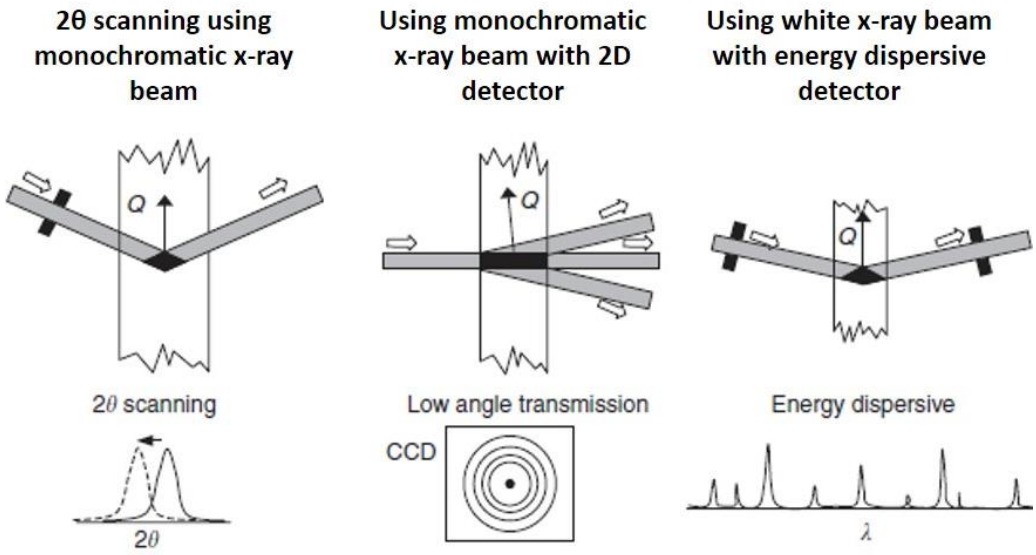

Figure 3.3 Schematics showing measurement geometries for the three methods for determining residual elastic strain utilising synchrotron x-ray source[110]. The vector Q represents the direction of strain measurement.

The θ/2θ scanning technique utilises the phenomenon of shifts in Braggs' diffracted intensity peak to determine the residual elastic strain and is briefly explained here. The x-rays are diffracted from the atomic planes of a crystal lattice based on the well-known Braggs' law[118]:

$$n\lambda = 2d\sin\theta \qquad 3.1$$

where λ is the wavelength, n is the order number of the wavelength, d is the distance between the atomic planes and θ is the diffraction angle. The angle at which a diffracted intensity peak is detected is measured using a diffractometer and the lattice spacing is thus calculated from the Braggs' law. The presence of elastic strain causes a change in the lattice spacing and this causes a change in the angle at which the diffracted intensity peak is detected. The residual strain can, therefore, be calculated from the angular shift in the Braggs' diffracted intensity peak using the following relation:

$$\varepsilon = \frac{d - d_0}{d_0} \qquad 3.2$$

where θ_0 is the angle at which the diffracted intensity peak is detected for the strain-free lattice spacing, d_0. The accuracy of the residual elastic strain measurement depends primarily on the reliable evaluation of the representative strain-free lattice spacing, d_0 for the material being investigated. An effective approach, reported by Hughes et al[119], for determining d_0 is by the use of comb-teeth shaped specimen, which is fabricated using electric discharge machining from the same material from which the samples, in which the residual elastic strain measurements need to be performed, are made. The electric discharge machining of the comb-teeth shaped structure relieves any macro scale residual elastic strains present along the teeth profile, which makes them suitable for the d_o measurements. Hughes and his co-workers[119] have demonstrated that the most suitable location for obtaining consistent d_0 values is from the free ends of the teeth.

3.4 Summary

An overview of the three main measurement techniques i.e. digital image correlation (DIC), thermoelastic stress analysis (TSA) and synchrotron x-ray diffraction (SXRD) has been provided in this chapter. DIC was selected to study the hole deformation resulting from split sleeve cold expansion because it had been identified in an earlier work[6], based on the rational decision methodology of Olden and Patterson[93], as the most suitable technique for measuring strains around fastener holes. TSA was employed for the quantitative analysis of fatigue crack emanating from cold-expanded holes because of its capability in determining ΔK_{eff}

directly from the captured thermoelastic data representing the cyclic stress fields ahead of the fatigue crack. SXRD was used for measuring residual stresses around cold-expanded holes due to its potential of performing high resolution residual stress measurements, non-destructively, at greater penetration depths in metals.

4 MATERIAL, SPECIMENS AND EXPERIMENTAL PROCEDURES

This chapter provides details about the material and the specimen geometry used in this research. Different experimental setups utilised during the course of this research are also described here.

4.1 Material

The material used in this research was aluminium alloy 2024 in the form of a sheet with a temper designation of either T3 or T351, which is typically used in aircraft structural parts due to its high strength-to-weight ratio and fatigue resistance[120] 2024 belongs to the 2000 series of wrought aluminium alloys containing copper as the principal alloying element, which are strengthened by solution heat treatment and aging[121]. In T3 heat treatment, the sheet is solution heat-treated, then cold-worked and aged naturally[122]. T351 heat treatment is slightly different from T3 because the sheet is straightened and stress-relieved after solution heat treatment by controlled stretching ranging from 0.5 – 3 % before being left to age naturally[122].

The specimens utilised in the experimental work were machined from three aluminium alloy 2024 sheets. One of these sheets had a temper designation of T3 and a nominal thickness of 1.6 mm; and the other two had a temper designation of T351 and nominal thicknesses of 6.35 and 8 mm. Their chemical compositions, reproduced from the material certificates supplied with these sheets, are provided in Table 4.1.

Table 4.1 Chemical compositions for (a) 1.6 mm 2024-T3 (b) 6.35 mm 2024-T351 and (c) 8 mm 2024-T351 sheets.

Chemical composition	Si	Fe	Cu	Mn	Mg	Cr	Zn	Ti	Others
Weight %	0.07	0.19	4.5	0.57	1.4	0.01	0.17	0.02	0.03

(a)

Chemical composition	Si	Fe	Cu	Mn	Mg	Cr	Zn	Ti	Others
Weight %	0.11	0.19	4.7	0.7	1.5	0.01	0.14	0.03	0.02

(b)

Chemical composition	Si	Fe	Cu	Mn	Mg	Cr	Zn	Ti	Others
Weight %	0.08	0.10	4.5	0.7	1.5	0.01	0.12	0.04	-

(c)

4.1.1 Mechanical properties

The mechanical properties of the three aluminium sheets were determined along the sheet rolling and transverse directions by performing tensile tests conforming to the ASTM standard E8[123]. The schematic of the dog-bone specimens used for the tensile tests is shown in Figure 4.1. The tests were performed in a Instron 4505 universal test frame equipped with a 50 kN load cell. The specimens were loaded until failure in the position control mode by setting the cross-head speed to a constant value of 0.9 mm/min. The strains were measured using an extensometer with a gauge length of 50 mm. A total of six tests were performed in the sheet rolling direction on the specimens obtained from a 1.6 mm sheet for the purpose of determining the uncertainty in the measured mechanical properties. Once the uncertainty in the measured mechanical properties was determined from six tests

in the sheet rolling direction, only two tests were performed in the transverse direction. For the remaining two sheets, two tests were performed in each of the two principal sheet directions. The stress-strain curves are provided in Figures 4.2 – 4.4.

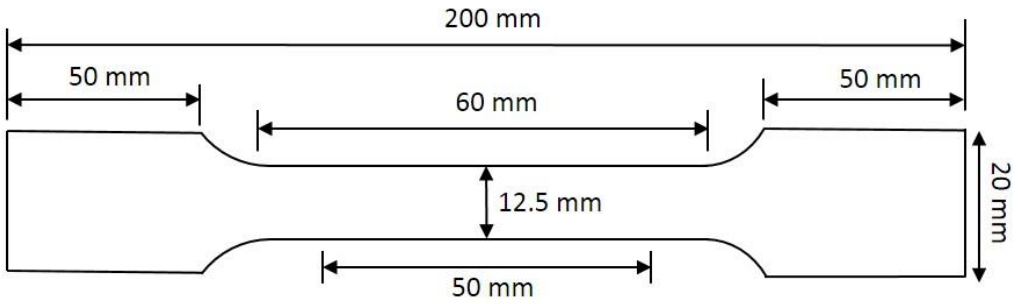

Figure 4.1 Schematic of dog-bone specimens used for tensile tests.

The values for the Young's modulus were determined from the slope of the linear segment of the stress-strain curves below the proportional limit, by fitting a least-squares regression line, as recommended in the ASTM standard E111[124]. Yield strength was determined as the 0.2 % proof stress using the Offset method[123]. In this method, a line is drawn parallel to the linear segment of the stress-strain curve and is offset from the origin by 0.2 % strain. The intersection of this line with the stress-strain curve gives the value for the yield stress. The strain hardening exponent was determined based on the method described in the ASTM standard E646[125]. The stress-strain curves shown in Figures 4.2 – 4.4, which represent the engineering stresses and strains, were first converted into true stress-strain curves. The logarithms of the non-linear segment of the true stress-strain curve were obtained and the strain-hardening exponent was then determined by fitting the logarithmic form of the Ramberg-Osgood power law[126] using least squares

regression. All the mechanical properties determined from these tensile tests are given in Table 4.2

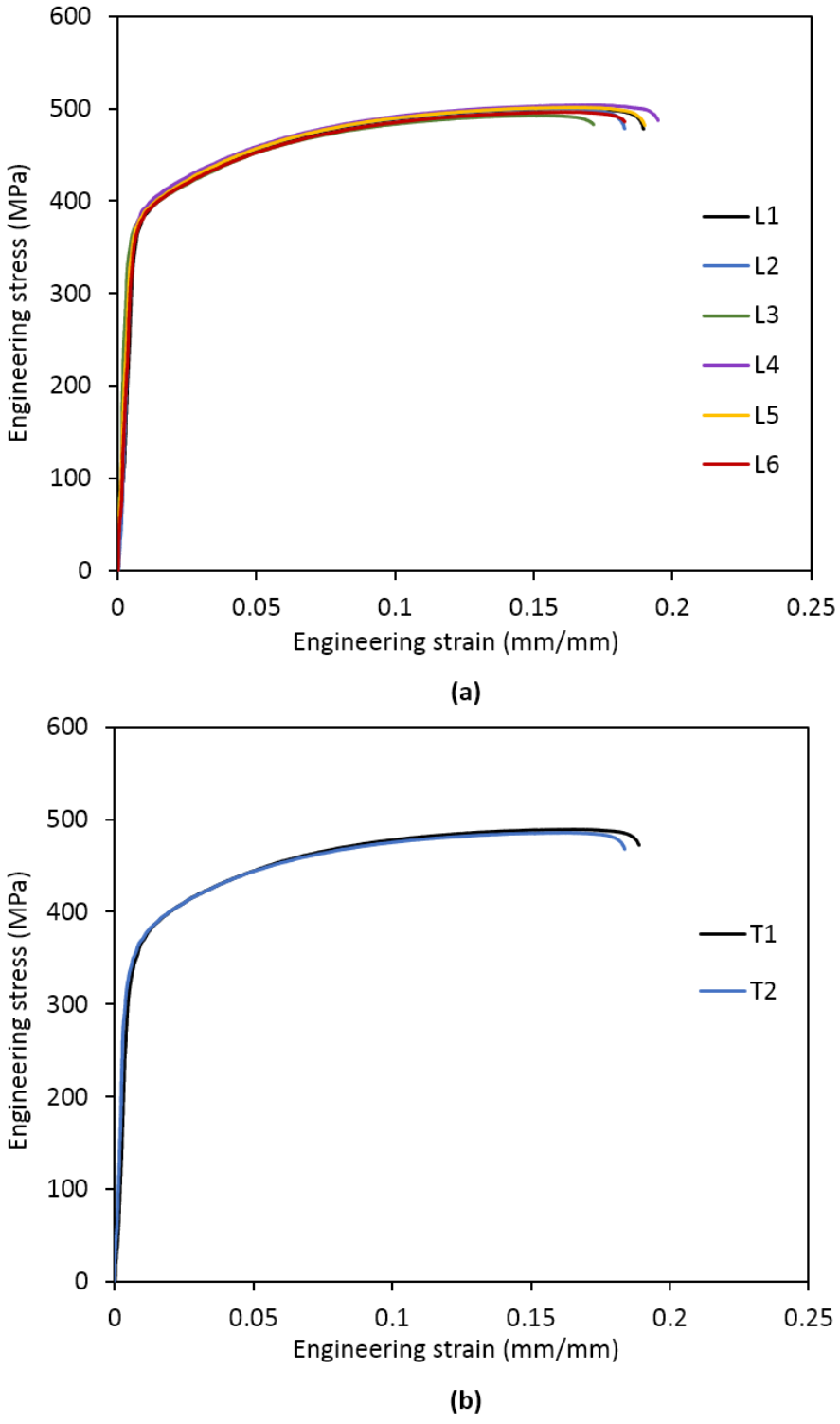

Figure 4.2 Stress-strain curves along (a) sheet rolling direction (b) transverse direction for 1.6 mm thick 2024-T3 sheet.

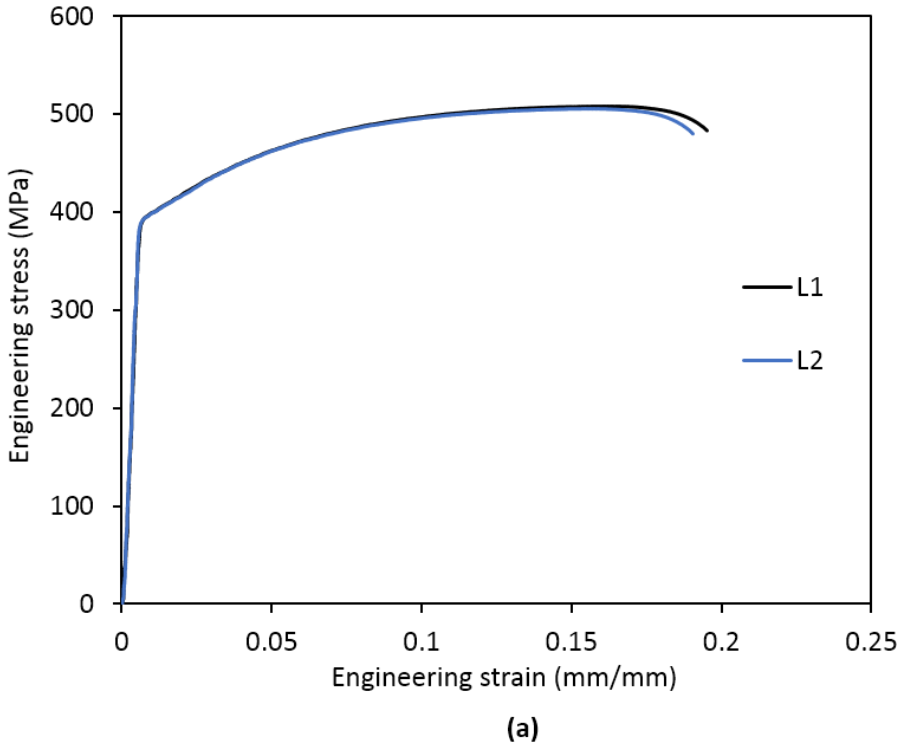

(a)

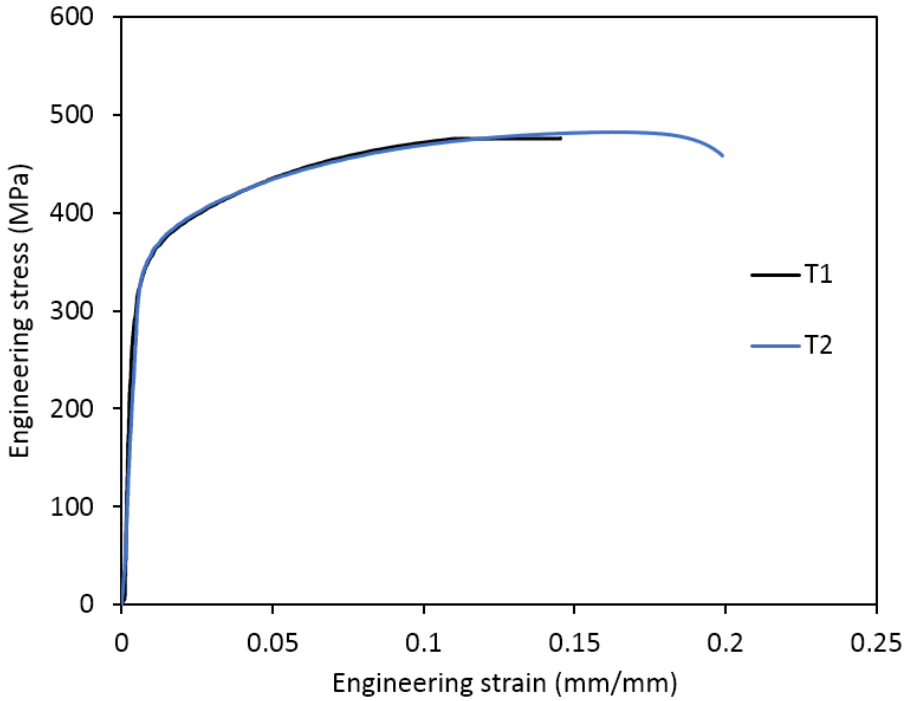

(b)

Figure 4.3 Stress-strain curves along (a) sheet rolling direction (b) transverse direction for 6.35 mm thick 2024-T351 sheet.

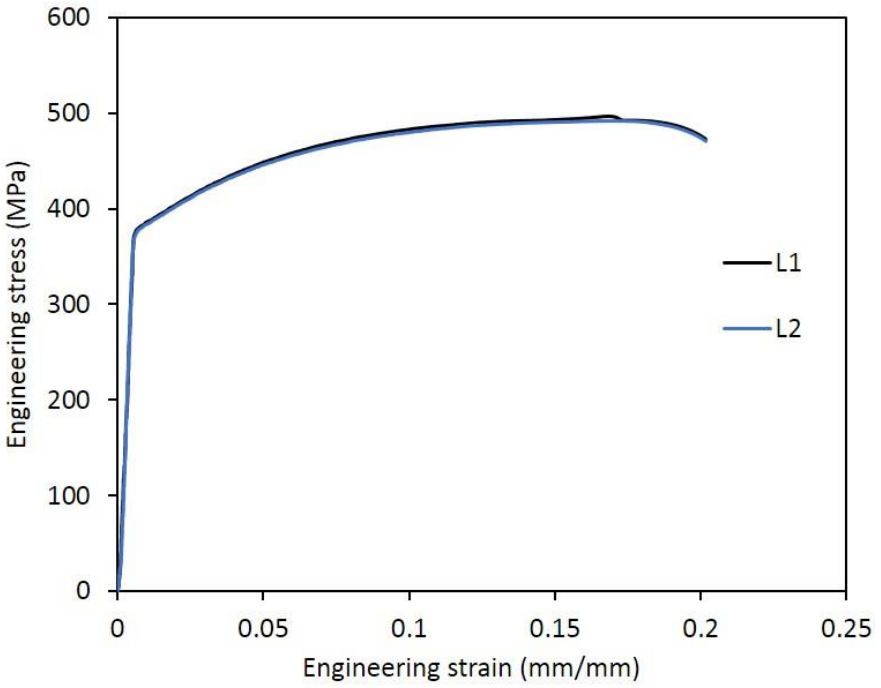

(a)

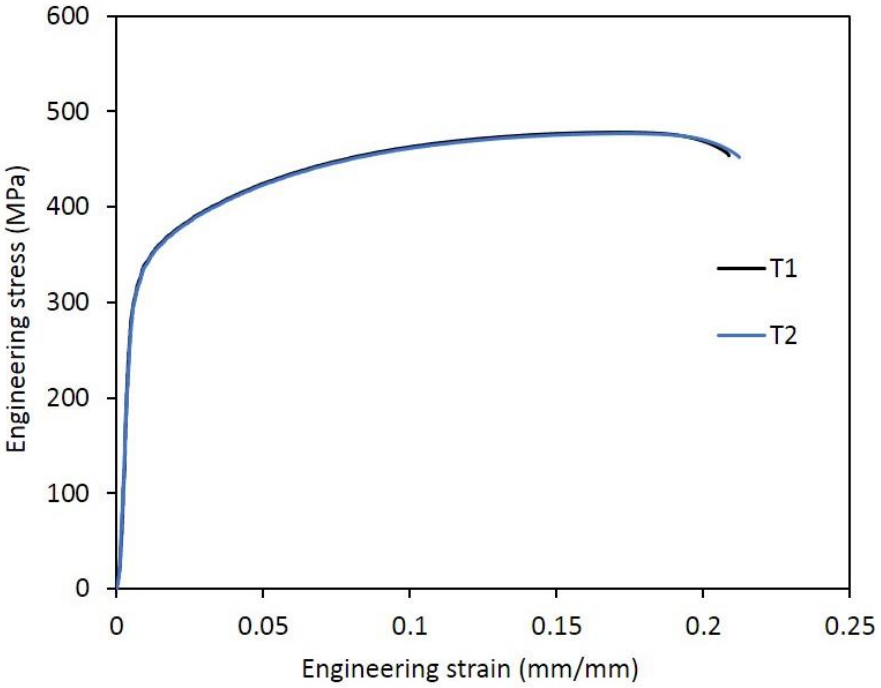

(b)

Figure 4.4 Stress-strain curves along (a) sheet rolling direction (b) transverse direction for 8 mm thick 2024-T351 sheet.

Table 4.2 Mechanical properties for (a) 1.6 mm 2024-T3 (b) 6.35 mm 2024-T351 and (c) 8 mm 2024-T351 sheet.

	0.2% Proof stress (MPa)	Elastic Modulus (GPa)	Ultimate tensile strength (MPa)	Elongation at fracture (%)	Strain hardening exponent (n)
Rolling direction	336 ± 15	74.6 ± 4.7	499 ± 4	18.4 ± 0.8	6.80 ± 0.21
Transverse direction	319	76	488	18.7	7.10

(a)

	0.2% Proof stress (MPa)	Elastic Modulus (GPa)	Ultimate tensile strength (MPa)	Elongation at fracture (%)	Strain hardening exponent (n)
Rolling direction	315	72	505	19.3	7.0
Transverse direction	300	71	485	20.7	6.20

(b)

	0.2% Proof stress (MPa)	Elastic Modulus (GPa)	Ultimate tensile strength (MPa)	Elongation at fracture (%)	Strain hardening exponent (n)
Rolling direction	325	72	493	20.2	6.75
Transverse direction	312	73	478	19.6	6.30

(c)

4.1.2 Grain structure

To obtain good average of the macro scale residual strains using x-rays, it is necessary to have sufficient number of diffracting grains in the gauge volume, which is defined by the intersection of incident and diffracted x-ray beams. The dimensions of the gauge volume are governed by the diffraction angle and the beam size. It is, therefore, important to characterise the grain structure of the material being investigated in order to determine suitable size of the x-ray beam

for the measurement of macro scale residual strains. The grain structures of the 1.6 mm and 6.35 mm thick aluminium sheets were determined along the planar, longitudinal and transverse principal planes. Three samples of 40 × 40 mm were sectioned using a band-saw from each of the two sheets. The samples were reduced to a size of approximately 20 × 20 mm by removing 10 mm of material from each side using a Buehler Isomet precious saw. This was done to ensure that the sample does not have any plastically deformed, heat-affected zone at the edges resulting from the band-saw cutting. The samples were mounted in three principal orientations using a thermosetting plastic resin in a Buehler Pneumet mounting press. The mechanical grinding and polishing of the samples involved several stages. The grinding was first performed with a coarse grit paper with a grit number of 320 and moving to a finer grit paper with each successive step. The last step of grinding involved a 2500 grit paper. The samples were then mounted in a Pneumet polishing machine. The polishing was performed first with a slurry of 1 micron alumina powder for a period of about 30 minutes and later using a 0.04 micron colloidal silica for an hour. Once cleaned and dried, chemical etching was performed to reveal the grain boundaries by immersing the specimens for about 10 seconds in a mixture of nitric, hydrochloric and hydrofluoric acid, commonly known as the Keller's reagent[127]. The images of grain structure along the three principal planes, shown in Figure 4.5 for both the types of sheets, were obtained using a Nikon optical microscope.

The average grain size diameter for each principal plane was determined using the Heyn Lineal Intercept method based on the guidelines provided in the ASTM standard E112[128] For each sample, three images were obtained from randomly

selected regions on the polished surface at a magnification of 50x. Four straight lines were drawn on each image, all having different orientations from each other. The grain boundary intersections per unit length of a test line, P was determined for each line and the values for all the test lines in the three images were averaged and inverted to obtain the mean lineal intercept length, $\bar{l}$ for a given plane. The ASTM grain size number, G was determined from $\bar{l}$ using the following equation[128]:

$$G = -3.2877 - 6.6439 \log_{10} \bar{l} \quad (4.1)$$

The mean grain diameter in mm, d was determined from G using the following equation[128]:

$$d = \sqrt{0.0645 \times 2^{1-G}} \quad (4.2)$$

The grain size parameters mentioned above are provided in table 4.3 for both the sheets. The grain elongation ratio or the anisotropy index, AI was also determined from the mean lineal intercepts along the sheet rolling and transverse directions on the longitudinal plane (see Figure 4.5) using the following equation[128]:

$$AI = \frac{\bar{l}_l}{\bar{l}_t} \quad (4.3)$$

where $\bar{l}_l$ and $\bar{l}_t$ are the mean lineal intercept lengths along the sheet rolling and transverse directions respectively. The values for AI are also provided in Table 4.3.

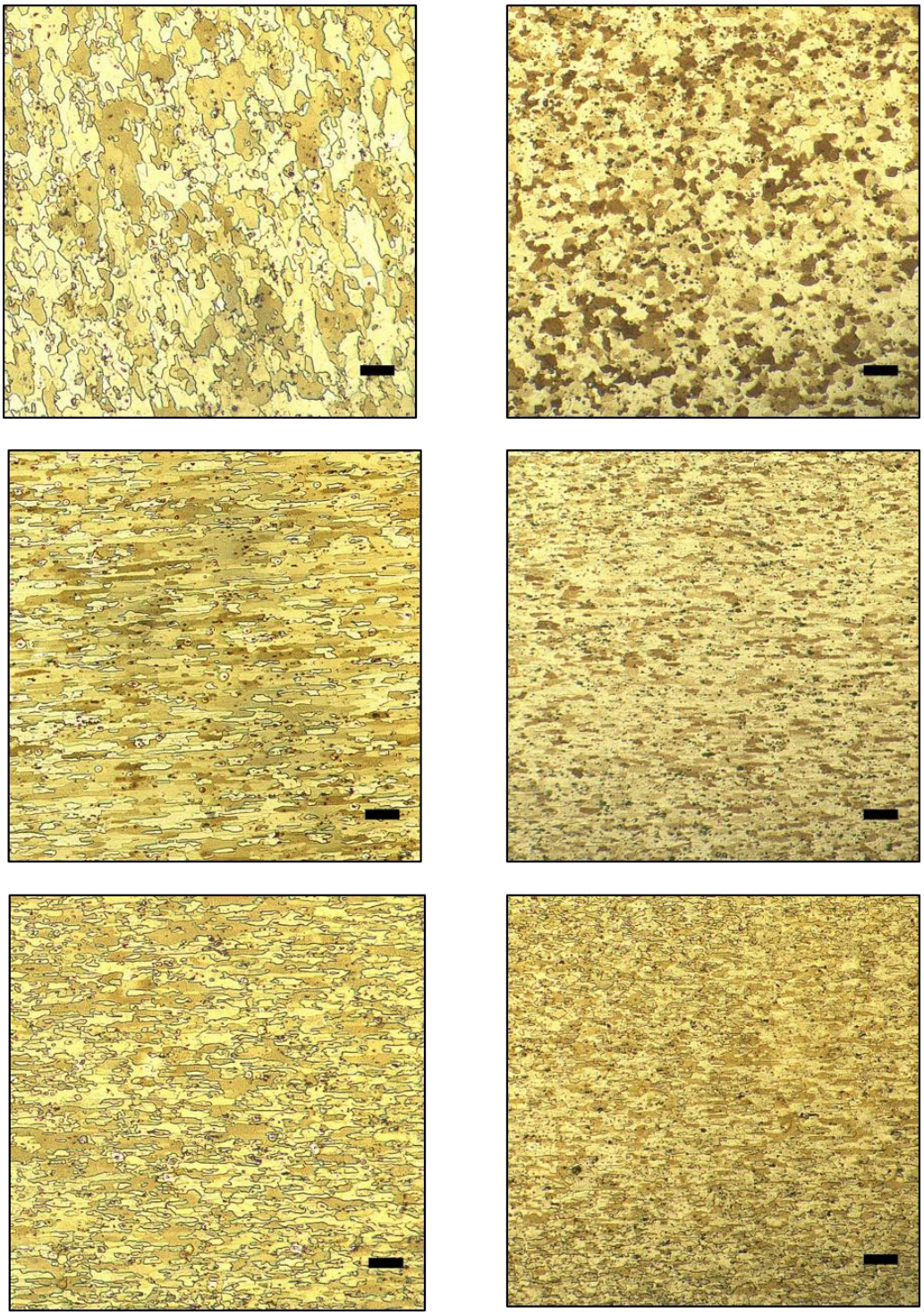

Figure 4.5 Images showing the grain structure on the planar (top), longitudinal (middle) and transverse (bottom) planes for the 6.35 mm (left) and 1.6 mm (right) thick aluminium sheets. The size of the scale bar on the images is 100 µm.

Table 4.3 Grain size parameters for (a) 1.6 mm and (b) 6.35 mm thick aluminium sheets.

	Mean lineal Intercept length $\bar{l}$ (μm)	**ASTM Grain size number G**	**Mean grain diameter d μm)**	**Anisotropy Index AI**
Planar plane	35.2	6.4	39.5	-
Longitudinal plane	23.9	7.5	26.9	2.5
Transverse plane	22.1	7.7	24.8	-

(a)

	Mean lineal Intercept length $\bar{l}$ (μm)	**ASTM Grain size number G**	**Mean grain diameter d μm)**	**Anisotropy Index AI**
Planar plane	48.2	5.5	54.1	-
Longitudinal plane	54.2	5.1	60.9	3.8
Transverse plane	40.1	6.0	45.0	-

(b)

4.2 Specimen geometry and cold expansion procedure

As mentioned in the Introduction chapter, the research reported in this thesis was motivated by the doctoral work carried out previously by Backman[6]. Therefore, to build upon this prior knowledge, it was decided to use specimens for the cold expansion tests with a geometry identical to the ones used by Backman[6]. The specimen geometry is shown in Figure 4.6. The actual thicknesses of the specimens, which were manufactured from the sheets with nominal thicknesses of 1.6 mm, 6.35 mm and 8 mm, were measured to be 1.59 mm, 6.02 mm and 8.05 mm respectively. A central hole of 6.36 mm diameter was drilled in all the specimens, giving nominal sheet thickness to hole diameter ratios (t/D_o) of 0.25, 1

and 1.26 for the specimens manufactured from 1.6 mm, 6.35 mm and 8 mm thick sheets, respectively. From this point onwards, the specimen's thickness and its t/D_o ratio will be stated based on the nominal thickness of the sheet from which it was manufactured.

The most important dimensional parameter, which needs to be considered for the effective cold expansion of the holes, is the edge margin (e/D_o), which is defined as the ratio of the distance between hole centre and the specimen short edge (e) to the initial hole diameter (D_o)[5]. A higher edge margin ensures that there is enough elastic material around the hole edge to constrain the plastic deformation resulting from cold expansion and generate a maximum spring-back effect for a given expansion level to induce a compressive residual stress field. It is recommended in the FTI manual for split sleeve cold expansion[5] that the edge margin should be at least 1.75. In the specimen geometry employed in this work, the edge margin was approximately 3.

To perform cold expansion, the specimen was placed in a retention fixture as shown in Figure 4.7. A hardened steel mandrel (CBM-8-1-N-1-40-V1; FTI) mounted on a manual puller unit (HP-20; FTI) was used for the hole expansion. In industry, the holes are typically cold-expanded by a pneumatic puller unit, however, the manual puller unit used in this work is certified for use in the aerospace industry by the FTI and has been used in the previously published studies[23, 25, 92]. The split sleeve (8-1-N; FTI) was placed on the mandrel shank such that the flared ends of the sleeve rested on the nose-cap of the puller unit (see Figure 1.1). To expand the hole, the mandrel was pulled though it by turning the nut at the back of the puller

unit. During cold expansion, the orientation of the split in the sleeve was along the longitudinal direction (0° in polar coordinates) of the specimen as shown in Figure 4.6. The combination of the over-sized mandrel head and split sleeve provided a maximum hole interference of 4.6%. The diameter of the expanded hole after mandrel removal was measured to be 6.58 mm, providing a retained expansion of 3.46 %.

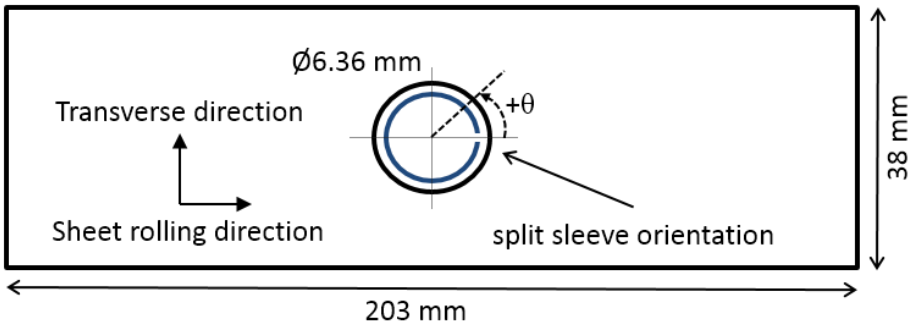

Figure 4.6 Schematic of centrally drilled hole specimen with the split sleeve orientation shown in the hole.

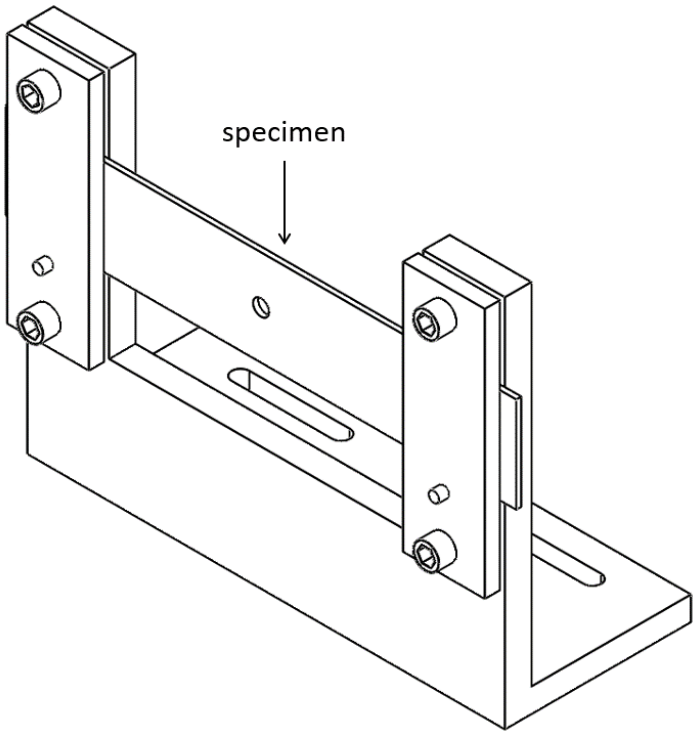

Figure 4.7 Retention holder for the specimen.

4.3 Experimental procedures

The three main measurement setups used in this research are described below:

4.3.1 Stereo-vision setup for strain measurement

To obtain full-field deformation measurements during the cold expansion process, the area of interest around the hole was painted with white paint (Plasti-Kote matt white) before being speckled black (CRC Pro matt black) and then images of the region around the hole were captured by a stereo-vision system (Dantec Dynamics, Germany) during the cold expansion process. The optical setup comprised of two identical digital cameras (Guppy PRO F-125; Allied Vision Technologies, Germany) with resolutions of 1292 × 964 pixels, mounted with an identical pair of 50 mm focal length lenses (Schneider Kreuznach, Germany). Two light-emitting diode (LED) light arrays (Dantec Dynamics) were used to illuminate the specimen surface. The cameras, mounted on a tripod, were positioned at a working distance of approximately 300 mm from the specimen surface, providing an effective field of view of about 29 mm × 24 mm and a spatial resolution of 0.025 mm/pixel. Figure 4.8 shows the optical setups for measuring surface deformations around cold-expanded holes on the mandrel entry and the exit faces. To capture data on the mandrel exit face, the specimen and mandrel were reversed so that the optical setup need not be disturbed.

The images, captured by the stereo-vision system, were processed by the DIC software, ISTRA (Dantec Dynamics)[129] to evaluate displacement fields and in-plane residual strains around the cold-expanded holes. ISTRA utilises a second-order

displacement function (shape function), defined by the following equations, to locate and map each subset to its distorted shape[130]:

$$x' = x_0 + u_0 + \frac{\partial u}{\partial x}\Delta x + \frac{\partial u}{\partial y}\Delta y + \frac{\partial^2 u}{\partial x\,\partial y}\Delta x\Delta y \qquad 4.4(a)$$

$$y' = y_0 + v_0 + \frac{\partial v}{\partial x}\Delta x + \frac{\partial v}{\partial y}\Delta y + \frac{\partial^2 v}{\partial x\,\partial y}\Delta x\Delta y \qquad 4.4(b)$$

where (x_0,y_0) and (x',y') are the position coordinates for the undeformed and the deformed facet centres respectively, whereas u_0 and v_0 define the horizontal and vertical displacements of the facet centre in the deformed image.

The resultant coefficients of the shape function, representing the first-order displacement gradients of a distorted subset, can be directly used to evaluate strains based on the following equations:

$$\varepsilon_{xx} = \frac{\partial u}{\partial x} + \frac{1}{2}\left[\left(\frac{\partial u}{\partial x}\right)^2 + \left(\frac{\partial v}{\partial x}\right)^2\right] \qquad 4.5(a)$$

$$\varepsilon_{yy} = \frac{\partial v}{\partial y} + \frac{1}{2}\left[\left(\frac{\partial u}{\partial y}\right)^2 + \left(\frac{\partial v}{\partial y}\right)^2\right] \qquad 4.5(b)$$

$$\varepsilon_{xy} = \frac{1}{2}\left[\frac{\partial v}{\partial x} + \frac{\partial u}{\partial y} + \frac{\partial u}{\partial x}\frac{\partial u}{\partial y} + \frac{\partial v}{\partial x}\frac{\partial v}{\partial y}\right] \qquad 4.5(c)$$

This method of evaluating strains directly from the shape function coefficients will be referred to as the subset distortion method and is used by ISTRA if no smoothing filter is used[129]. The image correlation was performed with a subset size of 47 pixels, a grid spacing of 5 pixels and the strains were evaluated using the subset distortion method. A brief investigation carried out to analyse the influence

of correlation parameters and strain evaluation method on the strain measurements is reported in Chapter 5.

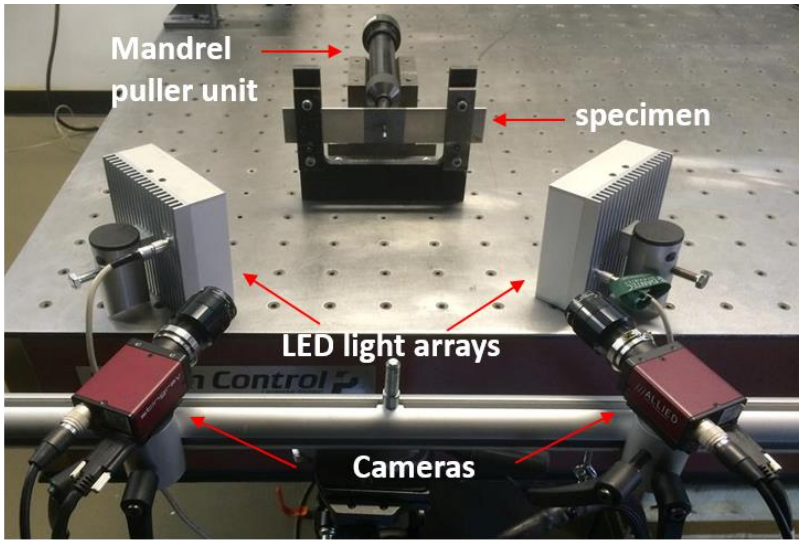

(a)

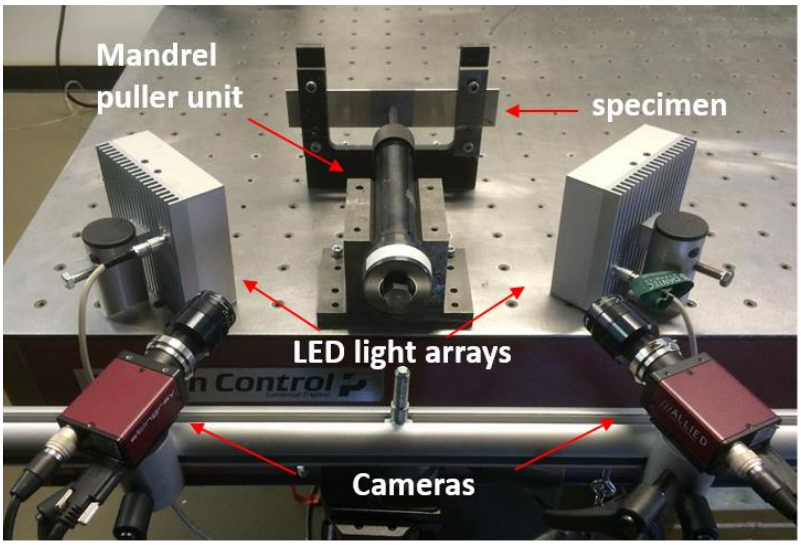

(b)

Figure 4.8 Stereo-vision setup for measuring surface deformations on (a) mandrel entry and (b) exit face of the specimen.

4.3.2 Thermoelastic stress analysis setup for fatigue analysis

Fatigue tests were performed in an Instron servo-hydraulic testing machine equipped with a 100kN load cell. The experiment setup used for the fatigue tests is shown in Figure 4.9. On the mandrel entry side of the cold-expanded specimens, an infrared camera (FLIR 7650; FLIR Systems Inc., USA), with a InSb detector array

of 640×512 pixels, was employed to simultaneously monitor the cracks and capture the thermoelastic response. The camera is capable of acquiring images using the full sensor at a maximum frame rate of 100 Hz. For these experiments, the camera was operated at a frame rate of 250 Hz with a reduced active sensor window of 320 × 256 pixels. A two-position zoom lens (Stressphotonics Ltd., USA) was used and provided a spatial resolution of 29.6 µm/pixel. On the mandrel exit side, the cracks were monitored optically using a pair of digital cameras (Guppy PRO F-125; Allied Vision Technologies, Germany) with a resolution of 1292×964 pixels. The digital cameras were mounted with a pair of identical Sigma macro lenses of 105 mm focal length, providing a spatial resolution of 8 µm/pixel. For the un-expanded specimens, the specimen faces facing the infrared camera and the pair of digital cameras will be referred to as the front and back faces, respectively, in the later sections.

Two different levels of maximum applied load were used for fatigue loading of the cold-expanded and the un-expanded specimens. For the cold-expanded specimens, the maximum applied load of 38.9 kN was used compared to 34.3 kN for the un-expanded ones. These load levels corresponded to the maximum remote nominal stresses of 170 and 150 MPa, respectively. The primary reason for using a lower maximum applied load for the un-expanded specimens was to reduce the crack growth rate in order to make it possible to manually track the tip of a growing crack and simultaneously capture the thermoelastic response from the crack tip region using an infrared camera; while a higher load was needed for the cold-expanded specimens to allow the tests to be conducted in a practical time period. All fatigue tests were performed using a load ratio of 0.1 and a frequency

of 19 Hz. The fatigue loads applied to the cold-expanded specimens were chosen to ensure that the maximum hoop stress at the hole edge, $\sigma_{h,max}$ did not exceed the yield stress in order to avoid large-scale plastic deformation. $\sigma_{h,max}$ was calculated by linear superposition of the hoop stress resulting from the maximum applied load and the compressive residual hoop stress developed from cold expansion. It is pertinent to mention here that $\sigma_{h,max}$ is a theoretical value for the superimposed elastic stresses, which did not necessarily represent the actual magnitude of hoop stresses being experienced at the hole edge; and its sole purpose was to determine whether the applied loads were expected to cause any yielding.

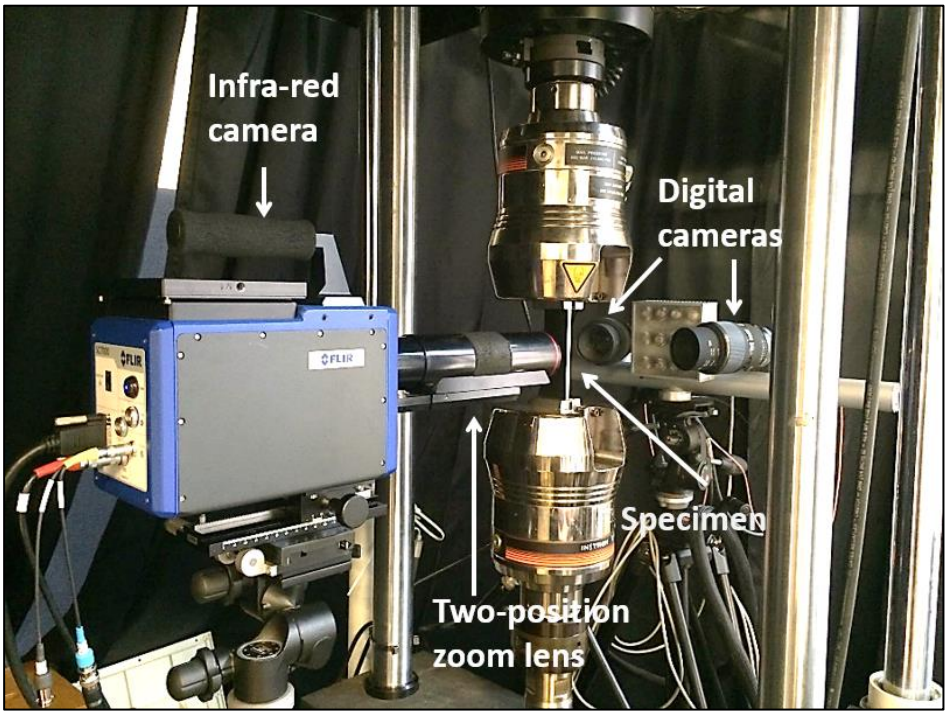

Figure 4.9 Experimental setup for the fatigue tests.

4.3.3 Synchrotron x-ray diffraction setup for residual elastic strain scanning

The residual elastic strain scanning was performed around the cold-expanded hole in the 6.35 mm thick specimens on a high-resolution powder diffraction beam line,

ID22 at the European Synchrotron Radiation Facility (ESRF), France. The key objectives were: (1) to determine the initial residual stress distribution developed from cold expansion; (2) to evaluate the uncertainty in the residual stresses; and (3) to measure the residual stresses in the specimens, which had been loaded in fatigue, for evidence of any significant residual stress relaxation. The prior full-field surface strain measurements using digital image correlation showed that the total residual (elastic + plastic) strain field developed around the cold-expanded hole was symmetric about an axis coincident with a diameter through the location of the split sleeve. This piece of knowledge was very helpful in identifying a region around a small portion of the hole (see blue shaded area in Figure 4.10 a) for the residual elastic strain scanning, which could provide information about the overall residual elastic strain field around the whole cold-expanded hole. From this point onwards, the residual elastic strains will be simply referred to as the residual strains.

The residual strains were measured over two measurement planes, which were defined at a depth of 2 mm from both the mandrel entry and exit faces of the specimen (see Figure 4.10 b). For the un-cracked specimen i.e. which was not loaded in fatigue prior to residual strain scanning, the residual strains were measured over a matrix of measurement points represented by the blue area, at a depth of 2 mm from the mandrel entry face (see Figure 4.10 a). The matrix had a uniform spacing of 0.4 mm between its adjacent data points. The residual strains were also measured in the un-cracked specimen, at a depth of 2 mm from the mandrel exit face, by scanning over the matrices shaded in red and green colours in Figure 4.10 a. The red and green matrices were a subset of the larger blue matrix

of measurement points. For the cracked specimens, the residual strains were measured over the red matrix at depths of 2mm from both the mandrel entry and exit faces. A series of line scans were also performed in various specimens over the middle row of the red matrix, which coincides with the transverse centre line of the specimen.

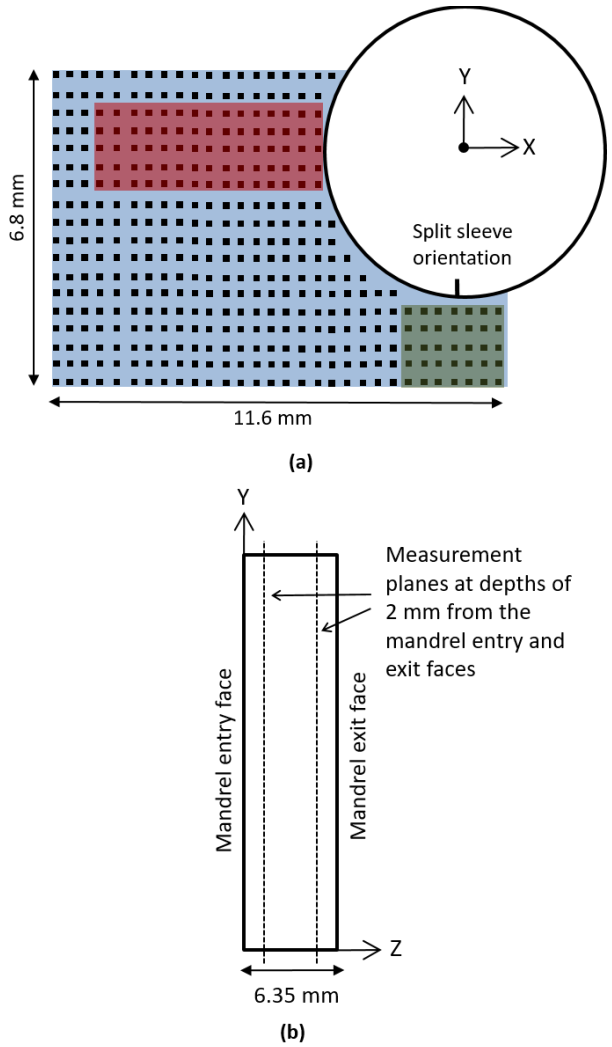

Figure 4.10 Schematic (a) represents the matrix of measurement points and (b) represents the planes over which residual strains were measured.

All measurements were performed in a transmission geometry using a monochromatic x-ray beam of 0.3 × 0.3 mm with a photon energy of 60 keV and the (311) plane was chosen for the residual strain measurements. The (311) plane has been reported by Clausen and his coworkers[131] to best represent the macro

scale residual strains and most of the investigations[18, 111-114, 116], which studied the macro scale residual strains in aluminium alloys, have performed measurements by selecting this plane. At 60 keV photon energy, the diffraction from the (311) plane was at $2\theta \approx 9.70$ approximately. Each specimen was mounted on a three-axis translation stage; and, for each measurement, the diffractometer was swept through a fixed 2θ angular range from 9.6 to 9.85^{o}, to measure the diffracted intensity peak. The experimental setup is shown in Figure 4.11. To resolve the residual strain components along two orthogonal directions, the specimens were mounted in two different orientations. The schematics of the specimen orientations for measuring residual strain along the X and Y directions are shown in Figure 4.12. The measurement volume, commonly referred to as the gauge volume, is defined by the intersection of the incident and the diffracted beams. Low diffraction angles at high x-ray photon energies, as dictated by the Braggs' law[118], result in an elongated diamond-shaped gauge volume. The dimensions of the gauge volume used in this experiment, resulted from the beam size and the diffraction geometry, are also provided in Figure 4.12.

The strain-free (311) plane spacing, d_o for aluminium was measured along the two orthogonal directions using the comb-teeth shaped specimens, which were manufactured using EDM from the same plate as the fatigue specimens. Two specimens were manufactured, one with its longitudinal axis along the sheet rolling direction and the other with its longitudinal axis along the sheet transverse direction. Nine measurements were obtained from each specimen, along each of the two orthogonal directions. The comb-teeth specimen geometry and the location of measurements points are shown in Figure 4.13. . The values for d_0 along

longitudinal and transverse directions were found to be 1.221679 ± 0.000206 Å and 1.220445 ± 0.000032 Å, respectively. The measured residual strains were converted to stresses using Hooke's law. The Poisson's ratio value of 0.33 was obtained from a materials handbook[122] for an aluminium 2024-T351 material and the Young's modulus value of 72 GPa along the sheet rolling direction, provided in Table 4.2(b), was used in the Hooke's law for conversion of residual strains to stresses. The difference between the measured values of Young's modulus along the sheet rolling and transverse directions is significantly less than the uncertainty in these measurements (see Table 4.2). The elastic modulus was, therefore, assumed to be isotropic and its value along the rolling direction was selected for use in the Hooke's law.

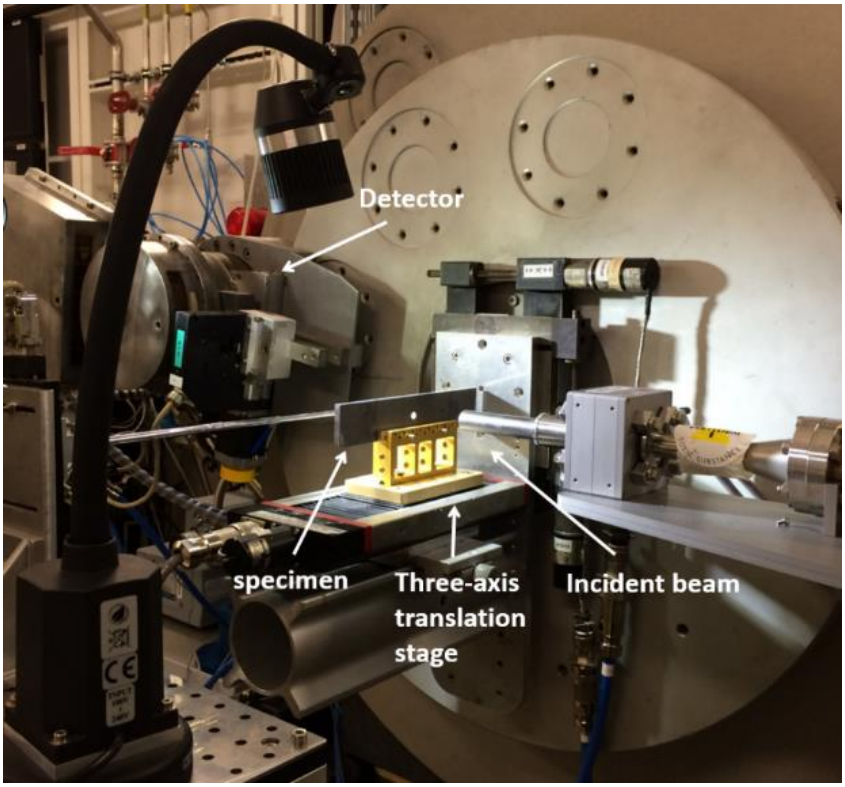

Figure 4.11 Residual strain scanning setup of beamline ID22 at ESRF.

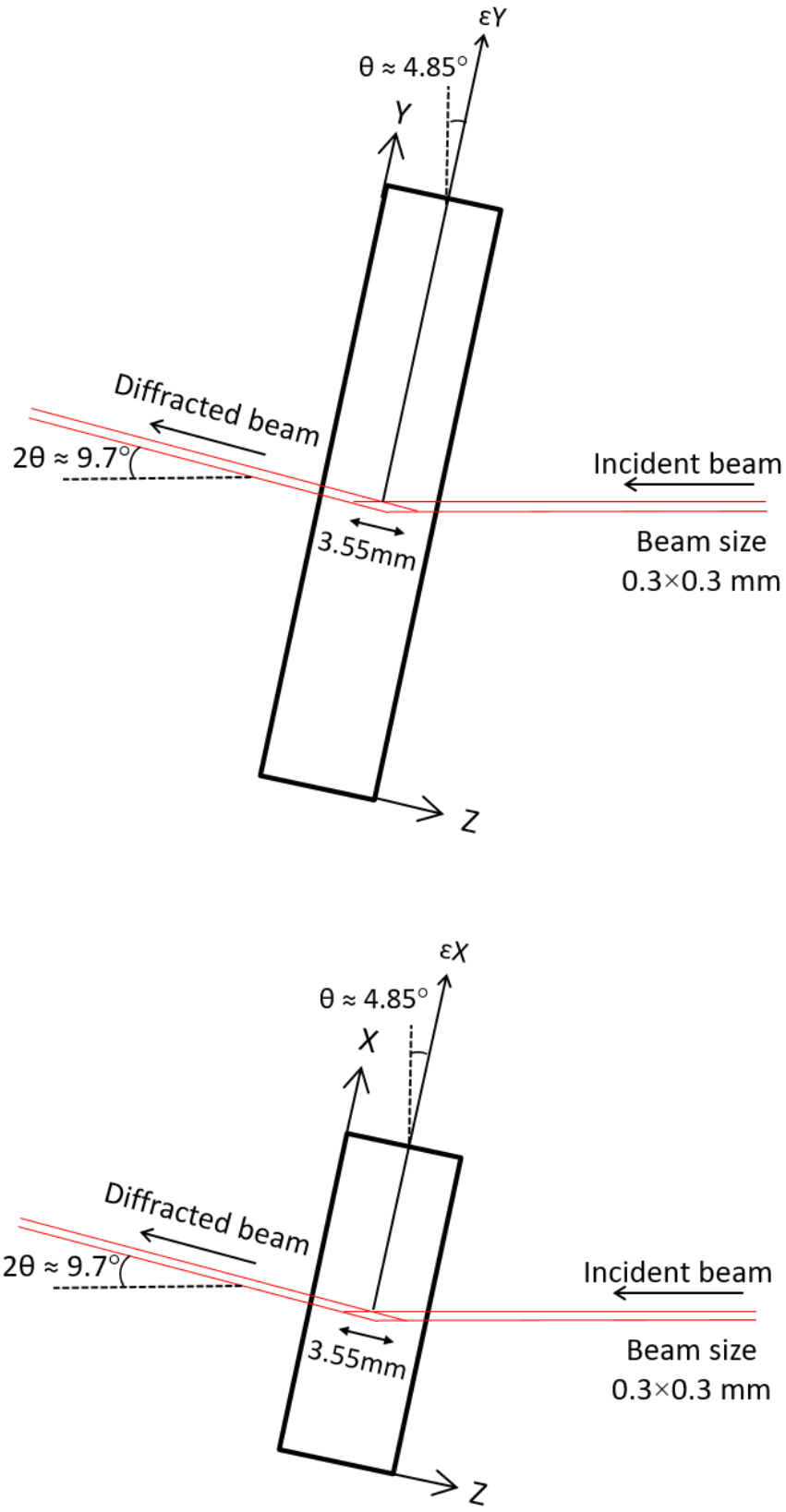

Figure 4.12 Schematics representing the specimen orientation and diffraction geometry for measuring residual strain along Y (top) and X (bottom) directions.

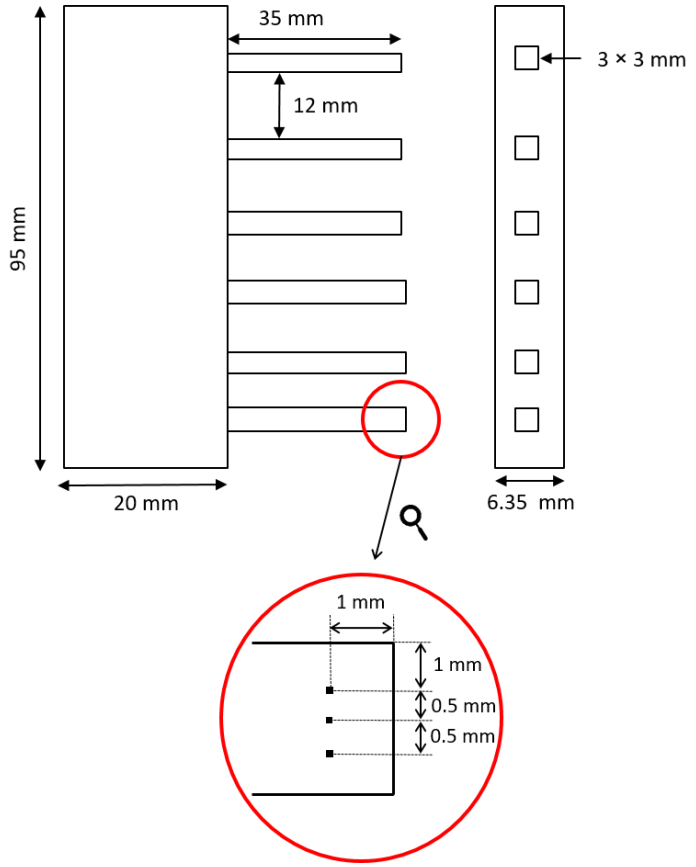

Figure 4.13 Schematic of comb teeth specimen. The diagram at the bottom enclosed in the circle highlights the locations on the comb tooth from where the measurements were obtained. A total of 9 measurements were obtained from the first three teeth for each specimen.

4.4 Summary

The first section of this chapter has presented the details of the three aluminium alloy 2024 sheets, which were the source of the centrally drilled hole specimens used in this research. One of these sheets had the temper designation of T3 and nominal thickness of 1.6 mm. The other two sheets had the temper designation of T351 and nominal thicknesses of 6.35 and 8 mm. The mechanical properties of the three aluminium sheets were determined along the sheet rolling and transverse directions by performing standard tensile tests on the dog-bone shaped specimens, which were manufactured from these sheets. The grain structures for the 1.6 and 6.35 mm thick sheets were also determined. The second section has

reported the dimensions of the centrally drilled hole specimens and the procedure for cold expansion of holes utilising the split sleeve. Finally, the experimental setups for the three main measurement techniques i.e. DIC, TSA and SXRD utilised in this research were described in the third section of this chapter.

5 COLD EXPANSION IN SINGLE SPECIMENS

A series of split sleeve cold expansion experiments were performed on the 1.6 mm and 6.35 mm thick specimens, with a thickness to hole diameter ratios (t/D_o) of 0.25 and 1 respectively, and the total residual strains were measured using the stereoscopic digital image correlation (DIC) setup described in section 4.3. In the first stage of this experimental work, a preliminary investigation was carried out to analyse the influence of the choice of speckle pattern, the image correlation parameters and the strain evaluation method on the strain measurements around the cold-expanded holes. Once, the above mentioned parameters were identified, the displacement and strain resolutions of the DIC setup were determined. The DIC setup was then used to assess the variability in the cold expansion process. Finally, a detailed comparison of the mechanics of hole deformation was made to determine the effectiveness of cold expansion process in the thick and thin specimens.

5.1 Influence of speckle pattern, correlation parameters and strain evaluation method

The DIC algorithm can uniquely identify the subsets of the reference image in the deformed image only if they are different from each other in terms of their grey-level intensity distribution. This is achieved by creating a speckle pattern comprising of randomly distributed black and white dots. In addition, for an accurate displacement or strain measurement, it is important to determine the optimum subset size for which the differences in the reference (undeformed) and the corresponding (deformed) subset are minimised using the sum of squared

deviations (SSD) correlation criterion, and in turn, this depends on the speckle pattern. Sutton et al[94] simplified the selection of a suitable speckle pattern and subset size by providing two rules of thumb: (1) image plane speckles should cover an array of at least 3 by 3 pixels and (2) each subset should contain at least 3 by 3 speckles. Lane et al[132] used a grey level co-occurrence matrix (GLCM), which is a second order statistical tool for describing the texture of a grey-scale image[133], to determine quantitatively the characteristics of a suitable speckle pattern. They proposed that the subset should be approximately 3 times bigger than the critical GLCM offset. While Pan et al[134] proposed that the measured displacement uncertainties are related to the mean intensity gradient of the speckle and a suitable speckle pattern possesses a higher value of mean intensity gradient.

A brief investigation was carried out to study the effect of different speckle patterns on evaluated strains around cold-expanded holes. The GLCM approach used by Lane et al[132] and the mean intensity gradient proposed by Pan et al[134] were used for the quantitative analysis of the speckle patterns. Three specimens, machined from the 1.6 mm thick aluminium sheet, were painted with a matt white base. A different black paint was used to generate the speckles on each specimen. A matt black paint (CRC Pro matt black) was sprayed onto specimen A using the spray can in which it was supplied. While an airbrush (AZTEK A7778; Testors Corp, USA) was used to apply Tamiya Model matt Black paint to specimen B and Vallejo Model Air black paint to specimen C. Figure 5.1 shows the reference images of the three speckle patterns and their corresponding grey-level intensity histograms.

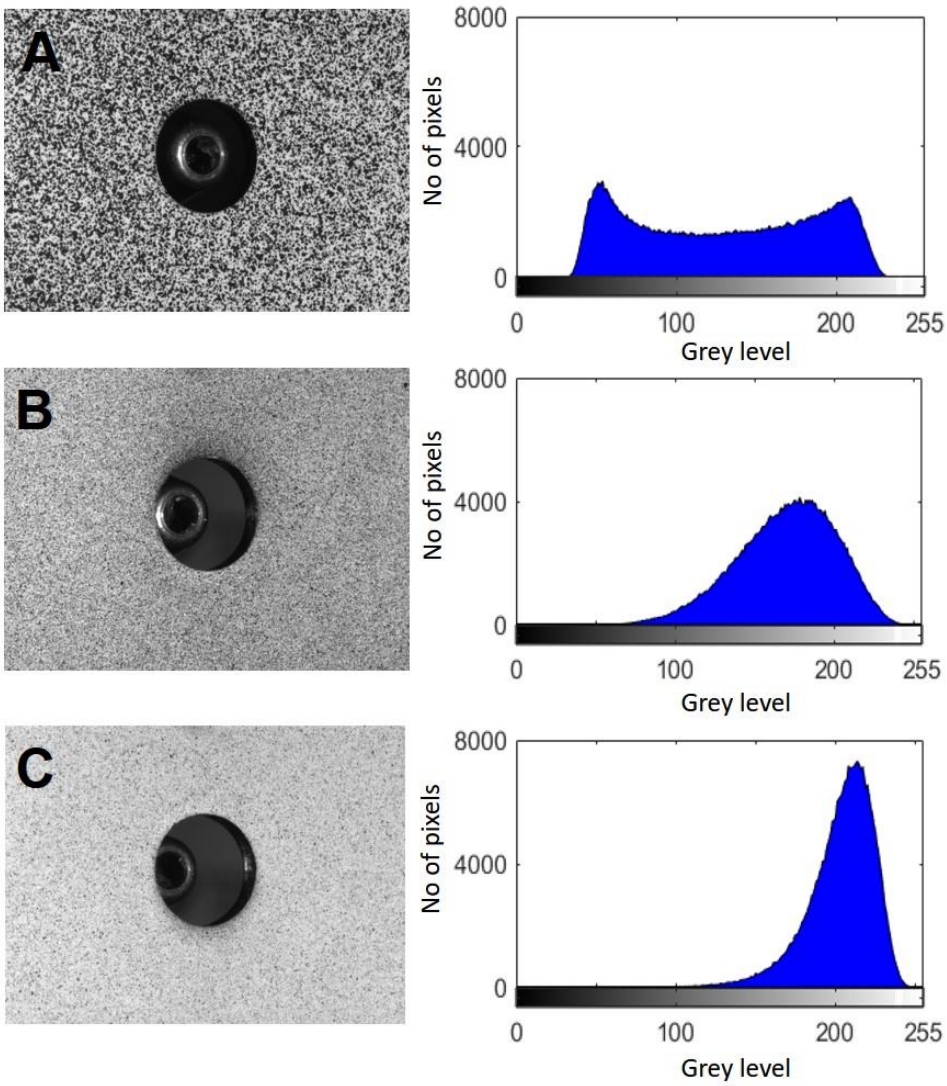

Figure 5.1 Reference images (left) and corresponding intensity histograms (right) for random speckle patterns produced using (A) CRC Pro Matt black paint in a spray can, (B) Tamiya Matt black paint and Vallejo Model Air black paint (C) applied with an airbrush.

Table 5.1 Comparison of the critical GLCM offset, nominal GLCM contrast and the mean intensity gradient for the three speckle patterns.

	Speckle pattern A	Speckle pattern B	Speckle pattern C
Critical GLCM offset (pixels)	12	8	9
Nominal GLCM contrast	6000	1480	680
Mean intensity gradient	21.4	10.1	16.1

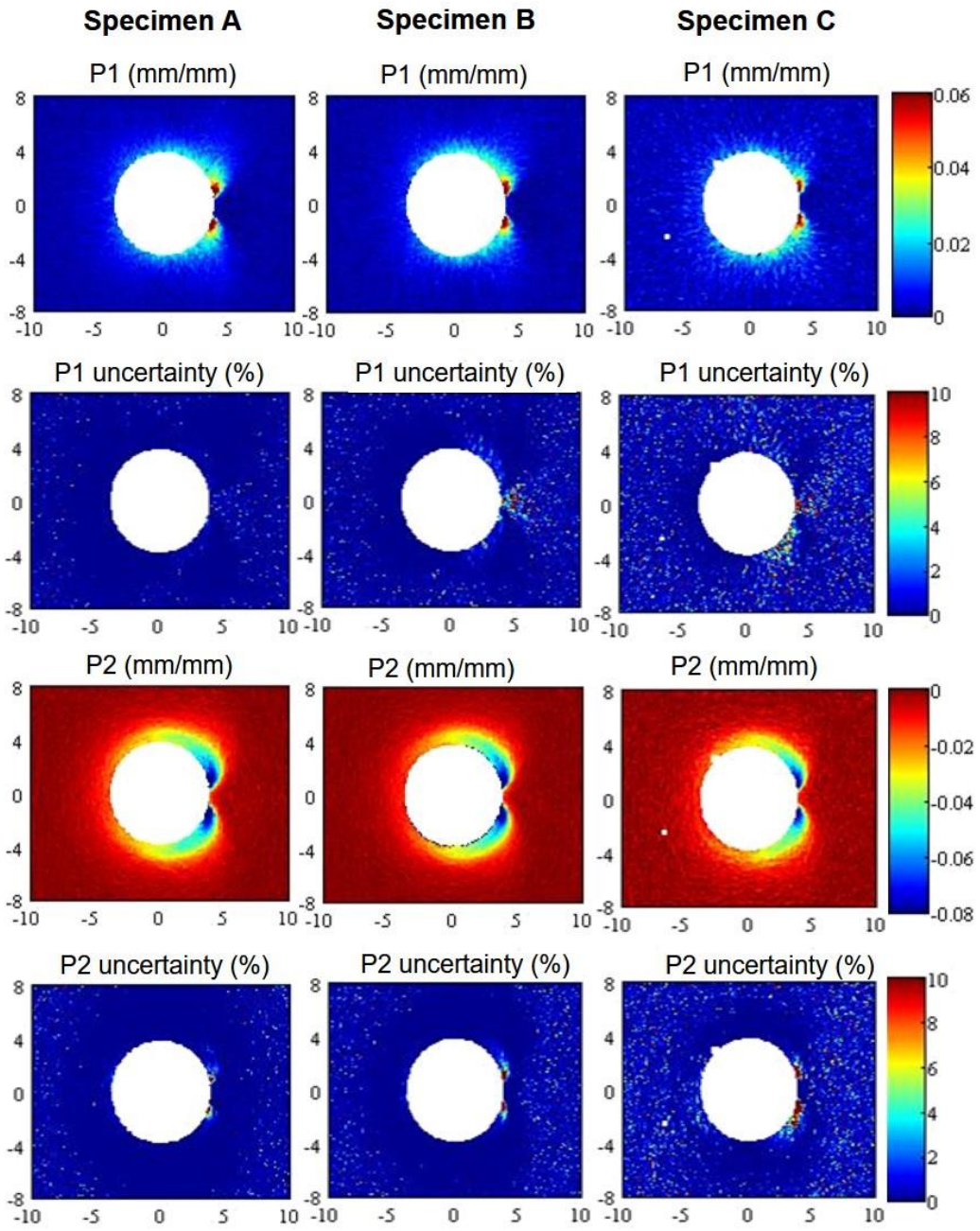

Figure 5.2 Comparison of normalized uncertainties in the in-plane maximum and minimum principal strains for the speckle patterns applied using the CRC (left), Tamiya (centre) and Vallejo (right) paint as in figure 4. All spatial dimensions are in mm.

The evaluated values of the critical GLCM offset, nominal GLCM contrast and the mean intensity gradients for the three speckle patterns are provided in Table 5.1. Cold expansion of the holes was performed on these three specimens and the images of the region around the hole, on the mandrel entry face of the specimen, were captured using the stereoscopic DIC setup (see Figure 4.8). The image

correlation was performed with a subset size of 21 pixels and grid spacing of 5 pixels using the ISTRA software[129]. Maps of the in-plane maximum and minimum principal strain, evaluated using the subset distortion method[129], and their corresponding normalised uncertainty maps are shown in Figure 5.2 for the three specimens. The normalisation was performed by dividing the uncertainty values from the ISTRA software by the corresponding values of evaluated strain. ISTRA provides estimates of the uncertainty in the strain measurements from the statistical errors in the evaluated coefficients of the shape function, which is defined by Equation 4.4, by the use of principles of error propagation.

In order to analyse the effect of the subset size and the strain evaluation method on the evaluated principal strains around the cold-expanded hole, displacements were computed by performing image correlation with the images from specimen A using subset sizes of 21 and 47 pixels with the grid spacing fixed at 5 pixels. The maximum (P1) and the minimum (P2) principal strains were evaluated from the computed displacement data by applying both the subset distortion and the more commonly applied point-wise least squares method proposed by Pan et al[135, 136]. According to many researchers[97, 135-137], the numerical differentiation of the displacement field using finite difference methods, for the purpose of determining strains, amplifies the inherent noise in the measured displacements. Therefore, local smoothing of the displacement field is essential for reliable evaluation of strains. In the point-wise least squares method[135, 136], used in this investigation as one of the methods of evaluating strains, a running least-squares fitting of two-dimensional, first-order polynomials was performed on a localised square region of the displacement field, known as the strain window. The resulting coefficients

of the polynomial were used to evaluate the strains. Pan et al[136] recommended a strain window between 11 × 11 and 21 × 21 points. However, to reduce the risk of over-smoothing of the displacement data, in particular close to the hole edge, a smaller strain window size of 9 × 9 points was employed.

For a quantitative comparison, radial line profiles of maximum and minimum principal strains along three radial lines at +45^{o}, +90^{o} and +135^{o} from the split in the sleeve (see angular orientation of split sleeve in Figure 4.6) have been plotted in Figure 5.3. These angles were selected to provide exemplar profiles containing high, intermediate and low strain gradients. The strain profiles obtained from the subset distortion method for a subset size of 21 pixels are noisier than those from the point-wise least squares method and in the latter case there appears to be some significant loss of strain resolution close to the hole edge. However, with a subset size of 47 pixels, both the subset distortion and the point-wise least squares method provide very similar results with an apparent loss of resolution close the hole edge compared to the results obtained with the smaller subsets using the subset distortion method. Figure 5.2 clearly shows that the uncertainties in the evaluated principal strains were lowest for the speckle pattern produced using a spray can on specimen A, which also has the highest mean intensity gradient (see Table 5.1). This reinforces the conclusions reported by Pan et al[134] that suitable speckle patterns possess higher mean intensity gradients. Lane et al[132] proposed that an optimum speckle pattern possesses a low critical GLCM offset and high nominal GLCM contrast, but they did not comment on which of these parameters has a greater influence on the DIC measurements. Specimen A had the highest nominal GLCM contrast but its critical GLCM offset was also slightly higher than

the other two specimens. On the basis of these quantitative measures, it was concluded that the speckle pattern obtained using the spray can (specimen A) was the most suitable for DIC measurements. The reason for its better performance is probably related to its relatively broad and flat intensity histogram in Figure 5.1.

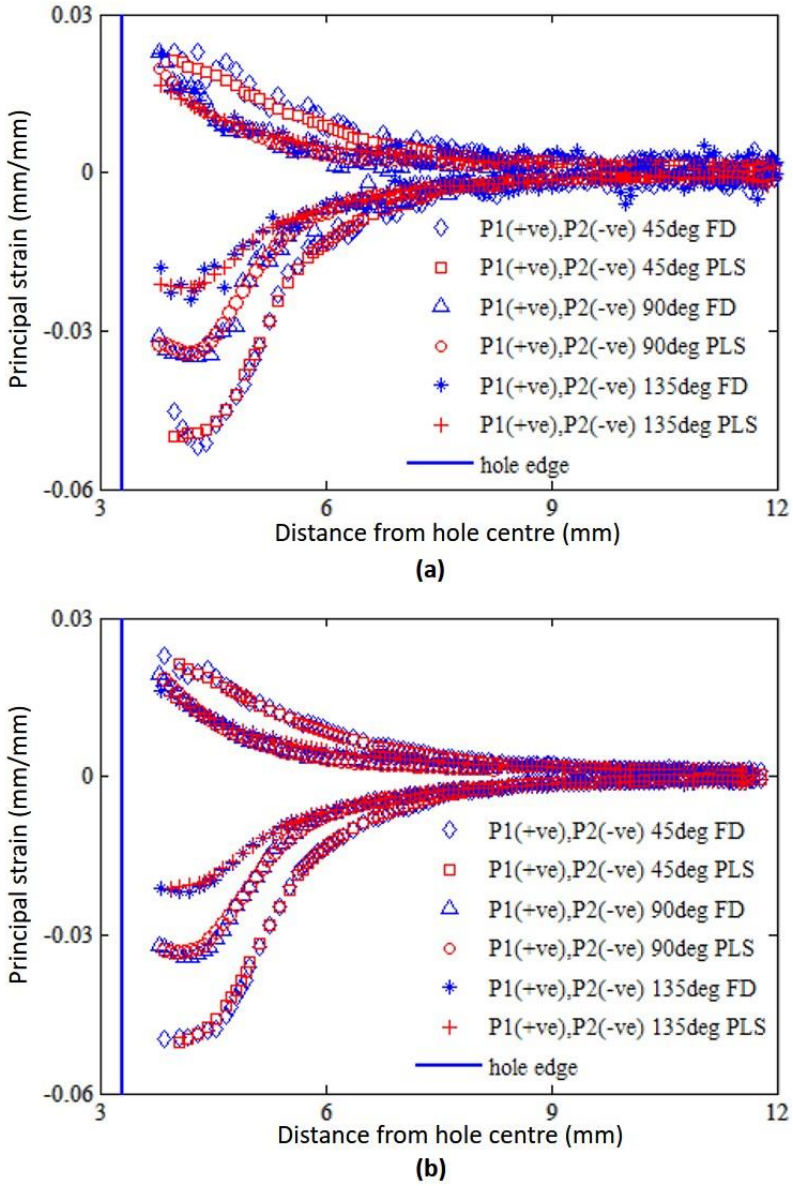

Figure 5.3 In-plane maximum and minimum principal strains along radial lines from centre of holes obtained using the Subset Distortion and the Point-wise Least Squares method for facet sizes of 21 (top) and 47 (bottom) pixels.

The results reported in Sections 5.2-5.4 were obtained by performing image correlation with a subset size of 47 pixels, and a grid spacing of 5 pixels and the strains were evaluated using the subset distortion method.

5.2 Displacement and strain resolutions of stereoscopic DIC setup

The resolution of the stereoscopic DIC setup was determined by placing the specimen in the retention holder and capturing images of the region of interest twice without applying any loads. Image correlation was performed to determine the displacement noise maps shown in Figure 5.4. The noise maps for the principal strains evaluated from the displacement noise maps are also presented in Figure 5.4. The resolution of the DIC setup is defined as the smallest significant value that can be measured. The displacement and the strain resolutions were determined by calculating the standard deviation of the noise maps and are reported as 95 % confidence limits for the mean value, or two standard deviations, in Table 5.2.

A periodic pattern can be observed in the displacement noise maps in Figure 5.4 which is likely caused by aliasing. When a large number of speckles of the order of 3×3 pixels are present in the speckle pattern, they are under-sampled by the camera sensor during the image digitization process. This results in 'aliased' speckles which could induce slight bias in the DIC measurements[94, 138]. Unfortunately, there is no direct method of determining whether the speckles in a given image has been 'aliased' because the information is lost once the speckle has been digitized[138]. However, to provide some evidence for the possibility of aliasing, the image of the speckle pattern which was created to determine the

resolution of the DIC setup is shown in Figure 5.5. The speckle pattern image was found to have large number of 'undersized' speckles of the order of 3×3 pixels indicating that they might have been aliased during image digitization. Figure 5.6 shows the comparison of the displacement noise maps with the maps of displacements resulting from split sleeve cold expansion. The magnitude of the periodic noise is negligible in comparison to the displacements resulting from cold expansion. Moreover, the DIC setup was used in this work primarily to perform strain measurements close to the hole edge i.e. within the plastic zone developed from the cold expansion process. The lowest strain in this area, witnessed at the boundary between the elastic and plastically deformed regions, is of the order of 2000 μ strain, which is significantly higher than the maximum uncertainty value of ± 72 μ strain (see Table 5.2). It can, therefore, be concluded that strain resolution of the DIC setup was sufficiently high to accurately measure the total residual strains resulting from cold expansion.

Table 5.2 Values for the displacement and strain resolutions of the DIC setup.

	Displacements (μm)			**Principal strains (μstrains)**	
	X	**Y**	**Z**	**Max.**	**Min.**
Mean	-2	-2	+2.2	+38	-37
Uncertainty (2×std.dev)	±0.1	±0.1	±0.3	±72	±68

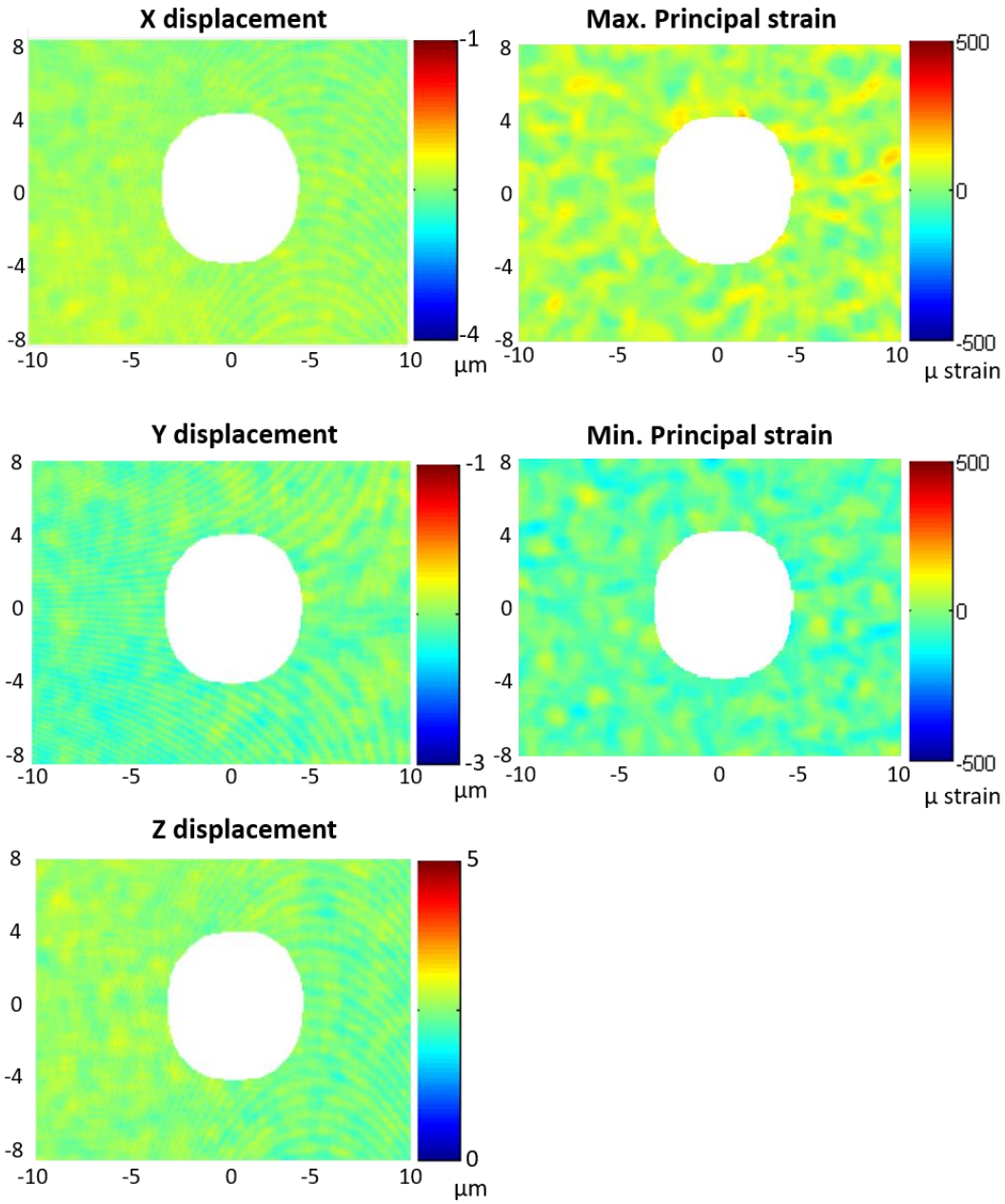

Figure 5.4 The noise maps for the three displacement components (left) and the principal strains (right). The map dimensions are in mm.

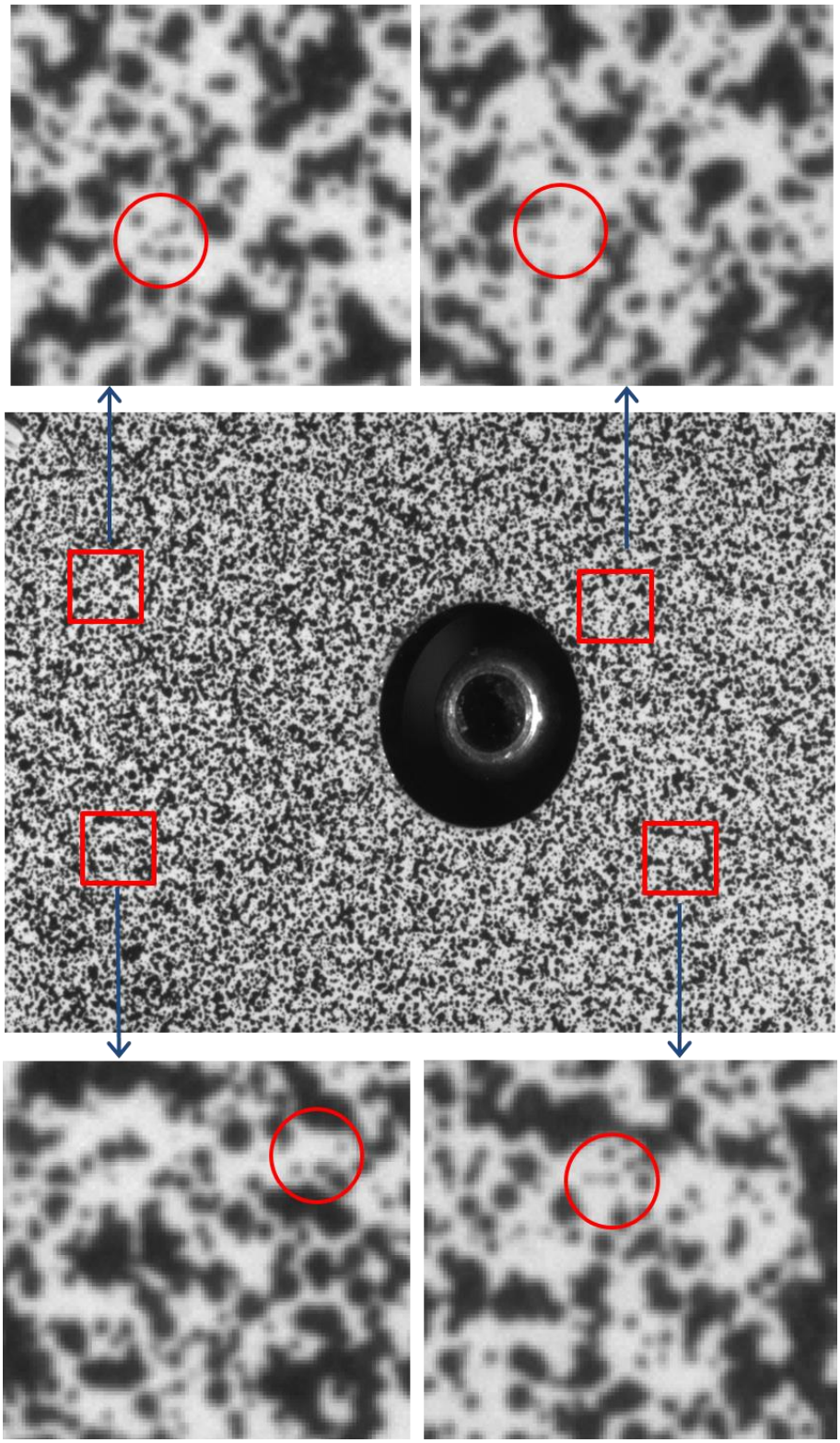

Figure 5.5 The image in the middle shows the speckle pattern created to determine the measurement resolution of the DIC setup. The zoomed-in images of the speckle pattern on the top and bottom show the presence of 'undersized' speckles highlighted by the red circles.

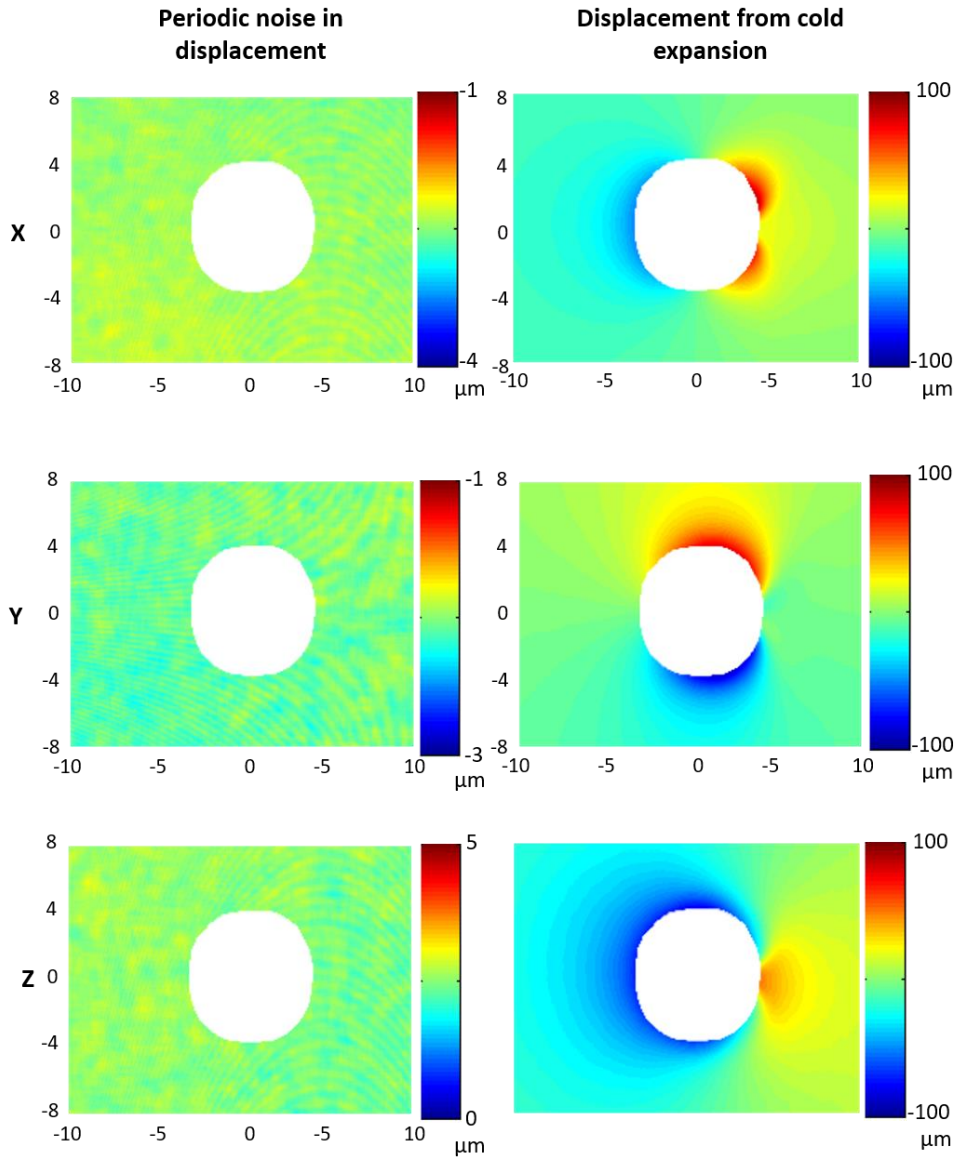

Figure 5.6 Comparison between the maps of noise in the displacement measurements (right) and the displacements resulting from split sleeve cold expansion (left).

5.3 Cold expansion process variability

To analyse the inherent variability in the split sleeve cold expansion process, altogether, twelve experiments were performed, involving 1.6 mm thick aluminium specimens, using identical camera setting and calibration parameters. For the first six experiments, strains were measured on the mandrel entry face of the specimen and for the last six experiments; strains were measured on the mandrel exit face. Figure 5.7 shows the average maximum and minimum principal

strain maps for the mandrel entry and exit faces, which were evaluated from the six data sets each on the two specimen faces. Figure 5.8 shows the corresponding uncertainties in the principal strain maps, which are represented by one standard deviation for the mean values. The uncertainties are of the order of 30 % of the mean values for principal strains in the region surrounding the location of split in the sleeve. The severe deformation caused by the split edges during cold expansion is highly localised, and therefore, is difficult to reproduce. A slight variation in the split sleeve orientation results in a significant variation in the resulting strain distribution, which seems to be the primary reason for high uncertainty in the strain measurements in this region.

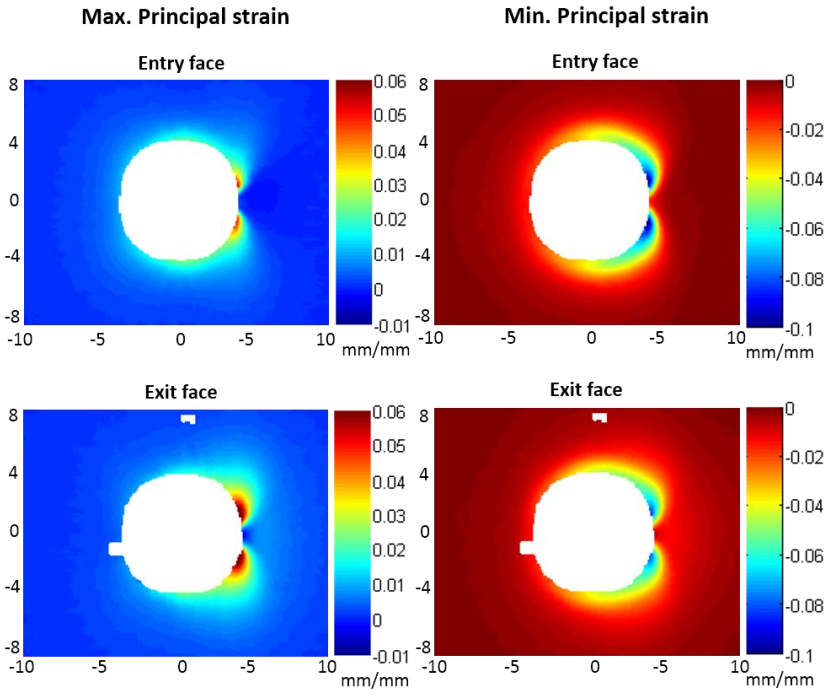

Figure 5.7 Maps of the mean values of maximum (left) and minimum (right) principal strains measured on the mandrel entry (top) and exit (bottom) faces of the specimen.

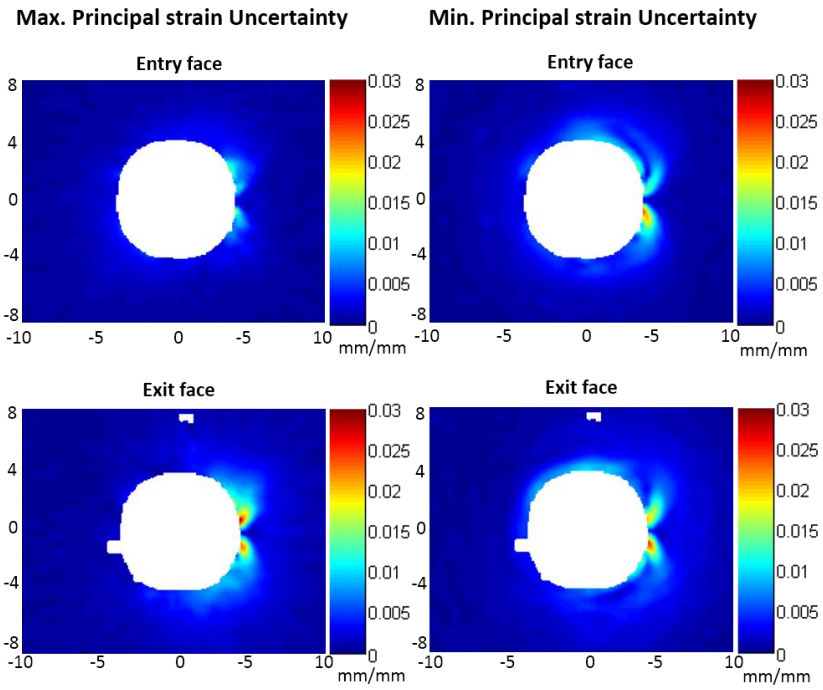

Figure 5.8 Maps of uncertainty in the mean values of the maximum (left) and minimum (right) principal strains measured on the mandrel entry (top) and exit (bottom) faces of the specimen.

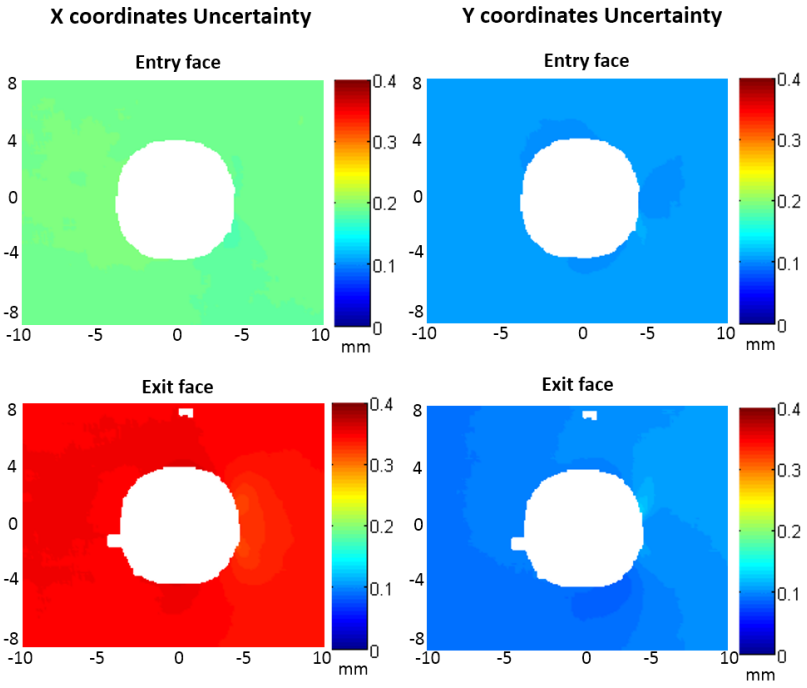

Figure 5.9 Maps of the uncertainty in the mean values of the X (left) and Y (right) coordinates for the measurement points on the mandrel entry (top) and exit (bottom) faces of the specimen.

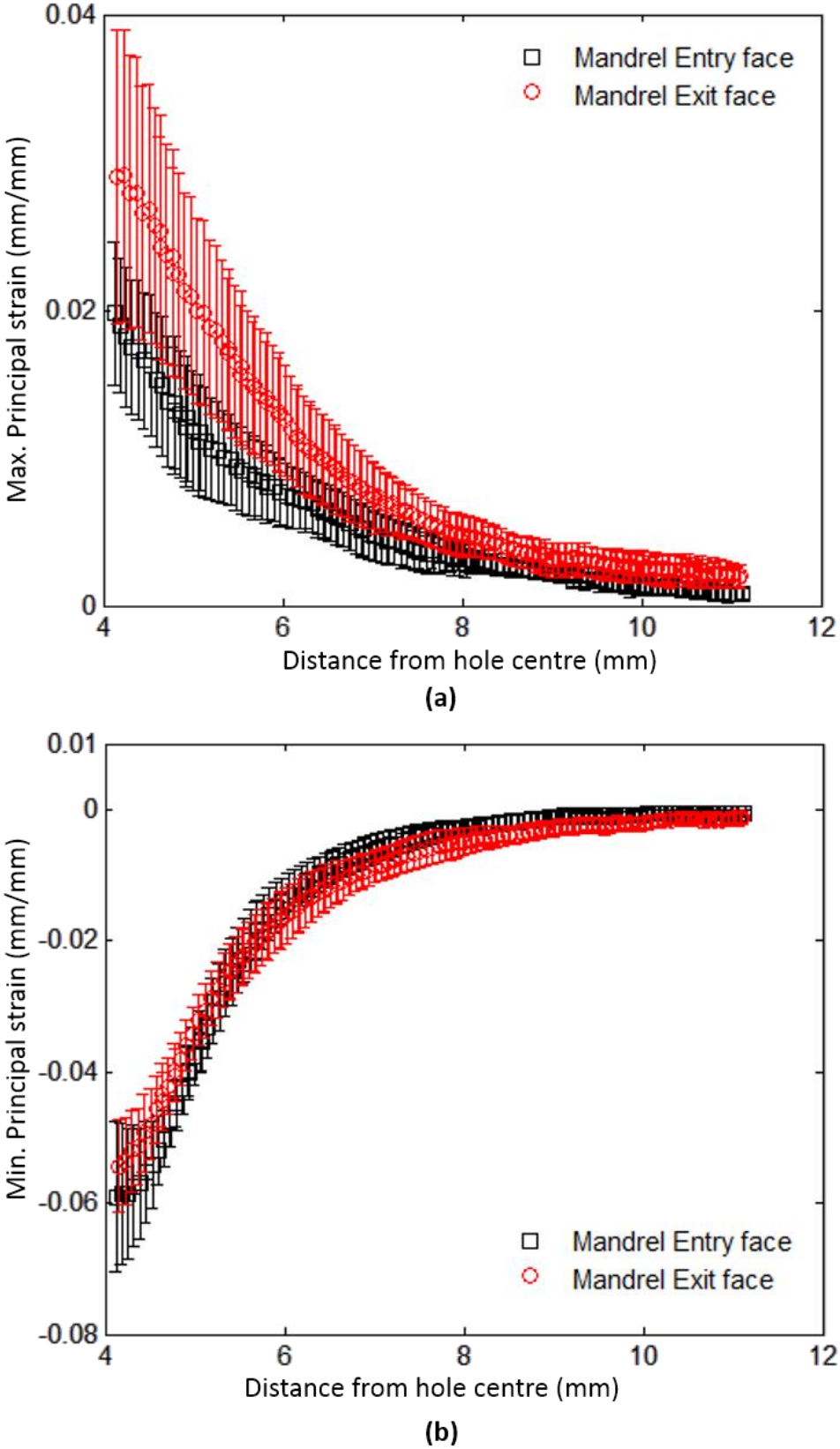

Figure 5.10 Plots of (a) maximum and (b) minimum principal strains along the radial line at 45º from the location of split in the sleeve.

Another key factor contributing to the uncertainty in the strain field developed by cold expansion is the variation in the location of specimen with respect to the mandrel axis. The standard deviation in the mean values for the horizontal (X) and vertical (Y) coordinates of the matrix of measurement points around the hole, with their origin defined at the hole centre, are presented in Figure 5.9. It can be concluded from the plots in figure 5.9 that the specimens were positioned in the retention holder for cold expansion with an accuracy of about ±0.19 & ±0.34 mm along the horizontal axis and ±0.12 & ±0.10 mm along the vertical axis for the mandrel entry and exit face measurements, respectively.

As mentioned in the earlier sections, many researchers[7-13] have reported non-uniform distributions of residual stresses, developed by cold expansion, through the specimen thickness. However, to the best of the author's knowledge, none of these studies have investigated the consistency in reproducing such residual stress distributions. A difference can be observed between the principal strain fields on the mandrel entry and exit faces in Figure 5.7, which reinforces three-dimensional nature of the cold expansion process. Figure 5.10 shows the plots of maximum and minimum principal strains for the mandrel entry and exit faces along the radial line at 45^{o} from the location of split in the sleeve. There is a clear difference between mandrel entry and exit face strains, in particular, close to the hole edge; however, the error bars representing the standard deviations in the mean values for mandrel entry and exit face strains overlap with each other. This shows that the difference between the mandrel entry and exit face strains is lower than the uncertainty in the strain measurements due to inherent variability in the split sleeve cold expansion process. The results presented in this section, therefore,

imply that it is important to take into account the uncertainty in the residual stress field resulting from cold expansion in the fatigue life assessment of cracks emanating from cold-expanded holes.

5.4 Comparison of cold expansion in thick and thin specimens

The principal strain maps on the mandrel entry and exit face of the 1.6 mm and 6.35 mm thick specimens are presented in Figures 5.11 and 5.12 respectively. In Figures 5.13 & 5.14 distributions of in-plane principal strains along radial lines are plotted along with the theoretical distributions for the thin and thick specimens, respectively. The theoretical strain distributions were obtained by implementing the axisymmetric hole expansion model of Zhang et al[57], briefly described in Section 2.1.4, using the mechanical properties provided in Table 4.2. This theoretical model is based on the assumption of a finite-width plate containing a central hole, which is being expanded axisymmetrically by a uniform pressure under the plane stress condition. The material of the plate is represented by an elastic non-linear strain-hardening model with the Baushinger effect present during spring-back from the surrounding elastic material upon unloading of the hole. The axisymmetric assumption of the theory implies that the maximum and minimum principal strains correspond to the hoop and radial strains, respectively.

5.4.1 Deviation from axisymmetric hole expansion

It is evident from the experimental data in Figures 5.11 and 5.12 that the split sleeve cold expansion is not axisymmetric about the hole centre, but there is

symmetry about the longitudinal axis of the specimens which coincides with the location of the split in the sleeve.

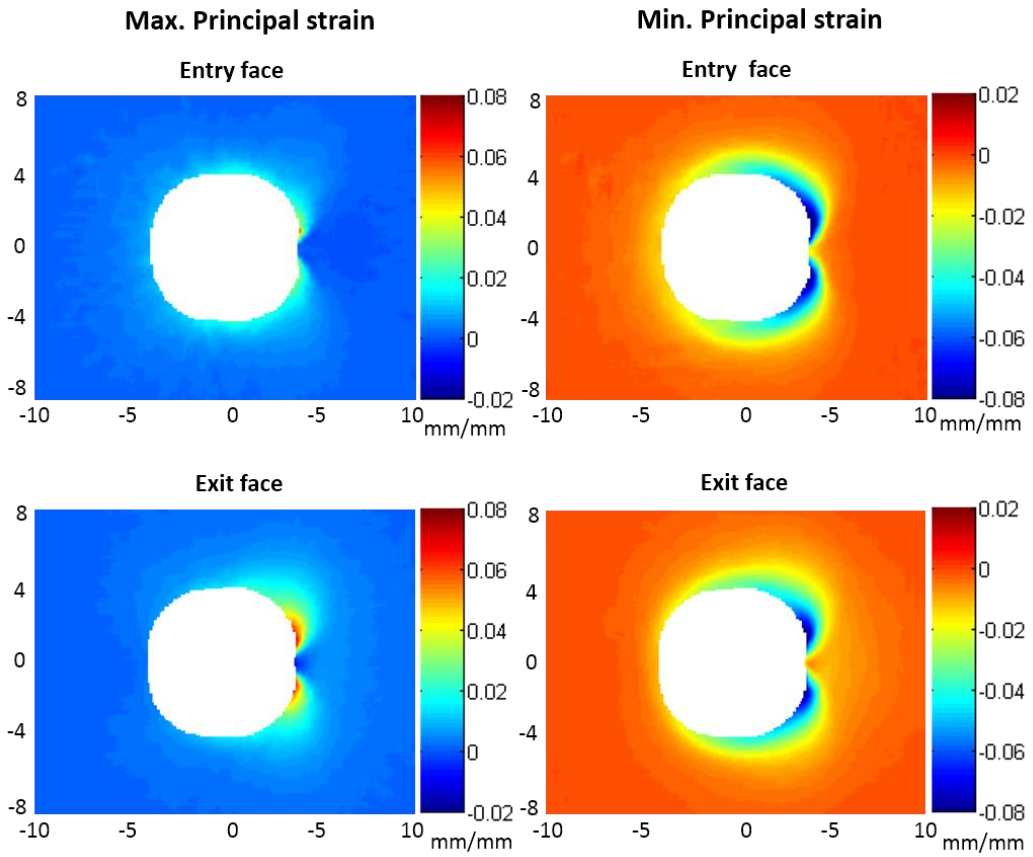

Figure 5.11 Maps of maximum (left) and minimum (right) principal strains on the mandrel entry (top) and exit (bottom) face of the 1.6 mm thick specimen.

The peak strains are observed along radial lines at approximately 45° from the location of the split sleeve, which is close to the edges of the region influenced by the split in the sleeve during the expansion process (see Figures 5.13 & 5.14). The magnitude of the strain distributions decreases circumferentially away from the edges of the split to a minimum at 180° from the split. This trend is more apparent in the strain profiles for the thin specimens. In both cases, the magnitudes of the principal strains are low along the radial line emanating at the location of the split, which seems to imply that the expansion of hole is less at this location causing a break in the strain distribution around the hole that can also be observed in the

principal strain maps in Figures 5.11 and 5.12. The distributions of minimum principal strain for the thin specimens in Figure 5.13 exhibit a reduction in gradient close to the hole edge which is not present in the data for the thick specimens in Figure 5.14 and appears to be indicative of a maximum close to the edge of the hole. This behaviour is unexpected because it has not been reported in previous experimental investigations and the theoretical model predicts a very rapid increase in strain close to the hole edge.

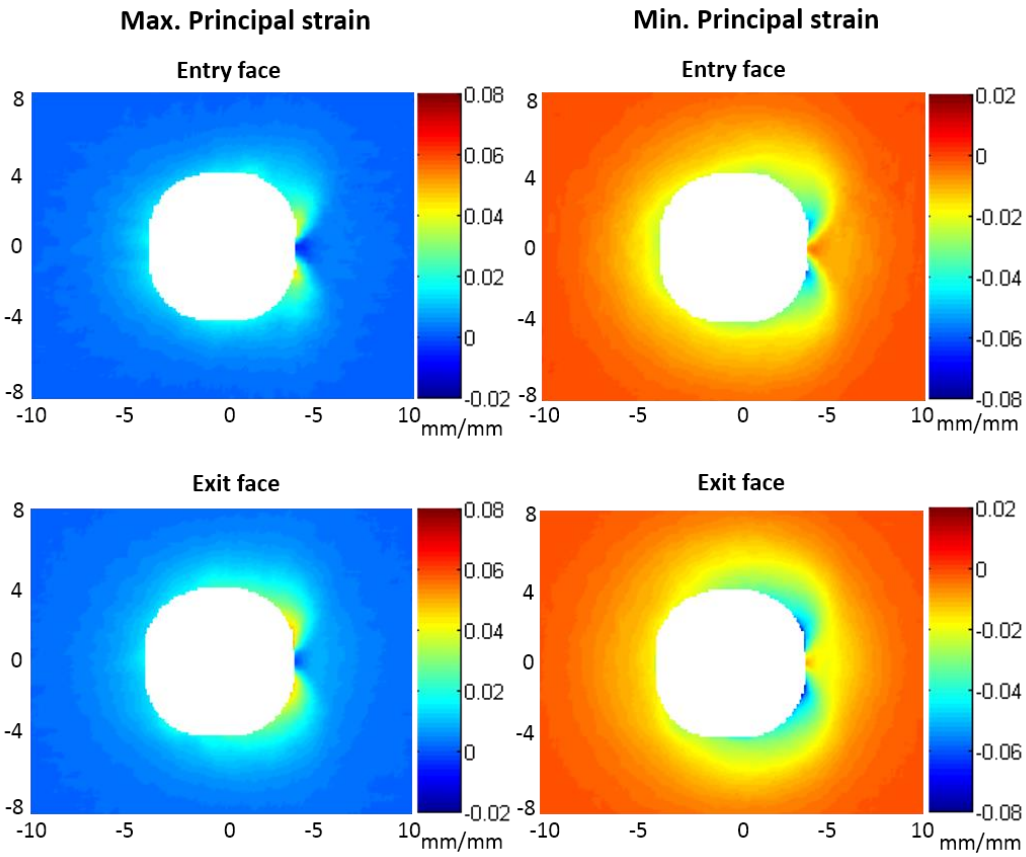

Figure 5.12 Maps of maximum (left) and minimum (right) principal strains on the mandrel entry (top) and exit (bottom) face of the 6.35 mm thick specimen.

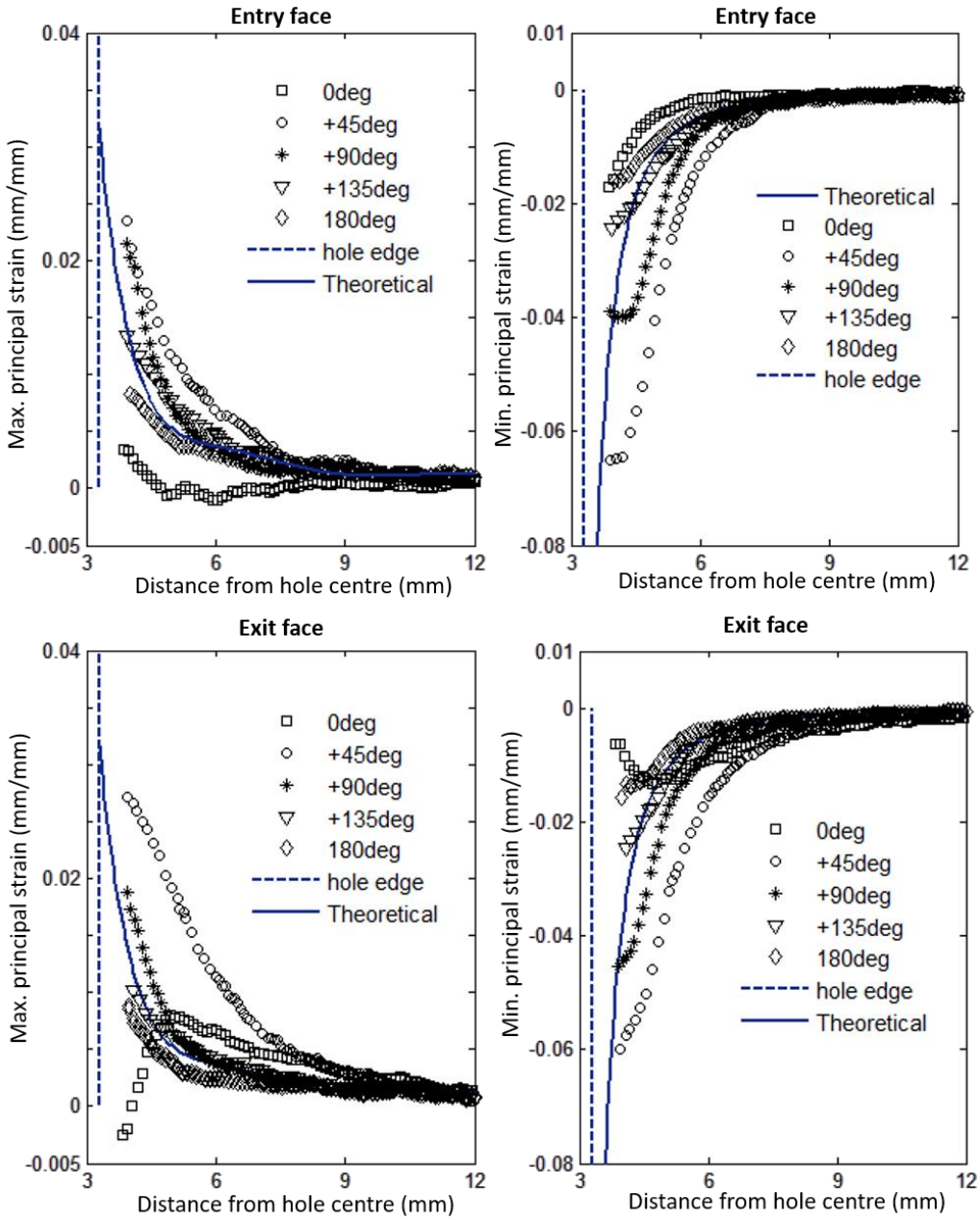

Figure 5.13 Maximum (left) and minimum (right) principal strains along radial lines from the centre of the hole on the mandrel entry (top) and exit (bottom) face for 1.6 mm thick specimen.

5.4.2 Effect of split sleeve on hole expansion

During the cold expansion process, as the mandrel's oversized head approaches the hole for expansion, the gap between the edges of the split in the sleeve will increase which would potentially cause some relative motion or a circumferential slip between the sleeve and the internal edge of the hole. The hole region between

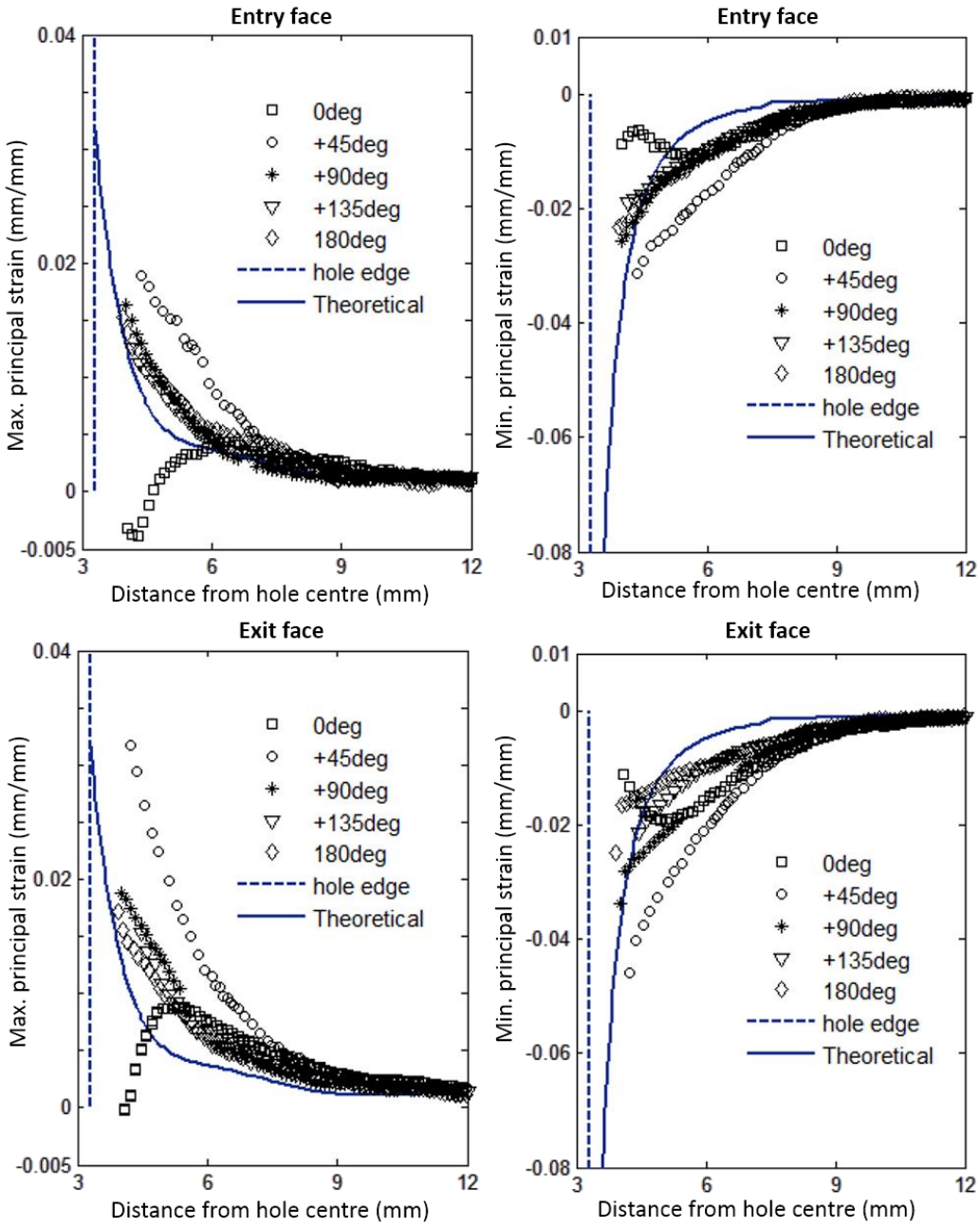

Figure 5.14 Maximum (left) and minimum (right) principal strains along radial lines from the centre of the hole on the mandrel entry (top) and exit (bottom) face for 6.35 mm thick specimen.

the edges of the split in the sleeve is, therefore, expected to expand as a result of the direct contact of the mandrel head with the internal edge of the hole, which will likely cause material to be 'dragged' through the hole axially rather than expanded radially and circumferentially. This region is expected to be demarcated

by a pair of boundaries extending along radial lines that approximately subtend the angle enclosed by edges of the split during hole expansion (see Figure 5.15).

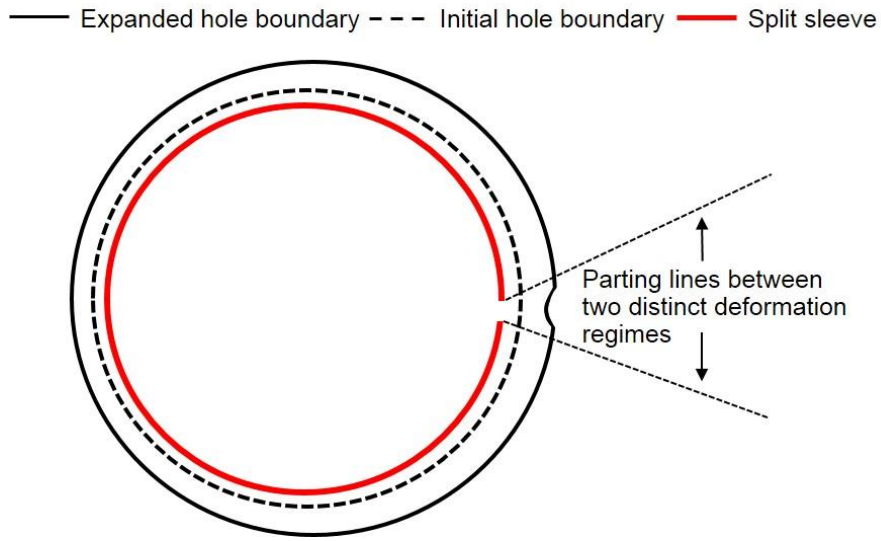

Figure 5.15 Schematic diagram of the influence of the edges of the split in the sleeve on the deformation. The parting lines are drawn at an arbitrary angle.

The influence of the split in the sleeve on the overall hole deformation was examined by plotting the shear strains in polar coordinates along radial lines at angles between 0° and 50° from the location of the split in Figures 5.16 and 5.17 for the thin and the thick specimens respectively. It can be observed in these figures that the shear strains are negligible along the 0^o radial line. This is because of the fact that the radial line at 0^o coincides with the line of symmetry of the strain field developed from split sleeve cold expansion (see e.g. Figure 5.11). Shear strains are expected to be significant along the radial lines at all other angles due to non-axisymmetric expansion of the hole; this also explains the reason for a significant difference between the magnitude of shear strains along the radial lines at 0^o and 10^o in Figures 5.16 and 5.17. Distinct turning points in the distribution of shear strain along the radial lines at 20° and 30° imply that these radial lines intersect with the boundary separating the two distinct deformation regimes.

Also, the shear strains are higher along the radial lines at angles between 10° and 30° providing further evidence that the hole expansion deviates from an axisymmetric expansion close to the location of the split in the sleeve. It has been reported in an earlier investigation[8] that the residual elastic stress distributions along the 0° radial line, which corresponds to the position of the split in the sleeve, were significantly different in shape and less compressive in magnitude close to the hole edge in comparison to the distributions along a radial line at 90°. The results in Figures 5.16 and 5.17 highlight that the split in the sleeve influences the expansion of the hole over a much wider angular range, that is, -30° to +30° and therefore the residual elastic stress distributions developed in this region are expected to be significantly different from the theoretical predictions.

5.4.3 Plastic zones around cold-expanded holes

The size of the plastic zone developed around the cold-expanded hole is an indication of the effectiveness of cold expansion process. The development of a larger plastic zone during hole expansion results in a higher spring-back force from the elastic material surrounding the plastically deformed material, thus creating a more compressive residual elastic stress field. Polar plots of the radius of the plastic zone around the cold-expanded hole are presented in Figure 5.18 and represent the shape of the plastic zone. They were obtained by calculating the von Mises stress, or equivalent tensile stress[139] along radial lines at 20° increments around the hole and identifying the radius of the plastic zone as where the von Mises stress was equal to the yield stress, based on the mechanical properties along the sheet rolling direction in Table 4.2.

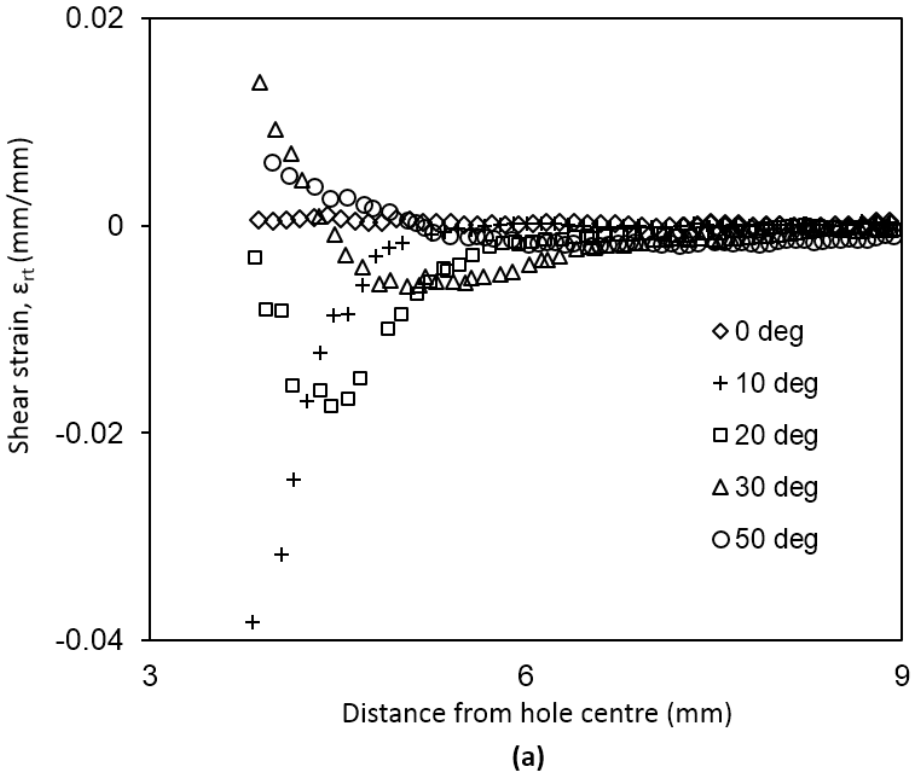

(a)

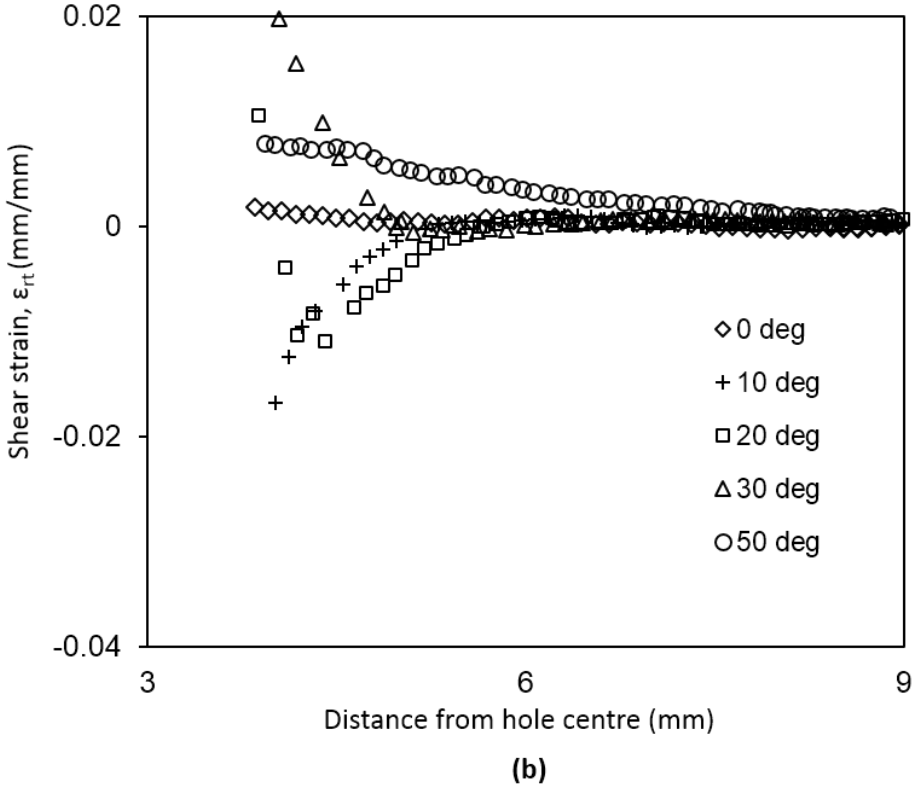

(b)

Figure 5.16 Shear strain components in polar coordinates on the (a) mandrel entry and (b) exit face along the radial lines from the centre of the hole close to the location of the split in sleeve for 1.6 mm thick specimens.

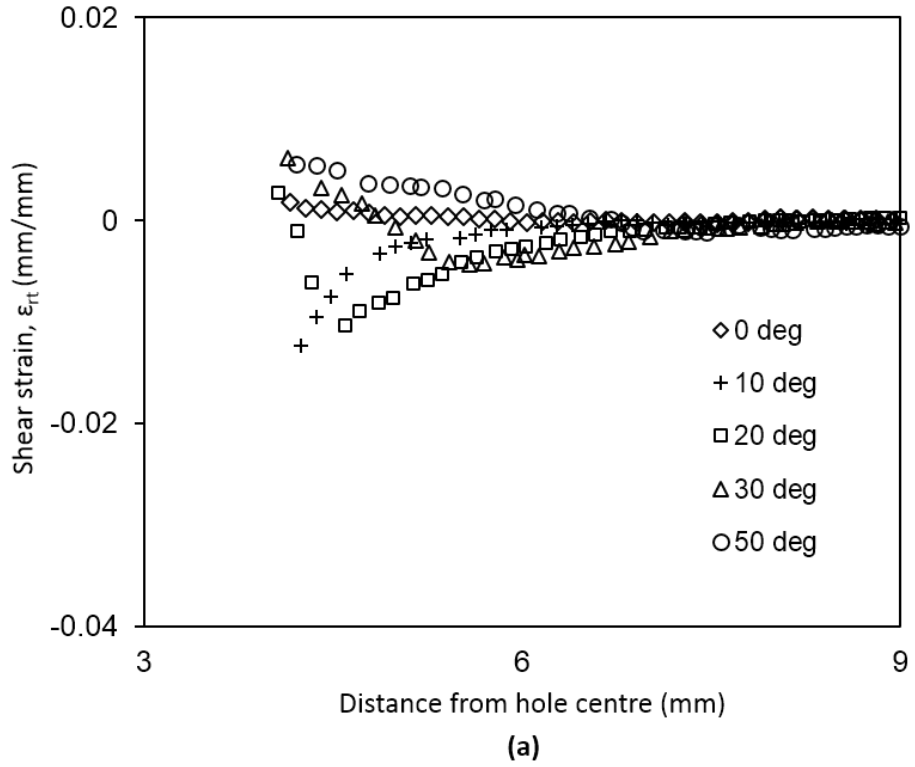

(a)

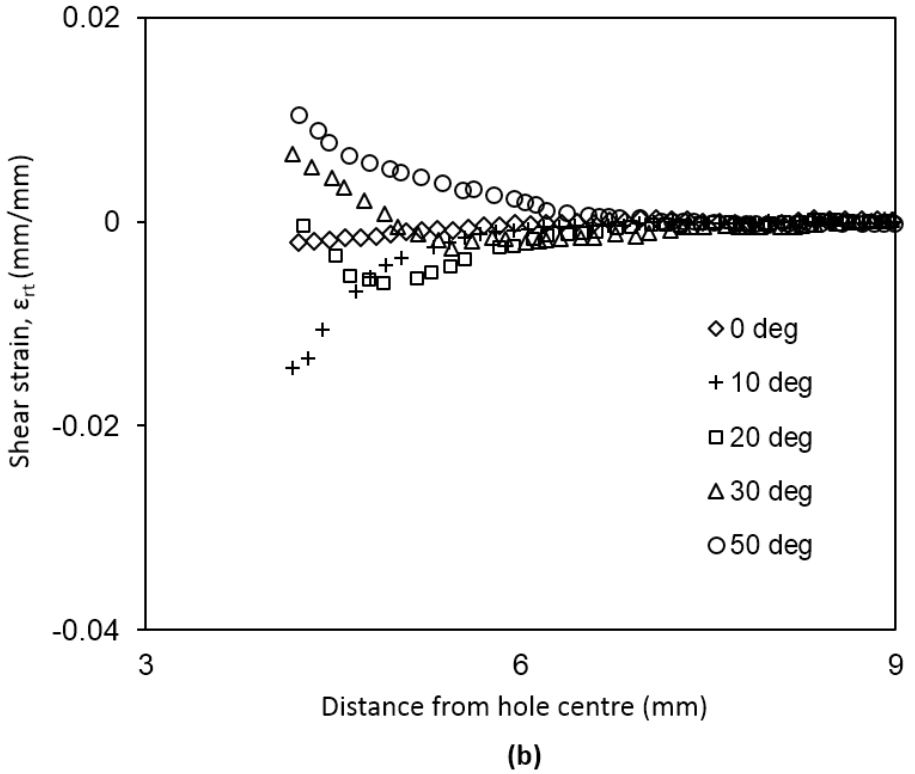

(b)

Figure 5.17 Shear strain components in polar coordinates on the (a) mandrel entry and (b) exit face along the radial lines from the centre of the hole close to the location of the split in sleeve for 6.35 mm thick specimens.

For thin specimens, the plastic zone shape on the mandrel entry and exit faces exhibits a high level of deviation from axisymmetry about the hole centre. On the other hand, on both the entry and exit face in the thick specimens, the plastic zone is more axisymmetric and overall larger in size compared to the thin specimens. The plastic zone on the exit face is consistently slightly larger than on the entry face, which implies that the residual elastic stresses will be higher on the exit face. Several earlier investigations[7-13] have reported this trend of higher compressive stresses on the mandrel exit face. It is pertinent to mention here that the size of the plastic zone developed around the expanded hole for identical specimen geometry and hole expansion level depends on the material properties of the specimen. The material properties provided in Table 4.2 for the two types of specimens are very similar and there is a negligible difference in the size of theoretical plastic zones for the thin and the thick specimens, presented in Figure 5.18.

To evaluate the uncertainty in the plastic zone size resulting from the inherent variability in the split sleeve cold expansion process, the plastic zones were determine for the twelve, 1.6 mm thick, specimens involved in the study about the cold expansion process variability, which is reported in the previous section. Figure 5.19 shows the set of six plastic zone shapes determined for each of the two specimen faces. The maximum standard deviation in the radii of the plastic zones was found to be ±0.24 and ±0.29 mm for the mandrel entry and exit faces respectively. This confirms that the difference between the size of the plastic zones, developed around the cold-expanded hole, in the thick and the thin

specimens in Figure 5.18 is entirely due to the distinct mechanics of hole deformation during cold expansion in the two types of specimens.

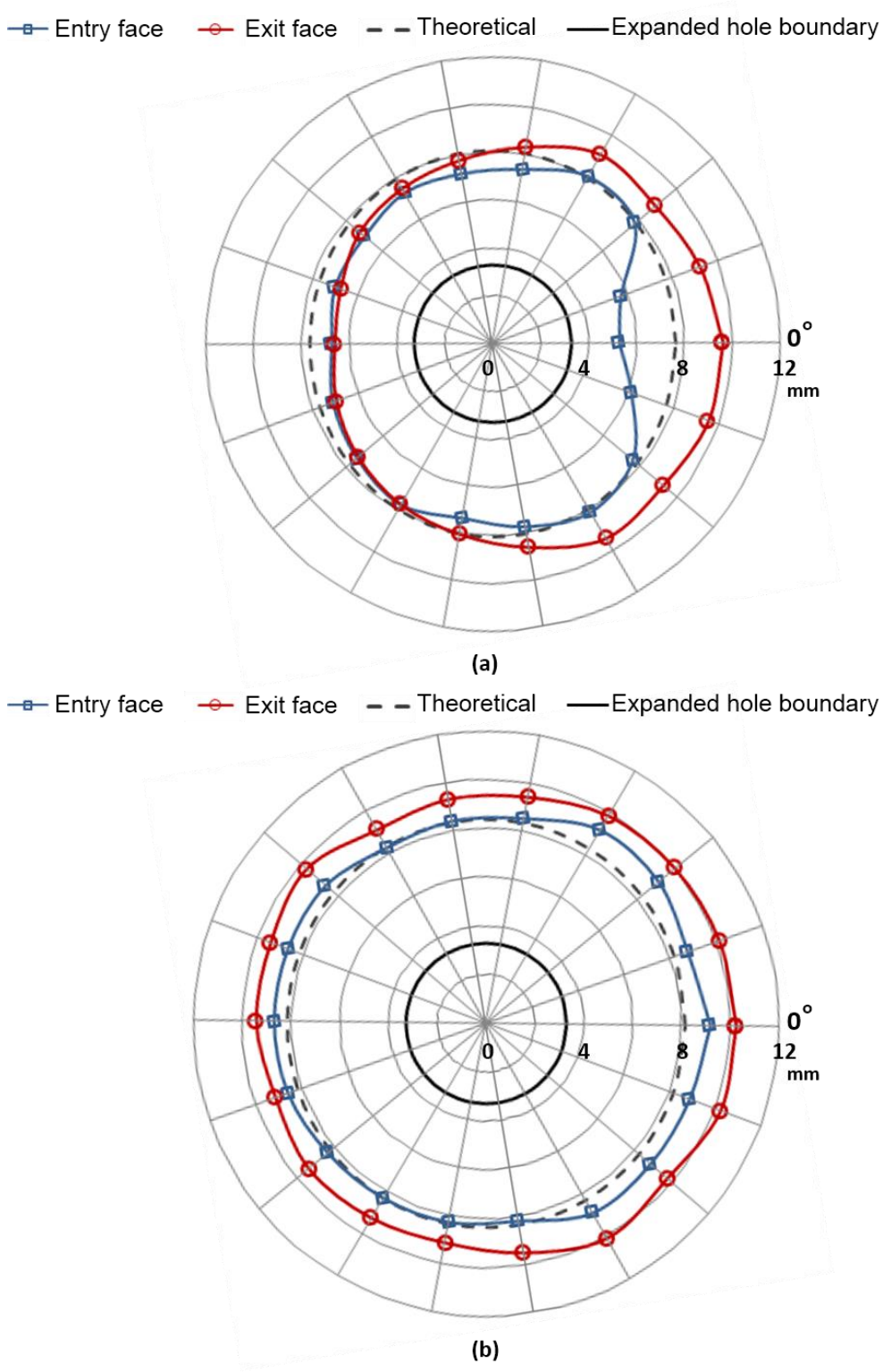

Figure 5.18 Plots of the shape of the plastic zone for (a) 1.6 mm and (b) 6.35 mm specimen.

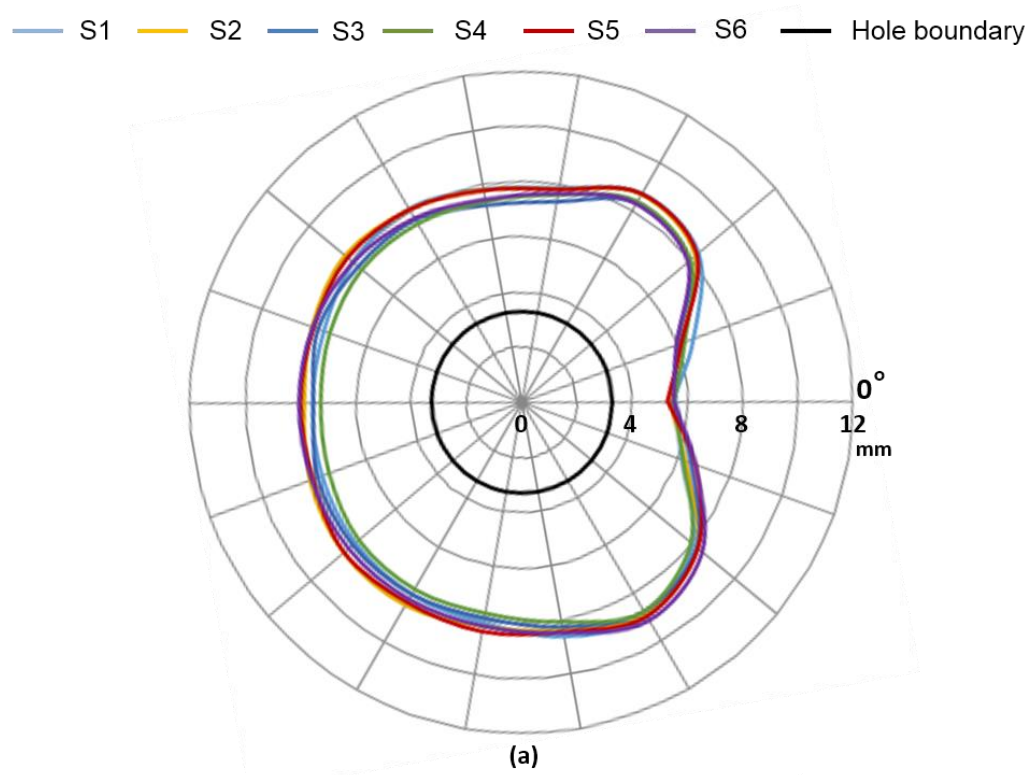

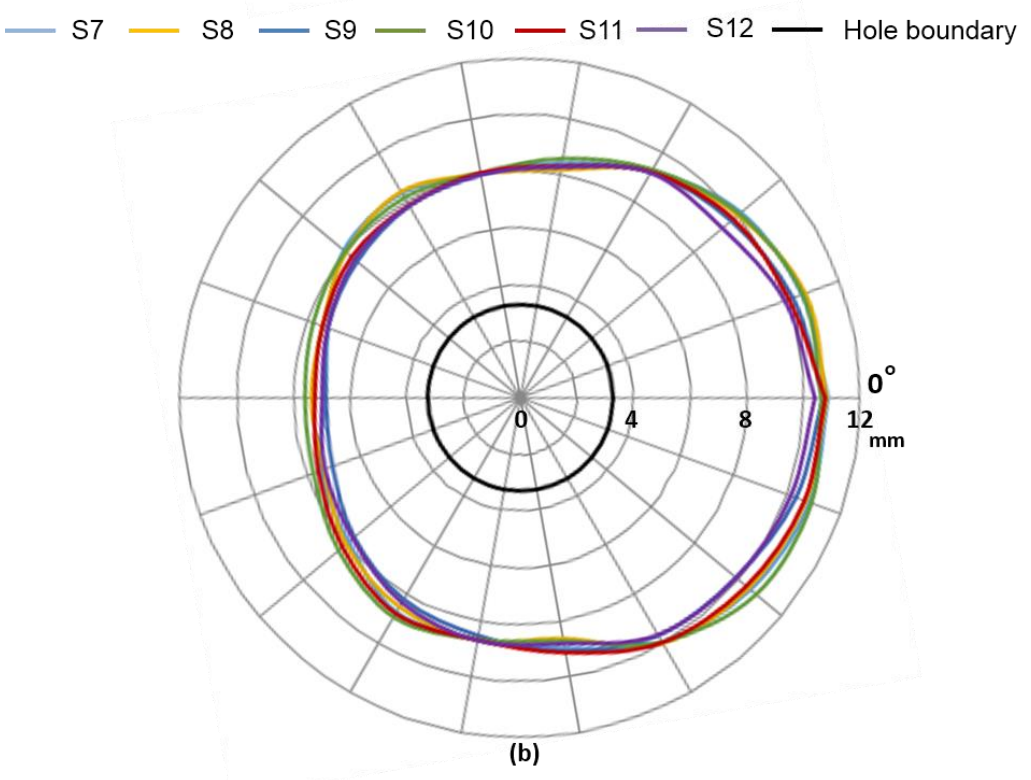

Figure 5.19 Plots of the shape of the plastic zone for 1.6 mm thick specimens on (a) mandrel entry (b) exit face.

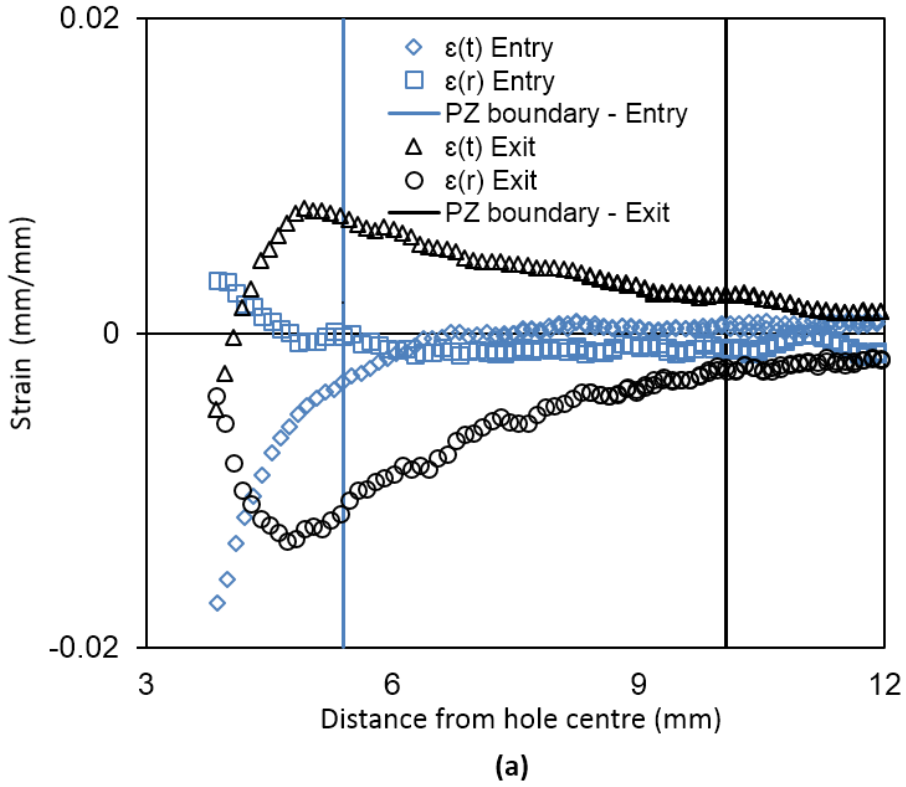

Figure 5.20 Distributions of hoop (εt) and radial (εr) strain components along a radial line from the hole centre at 0º from the split sleeve orientation for (a) 1.6 mm and (b) 6.35 mm thick specimen. The two vertical lines represent the extent of plastic zone boundary on the mandrel entry and exit faces.

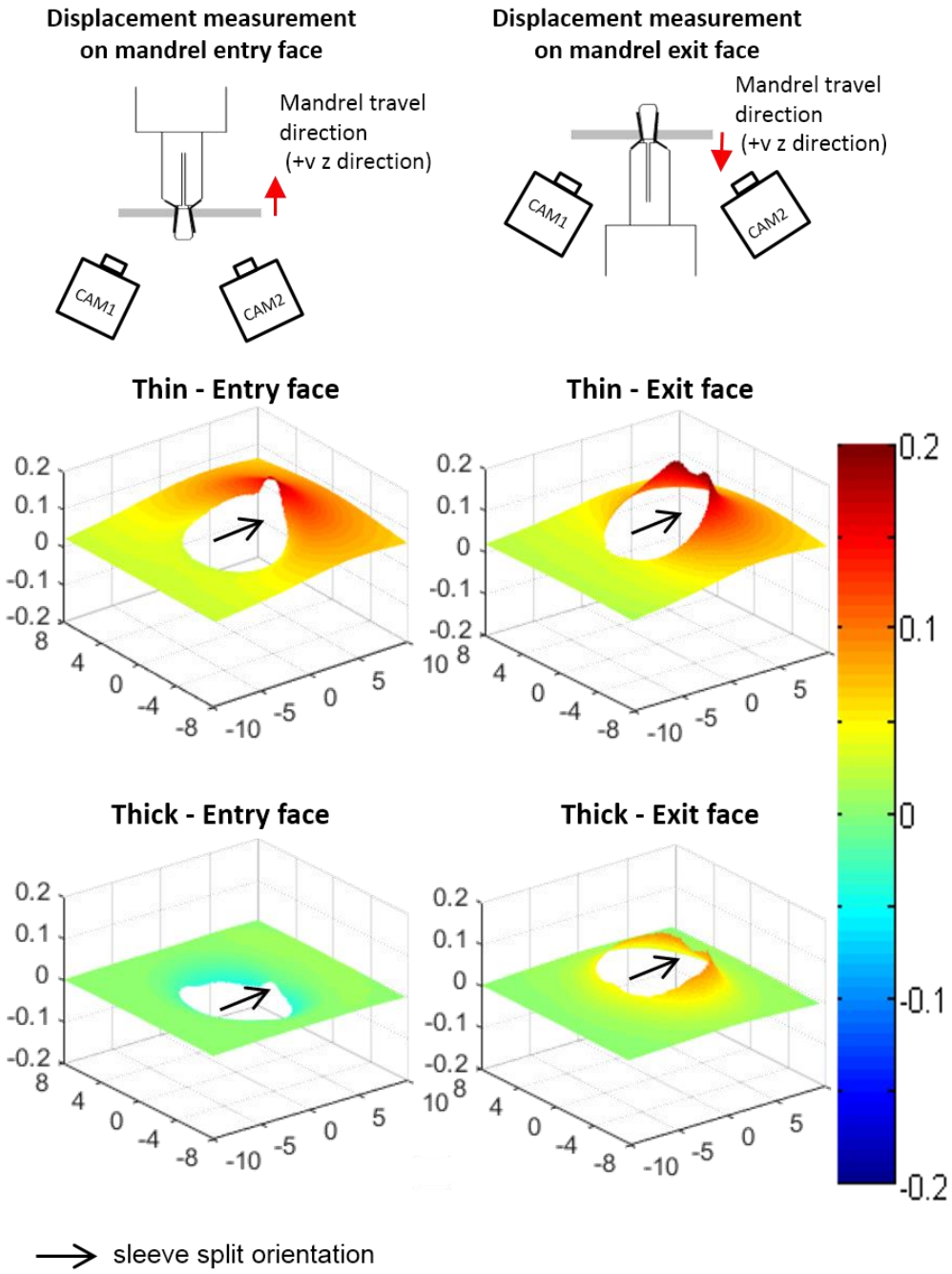

Figure 5.21 Comparison of the out-of-plane displacement fields on the mandrel entry (left) and and exit (right) faces for the the 1.6 mm (top) and 6.35 mm (bottom) thick specimens. All dimensions are in mm.

There is a significant difference in the size of the plastic zone on mandrel entry and exit faces at the location of the split in the sleeve for the thin specimen. To investigate this discrepancy, distributions of the hoop and radial strain components have been plotted along the 0° radial line in Figure 5.20. As a

consequence of in-plane radial expansion of the hole, the hoop strains are expected to be tensile and the radial strains to be compressive; however the plots in Figure 5.20 reveal that the hoop strains at the elastic-plastic boundary are compressive on the entry face and tensile on the exit face for the thin specimen indicating that the hole is not being deformed primarily in the radial direction; whereas the hoop strains on both the entry and the exit faces are tensile for the thick specimen.

5.4.4 Out-of-plane displacements

The measured out-of-plane displacements on the mandrel entry and exit faces have been plotted in Figure 5.21. The direction of positive out-of-plane displacement corresponds to the direction of travel of the mandrel. These out-of-plane displacement fields can be considered to be a combination of a global deformation field caused by the pull-force exerted on the mandrel and a local deformation field close to the hole edge associated with expansion of the hole. The data in Figure 5.21 implies that the thin specimens undergo localised warping close to the edge of the hole with a large positive out-of-plane displacement at the location of the split in the sleeve and smaller out-of-plane deformations on the opposite side of the hole. There is also evidence of global out-of-plane bending of the specimen which is more severe in the vicinity of the split in the sleeve. It is postulated that the decrease in the gradient of the minimum principal strain close to the edge of the hole in thin specimen (see Figure 5.13) is caused by this local warping i.e. the hole edge being pushed in by the mandrel pulling on the ends of the split in the sleeve at the 0° orientation. The dome-shaped out-of-plane deformation of the mandrel entry face at the location of the split in the sleeve in

the thin specimen explains the unexpected compressive hoop strain distribution along the 0° radial line in Figure 5.20.

By contrast, in the thick specimens the surface locally bulges out from both the mandrel entry and the exit faces as a result of plastic deformation of the material around the circumference of the hole during its expansion with negligible global bending of the specimen. The magnitude of this bulge or out-of-plane expansion is higher on the mandrel exit face but overall the localised out-of-plane deformations are lower for the thick specimens, which can be attributed to its higher second moment of area of its cross-section. These results highlight that the mechanics of hole expansion is entirely different for the thick and the thin specimens and the hole expansion in thin specimens deviates significantly from the ideal case of in-plane and axisymmetric radial expansion of the hole.

5.5 Summary

This chapter has presented the results of the experimental study carried out to analyse the hole deformation resulting from split sleeve cold expansion in the 1.6 mm and 6.35 mm thick specimens with t/D_o ratios of 0.25 and 1 respectively. The first section of this chapter has described the preliminary experiments performed to identify the suitable parameters such as the choice of speckle pattern, image correlation parameters and the strain evaluation method for the reliable DIC measurements. The measurement resolution of the stereoscopic DIC setup used in this research has been discussed in the second section. The strain resolution of the DIC setup was found to be ±72 μstrain. The third section has reported the experiments performed on the 1.6 mm thick specimens to investigate the

reproducibility of the strain fields developed from split sleeve cold expansion. The results showed that a severe deformation caused by the split edges during cold expansion is highly localised, and therefore, is difficult to reproduce. A slight variation in the position of split in the sleeve results in a significant variation in the resulting strain distribution, which seems to be the primary reason for high uncertainty in the strain measurements in this region (see Figure 5.8). Finally, a comparison of the strain fields developed in the thick and thin specimens has been made in the fourth section. It was demonstrated that the plastic zone developed around the expanded hole is more axisymmetric and larger in size for the thick specimen in comparison to the thin one (see Figure 5.18). These results imply that the existing split sleeve cold expansion process is not effective in creating an axisymmetric compressive residual stress zone around fastener holes in thin as it is in the thick specimens.

6 COLD EXPANSION IN STACKED SPECIMENS

Most of the fastener holes drilled in an aircraft structure are associated with the joints connecting two or more layers of material together. Despite significant relevance to the aerospace industry, there has been limited research on the application of cold expansion to clamped multi-layer stacks. The focus of research in this context had been primarily on the effect of fretting on the fatigue performance of bolted or riveted lap joints with joint holes previously cold-expanded together as a stack[140-142]. To the best of the author's knowledge, the development of residual strain fields caused by cold expansion in a multi-layer stack has not been investigated experimentally in any of the previously published studies. This chapter extends the methodology reported in the previous chapter utilising stereoscopic DIC to study the effectiveness of the split sleeve cold expansion process in creating an axisymmetric residual stress zone in stacked specimens. The two primary objectives were (1) to determine if stacking offers any improvement in the development of axisymmetric residual stress zone in thin specimens with $t/D_0 = 0.25$ and (2) to establish whether the individual layers in the stack expand identically as a monolithic layer of equivalent thickness to the stack.

For this investigation, six specimens were produced from the 1.6 mm and one from the 8 mm thick aluminium sheets. The specimen geometry is provided in Chapter 4 (see Figure 4.6). A central hole of 6.38 mm was drilled in these specimens to keep the hole expansion level to approximately 4%. Hole cold expansion was performed in a multi-layer stack, which comprised of five thin specimens, providing a combined t/D_0 ratio of 1.25. For the purpose of comparison, cold

expansion was also performed in a single thin and thick specimen with t/D_o ratios of 0.25 and 1.25, respectively.

6.1 Procedure for performing measurements on individual specimens in the stack

The schematic diagram for split sleeve cold expansion of holes in a five-layer stack is shown in Figure 6.1. During cold expansion, the mandrel passed sequentially through five specimens, entering from the first specimen at the front (L1) and leaving from the last specimen in the stack at the back (L5). To obtain DIC measurements, the region around the hole on both faces of every specimen in the stack was painted with a random black and white speckle pattern. Each specimen was then clamped individually in the retention fixture to acquire initial (reference) image of the region of interested (ROI). The specimen was flipped to obtain reference image of the ROI on the opposite face. Once the reference images were acquired, all five specimens of the stack were clamped together in the retention fixture and cold expansion was performed. After cold expansion, the stacked specimens were removed from the retention fixture and clamped back individually to obtain the final (deformed) images of the ROI on both the specimen faces. Finally, image correlation was performed between the corresponding initial and final images to determine the displacement and strain fields on both faces of every specimen in the stack.

To ensure consistent clamping of the specimens, a torque limiting wrench was used to tighten the Allen bolts of the retention fixture by applying a maximum torque of 12 Nm. There was a potential risk of damage to the speckle pattern as a

result of relative displacement between the clamped specimens, close to the hole edge, as the mandrel sequentially passes through a hole in one specimen to another during cold expansion. However, no damage to the speckle patterns on the contacting faces was observed and the DIC software, ISTRA was able to perform image correlation between the corresponding initial and final images.

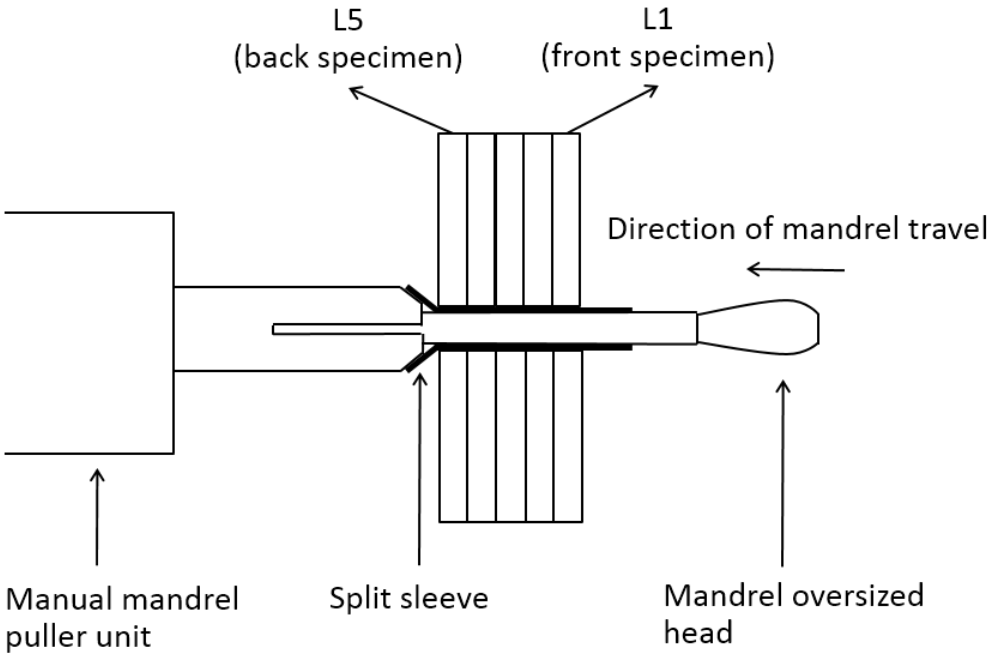

Figure 6.1 Schematic of split sleeve cold expansion in a multi-layer stack comprising of five 1.6 mm thick specimens.

6.2 Uncertainty in strain measurements resulting from rigid body displacement

The displacement field around the cold-expanded hole, obtained using the approach described in the previous section, can be considered to be a combination of a displacement field caused by the cold expansion process and a rigid body displacement resulting from a slight difference in the specimen locations before and after cold expansion. Theoretically, rigid body displacement does not affect the strain fields; however, a displacement field measured using DIC has inherent

noise which is induced during the image acquisition and image correlation processes. This inherent noise is further amplified when the strains are evaluated by differentiating the measured displacement field. To validate this approach for obtaining reliable strain measurements, the uncertainty in the evaluated strains was first determined.

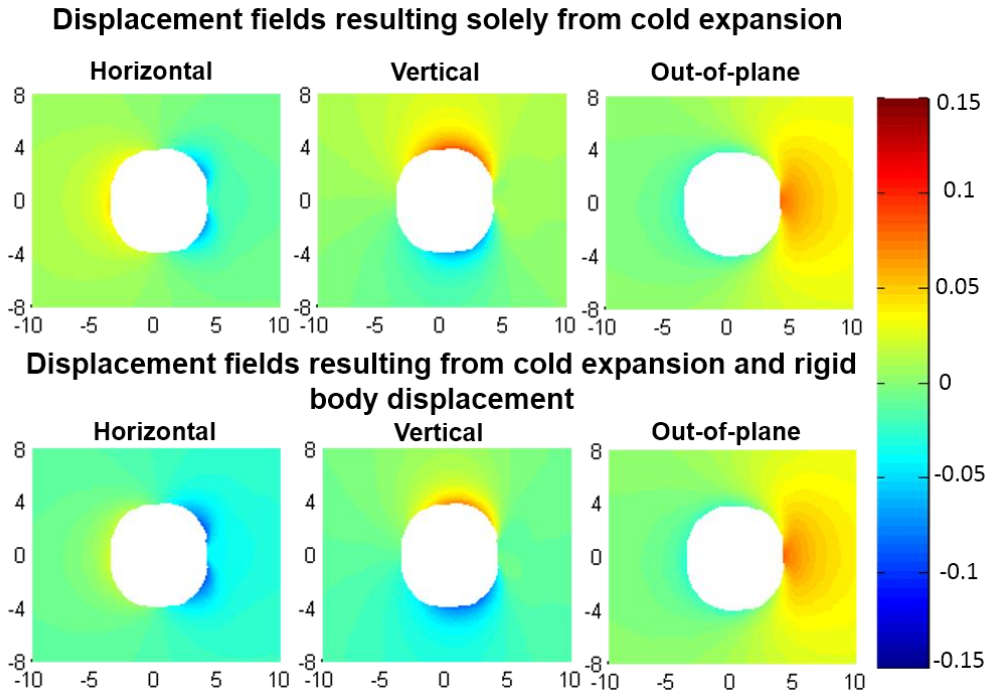

Figure 6.2 Comparison between the displacement maps of the primary data set and one of the six data sets which contained rigid body displacements. All dimensions are in mm.

To perform the uncertainty analysis, a single thin specimen was clamped in the retention fixture and cold expansion was performed. Initial and final images were captured using the DIC setup on the mandrel entry face of the specimen. The two images were correlated to obtain the displacement fields, which were then used to determine principal strains by applying the subset distortion method. This data set did not contain any rigid body displacement, and therefore, was considered as the primary data set. To determine the influence of rigid body displacement on the evaluated strains, the specimen was un-clamped and subsequently re-

clamped six times and each time an image of the ROI was captured. Each of the six final (deformed) images were correlated with the initial reference image and strains were determined.

Figure 6.2 shows the comparison between the displacement fields of the primary data set and one of the six data sets that was obtained by un-clamping and re-clamping the specimen. Both the horizontal and the vertical displacement fields in the bottom row show slightly negative displacements in comparison to the corresponding displacements fields of the primary data set in the top row. This indicates that the specimen had been displaced 'rigidly' from its original position when it was un-clamped and subsequently re-clamped in the retention fixture. The maximum and minimum principal strain maps of the primary data set and the mean of the six data sets, which contained rigid body displacements, are presented in Figure 6.3. The uncertainty maps, representing one standard deviation, are also provided in this figure. The highest standard deviation values for the maximum and minimum principal strains were found to be 210 and 440 μstrain respectively, which is relatively high for accurately measuring the elastic strains particularly in stiff materials. However, in this particular case, the aim was to measure strains within the plastic zone developed by the cold expansion process and, as mentioned in the previous chapter, the lowest magnitude of strains which were encountered at the elastic-plastic boundary were of the order of 2000 μstrain.

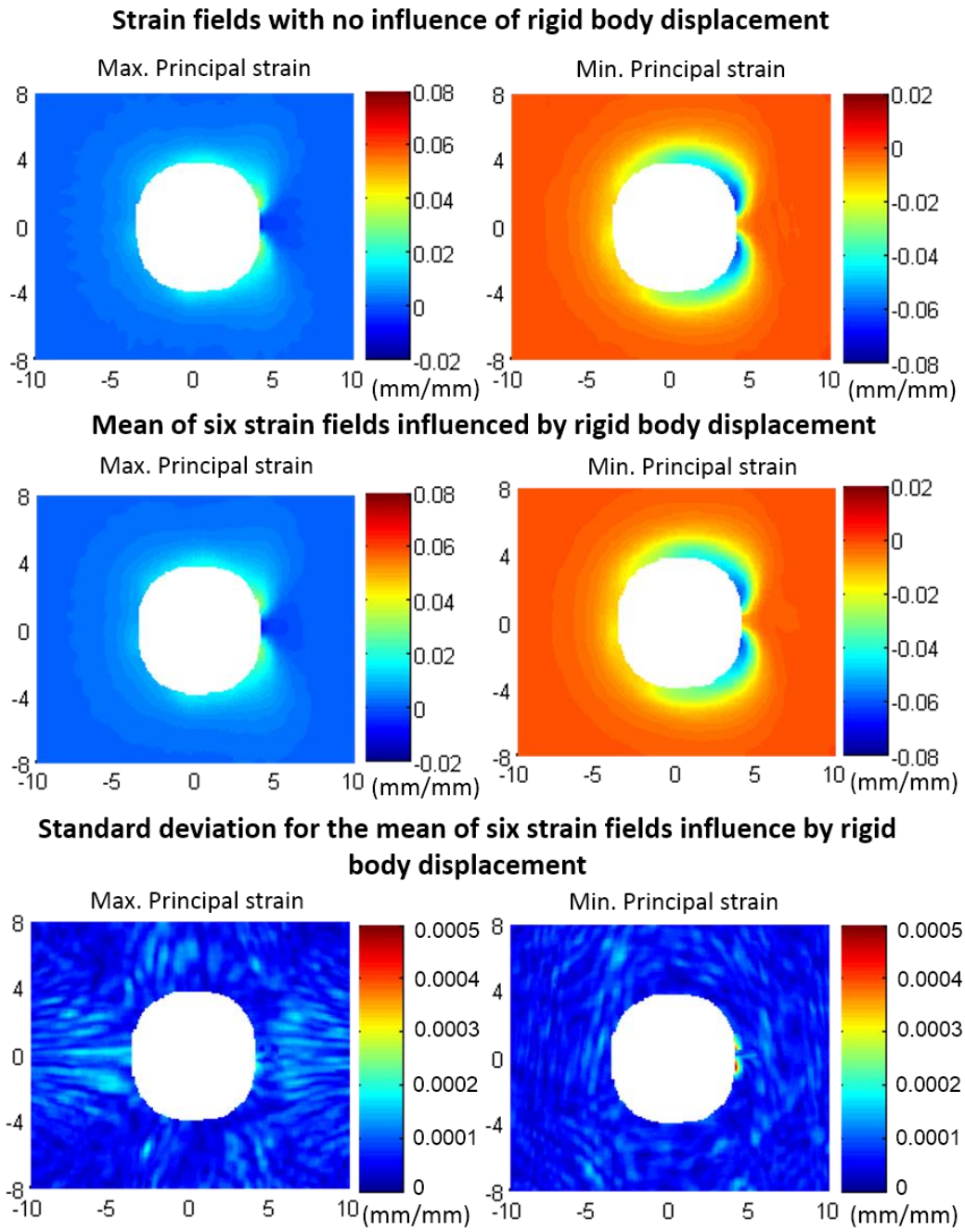

Figure 6.3 Top row shows the principal strains of the primary data set. Middle and bottom rows show the average principal strain maps and their standard deviation maps, respectively, for the six data sets which contained rigid body displacements.

One of the primary objectives of measuring these strains was to determine the shape and size of the plastic zone developed as a result of the split sleeve cold expansion. The plastic zones, obtained from the six data sets, which contained rigid body displacements, are shown in Figure 6.4. It can be concluded from these

plots that the rigid body displacement has negligible influence on the shape and size of the plastic zone determined from the strain measurements. The highest value for the standard deviation in the extent of plastic zone was found to be ± 0.13 mm. The average out-of-plane displacement field and its standard deviation for the six data sets are plotted in Figure 6.5. The results presented in Figures 6.3 - 6.5 unambiguously confirm the validity of the proposed approach in determining the strain fields in stacked specimens with reasonable accuracy.

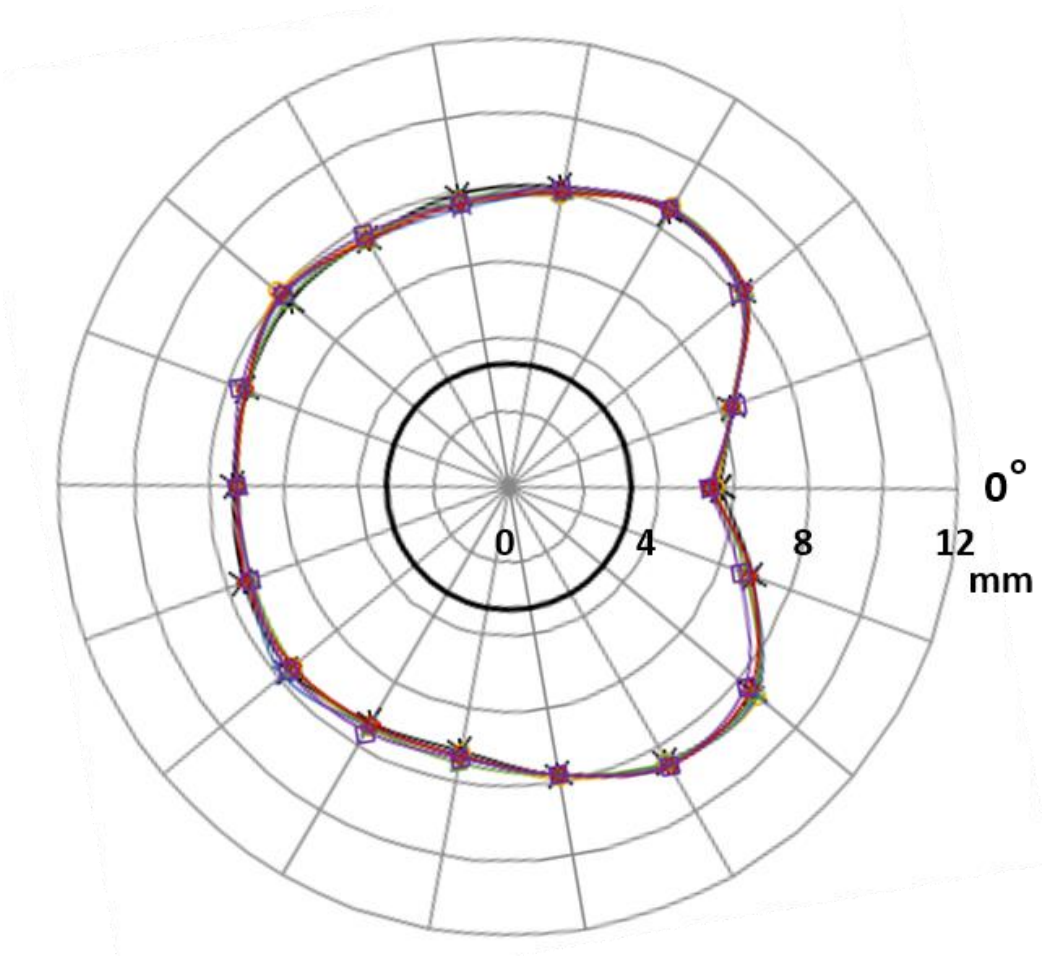

Figure 6.4 Plots of the shape of the plastic zone, on the mandrel entry face of the thin specimen, obtained from the six data sets which were influenced by the rigid body displacement.

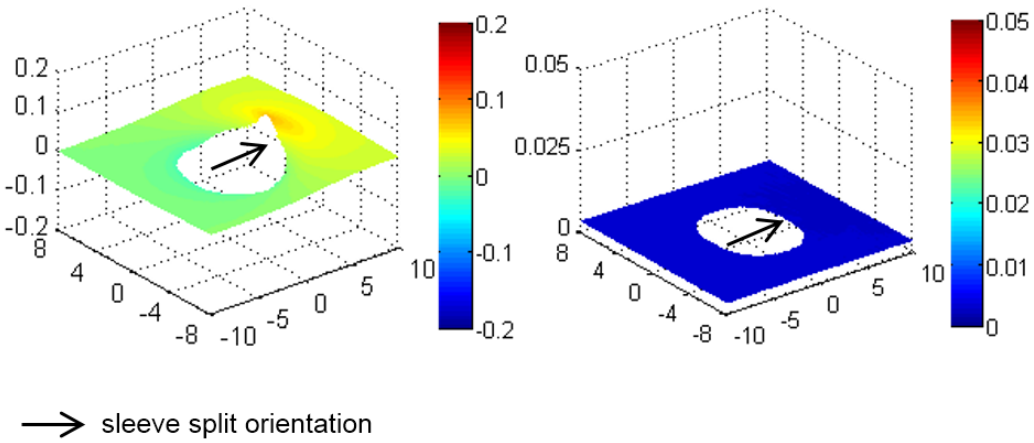

Figure 6.5 Plots for mean out-of-plane displacement field (left) and the corresponding standard deviation (right) for the six data sets which contained rigid body displacements. The direction of positive out-of-plane displacement corresponds to the direction of mandrel travel during cold expansion. All dimensions are in mm.

6.3 Analysis of split sleeve cold expansion in stacked specimens

The principal strain maps on the mandrel entry and exit faces for the single and the stacked specimens are provided in Figures 6.6 and 6.7. The von Mises yield criterion was applied to these principal strain maps to obtain the size and shape of the plastic zones developed as a result of split sleeve cold expansion, and these are presented in Figure 6.8. The ineffectiveness of the split sleeve cold expansion in developing a uniform axisymmetric plastic zone in single thin specimens has already been discussed in great detail in the previous chapter. Briefly, it was established from the results in the previous chapter that the single thin specimen undergoes severe out-of-plane warping, in particular, at the location where split in the sleeve is positioned i.e. 0^{o} angular orientation. This is the primary reason for the development of a highly non-axisymmetric plastic zone, which is also smaller in size, compared to the single thick specimen. A comparison between the plastic

zone shapes for the single thin and thick specimens in the top row of Figure 6.8 reaffirm these conclusions.

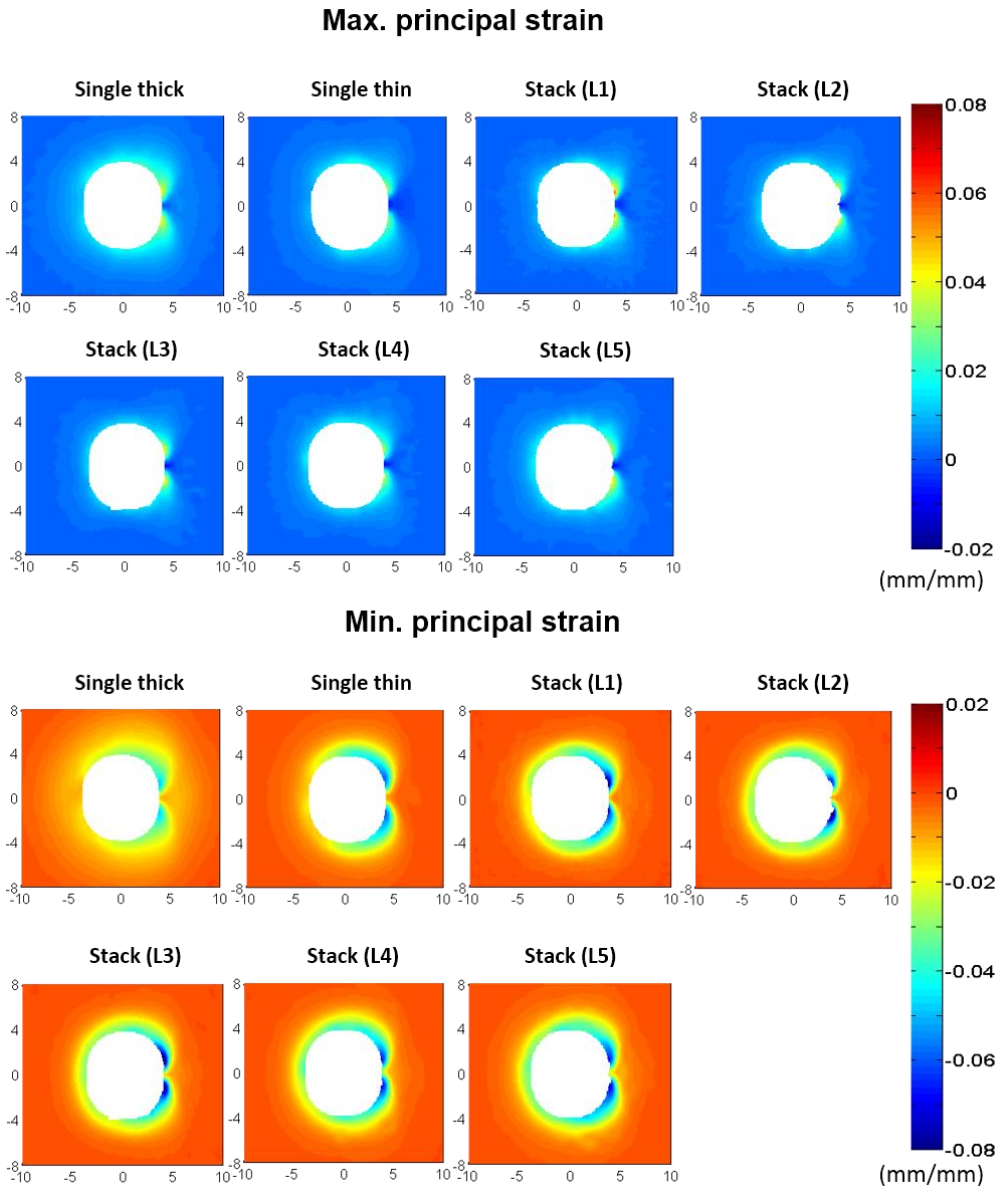

Figure 6.6 The maximum and minimum principal strain maps on the mandrel entry face for the single and the stacked specimens. The map dimensions are in mm.

The bottom row in Figure 6.8 shows the plots for the plastic zones developed on the mandrel entry and exit faces of the five thin specimens (L1 - L5) which comprised the stack. A significant improvement in the axisymmetry of these plastic zone shapes can be observed in comparison to the ones developed in the

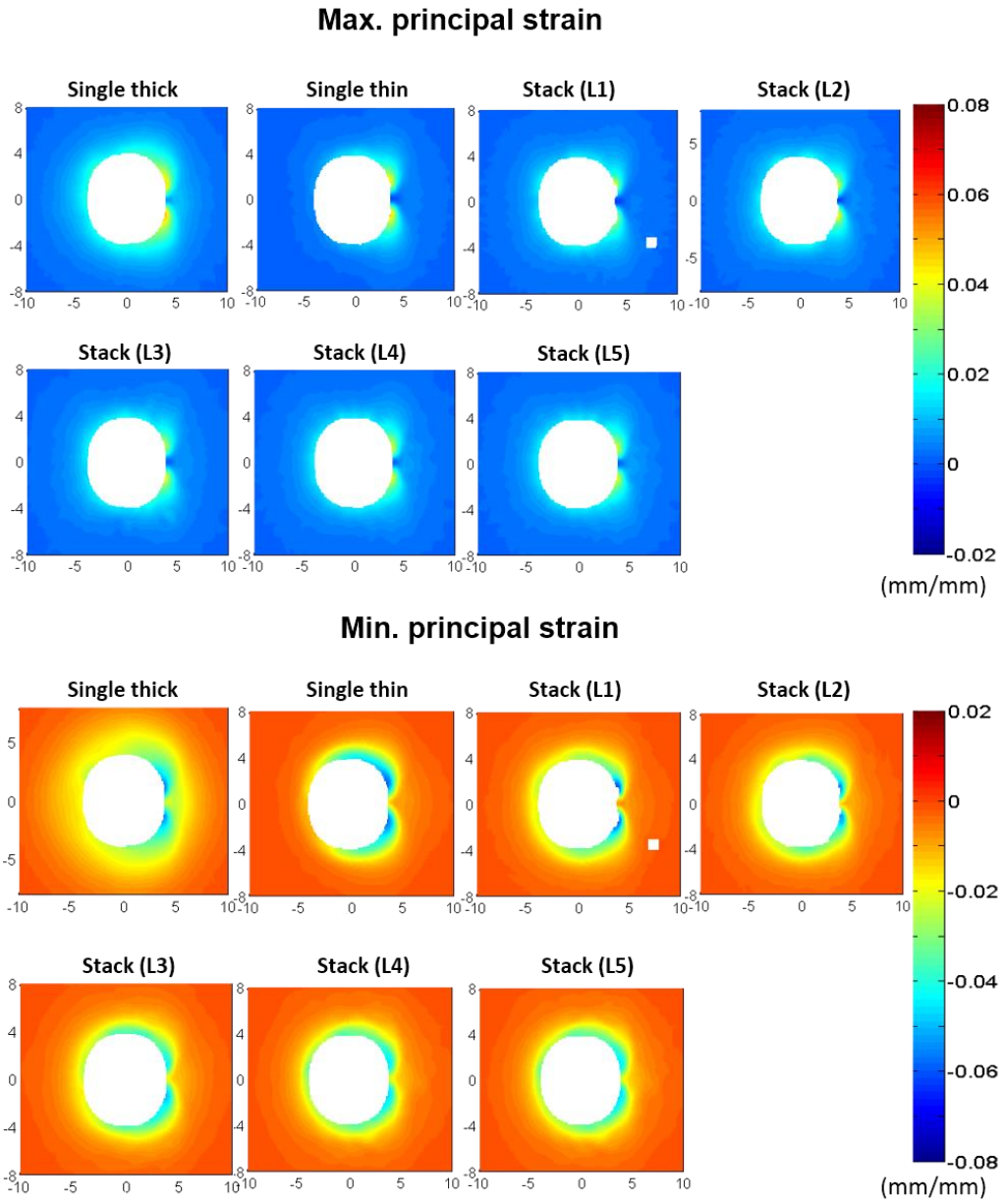

Figure 6.7 The maximum and minimum principal strain maps on the mandrel exit face for the single and the stacked specimens. The map dimensions are in mm.

single thin specimen. It was highlighted in the previous chapter that the characteristic decrease in the extent of plastic zone, along the 0^{o} radial line, on the mandrel entry face of the single thin specimen (see top-left plot in Figure 6.8) is due to mandrel pulling on the ends of the split in the sleeve; thereby, causing a dome-shaped out-of-plane deformation of the mandrel entry face at this location. This characteristic decrease in the extent of plastic zone is not present on the

mandrel entry face for any of the specimens in the stack (see bottom-left plot in Figure 6.8). To develop further understanding about this improvement in the extent of plastic zone along the 0^o radial line, the strain components in polar coordinates were determined, on the mandrel entry and exit faces, at the elastic-plastic boundary. The strain components are reported in Table 6.1 for both the single and the stacked specimens. In contrast to the single thin specimen, the hoop strains at the elastic-plastic boundary on both the mandrel entry and exit faces were found to be tensile for all five specimens of the stack. This indicates that, in the stacked specimens, the hole deformed predominantly in the radial direction instead of being distorted out-of-plane significantly.

The measured out-of-plane displacement fields on the mandrel entry and exit faces, for the single and the stacked specimens, have been plotted in Figures 6.9 and 6.10. There is evidence of out-of-plane warping on both the mandrel entry and exit faces in the stacked specimens; nonetheless, its severity in the vicinity of the split in the sleeve is significantly reduced compared to the single thin specimen. This appears to be the primary reason for overall improvement in the axisymmetry of the plastic zones developed in the stacked thin specimens. The size of these plastic zones, particularly on the mandrel entry face, is small in comparison to the plastic zone developed in the single thick specimen, which is equivalent in thickness to the stack. The variation in the shapes and sizes of the plastic zones between individual specimens of the stack can also be noticed in Figure 6.8. This establishes that the multi-layer stack does not expand as a monolithic layer of equivalent thickness during split sleeve cold expansion.

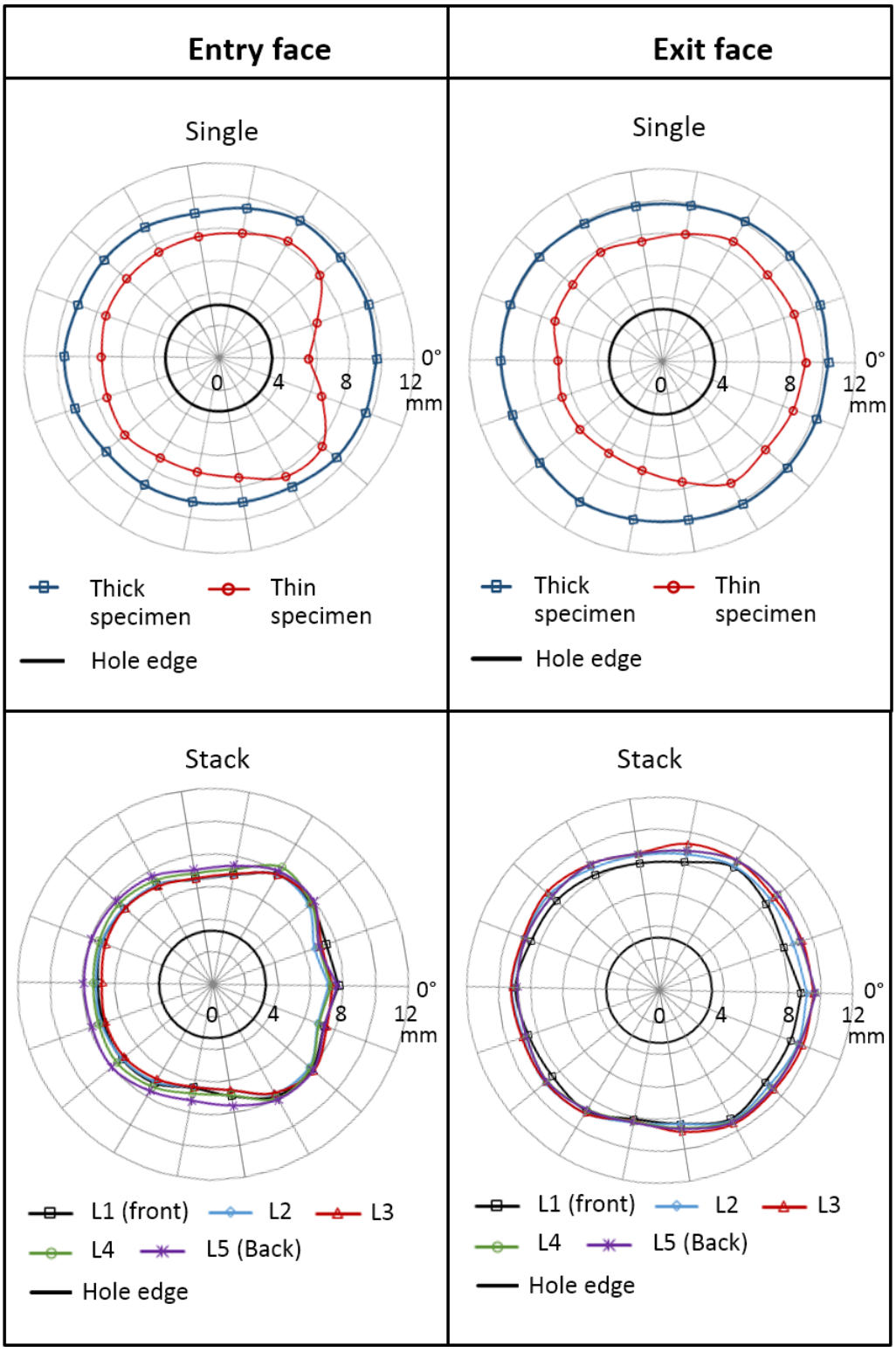

Figure 6.8 Plots of the shape of the plastic zone for single specimens (top row) and stacked specimens (bottom row).

Table 6.1 Values for the extent of plastic zone along the 0° radial line and the strain components in polar coordinates at the elastic-plastic boundary on the mandrel entry and exit faces for the single and the stacked specimens.

	Mandrel entry face		Mandrel exit face	
	Extent of plastic zone at 0° (mm)	**Polar strain components (μstrain)**	**Extent of plastic zone at 0° (mm)**	**Polar strain components (μstrain)**
Single thick	9.72	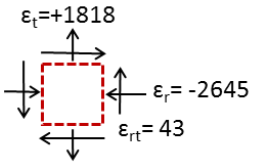	10.35	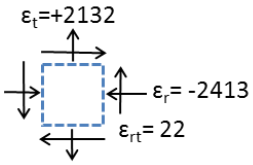
Single thin	5.52	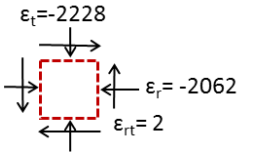	8.93	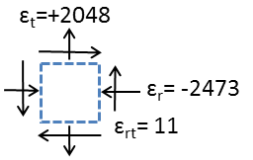
Stack (L1)	7.73	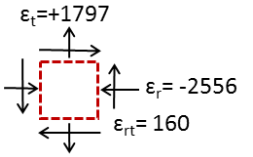	8.80	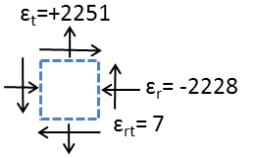
Stack (L2)	7.13	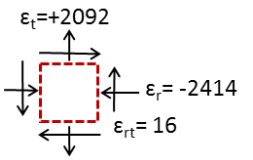	9.16	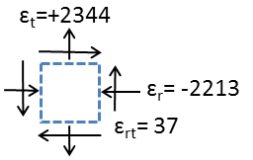
Stack (L3)	7.31	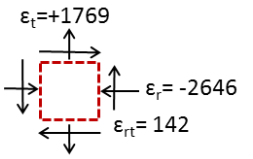	9.50	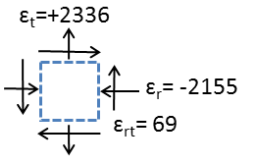
Stack (L4)	7.29	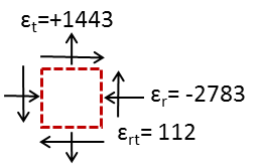	9.65	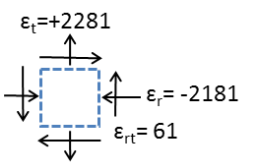
Stack (L5)	7.63	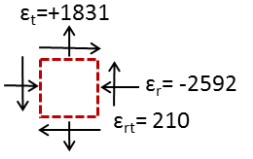	9.67	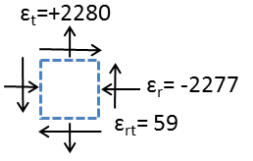

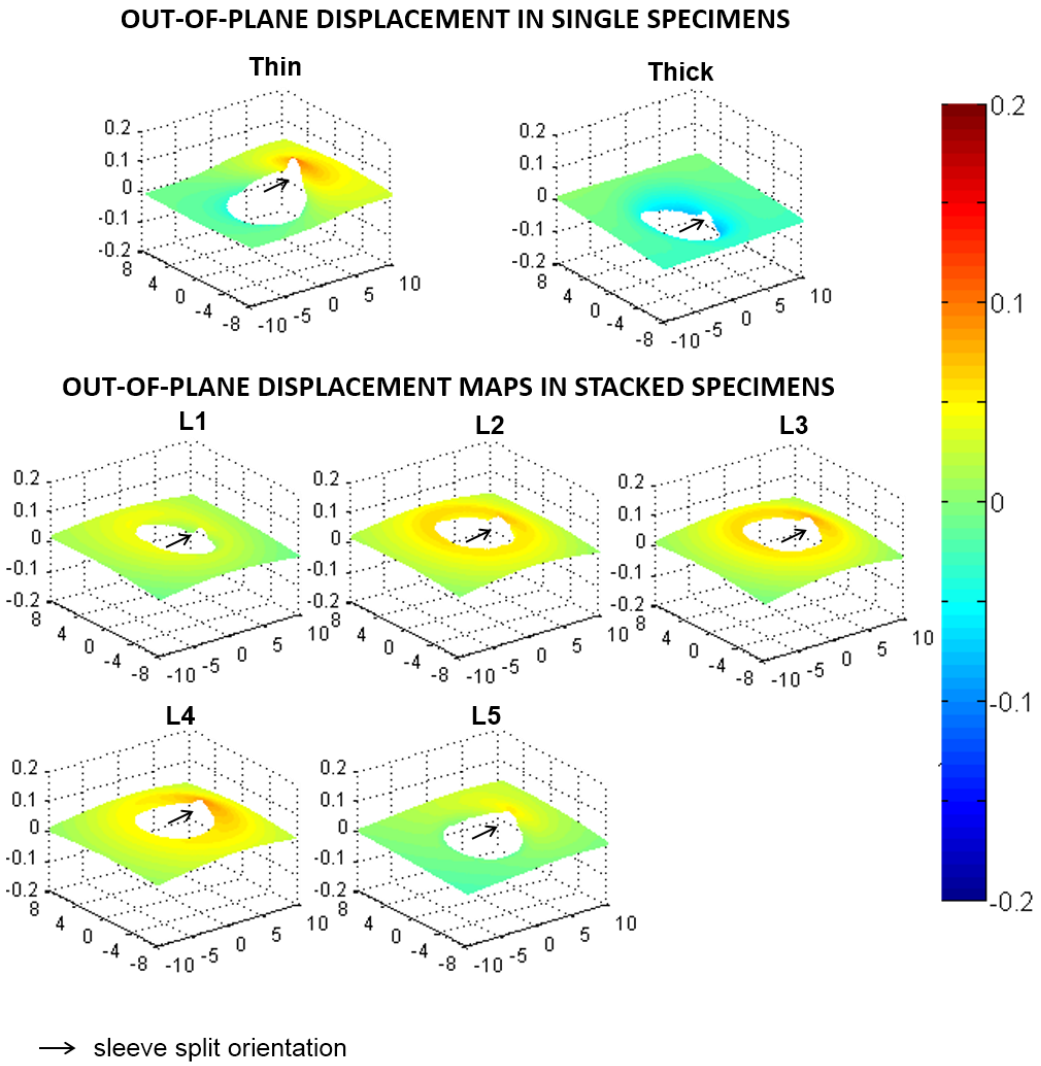

Figure 6.9 Comparison of the out-of-plane displacement fields on the mandrel entry face for the single and the stacked specimens. All dimensions are in mm.

Recently, Connolly[143] developed a finite element model to simulate the development of a residual stress field around the cold-expanded hole in a two-layer stack with a combined t/D_o ratio of 2.3. His simulation results showed that stacking caused an increase in the magnitude and extent of the compressive residual stress distribution on the two contacting faces i.e. the mandrel exit and the entry faces for the front and the back specimens, respectively. This implies the development of a bigger plastic zone size on these contacting faces. He concluded that the improvement in the size of the residual stress zone was primarily due to

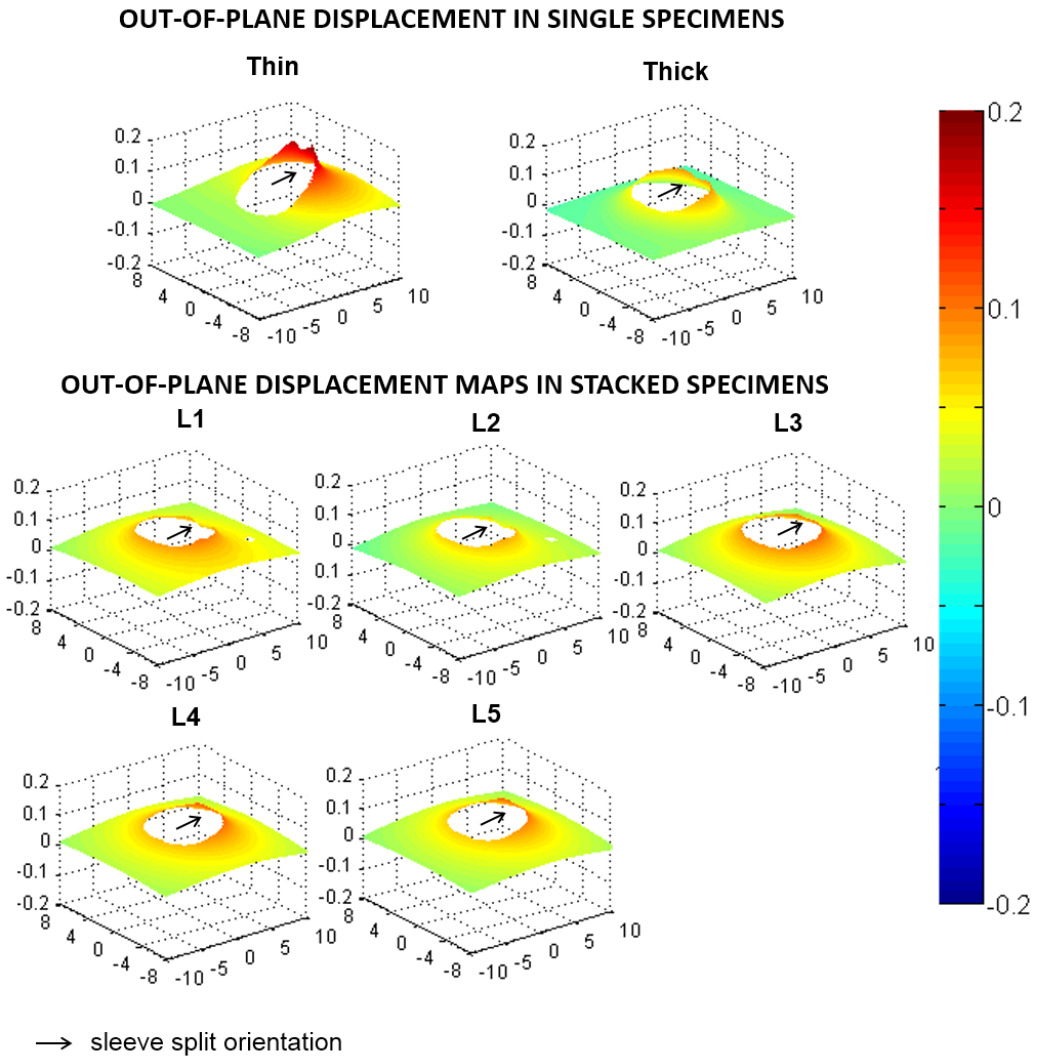

Figure 6.10 Comparison of the out-of-plane displacement fields on the mandrel exit face for the single and the stacked specimens. All dimensions are in mm.

the constraint on the out-of-plane deformation of the two contacting surfaces during cold expansion. These conclusions generally hold true for the experiment results presented in Figures 6.8 – 6.10 as well. The results in these figures additionally demonstrate that stacking also improves the axisymmetry and size of the plastic zones developed on the free faces of the specimens in the stack i.e. the mandrel entry and the exit faces for L1 and L5, respectively.

6.4 Summary

This chapter has reported the results of the experimental study aimed at investigating the cold expansion of holes in stacked specimens. Split sleeve cold expansion was performed on a multi-layer stack, which comprised of five 1.6 mm thick specimens, providing a combined t/D_o ratio of 1.25. The procedure for measuring the strain fields, developed from split sleeve cold expansion, on both faces of every specimen in the stack has been explained in the first section. The second section has discussed the uncertainty in the strain measurements resulting from the procedure adopted to determine strain fields developed in the stacked specimens. The hole deformation in the stacked specimens has been analysed in the third section. The results showed that stacking significantly reduces the out-of-plane warping on both the faces in the stacked specimens which causes an overall improvement in the axisymmetry of the plastic zones developed around the expanded holes.

7 ANALYSIS OF FATIGUE CRACKS EMANATING FROM COLD-EXPANDED HOLES

A detailed experimental study, utilising thermoelastic stress analysis (TSA) and synchrotron x-ray diffraction (SXRD) techniques, was carried out to investigate the propagation of fatigue cracks emanating from cold-expanded holes and their influence on the surrounding residual stresses with the aim of establishing the reasons for the potential redistribution of these residual stresses. This chapter presents the results obtained from first half of this study, which focused on the analysis of the behaviour of fatigue cracks using TSA. A total of twenty-three specimens were machined from the 6.35 mm thick aluminium plate (see Figure 4.6 for specimen geometry). Cold expansion was performed in seventeen of the specimens, whilst the remaining six specimens were left with un-expanded holes. A description of the cold expansion procedure can be found in Section 4.2.

All six un-expanded specimens were loaded in fatigue until failure. The details about the experimental setup used for these fatigue tests and the fatigue loading parameters are provided in Section 4.3. Out of the seventeen cold-expanded specimens, a set of six specimens were loaded in fatigue until failure. For another set of three cold-expanded specimens, the fatigue loading was stopped prior to failure for the purpose of performing residual stress measurements on them. In two of the cold-expanded specimens, a single load cycle with maximum compressive loads of -21.2 and -28.6 kN was applied, corresponding to the maximum remote nominal stresses of -92.7 and -125 MPa, respectively. These compressive loads were chosen to represent the service loads on the wing pivot

fitting of a fighter aircraft as reported by Pell et al[70]. After examining these specimens in a synchrotron, they were also loaded in fatigue until failure. No monotonic or fatigue loads were applied on the remaining set of six cold-expanded specimens. They were examined in a synchrotron to determine the uncertainty in the measurements of residual stress. The details of the fatigue test programme described above are summarised in Table 7.1.

A summary of fatigue lives is provided in Table 7.2 for the specimens tested. The average fatigue life of the six cold-expanded specimens is about 3.2 times higher than that of the six un-expanded specimens. This improvement is evident despite the fact that the maximum remote stress during fatigue loading for the cold-expanded specimens was 170 MPa compared to 150 MPa for the un-expanded ones. The number of cycles to failure for specimens C10 and C11, to which a single compressive stress cycle of -92.7 and -125 MPa were applied, respectively, are substantially lower than the mean fatigue life of the standard six cold-expanded specimens. The difference is greater than three standard deviations, which clearly indicates that the initial residual stress distribution was significantly relaxed by the applied compressive loads in these specimens.

7.1 Behaviour of fatigue crack propagation

To further investigate and characterise the typical behaviour of both types of holes, the test data for the three cold-expanded specimens (C4, C5 & C6) are plotted along with those for the three un-expanded ones (U3, U4 & U6) in Figures 7.1, 7.2, 7.4 and 7.6. These specimens were selected because their number of cycles to failure was closest to the mean fatigue life of their respective batches.

Table 7.1 Summary of fatigue tests performed in the experimental study. Different loads were applied in these tests in order to identify the loading conditions under which compressive residual stresses developed from cold expansion are expected to relax.

Specimen ID	**Hole expansion**	**Applied loads**	**Max. hoop stress at hole edge ($\sigma_{h,max}$)**	**Remarks**
U1-U6	Un-expanded	Fatigue parameters: • $\sigma_{R,max}$=150MPa • R=0.1 • Fr=19Hz	+465	• Fatigue loaded until failure
C1-C6	Cold-expanded	Fatigue parameters: • $\sigma_{R,max}$=170MPa • R=0.1 • Fr=19Hz	+185	• Fatigue loaded until failure
C7*	Cold-expanded	Fatigue parameters: • $\sigma_{R,max}$=170MPa • R=0.1 • Fr=19Hz	+185	• Loading stopped after 50k cycles • No cracks observed
C8*	Cold-expanded	Fatigue parameters: • $\sigma_{R,max}$=170MPa • R=0.1 • Fr=19Hz	+185	• Loading stopped after 150k cycles • Left and right hole edge cracks of 2.1 and 2.4mm measured on the specimen mandrel entry face
C9*	Cold-expanded	Fatigue parameters: • $\sigma_{R,max}$=170MPa • R=0.1 • Fr=19Hz	+185	• Loading stopped after 400k cycles • Left and right hole edge cracks of 3.8 and 3mm measured on the specimen mandrel entry face
C10*	Cold-expanded	Initial compressive load: • σ_c=-92.7MPa Fatigue parameters: • $\sigma_{R,max}$=170MPa • R=0.1 • Fr=19Hz	-627	• Fatigue loaded until failure after performing SXRD measurements
C11*	Cold-expanded	Initial compressive load: • σ_c=-125MPa Fatigue parameters: • $\sigma_{R,max}$=170MPa • R=0.1 • Fr=19Hz	-730	• Fatigue loaded until failure after performing SXRD measurements
C12-C17*	Cold-expanded	-	-	• No loads applied
**Examined in synchrotron*				

Table 7.2 Fatigue life cycles for the un-expanded and the cold-expanded specimens.

Specimen ID	**No of cycles to failure, N_f (× 10^3)**
Mean of U1-U6	107 ± 19.2
Mean of C1-C6	344.6 ± 40.6
C10	208.2
C11	130.3

These figures also contain the data for specimens, C10 and C11, to illustrate the effect of a single compressive load on the subsequent fatigue performance of the specimens with cold-expanded holes. The crack growth plots for the above-mentioned specimens are provided in Figure 7.1. For the un-expanded specimens, a single crack initiated from either the left or right-hand edge of the hole on the transverse axis and appeared almost simultaneously on both faces of the specimen. No crack, initiated from the opposite edge of the hole until the specimen failed. In the cold-expanded specimens, a crack first initiated from one end of the transverse diameter of the hole followed by a second crack at the opposite end. The crack that was the longer of the two, which eventually led to specimen failure, is referred to as the primary crack and the other crack, initiated at the opposite end, is referred to as the secondary crack. Both the cracks appeared only on the mandrel entry faces of these specimens. This was expected because of an established fact that the compressive residual stresses, resulting from cold expansion, are lower in magnitude on the mandrel entry face compared to the exit face[7-13]. In specimens C10 and C11, cracks propagated from both ends

of the transverse diameter of the hole and appeared first on the mandrel entry face and later on the exit face. It can be seen from the crack growth plots that, for almost all the specimens, the first crack was observed at about 100k cycles. This indicates that cold expansion improves the fatigue performance by retarding the crack growth rather than delaying the crack initiation, which is generally in agreement with the previously published findings[42, 72, 85].

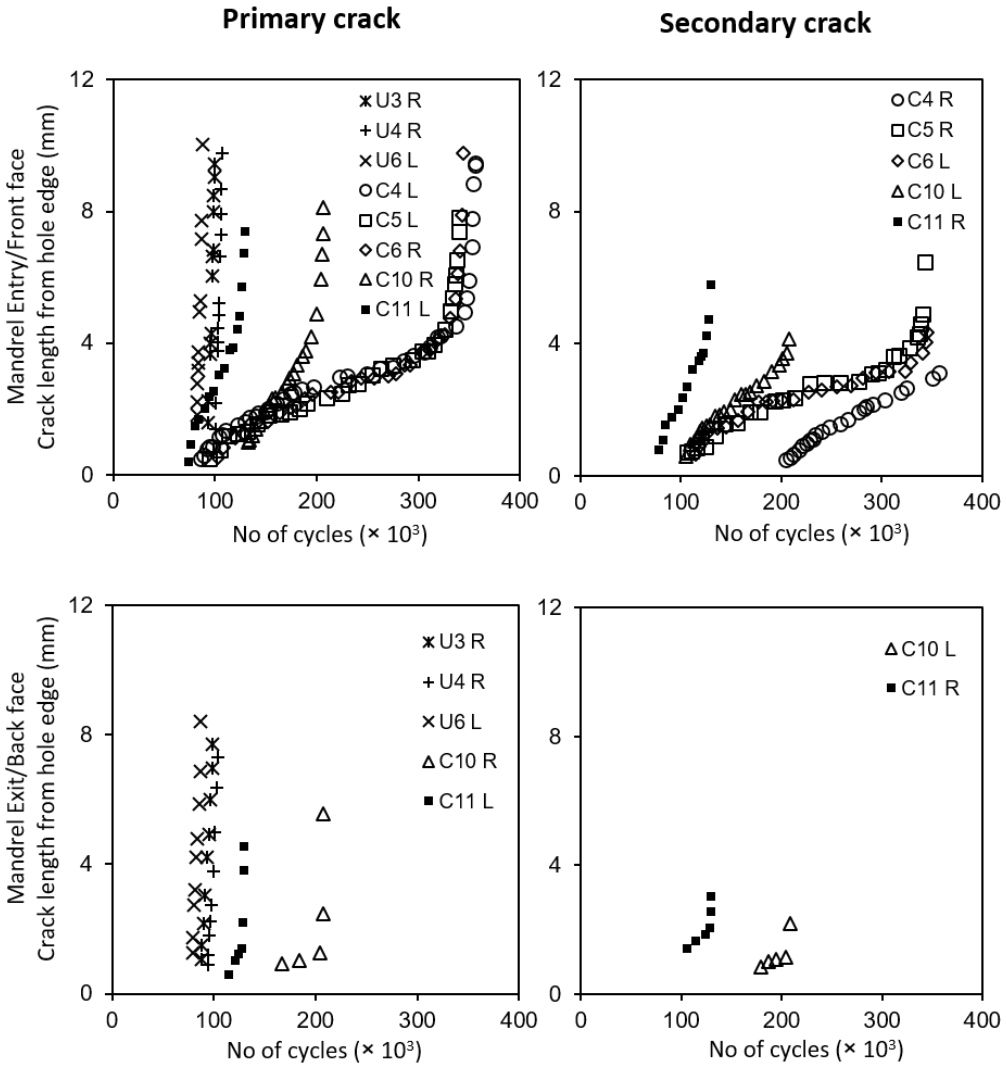

Figure 7.1 Crack growth plots for primary or secondary cracks initiating from either left or right-hand side of the hole edge and appearing on either the mandrel entry/front face (top) or mandrel exit//back face (bottom). Letters, L and R in the plot legends refer to the cracks originating from left and right sides of the hole edge respectively.

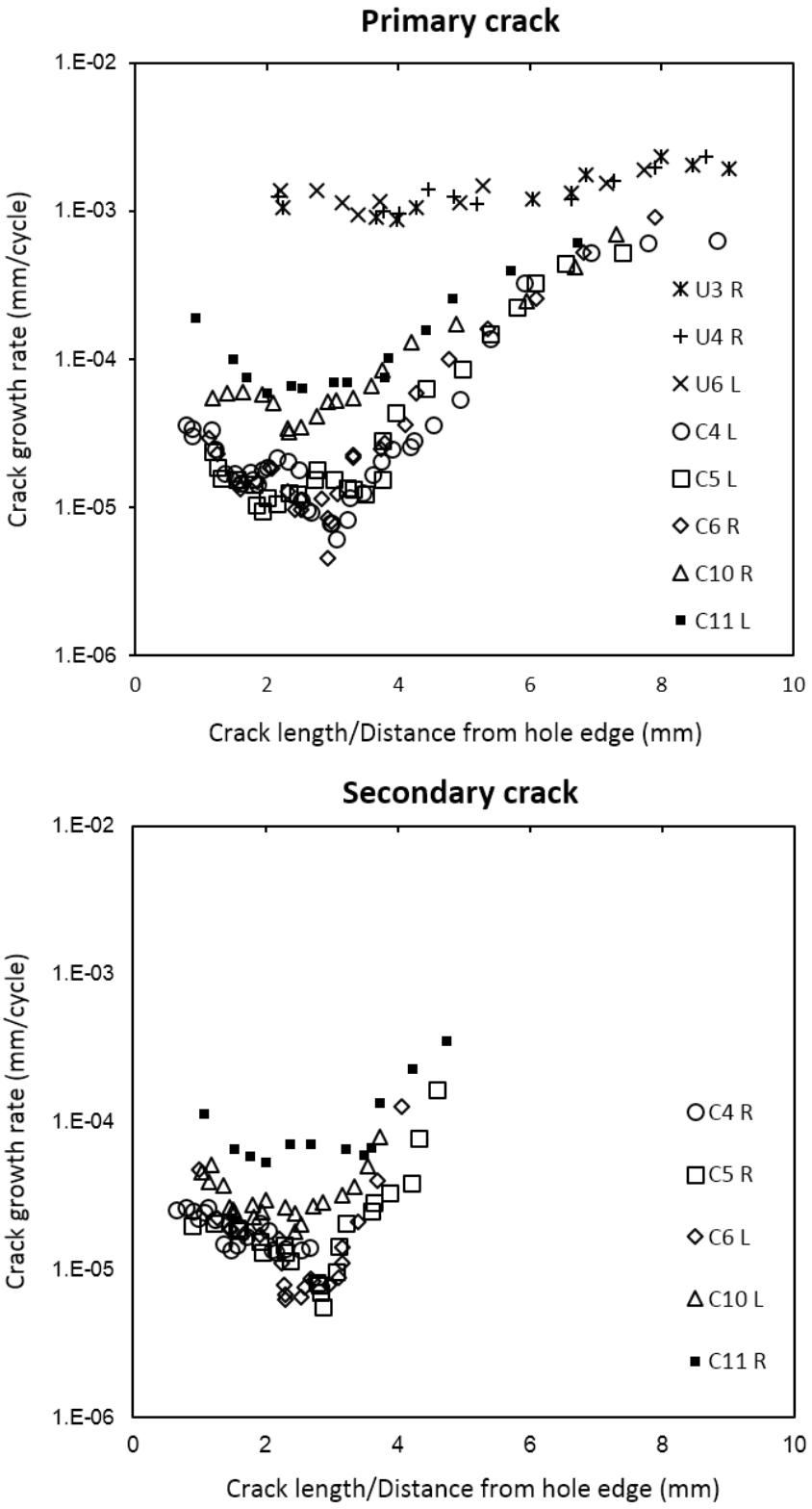

Figure 7.2 Plots of crack growth rate for cracks on the mandrel entry/front face of the specimens, as in Figure 7.1. Letters, L and R in the plot legends refer to the cracks originating from either left or right side of the hole edge respectively.

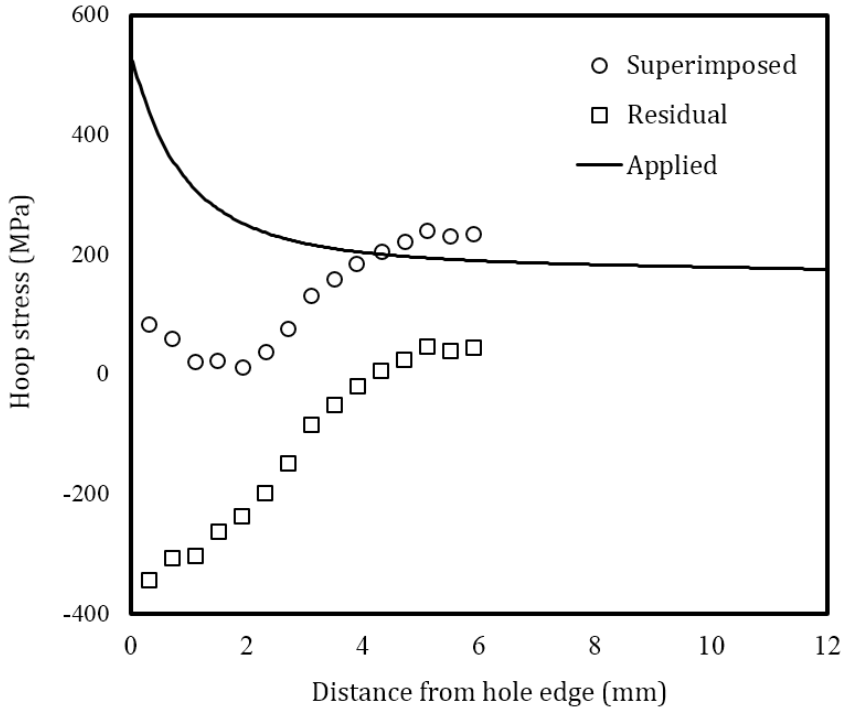

Figure 7.3 Plot of superimposed hoop stress profile along the transverse centre line of the specimen, which was determined by superposition of the tensile hoop stress profile resulting from the applied remote stress of 170 MPa and the compressive residual hoop stress profile developed by cold expansion.

The crack growth profiles for the mandrel entry/front face were differentiated by fitting a least-squares regression line to every five consecutive data points to obtain the growth rate plots shown in Figure 7.2. In cold-expanded specimens C4-C6, the cracks started off with a relatively higher crack growth rate of 0.03 µm/cycle, which decreased to a minimum value of 0.007 µm/cycle before increasing again. This characteristic trend is consistent in all three specimens for the cracks emanating from both ends of the transverse diameter through the hole. The average distance from the hole edge of the turning points in the crack growth rate plots was found to be 2.7 mm for the primary cracks and 2.2 mm for the secondary cracks in the three specimens. This characteristic trend is believed to result from a combined effect of decreasing applied stresses due to the reduced

influence of the stress concentration and the presence of a compressive residual stress distribution, which reduces to zero at 1 mm beyond the location of the turning point. To illustrate this, a superimposed hoop stress profile along the transverse centre line of the specimen is shown in Figure 7.3, which was determined by superimposing the tensile hoop stress profile resulting from the maximum remote stress of 170 MPa on the compressive residual stress profile determined from SXRD. As expected, the crack growth rate profiles in Figure 7.2 are in reasonable correlation with the superimposed hoop stress profile in Figure 7.3. The compressive residual stresses around cold-expanded holes, which were determined using SXRD, are discussed in more detail in the next chapter. A similar trend could also be observed in specimens C10 and C11; but, the turning points are progressively less pronounced, indicating increasing levels of residual stress relaxation in the two specimens. In contrast, the crack growth rates are consistently very high, of the order of 1.4 μm/cycle, for the three un-expanded specimens in the absence of any compressive residual stresses.

The values for effective stress intensity factor range, ΔK_{eff} were evaluated directly from the thermoelastic data using the methodology of Tomlinson et al[105], which is described in Section 3.2. This approach requires thermoelastic data collection from the singularity-dominated region surrounding the crack tip, which makes it difficult to apply for small cracks close to the hole edge. For this reason, ΔK_{eff} were evaluated when the cracks were at least 2 mm in length. The trends in the ΔK_{eff} plots shown in Figure 7.4 are very consistent with those of the crack growth rate plots in Figure 7.2.

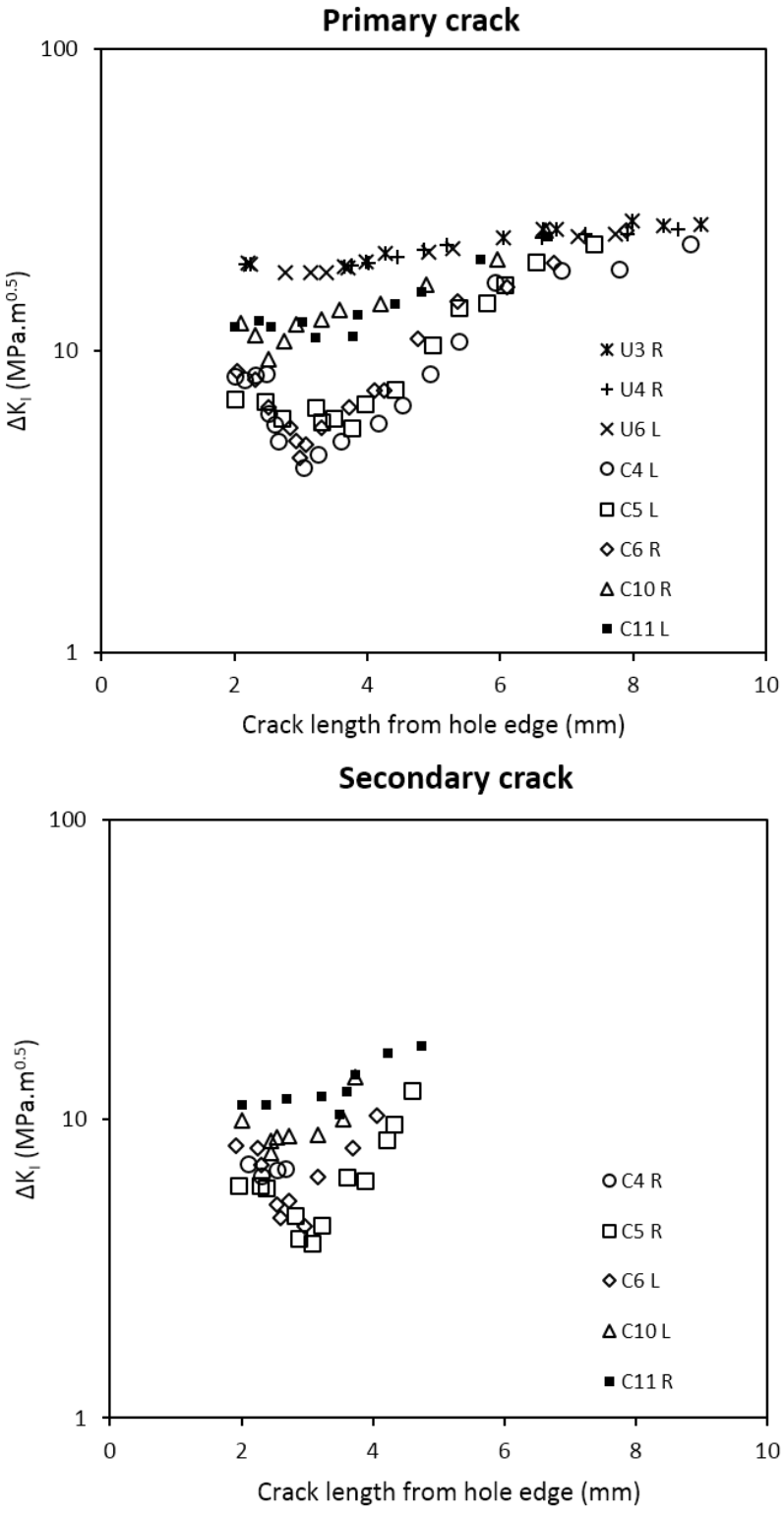

Figure 7.4 Plots of stress intensity factor range for cracks on the mandrel entry/front face of the specimens, as in Figure 7.1. Letters, L and R in the plot legends refer to the cracks originating from either left or right side of the hole edge respectively.

7.2 Plastic zones associated with the crack tip

The map of phase difference between the measured thermoelastic signal and the loading signal from the servo-hydraulic test machine can be used to identify regions on the specimen's surface where adiabatic conditions are lost due to heat generation associated with plastic deformation. This phase difference information has been used successfully in the past by Patki et al[108] and, more recently, by Yang et al[144] to determine the extent of the plastic zone associated with the crack tip. It was also utilised in this work to measure the shape and size of the crack tip plastic zones for cracks emanating from both the un-expanded and the cold-expanded holes. A typical phase difference map of the region surrounding a crack tip plastic zone and its shape determined from a phase difference map are shown in Figure 7.5.

The plots representing the variation in plastic zone size with increasing crack length are given in Figure 7.6. For cold-expanded specimens C4-C6, to which no initial compressive load cycle was applied, the plastic zones are consistently much smaller in size until the crack length reaches 4 mm, beyond which, the size of the plastic zone increases rapidly. This reduction of the plastic zone size is probably due to the presence of compressive residual stresses, which disappear at about 4 mm from the hole edge (see Figure 7.3). The comparison of the crack tip plastic zones for three specimens: U3, C6 and C10 are presented in Figure 7.7 at three different crack lengths i.e. 2, 4 and 6 mm. To illustrate the evolution of the plastic zones associated with both the primary and the secondary cracks in these three specimens, their shapes are provided in Appendix A.

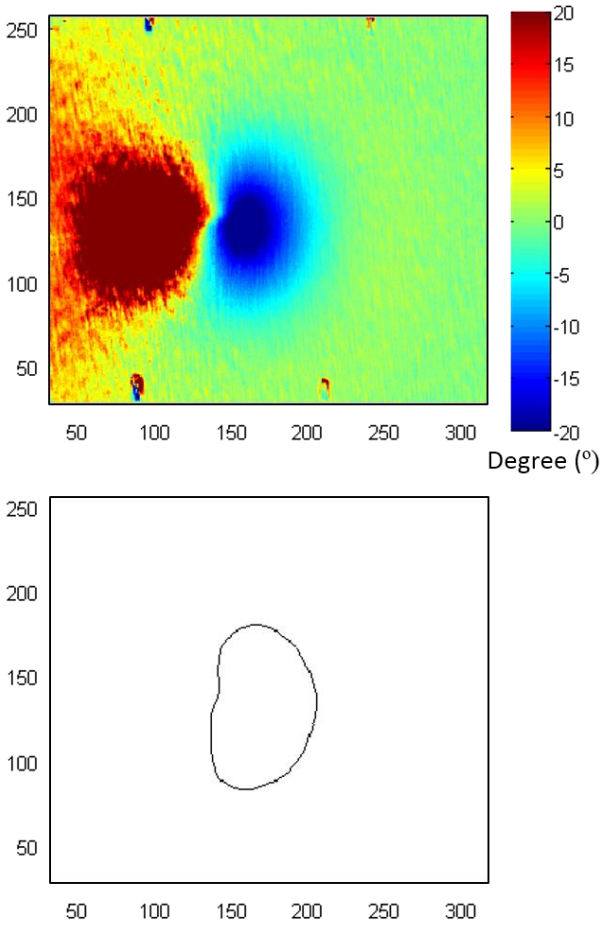

Figure 7.5 Top image shows the phase difference map of the region surrounding a crack tip and bottom image shows the shape and size of the plastic zone associated with the crack tip which was determined from the phase difference map. The dimensions of the images are in pixels (1px ≈ 0.03mm).

As described in Chapter 5, the shape and size of the plastic zone developed as a result of split sleeve cold expansion was determined on both the mandrel entry and exit faces of a 6.35 mm thick specimen using stereoscopic DIC setup (see Figure 5.16). The measured plastic zone is equivalent in shape and size to the residual stress zone developed from cold expansion. Its area, on the mandrel entry face, was found to be approximately 220 mm^2. The plastic zone associated with the crack tip for 4 mm crack was measured to be less than 2 mm^2. The schematic in Figure 7.8 shows a comparison of the two zones. The diameter of the crack tip plastic zone is 28 % of the annular thickness of the residual stress zone and its size

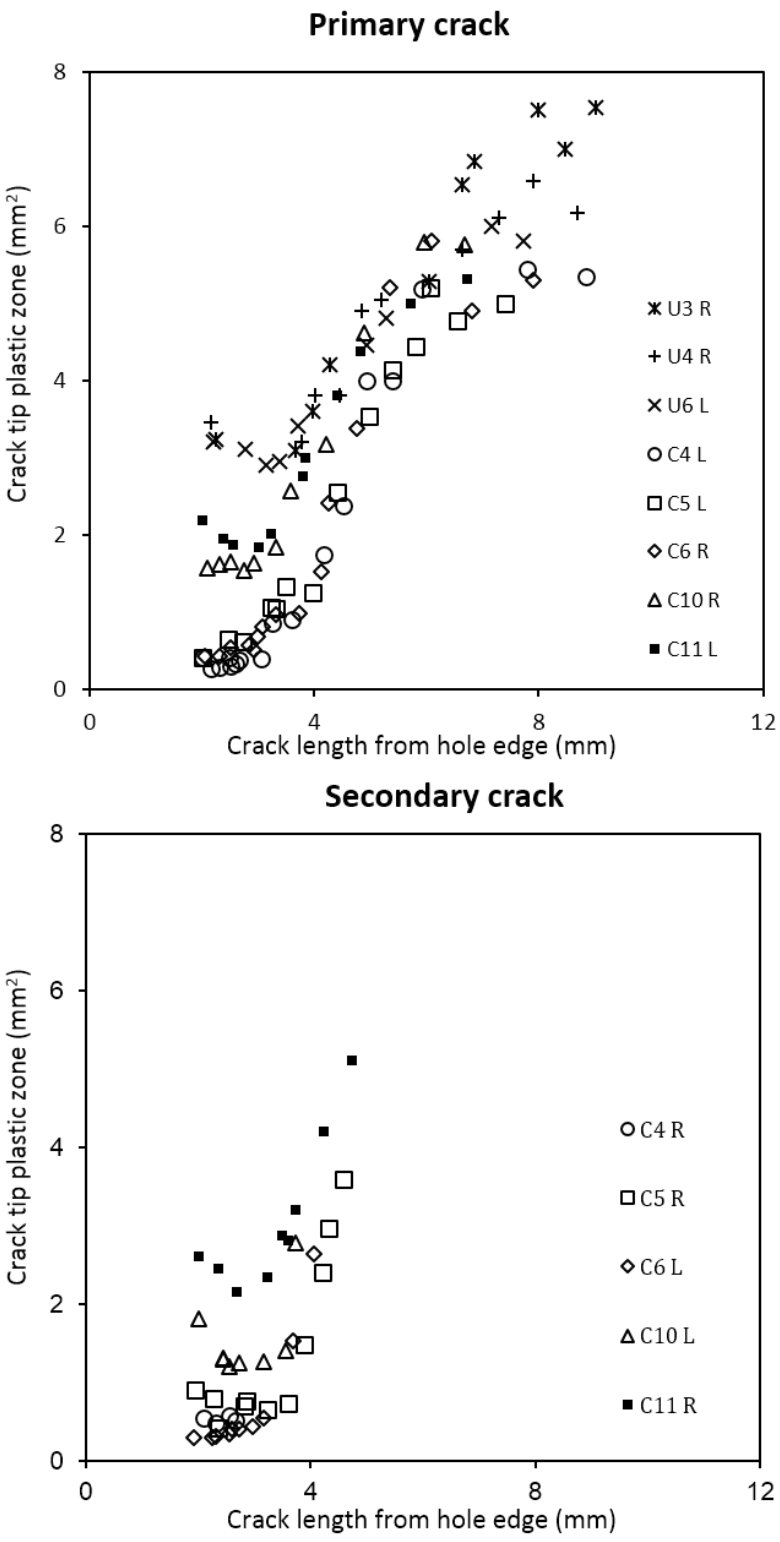

Figure 7.6 Plots of crack tip plastic zone area for cracks on the mandrel entry/front face of the specimens, as in Figure 7.1. Letters, L and R in the plot legends refer to the cracks originating from either left or right side of the hole edge respectively.

is about 1 % of the overall area of the residual stress zone. This demonstrates that, due to the large extent of the residual stress zone, the residual stresses induced by cold-working, which surround the crack geometrically, act as remote stresses; and, the localised plastic zone associated with the crack tip is not sufficiently significant in size to cause the displacements required for relaxation of these residual stresses.

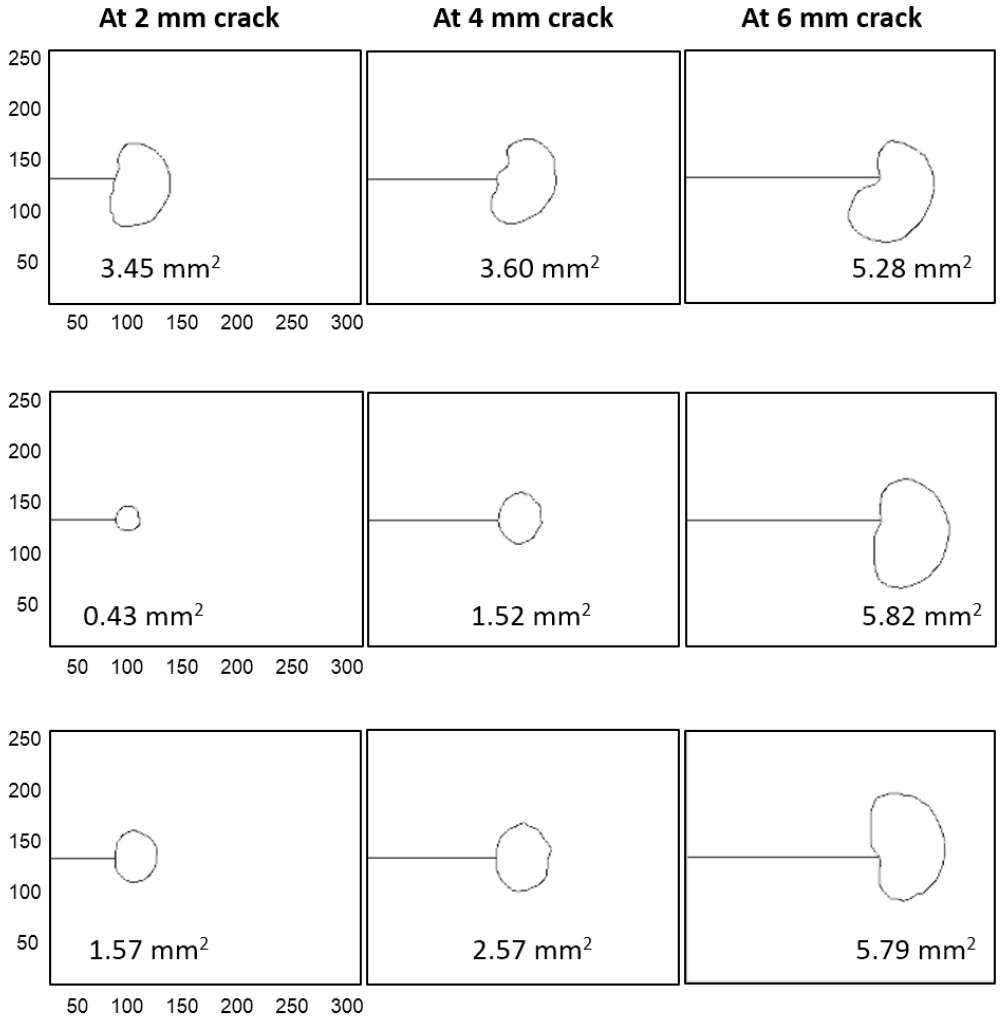

Figure 7.7 Plastic zones associated with the crack tip at three different lengths of the crack that led to failure for an un-expanded specimen, U3 (top), a cold-expanded specimen, C6 to which no initial compressive stress cycle was applied (middle) and a cold-expanded specimen, C10 to which single compressive stress cycle of -92 MPa was applied prior to fatigue loading (bottom). The spatial dimensions of the maps are in pixels (1px ≈ 0.03mm).

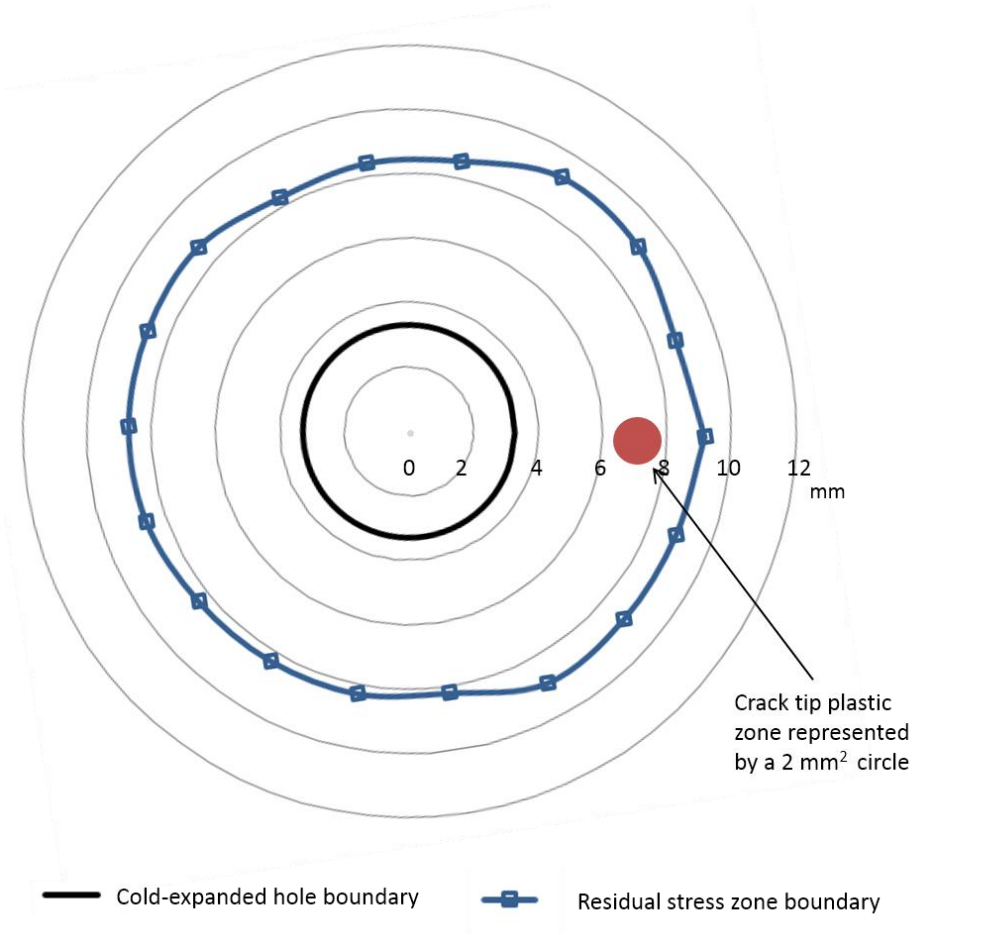

Figure 7.8 Schematic diagram showing a comparison between the size of residual stress zone, developed on the mandrel entry face by cold expansion and the plastic zone associated with the crack tip.

7.3 Fractographic analysis of fatigue failures

For qualitative analysis of the effect of residual stresses on fatigue crack initiation, the fatigue features on the fracture surface were observed in three specimens: U6, C6 and C10, using both an optical and scanning electron microscope (SEM). The optical images of the whole fracture surface were obtained using a stereo microscope (SZ61; Olympus, Japan), whereas, the images of crack initiation sites on the fracture surface were recorded using a SEM (JSM-7610F; JEOL Ltd., Japan). Figure 7.9 shows the fractographs of specimen, U6. The data recorded using TSA and a pair of digital cameras, during fatigue test, indicated the appearance of a fatigue crack on both the specimen faces only on the left side of the hole (see

Figure 7.1) and the specimen fractured due to overload of the right side ligament. The fatigue crack growth (FCG) region on the left side can be easily distinguished from a fast fracture region on the right by its surface roughness. The right side surface is much rougher indicating significant plastic deformation due to overload. Focusing on FCG region, it can be observed from SEM image 1 in Figure 7.9 that the features converge to a single location at the hole edge, on the mid-plane of the specimen, highlighting the point of initiation of the fatigue crack. The shape of the features also indicates that the crack grew with a semi-circular front. This trend of crack initiating from a single location at the hole edge on the mid-plane was found to be consistent in the other un-expanded specimens, which were loaded in fatigue (see fractographs of specimens, U3 and U4 in Appendix B).

The fractographs of the cold-expanded specimen, C6 are shown in Figure 7.10. The primary fatigue cracks, on both sides of the hole, initiated from the corner on mandrel entry face (see images 2 & 4) and propagated with a quarter-elliptical crack front. The presence of secondary fatigue cracks can also be seen in images 1 & 3 (in Figure 7.10) at the exit face corners, which are at different depths to the primary cracks. The fibrous features ahead of these secondary cracks represent rupture which occurred during specimen fracture. A consistent trend of the primary cracks being initiated at the hole edge from the mandrel entry face was found for the other cold-expanded specimens as well (see fractographs of specimens, C4 and C5 in Appendix B).

With reference to open cold-expanded holes under uniaxial fatigue loading, many fractographic investigations[40-46] have reported the initiation of a fatigue crack at

the hole edge from the mandrel entry face and the primary reason provided is the lower magnitude of the compressive residual stresses on the mandrel entry face in comparison with the exit face. These investigations involved specimens made of different materials and having different thicknesses, which suggest that the initiation of fatigue cracks from cold-expanded holes is not influenced by the microstructure or the specimen thickness; but, is solely governed by the through-thickness distribution of the residual stresses.

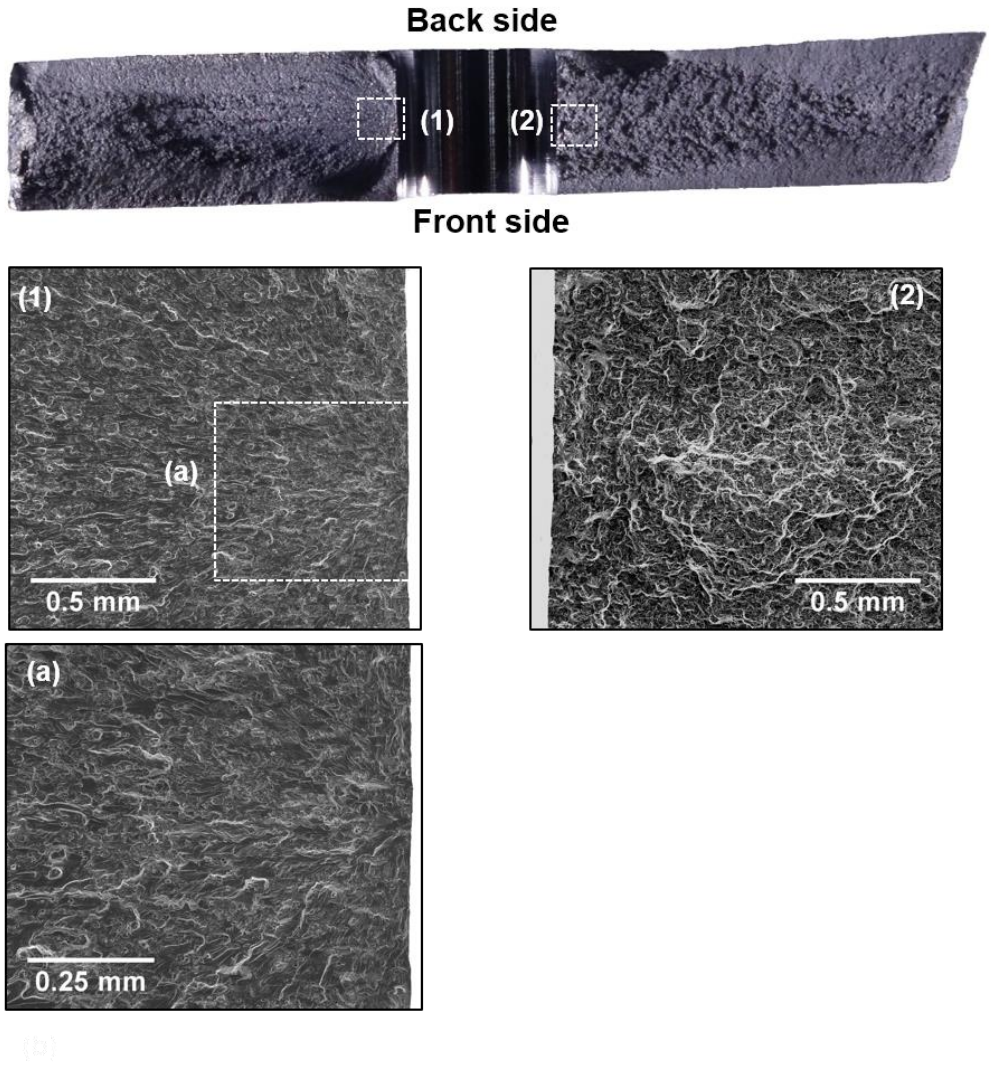

Figure 7.9 Fracture surface morphology of the un-expanded specimen, U6. The optical micrograph on top shows the whole fracture surface. SEM images on the left show the origin of fatigue crack initiating from left edge of the hole. SEM image on the right highlights the typical morphology which results from fast fracture.

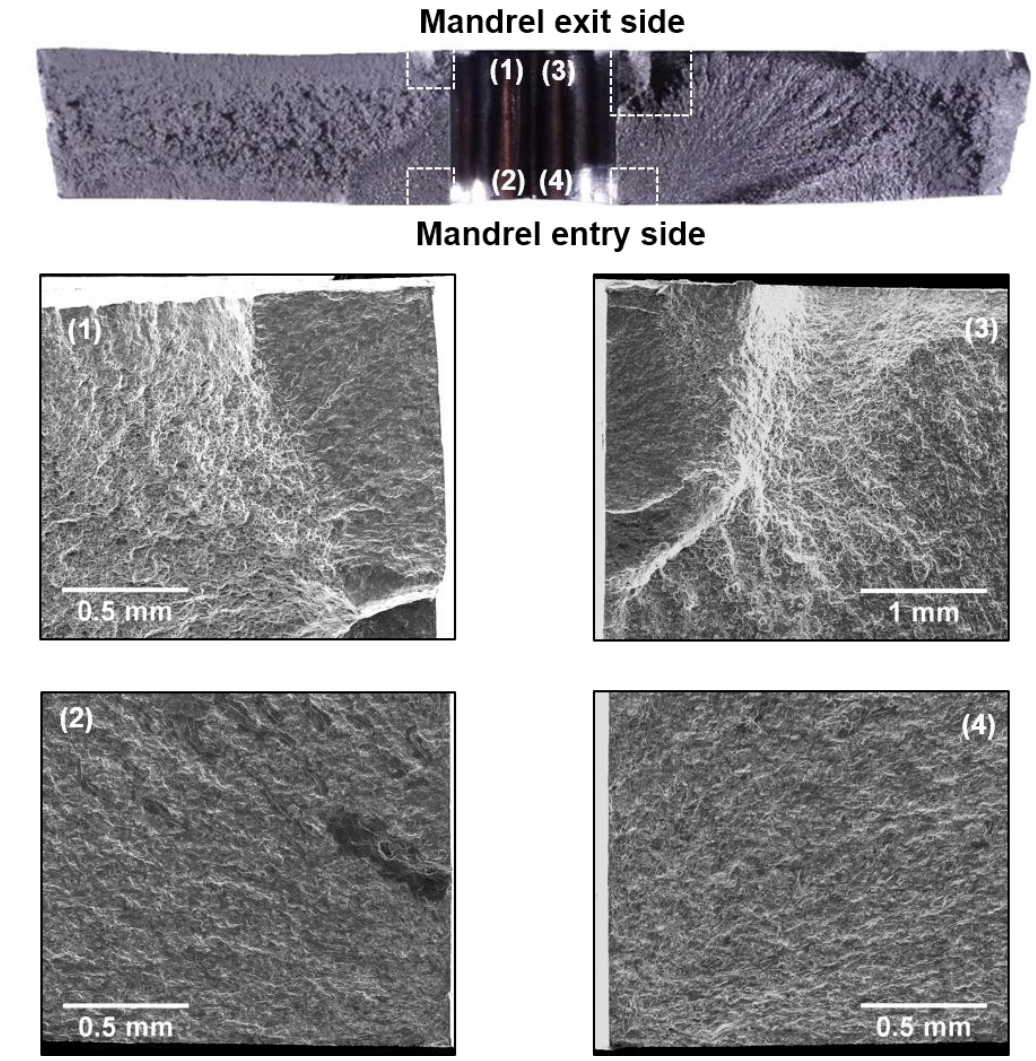

Figure 7.10 Fracture surface morphology of the cold-expanded specimen, C6 with unmodified residual stress distribution. The optical micrograph on top shows the whole fracture surface. SEM images 1 and 3 show the origin of secondary fatigue cracks initiating from left and right corners on the mandrel exit side, respectively. SEM images 2 and 4 show the origin of primary fatigue cracks initiating from left and right corners on the mandrel entry side, respectively.

In a very recent article by Wang et al[46], the fatigue behaviour of cracks initiating from cold-expanded holes in 6061-T6 aluminium specimens were investigated. The dog-bone fatigue specimens employed in their research were 3 mm thick with a reduced-section width of 34 mm. A central hole of 8 mm diameter drilled in these specimens was cold-expanded by 4 %. These specimens were reported to be loaded in fatigue until failure by applying a maximum remote stress of 210 MPa

with a stress ratio of 0.1. In this article, a fractograph of the failure surface of one of these specimens was presented, which shows a localised fast fracture zone within the FCG region (see Figure 7.11). The extent of this localised zone was from 0.5 to 2.5 mm from the hole edge and was reported to be bypassed by the fatigue crack due to the presence of tri-axial compressive stresses in this zone. Hence, the reduction in the fatigue crack growth rate was attributed to this localised fast fracture zone. No evidence of any such localised zone was found from the fractographic analysis performed in this work; but, the retardation in crack growth is still evident from Figure 7.2. The proposed explanation for crack growth retardation, therefore, is the combined effect of applied stresses that decrease away from hole edge, due to the reduced effect of the stress concentration, and the presence of compressive residual stresses, which the superimposed residual stress profile in Figure 7.3 confirms.

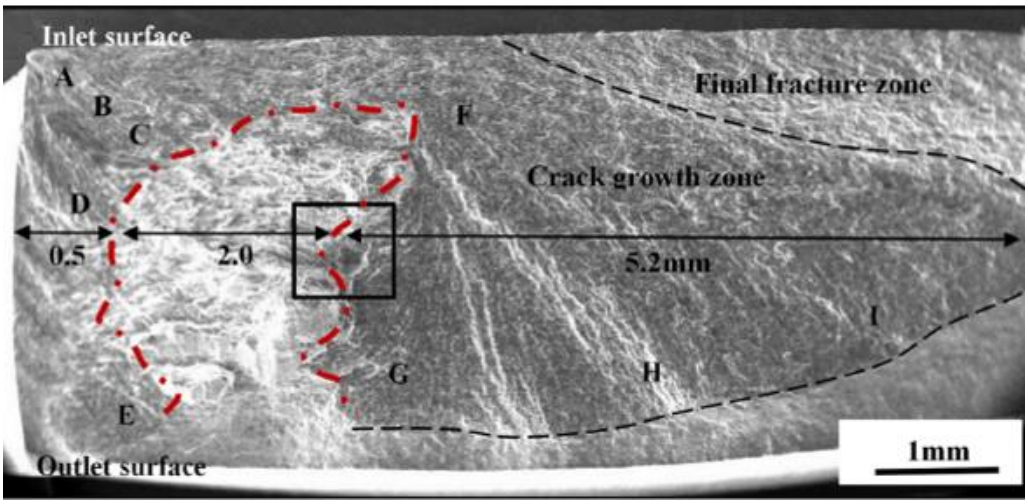

Figure 7.11 The SEM image of the failure surface of a cold-expanded specimen. The fast fracture region by-passed by the fatigue crack is highlighted in red. The image is reproduced from the article by Wang et al [46].

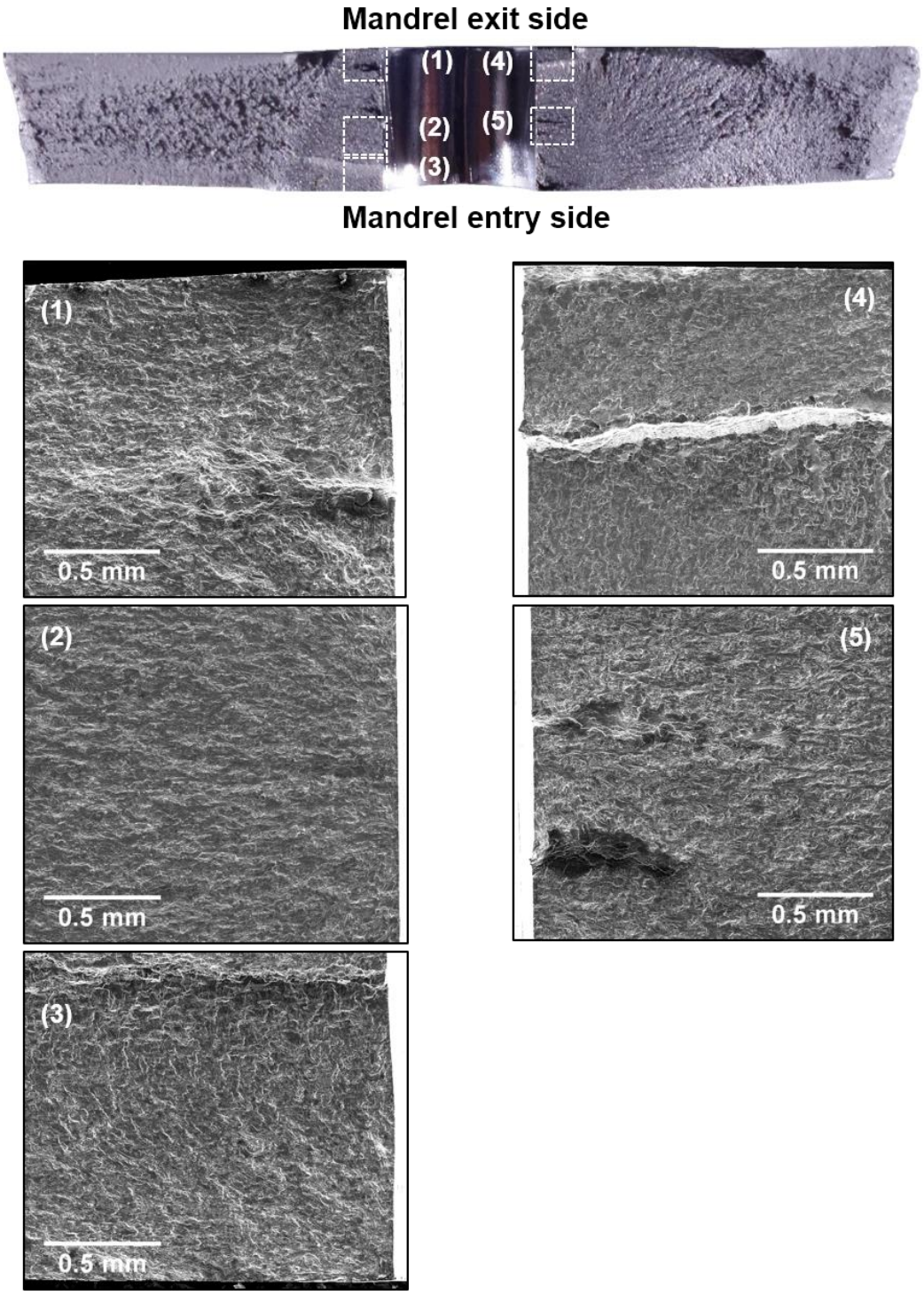

Figure 7.12 Fracture surface morphology of the cold-expanded specimen, C10 with modified residual stress distribution after a single compressive stress cycle of -92.7 MPa was applied prior to fatigue loading. The optical micrograph on top shows the whole fracture surface. SEM images on the left and right highlight multiple crack initiation sites along the left and right edges of the hole, respectively.

The fractographs of specimen, C10 to which a single compressive load cycle of -92.7 MPa was applied, are shown in Figure 7.12. The SEM images of the regions highlighted in white on the optical fractograph show the crack initiation sites. It can be seen that cracks initiated from multiple sites along the hole edge and merged at a later stage to form a single fatigue crack. The resulting crack front appears to be much straighter in comparison to the one developed in the cold-expanded specimen with the unmodified residual stress distribution (specimen C6 in Figure 7.10). This implies that the through-thickness variation in the modified residual stresses is significantly lower, which the residual stress measurements presented in the next chapter confirm. The multiple crack initiation sites along the hole edge were also observed on the failure surface of specimen, C11 to which a single compressive load cycle of -125 MPa was applied. The fractographs of C11 are provided in Appendix B.

7.4 Summary

This chapter has presented the results obtained from first half of the experimental study on fatigue performance of cold-expanded holes which focused on developing understanding of the behaviour of fatigue crack propagation utilising TSA. In the first section of this chapter, fatigue performance of cold-expanded holes was compared with the un-expanded ones. A characteristic trend was observed for cracks initiating from the cold-expanded holes: namely that, the crack growth rate decreased to a minimum at approximately 3 mm from the hole edge beyond which it increased as the crack grew out of the influence of the residual compressive stresses associated with cold expansion. In contrast, the growth rates were found to be consistently high for the cracks initiating from the

un-expanded holes in the absence of any compressive residual stresses. The plastic zones associated with the fatigue crack tip, which were determined from the TSA data, have been discussed in the second section of this chapter. The crack tip plastic zones were found to be insignificant in size in comparison to the residual stress zone resulting from cold expansion, which implied that they were unlikely to have had a notable impact on the surrounding residual stresses induced by the cold expansion. Finally, the third section has presented the fractographic analysis which qualitatively confirmed the influence on crack initiation of the residual stresses induced by the cold expansion.

8 RESIDUAL ELASTIC STRESSES AROUND COLD-EXPANDED HOLES

This chapter presents the results obtained from the synchrotron x-ray diffraction (SXRD) experiments performed at European Synchrotron Radiation Facility, France. These results are a continuation of the first half of the experimental study reported in the previous chapter and focus on the effect of fatigue loading and propagation of a fatigue crack on the beneficial compressive residual stresses around cold-expanded holes. The description of the SXRD technique and the details of experimental setup can be found in Sections 3.1 and 4.3, respectively.

8.1 Uncertainty in residual elastic strain measurements

As mention in Section 3.1, the accuracy of the residual elastic strain measurement depends primarily on the reliable evaluation of the representative strain-free lattice spacing, d_0 for the material being investigated. The standard deviation in the residual elastic strain measurement, resulting from variation in strain-free (311) plane spacing, along the longitudinal (Y) and horizontal (X) directions were found to be of ±169 and ±27 μstrain, respectively. In terms of Y and X components of residual elastic stresses, these values correspond to standard deviations of ±13 and ±5 MPa, respectively. Stefanescu et al[18], who utilised SXRD in one of their studies, reported an uncertainty of ±74 μstrain, resulting from variation in d_0, in their residual strain measurements around cold-expanded holes. The vertical and horizontal beam dimensions employed in their work ranged from 0.3 - 1 mm and 0.6 - 2 mm respectively, giving a relatively lower spatial resolution in comparison to the measurements performed in this work, where a beam size of 0.3 × 0.3 mm

was used. However, the strain resolution of ±169 μstrain for the Y direction residual strains was lower in this work compared to ±74 μstrain in the study by Stefanesu et al[18]. Nonetheless, the strain resolution was high enough to discern any potential residual strain relaxation due to fatigue crack propagation, which was reported to be of the order of 2400 μstrain close to the hole edge by Stefanescu et al[18]. It is pertinent to mention here that a detailed uncertainty analysis, taking into account the residual stresses due to cold expansion process variability, has not been carried out in any of the previous investigations and is essential to identify any significant redistribution or relaxation of such stresses. Therefore, the propagated uncertainties were evaluated in this work considering the influence of both the variation in d_0 and the cold expansion process as discussed in the later section.

8.2 Residual elastic stress distribution developed from cold expansion

Figures 8.1 and 8.2 show the maps of X and Y components of residual stresses, respectively, measured at a depth of 2 mm from both the specimen faces in one of the cold-expanded specimens, C12 to which no monotonic or fatigue loads were applied (see Table 7.1 for specimen loading history). The line plots of X and Y components of residual stresses (corresponding to radial and hoop stresses) along -90^o and 0^o directions are presented in Figure 8.3. The theoretical distributions of residual hoop and radial stresses are also plotted in Figure 8.3, which were determined by implementing the axisymmetric hole expansion model of Zhang et al[57]. The extent of plastic zone can be estimated from the hoop residual stress

profile along a given radial line by locating the inflection point, i.e. the point of maximum tensile stress. For the entry face hoop stress profile, along -90^{o} radial direction in Figure 8.3, the location of maximum tensile stress is at 8.4 mm from the hole centre. This was found to be in good agreement with the location of plastic zone boundary determined from the DIC measurements i.e. 8.1 mm from the hole centre (see Figure 5.18 b).

The entry face hoop stresses, close to the hole edge, were found to be lower by 7 and 6 % of the exit face values at -90^{o} and 0^{o} angular positions, respectively. The experimental measurements reported in the published literature[8-10, 13, 19, 36] had revealed that the magnitude of residual hoop stress, close to the hole edge, on the mandrel entry face could be lower by 7 to 50 % of the residual hoop stress value on the exit face. The primary reason for this through-thickness variation in the residual stresses, as discussed in Section 2.1, is believed to be the difference in the constraint conditions between the two faces during cold expansion. However, there are other factors which are likely influence this as well, such as the thickness-to-diameter ratio, cold expansion level and the type of process used for cold expansion. The results obtained from DIC, reported in Chapter 5, showed that the magnitude of strains resulting from cold expansion are low along the radial line emanating at the location of the split i.e. 0^{o} angular position, which imply lower hole expansion at this location. It is, therefore, expected that the magnitude of residual hoop stresses at this location will be low as well. It was determined from the residual stress plots in Figure 8.3 that the magnitude of hoop stress, close to the hole edge, at 0^{o} is lower by approximately 15 % of the hoop stress value at 90^{o}.

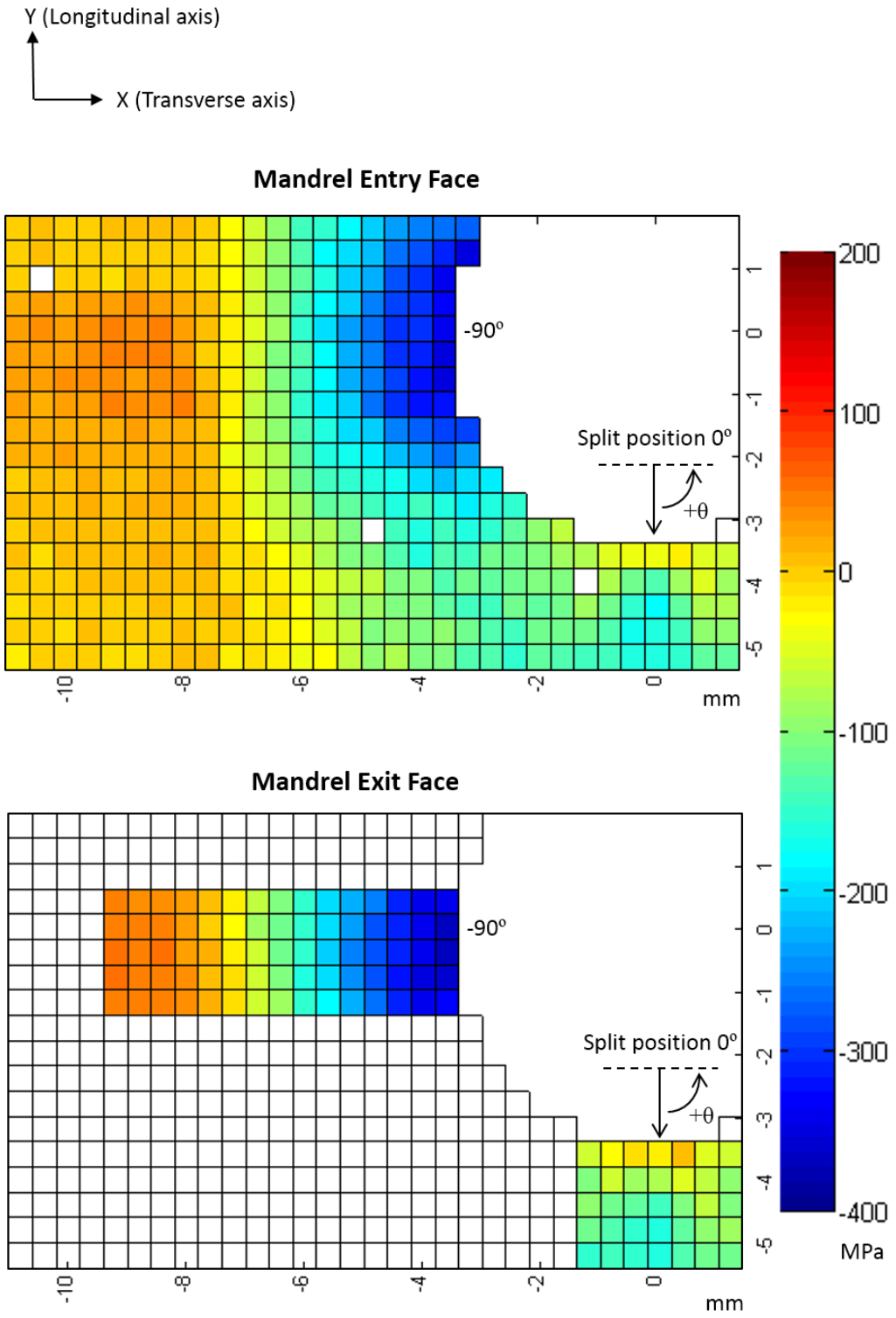

Figure 8.1 Maps of Y component of residual elastic stresses measured at a depth of 2 mm from the mandrel entry (top) and exit (bottom) faces in the cold-expanded specimen, C12.

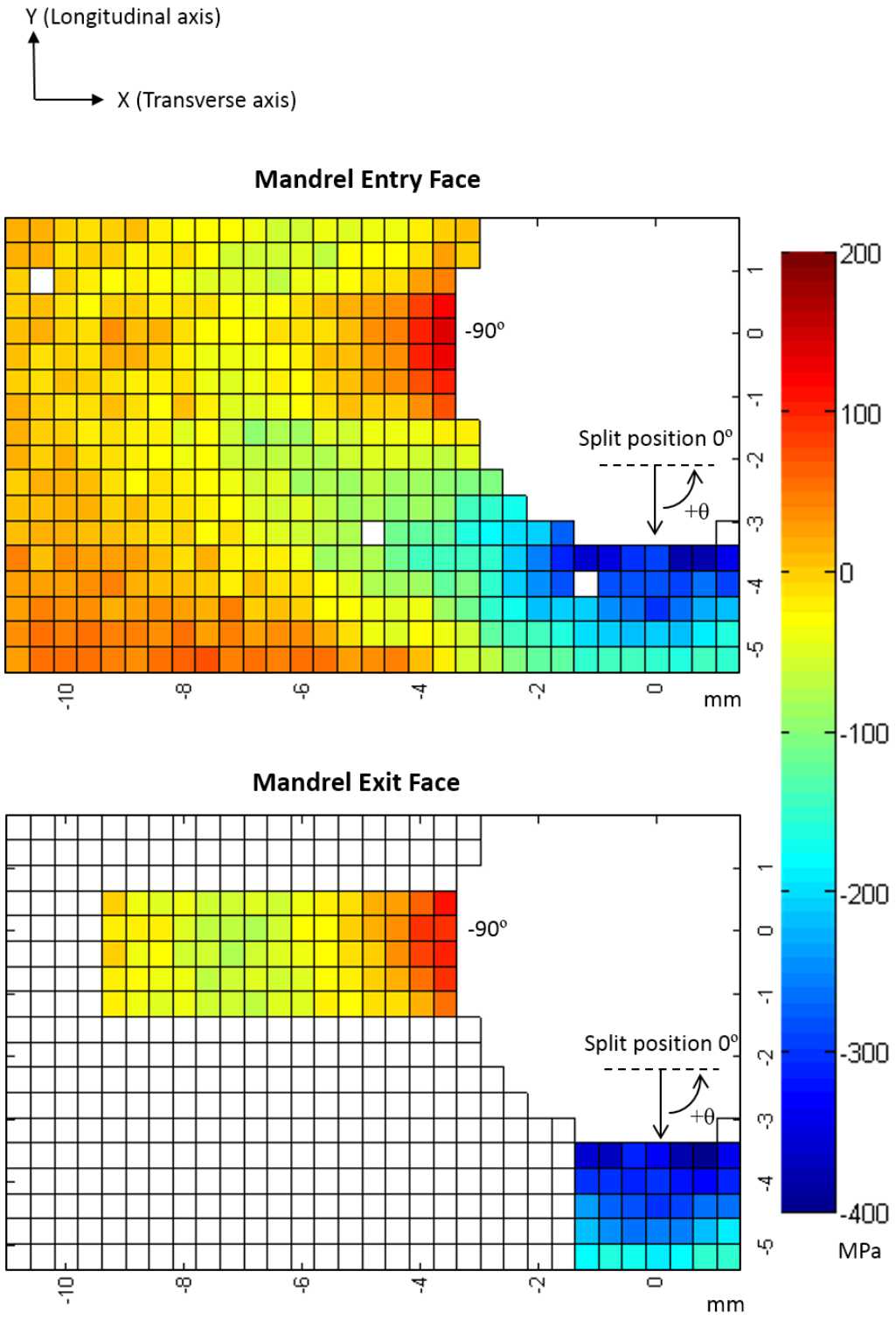

Figure 8.2 Maps of X component of residual elastic stresses measured at a depth of 2 mm from the mandrel entry (top) and exit (bottom) faces in the cold-expanded specimen, C12.

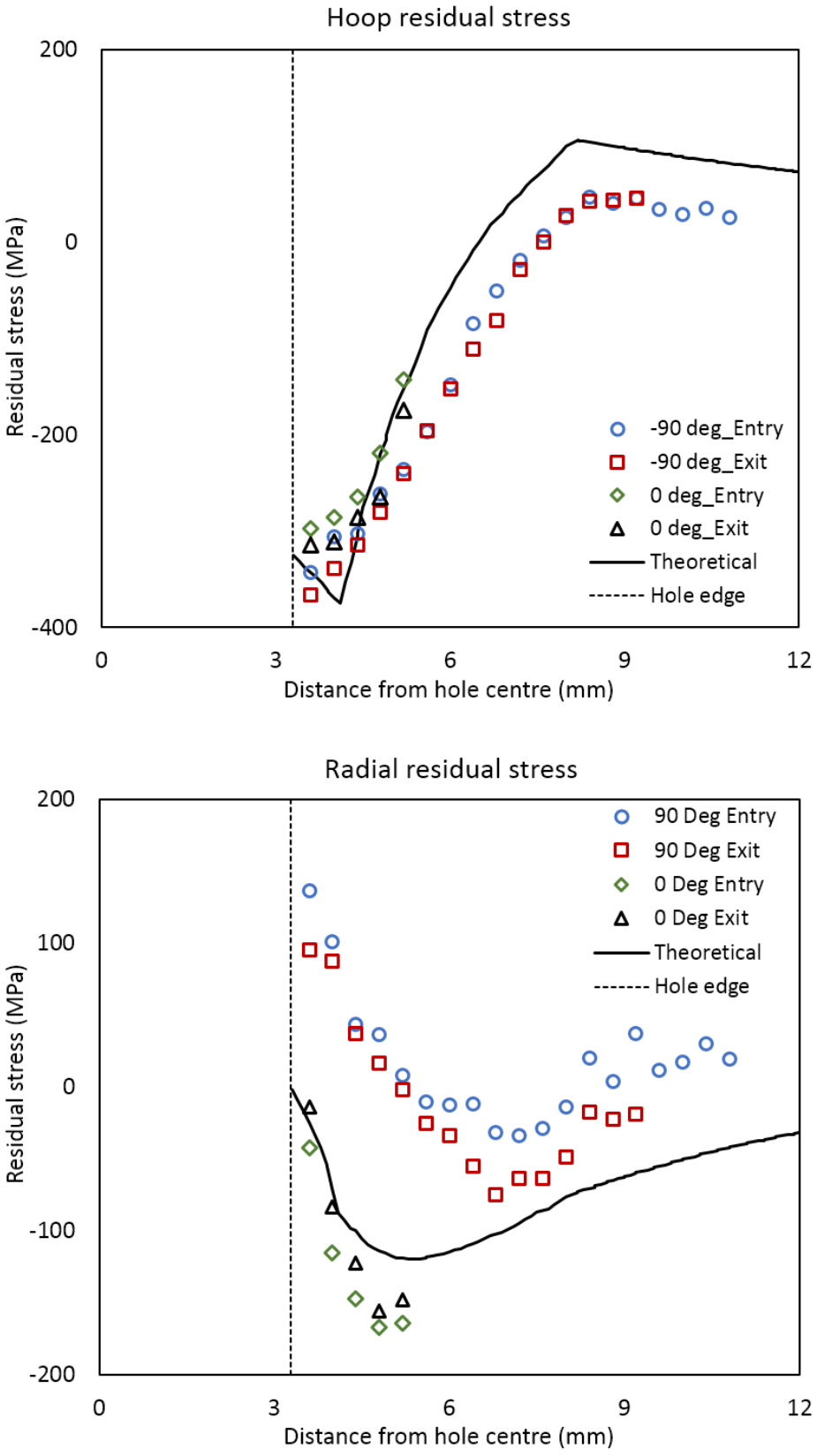

Figure 8.3 Hoop (top) and Radial (bottom) residual stress profiles along the 0° and -90° radial lines for the cold-expanded specimen, C12.

It can be observed in Figure 8.3 that the radial stresses along the 90^{o} direction are tensile close to the hole edge, whereas, the theoretical solution predicts predominantly compressive radial stress distribution. Majority of the previously published experimental investigations focused on measuring the component of residual stresses along hoop direction only because of its dominant role in the mechanism of fatigue crack initiation. However, Stefanescu et al[18] had determined the distribution of the component of residual stresses along the radial direction using SXRD which is presented in Figure 8.4. Their residual stress distribution show tensile radial stresses close to the hole edge which is generally in agreement with the radial stress distributions obtained in this research using SXRD (see Figure 8.3).

Pavier and his co-workers[60], demonstrated from their finite element (FE) simulation results that the residual stress distribution developed from hole expansion by the passage of a mandrel is substantially different from the one determined from a simplified assumption of hole expansion by a uniform radial force. The results from their FE model, which considered hole expansion by a mandrel, revealed tensile radial stresses near the hole edge. Later, Matos et al[63] analysed various FE cold expansion models with different levels of complexity and reaffirmed the conclusions drawn by Pavier et al[60]. The distribution of radial residual stresses predicted by a 3D FE model of Matos et al[63], which was based on a realistic hole expansion process involving a mandrel, is also presented in Figure 8.4.

The equilibrium requirement dictates that the component of residual stress along the radial direction must be zero at the hole edge. It can be observed from a FE

model predicted distribution in Figure 8.4 that the location of the maximum tensile stress is at 0.5 mm from the hole edge which then decrease to zero at the hole edge. The radial stress distributions determined experimentally using SXRD in this work (see Figure 8.3) and by Stefanescu et al[18], presented in Figure 8.4, show the maximum tensile stress at about 0.5 mm from the hole edge. It is unlikely that the sharp decrease in the radial residual stress over the length scale of 0.5 mm can be resolved by the SXRD measurements primarily because of the low spatial resolution of x-ray beam employed to perform these measurements.

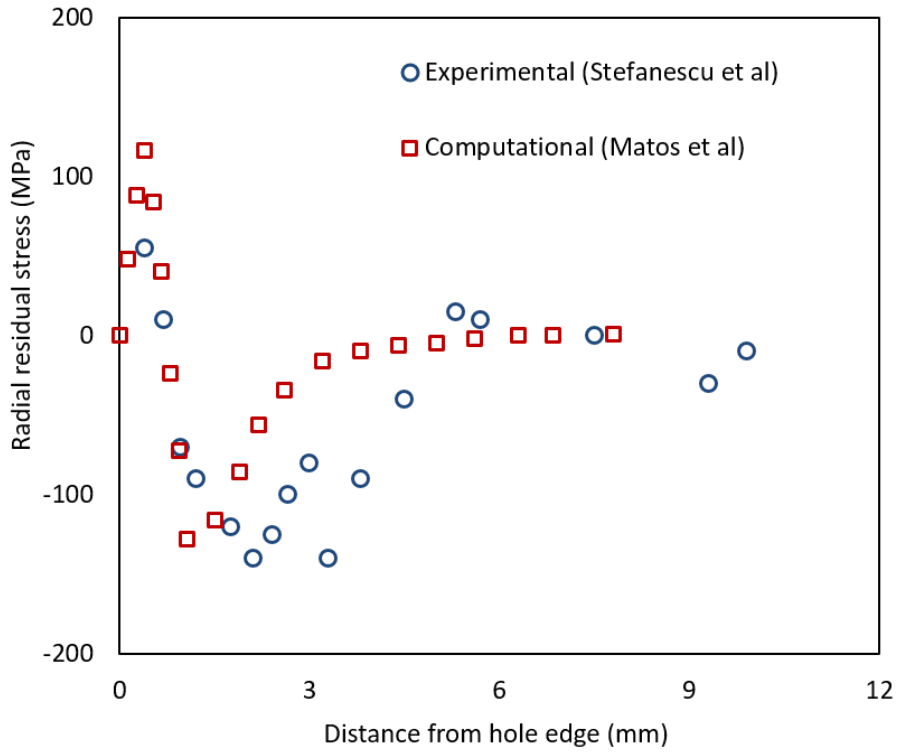

Figure 8.4 Distribution of radial residual stresses determined experimentally using SXRD by Stefanescu et al[18] and numerically by Matos et al[63].

8.3 Effect of fatigue crack propagation on the residual stresses

Prior to SXRD measurements, fatigue cracks of 2.1 and 3.8 mm in length were grown in cold-expanded specimens, C8 and C9, after cyclically loading them for 150k and 400k cycles respectively (see Table 7.1). These cracks emanated from the left hole edge and were observed on the mandrel entry face of the specimens. The residual stresses were measured from a region surrounding the crack (see matrix of measurement points, highlighted in red, in Figure 4.10). To determine the extent of fatigue crack through the specimen thickness, the specimens were fractured by applying a tensile overload after performing the SXRD measurements and the fractographs are provided in Appendix B. Figures 8.5 and 8.6 show the maps of residual stresses measured at a depth of 2 mm from the mandrel entry and exit faces respectively in specimens C8 and C9. For the purpose of comparison, residual stress maps for the un-cracked specimen, C12 are also provided in these figures. Only the Y component of the residual stresses are presented as they act perpendicular to the crack, thereby playing a dominant role in the mechanism of fatigue crack propagation. The plots for X component of residual stresses are provided in Appendix C. There does not seem to be any significant residual stress relaxation in specimens C8 and C9 as their stress fields appear to be very similar to those of the un-cracked specimen, C12. To perform a detailed uncertainty analysis, taking into account the variation in the strain-free lattice spacing and the cold expansion process, residual stresses were measured in six un-cracked specimens, C12-C17, along the transverse centre line at a depth of 2 mm from mandrel exit face. The average residual stress distribution for the six specimens is

shown in Figure 8.7. The values for the propagated uncertainty were calculated based on the principles defined in the guide to measurement uncertainty[145] and are shown as 95% confidence limits for the mean value, or two standard deviations.

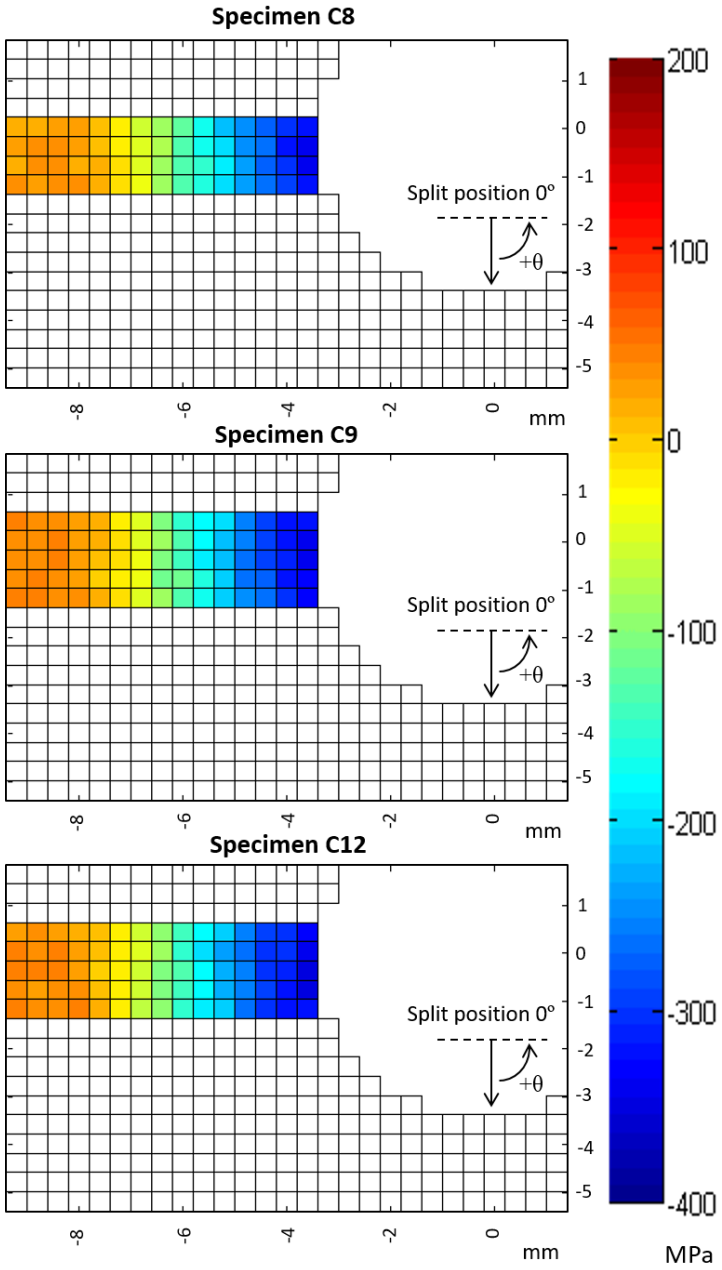

Figure 8.5 Maps of Y component of residual stresses close to the mandrel entry face for cold-expanded specimens, C8 with a 2.1 mm crack (top), C9 with a 3.8 mm crack (middle) and C12 to which no loads were applied (bottom).

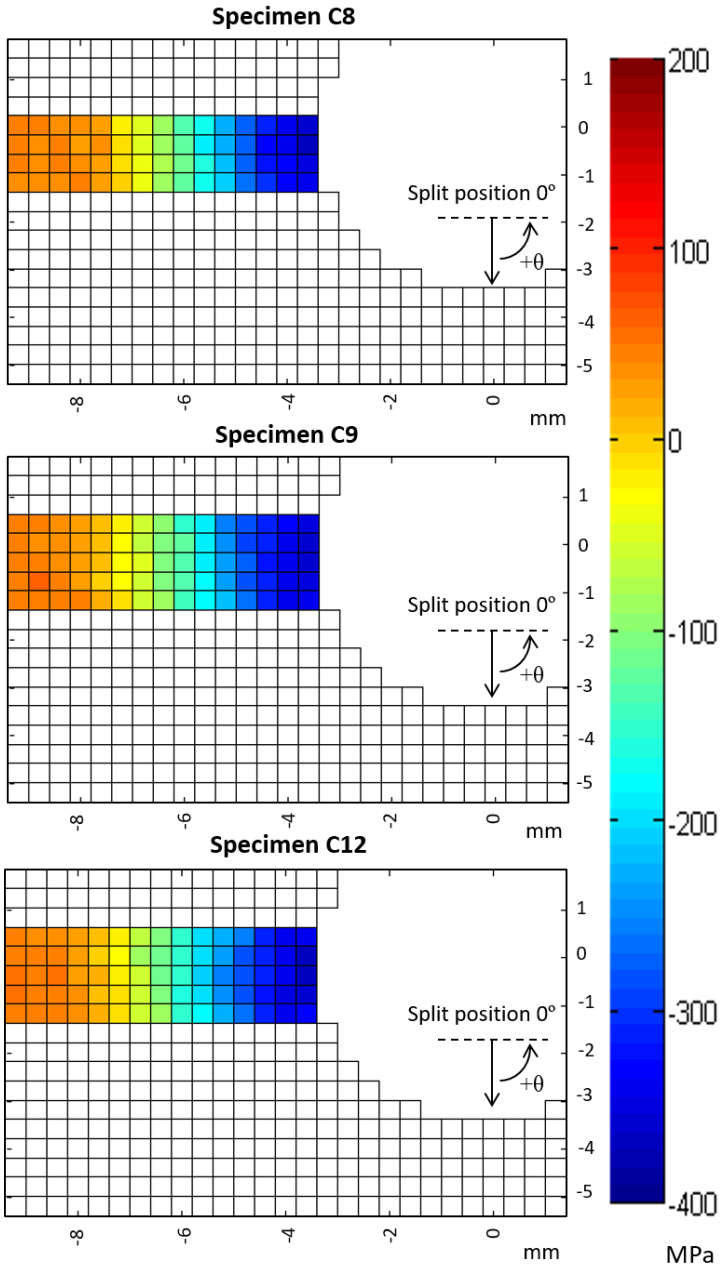

Figure 8.6 Maps of Y component of residual stresses close to the mandrel exit face for cold-expanded specimens, C8 with a 2.1mm crack (top), C9 with a 3.8 mm crack (middle) and C12 to which no loads were applied (bottom).

For a more quantitative comparison of the measured residual stresses in specimens C8, C9 and C12, their distributions are plotted in Figure 8.8 along the crack line, which also coincides with the transverse centre line of the specimen. The plot also includes the distribution for specimen, C7 to which 50k cycles of fatigue loading was applied, with the purpose of determining whether fatigue

loading on its own brings about any redistribution of residual stresses prior to initiation of a primary fatigue crack, as reported by Özdemir and Edwards[35]. The residual stress profiles for specimens C7-C9 were subtracted from those of the un-cracked specimen, C12 and the differences are plotted in Figure 8.8. All the values are within the propagated uncertainty bounds, which were obtained from the uncertainty analysis of the measurements made in the six un-cracked specimens, C12-C17. This clearly shows that there is no significant relaxation or redistribution of residual stresses resulting either from fatigue loading or due to propagation of a fatigue crack. This reinforces the conclusions drawn from the TSA results that there is negligible influence of crack tip plastic zone on the surrounding residual stresses. In contrast to the findings of Stefanescu and his co-workers[18], the plots in Figure 8.8 do not show any pronounced relaxation, even at the hole edge. In their work, cracks were grown from an EDM notch, whereas in this work, the fatigue cracks were initiated naturally as a result of fatigue loading. This supports the argument that installing a notch involves material removal and associated plastic work together with the creation of a geometric discontinuity resulting in a relaxation of the residual stresses around the edge of the hole.

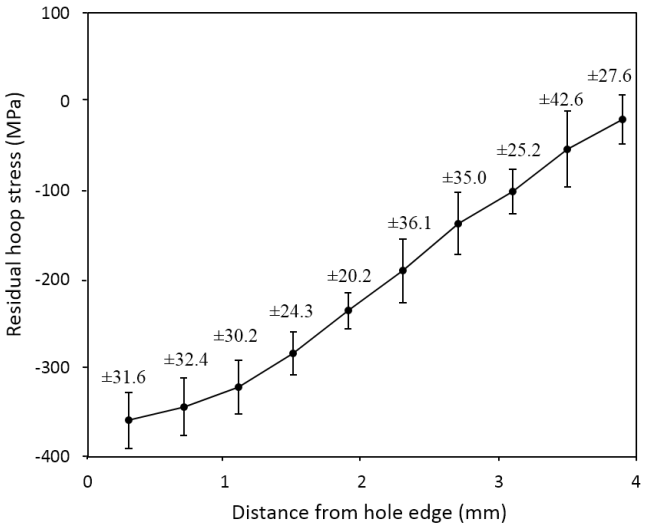

Figure 8.7 Average residual hoop stress profile, close to the mandrel exit face, for cold-expanded specimens, C12-C17 to which no loads were applied.

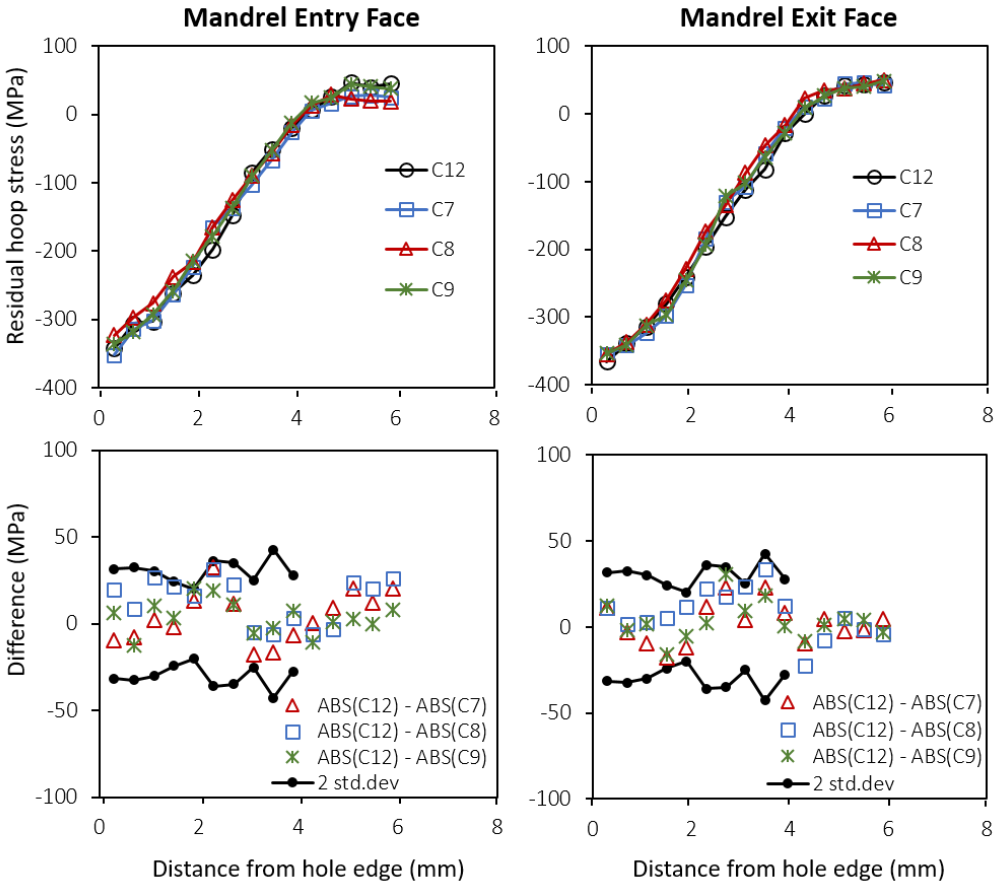

Figure 8.8 Plots of residual hoop stress profiles (top) and difference in their magnitudes (bottom) close to the mandrel entry (left) and exit (right) faces for cold-expanded specimens, C7 to which 50k cycles of fatigue loading was applied with no cracks observed during loading, C8 with a 2.1 mm crack, C9 with a 3.8 mm crack and C12 to which no loads were applied.

8.4 Effect of compressive loads on the residual stresses

For specimens, C10 and C11, the maximum hoop stress at the hole edge, $\sigma_{h,max}$ due to the applied compressive loads were calculated to be -635 and -725 MPa, respectively, which are substantially higher than the ultimate tensile strength of the material i.e. 505 MPa. The 2024-T351 aluminium plate material used in this research is known to have slightly lower yield and ultimate strengths in compression in comparison to tension[122]. This implies that there will be large-scale plastic deformation causing a redistribution of the initial residual stresses. Figure 8.9 shows the adversely affected residual stress profiles for specimens C10 and C11, which suggests an explanation for the higher crack growth rates; and consequently, higher ΔK_{eff} values and larger crack tip plastic zones in these specimens, as shown in Figures 7.2, 7.4 and 7.6 in the previous chapter. For specimens C10 and C11, the stress relaxation at the hole edge was found to be 34 & 62 % close to the mandrel entry face and 40 & 66 % close to the exit face, respectively. It was expected that there would be a slightly higher relaxation on the exit face due to the higher magnitude of the compressive residual stresses on the exit face in comparison to the entry face.

It was highlighted in Section 7.3 that the crack fronts for specimens C10 and C11 appear to be much straighter in comparison to the one developed in the cold-expanded specimen with the unmodified residual stress distribution (See for example Figures 7.10 & 7.12). This implies that the though-thickness variation in the residual stress distributions which were modified by the compressive loads are significantly lower compared to the unmodified residual stress distribution. The difference between the entry and exit face residual hoop stresses close to the hole

edge were found to be 5 and 3 MPa for C10 and C11 respectively in comparison to 30 MPa for C12 with an unmodified residual stress distribution.

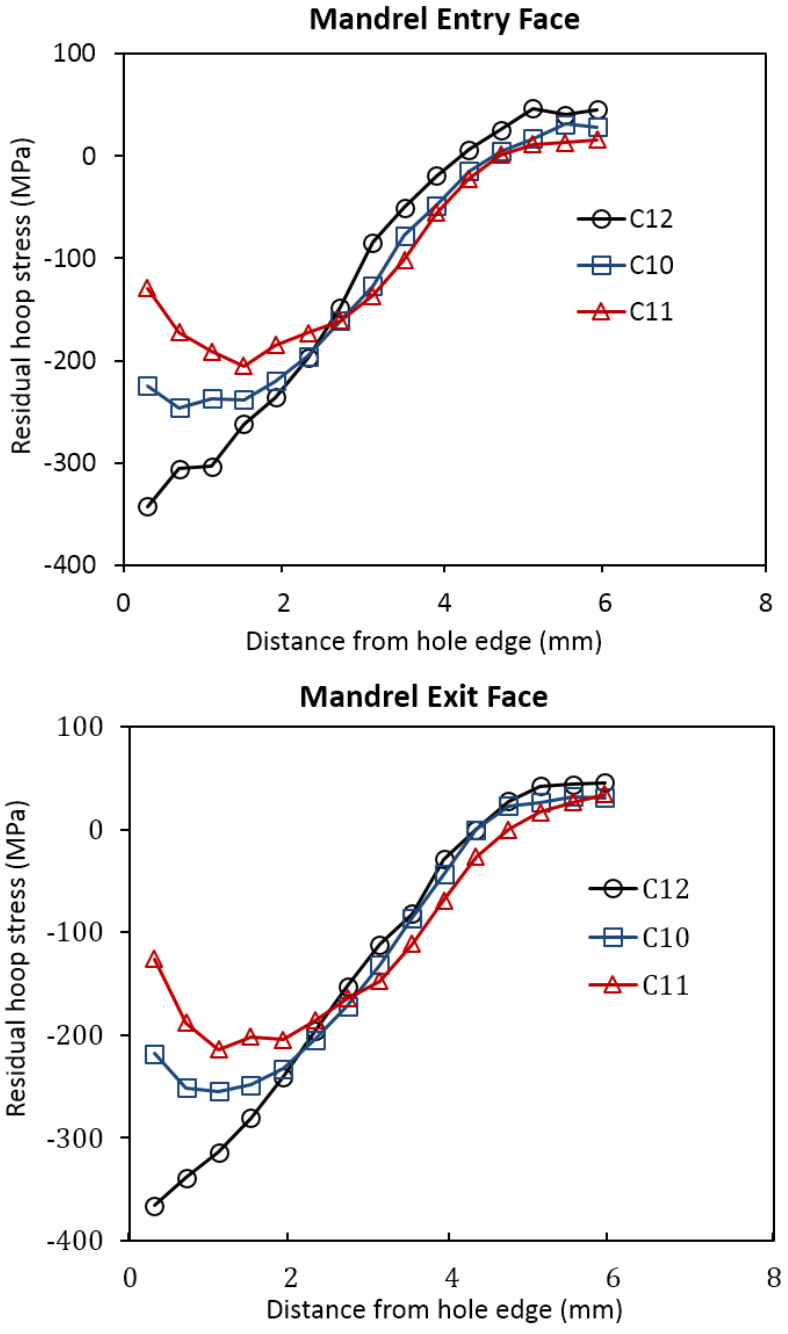

Figure 8.9 Plots of residual hoop stress profiles close to the mandrel entry (top) and exit (bottom) faces for cold-expanded specimens, C10 to which single compressive stress cycle of -92.7 MPa was applied, C11 to which single compressive stress cycle of -125 MPa was applied and C12 to which no loads were applied.

8.5 Summary

This chapter has presented the results obtained from second half of the experimental study on the fatigue performance of cold-expanded holes which focused on determining the influence of fatigue cracks on the beneficial compressive residual stresses induced by the cold expansion using SXRD. The first section of this chapter has discussed the uncertainty in the residual elastic strain measurements. The resolution of these measurements was found to be high enough to discern any potential residual strain relaxation due to fatigue crack propagation. The second section has presented the residual elastic stress distribution developed from the split sleeve cold expansion. The effect of fatigue crack propagation on the residual stresses has been analysed in the third section. The residual stress distributions measured along the direction of crack growth showed no signs of any significant stress relaxation or redistribution, which validates the conclusions drawn from the TSA results reported in the previous chapter. The last section focused on investigating the influence of compressive loads on the residual stresses. It was found that the application of single compressive overload caused a relaxation in the residual stresses, which has wider implications for improving the fatigue life.

9 DISCUSSION

A major motivation for this research was to develop an understanding of the behaviour of fatigue cracks which initiate naturally at the edge of cold-expanded holes in the absence of any starter notch, with a particular emphasis on the influence of these cracks on the surrounding compressive residual stresses. In view of this initial motivation, a detailed review of the literature on cold expansion was carried out at the beginning of this PhD research to attain comprehensive knowledge about different aspects of the behaviour of cold-expanded holes and identify the knowledge gaps where original contributions were required. From the literature review, it was realised that there are two intimately related areas of research regarding the behaviour of cold-expanded holes i.e. the study of hole deformation resulting from cold expansion and the fatigue performance of cold-expanded holes. In the literature there is a lack of clarity on the role of component thickness to hole diameter ratio (t/D_o) on the effectiveness of the cold expansion process in creating a uniform, axisymmetric residual stress zone around cold-expanded holes. It was also revealed there is an ambiguity about the influence of fatigue loading or the propagation of a fatigue crack on the beneficial compressive residual stresses around cold-expanded holes. Based on these identified knowledge gaps, the aim of this research programme was first studying the development of residual strain field from the cold expansion process and then investigating the mechanism of fatigue crack propagation through such a field. The split sleeve cold expansion process was selected to be studied in this research because of its wide use in the aerospace industry.

9.1 Hole deformation from cold expansion

FTI[5], the manufacturer of the split sleeve cold expansion tooling, supports the cold expansion of holes as small as $t/D_o = 0.2$. On the other hand, a discussion with some sectors of the aerospace industry implied that the current practice is to stack thin sheet components together to ensure that the combined t/D_o ratio is at least 1. In order to establish the role of t/D_o ratio on the effectiveness of the cold expansion process, the hole deformation was analysed in aluminium specimens of two different thicknesses giving t/D_o ratios of 0.25 and 1 using a stereoscopic DIC setup. The out-of-plane displacement plots in Figure 5.21 reveal that the thin specimen with t/D_o ratio of 0.25 undergoes combination of global bending and significant localised warping during the cold expansion process. Close to the hole edge, this localised warping causes a reduction in the gradient of the minimum principal strains along radial lines emanating from the centre of the hole (see Figure 5.13). In contrast, the thick specimens with t/D_o ratio of 1 do no bend globally mainly because of the high second moment of area of their cross sections. The material close to the hole edge bulges out from both the faces of the specimen as a result of plastic deformation. Overall, the localised out-of-plane deformations are lower in the thick specimens in comparison to the thin ones.

The out-of-plane displacements around cold-expanded holes have been analysed in several previously published investigations[27, 31, 32, 140]. In most of these investigations, the out-of-plane displacements were measured either to estimate the extent of plastic zone developed from cold expansion[27, 31, 32] or to determine their influence on the initiation of fatigue cracks induced by fretting in bolted specimens with joint holes previously cold-expanded[140]. To the best of the

author's knowledge, no investigation has reported the phenomenon of out-of-plane warping resulting from cold expansion of holes in thin specimens.

0The plastic zone developed around a cold-expanded hole can provide some meaningful insights into the effectiveness of the cold expansion process. It is considered to be equivalent in shape and size to the residual stress zone created as a result of cold expansion. Therefore, development of a larger plastic zone implies a higher spring back force from the elastic material surrounding the plastically deformed material, thus creating a more compressive residual elastic stress field. Also, the axisymmetry of the plastic zone shape about the hole axis indicates that the residual stress zone would be equally effective in retarding the growth of a fatigue crack irrespective of the angular position at which it initiates from the hole edge. Several researchers[27, 28, 30-32] attempted to measure the extent of the plastic zone. However, these measurements were discrete, and in most cases, the extent of plastic zone was determined along the radial line at 90° from the position of split in the sleeve. In this research, the capability of the DIC technique in providing full-field strain measurements was exploited, for the first time, to determine the actual shape and size of the plastic zone developed from cold expansion by applying the Von Mises yield criterion to the measured strain data.

The plastic zone developed around the cold-expanded hole in the thin specimen was found to be highly non-axisymmetric in shape and there was a significant difference between the size of plastic zones on the mandrel entry and the exit faces at the location of split in the sleeve (see Figure 5.18). The development of

non-axisymmetric plastic zone results from the fact that the hole instead of deforming primarily in the radial direction undergoes significant out-of-plane warping during the cold expansion process. On the other hand, for the thick specimens, the plastic zone developed around the expanded hole was found to be more uniform about the hole axis and overall larger in size. These results demonstrate that the mechanics of hole deformation is significantly different for the thick and thin specimens and that the existing split sleeve cold expansion process is not as effective in creating a uniform compressive residual elastic stress field around fastener holes in thin as it is in the thick specimens. The thin specimens used in this investigation were equivalent in thickness to sheet material commonly used in an aircraft fuselage or wing skins and the results indicate that there is a need to review the use of cold expansion process using a split sleeve and mandrel for holes in thin sheets.

The strain profiles measured around the cold-expanded hole in both thick and thin specimens were compared with the theoretical strain profiles based on the model by Zhang et al[57]. The theoretical strain predictions did not correlate with the measured strain profiles for either thickness of specimen (see Figures 5.13 and 5.14). This was primarily due to the assumption of axisymmetric expansion by a uniform pressure in the existing theoretical models[51-57] that also do not account for the complex out-of-plane deformations, which have been observed during cold expansion with a split sleeve and mandrel and are believed to have a significant influence on the residual stress distributions. These conclusions are generally in agreement with the conclusions drawn in several numerical studies on the cold expansion process[11, 60, 63]. It was emphasized in these studies that the assumption

of axisymmetric hole expansion by a uniform pressure, under plane stress or plane strain condition, in the theoretical or FE models is inadequate in approximating the strain fields resulting from the actual cold expansion process.

Most of the fastener holes drilled in an aircraft structure are associated with the joints connecting two or more layers of material together. Despite significant relevance to the aerospace industry, the strain fields developed as a result of simultaneous cold expansion of holes in multiple layers stacked together have not been studied experimentally in any of the previously published findings. The methodology adopted to analyse cold expansion in single thick and thin specimens was applied to analyse cold expansion in a multi-layer stack, which comprised of five thin specimens giving a combined t/D_o ratio of 1.25. The plastic zones developed from cold expansion in individual layers of the stack were found to be significantly more axisymmetric in comparison to the ones developed in single thin specimens (see Figure 6.8). This improvement in axisymmetry of the plastic zones in the stacked thin specimens was primarily due to a marked reduction in the out-of-plane hole distortion in the vicinity of the split in the sleeve (see Figures 6.9 and 6.10). These results show that stacking offers some improvement in the cold expansion of thin specimens. However, the size of the plastic zones in stacked specimens, particularly on the mandrel entry face, is small in comparison to the plastic zone developed in a single thick specimen, which is equivalent in thickness to the stack. The variation in the shapes and sizes of the plastic zones between individual specimens of the stack can also be noticed in Figure 6.8. This establishes that the multi-layer stack does not expand as a monolithic layer of equivalent thickness during cold expansion.

As mentioned earlier, the current practice in some sectors of the industry is to cold expand holes when the t/D_o ratio is at least 1. This piece of knowledge was the main reason for the choice of five thin specimens in the stack giving combined t/D_o above 1. The multi-layer stack investigated in this research does not represent a real joint in an aircraft structure, hence these results can be considered to be preliminary in nature. One of the major reasons for performing this analysis was to demonstrate that the simple approach adopted in these experiments to obtain strain fields developed in individual layers of the stack works and can be applied effectively to a real joint configuration of an airframe structure. The results discussed in this section meet the objectives A and B of this research reported in Section 2.4.

9.2 Fatigue of cold-expanded holes

A detailed experimental study about the fatigue behaviour of cold-expanded holes was carried out in this research utilising TSA and SXRD techniques. The focus of this study was in developing a clear understanding about the potential for and causes of any relaxation of the beneficial compressive residual stresses developed from cold expansion. A characteristic trend was observed for cracks initiating from cold-expanded holes: namely that, the crack growth rate decreased to a minimum at approximately 3 mm from the hole edge beyond which it increased as the crack grew out of the influence of the compressive residual stresses associated with cold expansion (see Figure 7.2). This characteristic trend is believed to result from a combined effect of decreasing applied stresses due to the reduced influence of the stress concentration and the presence of a compressive residual stress distribution, which reduces to zero about 1 mm beyond the location of the turning

point (see Figure 7.3). To illustrate this combined effect of the applied and residual stresses on the fatigue crack growth rate, a superimposed stress profile along the crack line is presented in Figure 7.3 which was determined by superimposing the tensile hoop stress profile, resulting from the maximum applied load in the fatigue cycle, on the compressive residual stress profile determined from SXRD. The characteristic trend of the crack growth rate in Figure 7.2 correlated well with the superimposed hoop stress profile in Figure 7.3.

The potential cause of this reduction in the crack growth rate has also been recently investigated by Wang et al[46]. They presented a fractograph of the failure surface of one of their specimen containing a cold-expanded hole which was failed from fatigue loading (see Figure 7.11). A fast fracture zone was identified in this fractograph which, according to Wang et al[46], was bypassed by the fatigue crack due to the presence of tri-axial compressive residual stresses in this zone. Hence, the reduction in crack growth rate was attributed to this localised fast fracture zone. No evidence of any such localised fast facture zone was found in the fractographic analysis performed in this research (see e.g. Figure 7.10). It is, therefore, concluded that the propagation of a fatigue crack emanating from the cold-expanded hole edge is primarily governed by the superimposed residual stress profile along the transverse centre line of the hole as shown in Figure 7.3.The evolution of the plastic zones associated with the crack tip, which were determined from the TSA data, are presented in Figures 7.6 and 7.7 (see also figures in Appendix A). The plots of crack tip plastic zone size against the crack length in Figure 7.6 demonstrate that the crack tip plastic zone is significantly smaller in size until the crack length reaches 4 mm, beyond which, the size of the

plastic zone increases rapidly. This reduction of the plastic zone size is primarily due to the presence of compressive residual stresses, which disappear at 4 mm from the hole edge as shown in Figure 7.3 (. The size of the residual stress zone developed from cold expansion, which was determined using DIC, is compared with the size of the crack tip plastic zone for a 4 mm crack in Figure 7.8. This figure demonstrates that, due to the large extent of the residual stress zone, the residual stresses induced by cold expansion, which surround the crack geometrically, act as remote stresses; and, the localised plastic zone associated with the crack tip is not sufficiently significant in size to cause the displacements required for relaxation or redistribution of these residual stresses. These conclusions do not support the results reported by Özdemir and Edwards[35] which implied that the plastic zone associated with the crack tip could potentially affect the initial distribution of residual stresses.

To validate the conclusions drawn from the TSA results, residual stresses were measured in both the un-cracked and the cracked cold-expanded specimens using SXRD. The uncertainty in the residual stress measurements, induced from two primary sources i.e. variation in the strain-free (311) plane spacing and the cold expansion process, was determined. The differences between the hoop residual stress profiles for the un-cracked and the cracked cold-expanded specimens were found to be lower than the uncertainty in the residual stress measurements (see Figure 8.8). These results clearly show that there is no significant relaxation of residual stresses resulting either from fatigue loading or due to propagation of a fatigue crack, as long as the applied loads are not high enough to cause large-scale plastic deformation at the hole edge. This reinforces the conclusions drawn from

the TSA results that there is negligible influence of the crack tip plastic zone on the surrounding residual stresses. These conclusions are in contrast to the previously published experimental findings by Özdemir and Edwards[35] and Stefanescu et al[18, 38], who reported pronounced stress relaxation as a result of fatigue crack formation. However, it is important to highlight here that in the work performed by Stefanescu et al[18], the crack was grown from an EDM notch and the residual hoop stresses were reported to be relaxed only close to the hole edge. Installing a notch involves material removal which could potentially cause a geometric discontinuity significant enough to cause relaxation of such residual stresses. Therefore, the stress relaxation reported in their work was not necessarily caused by the formation of a fatigue crack.

At the time of writing this thesis, a detailed study addressing the issue of residual stress relaxation in cold-expanded holes was published by Jones and Bush[146]. In this study, residual hoop stress profiles were determined in both the cracked and the un-cracked cold-expanded aluminium specimens using a destructive slitting method. They reported no evidence of any significant stress relaxation as a result of fatigue crack propagation. They also highlighted that any potential relaxation which might have occurred was less than the maximum uncertainty in the residual stress measurements, which was evaluated to be ±78 MPa. The maximum uncertainty in the residual hoop stress measurements, performed using SXRD in this research, was found to be much lower i.e. ±42.6 MPa (see Figure 8.7). Their findings, therefore, further validate the conclusions drawn in this research from the TSA and the SXRD results that there is no significant relaxation of residual compressive stresses as a result of fatigue crack formation, as long as the applied

loads are not high enough to cause large-scale plastic deformation at the hole edge. These results meet the objectives C and D of this research programme reported in Section 2.4.

An investigation was also conducted of the influence on the initial residual stress distribution of applied loads that were large enough to cause local yielding at the edge of the hole. As a consequence of the compressive nature of the residual stresses, only relatively small applied compressive loads were required to cause yielding. The SXRD measurements revealed substantial relaxation of the initial residual stress distribution due to the application of compressive loads (See Figure 8.9). As mentioned in Chapter 2, compliance with the damage tolerance requirements of an airframe structure needs to be achieved without considering the beneficial effects of cold expansion[86]. One of the reasons for a reluctance to account for these beneficial effects is the lack of clarity about the potential for, and causes of, any redistribution of the compressive residual stresses developed from cold expansion. It is believed that these results, which clearly highlight the loading conditions under which the beneficial compressive residual stresses are expected to relax, will be significant in improving the fatigue life prediction models for cold-expanded holes.

Qualitative analysis of the effect of residual stresses on fatigue crack initiation was performed by observing the fatigue features on the fractured surfaces of the specimens. The fractographs for the cold-expanded specimens in which the initial residual stress distribution was not modified by the applied compressive loads show that the primary fatigue crack always initiates preferentially from the

mandrel entry face of the specimen (see for example Figure 7.10). Several fractographic investigations[40-46] have reported the initiation of a fatigue crack at the hole edge from the mandrel entry face and the primary reason provided is the lower magnitude of compressive residual stresses on the mandrel entry face in comparison with the exit face. These investigations involved specimens made of different materials and having different thicknesses, which suggest that the initiation of fatigue cracks from cold-expanded holes is not influenced by the microstructure or the specimen thickness; but, is solely governed by the through-thickness distribution of the residual stresses. For the cold-expanded specimens in which the initial residual stress distribution was modified by the compressive loads, cracks initiated from multiple sites along the hole edge (see Figures 7.12 and B5 in Appendix B). The resulting fatigue crack fronts were found to be much straighter in comparison to the one developed in the cold-expanded specimens with the unmodified residual stress distribution. This implies that the through-thickness variation in the modified residual stresses is significantly lower, which the residual stress measurements from SXRD confirmed.

Cold expansion is usually performed in aerospace materials such as aluminium, titanium and steel alloys. Despite having significantly different mechanical properties, they all exhibit similar strain hardening; and hence, the three-dimensional (3D) residual stress field developed as a result of cold expansion will have a similar form in these materials. The major difference will be in the magnitude and extent of the residual stress field, which is dictated by the mechanical properties of the material. The findings reported in this thesis provide some meaningful insights into the mechanism of fatigue crack propagation

through a highly compressive residual stress field and the interaction of the crack tip plastic zone of a growing crack with the surrounding residual stresses. They also clearly demonstrate that the behaviour of fatigue crack propagation is governed primarily by the three-dimensional distribution of residual stresses; which, as mentioned above, is similar for the commonly used aerospace materials. This implies that the conclusions drawn from these findings should not be restricted to the particular grade of aluminium alloy material investigated in this research. It was also established that the initial residual stress distribution developed from cold expansion undergoes redistribution when the applied loads are large enough to cause yielding at the edge of cold-expanded holes. A simple approach of linear superposition of hoop stress at the hole edge resulting from the applied load and the compressive residual stress can be used as an initial estimate to determine whether a given applied load is expected to cause yielding at the hole edge. In this research, uniaxial compressive loads have been used to demonstrate residual stress redistribution but this simple approach for determining the potential for a given load to cause residual stress redistribution can be extended to other loading scenarios.

10 CONCLUSIONS

There are two strands of the research presented in this thesis; first being related to the study of hole deformation resulting from split sleeve cold expansion and the second one focused on the fatigue behaviour of cracks emanating from cold-expanded holes. The results obtained over the course of this research programme met all the identified objectives reported in Section 2.4. These results are believed to advance the existing body of knowledge on the subject of cold expansion. The key contributions presented in this thesis are summarised below:

A method of exploiting the capability of the stereoscopic DIC technique in providing full-field strain data was proposed and implemented to determine the shape and size of the plastic zone developed from cold expansion. The determination of plastic zones provides meaningful insights into the effectiveness of the cold expansion process in creating a uniform compressive residual elastic stress field around cold-expanded holes. This method was applied to determine plastic zones in aluminium specimens of two different thicknesses giving specimen thickness to initial hole diameter ratios (t/D_o) of 0.25 and 1. The results showed that the plastic zones developed on both the faces of the thin specimen were highly non-axisymmetric and significantly smaller in size in comparison to the ones developed in the thick specimen. It was established from this experimental investigation that the existing split sleeve cold expansion process is not as effective in creating an axisymmetric compressive residual elastic stress field around the fastener holes in thin as it is in the thick sheets. The thin specimens used in this investigation were equivalent in thickness to sheet material commonly used in an

aircraft fuselage or wing skins and the results indicate that there is a need to review the use of cold expansion process using a split sleeve and mandrel for holes in thin sheets.

A simple approach utilising DIC was presented to measure the strain fields developed from cold expansion in the individual specimens of a multi-layer stack. Stacking sheet materials together for cold expansion is currently being practiced in the aerospace industry. The results showed that stacking offers some improvement in the cold expansion of thin sheet components. The plastic zones developed in the stacked thin specimens were found to be more axisymmetric compared to the single thin specimen. These results clearly demonstrate the workability of this approach which can be applied effectively to analyse cold expansion of fastener holes associated with a real joint configuration in an airframe.

A long-standing ambiguity in the literature regarding the potential relaxation of beneficial compressive residual stresses as a result of fatigue crack propagation has been addressed and it was established from TSA and SXRD results that the formation or propagation of a fatigue crack does not cause any significant relaxation of these residual stresses. The findings from TSA and SXRD provide some meaningful insights into the mechanism of fatigue crack propagation through a highly compressive residual stress field and the interaction of the crack tip plastic zone of a growing crack with the surrounding residual stresses. They also clearly identified the loading conditions under which the residual stresses are expected to relax. This information is important in improving the theoretical

models for fatigue life assessment of cold-expanded holes. It would also be useful for the engineers in the aerospace industry to realise the full potential of the cold expansion process and to utilise it more effectively in the manufacturing of airframes leading to improved fatigue endurance under different loading conditions.

10.1 Publications and conference proceedings

The publications and conference proceedings based on the outcomes of this research programme are listed below:

Journal articles:

- Amjad K, Wang WC and Patterson EA. A comparison of split sleeve cold expansion in thick and thin plates. *Journal of Strain Analysis for Engineering Design* 2016; 51: 375-386.
- Amjad K, Asquith D, Paterson EA, Sebastian CM and Wang WC. The interaction of fatigue cracks with a residual stress field using thermoelastic stress analysis and synchrotron x-ray diffraction experiments. *Royal Society Open Science* 2017; 4: 171100.

Conference Proceedings:

- Amjad K, Patterson EA and Wang WC. Analysis of total residual strains around cold-expanded holes. In: 10th International Conference on Advances in Experimental Mechanics 2015 The British Society for Strain Measurement, Edinburgh, UK.
- Amjad K, Patterson EA and Wang WC. Analysis of the effectiveness of cold expansion in multi-layer stack using Digital Image Correlation. In: 12th International Conference on Advances in Experimental Mechanics 2017 The British Society for Strain Measurement, Sheffield, UK.

10.2 Further work

The results presented in this research suggest that the use of split sleeve cold expansion process for fastener holes in thin aluminium sheets commonly used in an aircraft fuselage or wing skins, should be reviewed. As a first step, it is important to determine the near surface residual stress distribution around cold-expanded holes in thin specimens. The SXRD experiments performed in this research cannot be used effectively to measure residual stresses with a high spatial resolution through the specimen thickness due to an elongated shape of the measurement volume (see Figure 4.12). Grazing Incidence x-ray diffraction (GIXD) technique might be a suitable alternative which has the potential to evaluate the near surface residual stresses with high through-thickness spatial resolution.

It is well-established that the current cold expansion process is effective in extending the fatigue life by reducing the growth rate of fatigue cracks past the short crack regime. Cold expansion has been found to be minimally effective in reducing the growth rate of short cracks lower than 1 mm in length. One potential reason for this is the initiation of fatigue crack preferentially from the mandrel entry face because of lower magnitude of compressive residual stresses present on this face in comparison to the exit face. This difference in the compressive residual stresses between the mandrel entry and exit faces is believed to be due to the different geometric constraints which exist at the two faces during the cold expansion process. One simple approach to resolve the issue of through-thickness variation in the residual stresses is to repeat the cold expansion process by reversing the mandrel direction so that the component face which was the mandrel entry face in the first cold expansion becomes the exit face in the second

one[9, 49, 50]. Stefanescu[9] have demonstrated that this approach is effective in reducing the through-thickness variation in the residual stresses. Despite this approach being straight-forward is not practical and cannot be applied to structures for which only one side is accessible for performing cold expansion. There is a need to develop new cold expansion tools capable of creating axisymmetric residual stress field around the hole which is also uniform through the thickness of the component. One possible direction for future investigation would be to analyse and modify the design of the existing mandrel used in the split sleeve cold expansion process with the aim of reducing the difference in the geometric constraint between the mandrel entry and exit faces.

Maximov et al[4] has recently proposed a novel cold expansion process which eliminates the use of split sleeve. They claimed that this process minimises the surface upset and ensures axisymmetric radial expansion of the hole. So far, finite element analysis has been performed to predict the residual stress field developed from this new process but was not corroborated against any experimental results. It will be interesting to experimentally demonstrate whether this process could improve cold expansion of holes, particularity in thin specimens. The approach presented in this thesis to analyse hole expansion would be ideal to determine its effectiveness compared to the split sleeve cold expansion process.

An accurate prediction of three-dimensional residual stress field developed from split sleeve cold expansion is only possible using finite element modelling. However, theoretical models which are based on the assumption of axisymmetric hole expansion are a useful design tool to determine reasonable estimates of

residual hoop stress distribution with much less effort. The results reported in this thesis highlight the loading conditions under which residual stresses are expected to redistribute significantly. Based on these results, the existing theoretical models could be developed further to predict the redistributed residual hoop stress distribution.

REFERENCES

1. Gran R, Orazio FD, Paris P, Irwin G and Hertzberg R. Investigation and Analysis Development of Early Life Aircraft Structural Failures. Ohio US: Air Force Flight Dynamics Laboratory, Wright-Patterson Air Force Base; 1971. Available from: www.dtic.mil

2. Champoux R. An overview of hole cold expansion methods. In: Fracture Prevention and Design: International Conference Proceedings (ed: Barnby J) Amsterdam: EMAS; 1986.

3. Fu Y, Ge E, Su H, Xu J and Li R. Cold expansion technology of connection holes in aircraft structures: A review and prospect. Chinese J Aeronaut 2015; 28: 961-973.

4. Maximov J, Duncheva G and Amudjev I. A novel method and tool which enhance the fatigue life of structural components with fastener holes. Eng Failure Anal 2013; 31: 132-143.

5. Process specification 8101J: Cold expansion of holes using the standard split sleeve system and countersink cold expansion. Seattle US: Fatigue Technology Inc; 2014. Available from http://www.fatiguetech.com

6. Backman D. An Experimental and Theoretical Analysis of Cold Working and Riveting in Fibre Metal Laminate Materials. PhD thesis. Michigan US: Michigan State University; 2011.

7. Priest M, Poussard C, Pavier M and Smith D. An assessment of residual-stress measurements around cold-worked holes. Exp Mech 1995; 35: 361-366.

8. Özdemir A and Edwards L. Measurement of the three-dimensional residual stress distribution around split-sleeve cold-expanded holes. J Strain Analysis 1996; 31: 413-421.

9. Stefanescu D. Experimental study of double cold expansion of holes. J Strain Analysis 2003; 38: 339-347.

10. Pina J, Dias A, De Matos P, Moreira P and De Castro P. Residual stress analysis near a cold expanded hole in a textured alclad sheet using X-ray diffraction. Exp Mech 2005; 45: 83-88.

11. Maximov J, Duncheva G, Ganev N and Bakalova T. The benefit from an adequate finite element simulation of the cold hole expansion process. Eng Fail Anal 2009; 16: 503-511.

12. Achard V, Daidie A, Paredes M and Chirol C. Optimization of the Cold Expansion Process for Titanium Holes. Adv Eng Mater 2016.

13. Lapalme M, Hoseini M, Bocher P, Colle AR and Lévesque M. Realistic cold expansion finite element model and experimental validations for aluminium alloys. Exp Mech 2014; 54: 841-855.

14. Nigrelli V and Pasta S. Finite-element simulation of residual stress induced by split-sleeve cold-expansion process of holes. J Mater Process Tech 2008; 205: 290-296.

15. Liu YS, Gou BW, Shao X, Jiang ZF and Yue Z. Effect of Thickness on Residual Stress Fields of Cold Expansion Hole. Adv Mat Res 2010; 97: 601-604.

16. Özdemir A and Hermann R. Effect of expansion technique and plate thickness on near-hole residual stresses and fatigue life of cold expanded holes. J Mater Sci 1999; 34: 1243-1252.

17. Hermann R. Three-dimensional stress distribution around cold expanded holes in aluminium alloys. Eng Fract Mech 1994; 48: 819-835.

18. Stefanescu D, Steuwer A, Owen R, Nadri B, Edwards L, Fitzpatrick M and Withers P. Elastic strains around cracked cold-expanded fastener holes measured using the synchrotron x-ray diffraction technique. J Strain Analysis 2004; 39: 459-469.

19. Lacarac V, Smith D and Pavier M. The effect of cold expansion on fatigue crack growth from open holes at room and high temperature. Int J Fatigue 2001; 23: 161-170.

20. Cloud GL. Measurement of strain fields near coldworked holes. Exp Mech 1980; 20: 9-16.

21. Link R and Sanford R. Residual strains surrounding split-sleeve cold expanded holes in 7075-T651 aluminum. J Aircraft 1990; 27: 599-604.

22. Heller M, Jones R and Williams J. Analysis of cold-expansion for cracked and uncracked fastener holes. Eng Fract Mech 1991; 39: 195-212.

23. Beaver P, Mann JY and Sparrow JG. A grid technique for the measurement of strains close to cold-expanded holes. In: Proceedings of the First International Conference of the Engineering Integrity Society (ed: Tunna J) UK: EMAS, 1986.

24. Ball D and Lowry D. Experimental investigation on the effects of cold expansion of fastener holes. Fatigue Fract Eng Mater Struct 1998; 21: 17-34.

25. Backman D, Liao M, Crichlow L, Yanishevsky M and Patterson E. The use of digital image correlation in a parametric study on the effect of edge distance and thickness on residual strains after hole cold expansion. J Strain Analysis 2008; 43: 781-789.

26. Backman D and Patterson EA. Measuring residual strains in aluminum and fiber metal laminate materials during cold expansion and riveting. In: Society for Experimental Mechanics-11th International Congress and Exhibition on Experimental and Applied Mechanics. Orlando US: SEM; 2008.

27. Poolsuk S and Sharpe W. Measurement of the Elastic-Plastic Boundary Around Coldworked Fastener Holes. J Appl Mech 1978; 45: 515-520.

28. Arora P, Dattaguru B and Hande HS. A method for estimation of the radius of elastic-plastic boundary around cold-worked holes. J Test Eval 1992; 20: 369-375.

29. O'brien E. Beneficial residual stress from the cold expansion of large holes in thick light alloy plate. J Strain Analysis 2000; 35: 261-276.

30. Cirello A and Pasta S. Displacement Measurement Through Digital Image Correlation and Digital Speckle Pattern Interferometry Techniques in Cold-Expanded Holes. Strain 2010; 46: 581-588.

31. Sanford R and Link R. Holographic measurement of the elastic–plastic boundary surrounding cold-expanded holes. J Strain Analysis 1989; 24: 103-106.

32. D'Acquisto L and Pasta S. On the Measurement and Prediction of the Out-of-Plane Displacement Surrounding Cold-Expanded Holes. Exp Mech 2011; 51: 11-22.

33. Cannon D, Sinclair J and Sharpe K. In: Fatigue life: analysis and prediction: Proceedings of the fatigue program and related papers presented at the International Conference and Exposition on Fatigue, Corrosion Cracking, Fracture Mechanics and Failure Analysis (ed: Goel V) OH, US: ASM; 1986.

34. Hermann R and Moffatt J. Experiments and Analysis of the Fatigue Life Improvement in Fastener Holes of Aluminium-Lithium Alloy 2091. In: Aluminium-lithium: Proceedings of the 6th International Aluminium-Lithium Conference (ed: Peter JW) DGM Informationsgesellschaft Verlag; 1992.

35. Özdemir A and Edwards L. Relaxation of residual stresses at cold-worked fastener holes due to fatigue loading. Fatigue Fract Eng Mater Struct 1997; 20: 1443-1451.

36. Özdemir A and Edwards L. Through-thickness residual stress distribution after the cold expansion of fastener holes and its effect on fracturing. J Eng Mater Technol 2004; 126: 129-135.

37. Stefanescu D, Dutta M, Wang D, Edwards L and Fitzpatrick M. The effect of high compressive loading on residual stresses and fatigue crack growth at cold expanded holes. J Strain Analysis 2003; 38: 419-427.

38. Stefanescu D. Measurement and prediction of fatigue crack growth from cold expanded holes Part 1: the effect of fatigue crack growth on cold expansion residual stresses. J Strain Analysis 2004; 39: 25-38.

39. Stefanescu D, Santisteban J, Edwards L and Fitzpatrick M. Residual stress measurement and fatigue crack growth prediction after cold expansion of cracked fastener holes. J Aerospace Eng 2004; 17: 91-97.

40. Su X, Gu M and Yan M. A simplified residual stress model for predicting fatigue crack growth behavior at coldworked fastener holes. Fatigue Fract Eng Mater Struct 1986; 9: 57-64.

41. Chao L and Xiulin Z. Effects of cold expansion of a hole on fatigue crack initiation location and life of an LY12CZ alloy. Fatigue Fract Eng Mater Struct 1992; 15: 241-247.

42. Zhang X and Wang Z. Fatigue life improvement in fatigue-aged fastener holes using the cold expansion technique. Int J Fatigue 2003; 25: 1249-1257.

43. Chakherlou T and Vogwell J. The effect of cold expansion on improving the fatigue life of fastener holes. Eng Fail Anal 2003; 10: 13-24.

44. Yongshou L, Xiaojun S, Jun L and Zhufeng Y. Finite element method and experimental investigation on the residual stress fields and fatigue performance of cold expansion hole. Mater Design 2010; 31: 1208-1215.

45. Yuan X, Yue Z, Wen S, Li L and Feng T. Numerical and experimental investigation of the cold expansion process with split sleeve in titanium alloy TC4. Int J Fatigue 2015; 77: 78-85.

46. Wang Y, Zhu Y, Hou S, Sun H and Zhou Y. Investigation on fatigue performance of cold expansion holes of 6061-T6 aluminum alloy. Int J Fatigue 2017; 95: 216-228.

47. Forgues S, Bernard M and Bui-Quoc T. 3-D axisymmetric numerical analysis and experimental study of the fastener hole coldworking process. In: WIT Transactions on Engineering Sciences (eds: Brebbia CA and Aliabadi M) UK: WIT Press; 1993.

48. Babu NM, Jagadish T, Ramachandra K and Sridhara S. A simplified 3-D finite element simulation of cold expansion of a circular hole to capture through thickness variation of residual stresses. Eng Fail Anal 2008; 15: 339-348.

49. Bernard M, Bui-Quoc T and Burlat M. Effect of re-cold working on fatigue life enhancement of a fastener hole. Fatigue Fract Eng Mater Struct 1995; 18: 765-775.

50. Jang J and Kim D. Re-cold expansion process simulation to impart the residual stresses around fastener holes in 6061 A-T6 aluminium alloy. P I Mech Eng B-J ENG 2008; 222: 1325-1332.

51. Nadai A. Theory of the expanding of boiler and condenser tube joints through rolling. Trans ASME 1943; 65: 865-880.

52. Hsu Y and Forman R. Elastic-plastic analysis of an infinite sheet having a circular hole under pressure. J Appl Mech 1975: 347.

53. Rich D and Impellizzeri L. Fatigue analysis of cold-worked and interference fit fastener holes. In: The symposium on Cyclic Stress-Strain and Plastic Deformation Aspects of Fatigue Crack Growth (ed: Jane B) US: ASTM; 1977.

54. Wang G. An elastic-plastic solution for a normally loaded center hole in a finite circular body. Int J Pressure Vessels Piping 1988; 33: 269-284.

55. Wanlin G. Elastic-plastic analysis of a finite sheet with a cold-worked hole. Eng Fract Mech 1993; 46: 465-472.

56. Ball D. Elastic-plastic stress analysis of cold expanded fastener holes. Fatigue Fract Eng Mater Struct 1995; 18: 47-63.

57. Zhang Y, Fitzpatrick M and Edwards L. Analysis of the Residual Stress around a Cold-expanded Fastener Hole in a Finite Plate. Strain 2005; 41: 59-70.

58. Hill R. The mathematical theory of plasticity. UK: Oxford university press, 1998.

59. Poussard C, Pavier M and Smith D. Analytical and finite element predictions of residual stresses in cold worked fastener holes. J Strain Analysis 1995; 30: 291-304.

60. Pavier M, Poussard C and Smith D. A finite element simulation of the cold working process for fastener holes. J Strain Analysis 1997; 32: 287-300.

61. Papanikos P and Meguid S. Three-dimensional finite element analysis of cold expansion of adjacent holes. Int J Mech Sci 1998; 40: 1019-1028.

62. Kang J, Johnson WS and Clark DA. Three-dimensional finite element analysis of the cold expansion of fastener holes in two aluminum alloys. J Eng Mater-T ASME 2002; 124: 140-145.

63. De Matos P, Moreira P, Camanho P and De Castro P. Numerical simulation of cold working of rivet holes. Finite Elem Anal Des 2005; 41: 989-1007.

64. Karabin M, Barlat F and Schultz R. Numerical and experimental study of the cold expansion process in 7085 plate using a modified split sleeve. J Mater Process Tech 2007; 189: 45-57.

65. Ismonov S, Daniewicz S, Newman J, Hill M and Urban M. Three dimensional finite element analysis of a split-sleeve cold expansion process. J Eng Mater-T ASME 2009; 131: 031007.

66. Farhangdoost K and Hosseini A. The effect of mandrel speed upon the residual stress distribution around cold expanded hole. Procedia Engineering 2011; 10: 2184-2189.

67. Houghton S and Campbell S. Identifying the residual stress field developed by hole cold expansion using finite element analysis. Fatigue Fract Eng Mater Struct 2012; 35: 74-83.

68. Petrak G and Stewart R. Retardation of cracks emanating from fastener holes. Eng Fract Mech 1974; 6: 275-282.

69. Beaver P, Mann J and Sparrow J. Fatigue Life Enhancement by the Cold-Expansion of Holes - Research and Case Study. In: Fatigue life: analysis and prediction : Proceedings of the fatigue program and related papers presented at the International Conference and Exposition on Fatigue, Corrosion Cracking, Fracture Mechanics and Failure Analysis (ed: Goel V) OH, USA: ASM; 1986.

70. Pell RA, Beaver PW, Mann JY and Sparrow JG. Fatigue of thick-section cold expanded holes with and without cracks. Fatigue Fract Eng Mater Struct 1989; 12: 553-567.

71. Grandt AF. Stress intensity factors for some through-cracked fastener holes. Int J Fracture 1975; 11: 283-294.

72. Chandawanich N and Sharpe WN. An experimental study of fatigue crack initiation and growth from coldworked holes. Eng Fract Mech 1979; 11: 609-620.

73. Cathey W and Grandt A. Fracture mechanics consideration of residual stresses introduced by coldworking fastener holes. J Eng Mater-T ASME 1980; 102: 85-91.

74. Clark G. Modelling residual stresses and fatigue crack growth at cold-expanded fastener holes. Fatigue Fract Eng Mater Struct 1991; 14: 579-589.

75. Toparli M, Özel A and Aksoy T. Effect of the residual stresses on the fatigue crack growth behavior at fastener holes. Mater Sci Eng A 1997; 225: 196-203.

76. Pavier M, Poussard C and Smith D. Effect of residual stress around cold worked holes on fracture under superimposed mechanical load. Eng Fract Mech 1999; 63: 751-773.

77. Stefanescu D. Measurement and prediction of fatigue crack growth from cold expanded holes Part 2: Prediction of fatigue crack growth from cold expanded holes. J Strain Analysis 2004; 39: 41-52.

78. Paris P and Erdogan F. A critical analysis of crack propagation laws. J Basic Eng-T ASME 1963; 85(4): 528-533.

79. Bueckner H. Novel principle for the computation of stress intensity factors. ZAMM-Z ANGEW MATH ME 1970; 50: 529-548.

80. Rice JR. Some remarks on elastic crack-tip stress fields. Int J Solids Struct 1972; 8: 751-758.

81. Liu Y, Gou B, He J and Yue Z. Effect of Cold Expansion on Crack Opening Displacement and Stress Intensity Factor. Key Eng Mat 2010; 417: 477-480.

82. Semari Z, Aid A, Benhamena A, Amrouche A, Benguediab M, Sadok A and Benseddiq N. Effect of residual stresses induced by cold expansion on the crack growth in 6082 aluminum alloy. Eng Fract Mech 2013; 99: 159-168.

83. Pavier M, Poussard C and Smith D. Finite element modelling of the interaction of residual stress with mechanical load for a crack emanating from a cold worked fastener hole. J Strain Analysis 1998; 33: 275-289.

84. Fitzpatrick M and Edwards L. Fatigue crack/residual stress field interactions and their implications for damage-tolerant design. J Mater Eng Perform 1998; 7: 190-198.

85. Lacarac V, Smith D, Pavier M and Priest M. Fatigue crack growth from plain and cold expanded holes in aluminium alloys. Int J Fatigue 2000; 22: 189-203.

86. JSSG-2006 Department of Defense Joint Service Specification Guide: Aircraft Structures. US Department of Defense; 1998.

87. McClung R. A literature survey on the stability and significance of residual stresses during fatigue. Fatigue Fract Eng Mater Struct 2007; 30: 173-205.

88. Maximov JT, Duncheva GV and Mitev IN. Modelling of residual stress relaxation around cold expanded holes in carbon steel. J Constr Steel Res 2009; 65: 909-917.

89. Chakherlou T and Yaghoobi A. Numerical simulation of residual stress relaxation around a cold-expanded fastener hole under longitudinal cyclic loading using different kinematic hardening models. Fatigue Fract Eng Mater Struct 2010; 33: 740-751.

90. Chakherlou T and Ajri M. Strain ratcheting and stress relaxation around interference-fitted single-holed plates under cyclic loading: experimental and numerical investigations. Fatigue Fract Eng Mater Struct 2013; 36: 327-339.

91. Boni L, Fanteria D, Lanciotti A and Polese C. Experimental and analytical assessment of fatigue and crack propagation in cold worked open hole specimens. Fatigue Fract Eng Mater Struct 2013; 36: 930-941.

92. Backman D, Cowal C and Patterson E. Analysis of the effects of cold expansion of holes using thermoelasticity and image correlation. Fatigue Fract Eng Mater Struct 2010; 33: 859-870.

93. Olden E and Patterson E. A rational decision making model for experimental mechanics. Exp Tech 2000; 24: 26-32.

94. Sutton MA, Orteu JJ and Schreier H. Image correlation for shape, motion and deformation measurements: basic concepts, theory and applications. US: Springer Verlag US; 2009.

95. Sutton M, Wolters W, Peters W, Ranson W and McNeill S. Determination of displacements using an improved digital correlation method. Image Vision Comput 1983; 1: 133-139.

96. Sutton M, McNeill S, Helm J and Chao Y. Advances in two-dimensional and three-dimensional computer vision. Photomechanics (Topics in Applied Physics) 2000: 323-372.

97. Sutton MA. Digital image correlation for shape and deformation measurements. In: Springer handbook of experimental solid mechanics. (ed: William S) US: Springer Verlag US; 2008., p.565.

98. Thomson W. XV. On the Dynamical Theory of Heat, with numerical results deduced from Mr Joule's Equivalent of a Thermal Unit, and M. Regnault's Observations on Steam. Earth Env Sci T R So 1853; 20: 261-288.

99. Pitarresi G and Patterson E. A review of the general theory of thermoelastic stress analysis. J Strain Analysis 2003; 38: 405-417.

100. Greene RJ, Patterson EA and Rowlands RE. Thermoelastic stress analysis. In: Springer handbook of experimental solid mechanics (ed: William S) US: Springer Verlag US; 2008.

101. Robinson A, Dulieu-Barton J, Quinn S and Burguete R. Paint coating characterization for thermoelastic stress analysis of metallic materials. Meas Sci Technol 2010; 21: 085502.

102. Tomlinson RA, Du Y and Patterson EA. Understanding crack tip plasticity–a multi-experimental approach. Applied Mechanics and Materials 2011; 70: 153-158.

103. Diaz F, Patterson E, Tomlinson R and Yates J. Measuring stress intensity factors during fatigue crack growth using thermoelasticity. Fatigue Fract Eng Mater Struct 2004; 27: 571-583.

104. Tomlinson R and Olden E. Thermoelasticity for the analysis of crack tip stress fields—a review. Strain 1999; 35: 49-55.

105. Tomlinson R, Nurse A and Patterson E. On determining stress intensity factors for mixed mode cracks from thermoelastic data. Fatigue Fract Eng Mater Struct 1997; 20: 217-226.

106. Muskhelishvili NI. Some basic problems of the mathematical theory of elasticity. Netherlands: Springer Netherlands, 1977.

107. Tomlinson RA and Marsavina L. Thermoelastic investigations for fatigue life assessment. Exp Mech 2004; 44: 487-494.

108. Patki A and Patterson E. Thermoelastic stress analysis of fatigue cracks subject to overloads. Fatigue Fract Eng Mater Struct 2010; 33: 809-821.

109. Noyan IC and Cohen JB. Residual stress: measurement by diffraction and interpretation. NY: Springer; 2013.

110. Fitzpatrick ME and Lodini A. Analysis of residual stress by diffraction using neutron and synchrotron radiation. London: Taylor and Francis, 2003.

111. Webster P, Oosterkamp LD, Browne P, Hughes D, Kang W, Withers P and Vaughan GM. Synchrotron X-ray residual strain scanning of a friction stir weld. J Strain Analysis 2001; 36: 61-70.

112. Owen R, Preston R, Withers P, Shercliff H and Webster P. Neutron and synchrotron measurements of residual strain in TIG welded aluminium alloy 2024. Mater Sci Eng A 2003; 346: 159-167.

113. James M, Hattingh D, Hughes D, WEI L, Patterson E and Da Fonseca JQ. Synchrotron diffraction investigation of the distribution and influence of residual stresses in fatigue. Fatigue Fract Eng Mater Struct 2004; 27: 609-622.

114. Ganguly S, Fitzpatrick M and Edwards L. Use of neutron and synchrotron X-ray diffraction for evaluation of residual stresses in a 2024-T351 aluminum alloy variable-polarity plasma-arc weld. Metall Mater Trans A 2006; 37: 411-420.

115. Preston R, Shercliff H, Withers P, Hughes D, Smith S and Webster P. Synchrotron X-ray measurement and finite element analysis of residual strain in tungsten inert gas welded aluminum alloy 2024. Metall Mater Trans A 2006; 37: 3629-3637.

116. Khan M, Fitzpatrick M, Hainsworth S, Evans A and Edwards L. Application of synchrotron X-ray diffraction and nanoindentation for the determination of residual stress fields around scratches. Acta Mater 2011; 59: 7508-7520.

117. Asquith D, Yerokhin A, James N, Yates J and Matthews A. Evaluation of residual stress development at the interface of plasma electrolytically oxidized and cold-worked aluminum. Metall Mater Trans A 2013; 44: 4461-4465.

118. Bragg WH and Bragg WL. The reflection of X-rays by crystals. Proceedings of the Royal Society of London.Series A, Containing Papers of a Mathematical and Physical Character 1913; 88: 428-438.

119. Hughes D, James M, Hattingh D and Webster P. The use of combs for evaluation of strain-free references for residual strain measurements by neutron and synchrotron X-ray diffraction. J Neutron Res 2003; 11: 289-293.

120. Heinz A, Haszler A, Keidel C, Moldenhauer S, Benedictus R and Miller W. Recent development in aluminium alloys for aerospace applications. Mater Sci Eng A 2000; 280: 102-107.

121. Davis JR. Metals handbook. US: ASM international, 1998.

122. Handbook-MIL-HDBK-5H. Metallic Materials and Elements for Aerospace Vehicle Structures.US Department of Defence, 1998.

123. ASTM E8/E8M. Standard test methods for tension testing of metallic materials.PA, US: ASTM International; 2011. Available from: http://www.astm.org

124. ASTM Standard E111-04. Standard test method for Young's modulus, tangent modulus, and chord modulus. PA, US: ASTM International; 2004. Available from: http://www.astm.org

125. ASTM Standard E646-07. Standard test method for tensile strain-hardening exponents (n-values) of metallic sheet materials. PA, US: ASTM International; 2007. Available from: http://www.astm.org

126. Ramberg W and Osgood W R. Description of stress-strain curves by three parameters. US: US National Advisory Committee for Aeronautics; 1943.

127. ASTM standard E407. Standard Practice for Microetching Metals and Alloys. PA, US: ASTM International; 2015. Available from: http://www.astm.org

128. ASTM E112-13. Standard Test Methods for Determining Average Grain Size. PA, US: ASTM International; 2013. Available from: http://www.astm.org

129. ISTRA 4D 2.4.0. Software manual Q-400 system. Germany: Dantec Dynamics GmbH; 2012. Available from: http://www.dantecdynamics.com

130. Siebert T, Becker T, Spiltthof K, Neumann I and Krupka R. Error estimations in digital image correlation technique. Adv Appl Mech 2007; 7: 265-270.

131. Clausen B, Lorentzen T and Leffers T. Self-consistent modelling of the plastic deformation of fcc polycrystals and its implications for diffraction measurements of internal stresses. Acta Mater 1998; 46: 3087-3098.

132. Lane C, Burguete RL and Shterenlikht A. An objective criterion for the selection of an optimum DIC pattern and subset size. In: Proceedings of the XIth International Congress and Exposition. Orlando, FL: SEM; 2008.

133. Serra J. Image analysis and mathematical morphology, Volume 1. US: Academic press Inc; 1982.

134. Pan B, Lu Z and Xie H. Mean intensity gradient: an effective global parameter for quality assessment of the speckle patterns used in digital image correlation. Opt Laser Eng 2010; 48: 469-477.

135. Pan B, Xie H, Guo Z and Hua T. Full-field strain measurement using a two-dimensional Savitzky-Golay digital differentiator in digital image correlation. Opt Eng 2007; 46: 033601-033601-10.

136. Pan B, Asundi A, Xie H and Gao J. Digital image correlation using iterative least squares and pointwise least squares for displacement field and strain field measurements. Opt Laser Eng 2009; 47: 865-874.

137. Moulart R, Pierron F, Hallett SR and Wisnom MR. Full-field strain measurement and identification of composites moduli at high strain rate with the virtual fields method. Exp Mech 2011; 51: 509-536.

138. Reu P. All about speckles: aliasing. Exp Techniques 2014; 38: 1-3.

139. Boresi AP, Schmidt RJ and Sidebottom OM. Advanced mechanics of materials. NY: Wiley NY; 1993.

140. Mann J, Sparrow J and Beaver P. Fatigue characteristics of joints with holes cold-expanded in a multi-layer stack. Int J Fatigue 1989; 11: 214-220.

141. Finney J and Evans R. Extending the fatigue life of multi-layer metal joints. Fatigue Fract Eng Mater Struct 1995; 18: 1231-1247.

142. Boni L, Lanciotti A and Polese C. Some contraindications of hole expansion in riveted joints. Eng Fail Anal 2014; 46: 140-156.

143. Connolly KB. . Cold Working Holes in Multi-Layer Members. PhD thesis. Virginia US: Virginia Polytechnic Institute and State University; 2014.

144. Yang Y, Crimp M, Tomlinson R and Patterson E. Quantitative measurement of plastic strain field at a fatigue crack tip. Proc. R. Soc. A 2012; 468: 2399-2415.

145. JCGM 100: 2008. Evaluation of measurement data - Guide to the expression of uncertainty in measurement. Bureau International des Poids et Mesures, France; 2008. Available from: http://www.bipm.org

146. Jones KW and Bush RW. Investigation of residual stress relaxation in cold expanded holes by the slitting method. Eng Fract Mech 2017; 179: 213-224.

APPENDIX A Crack tip plastic zones

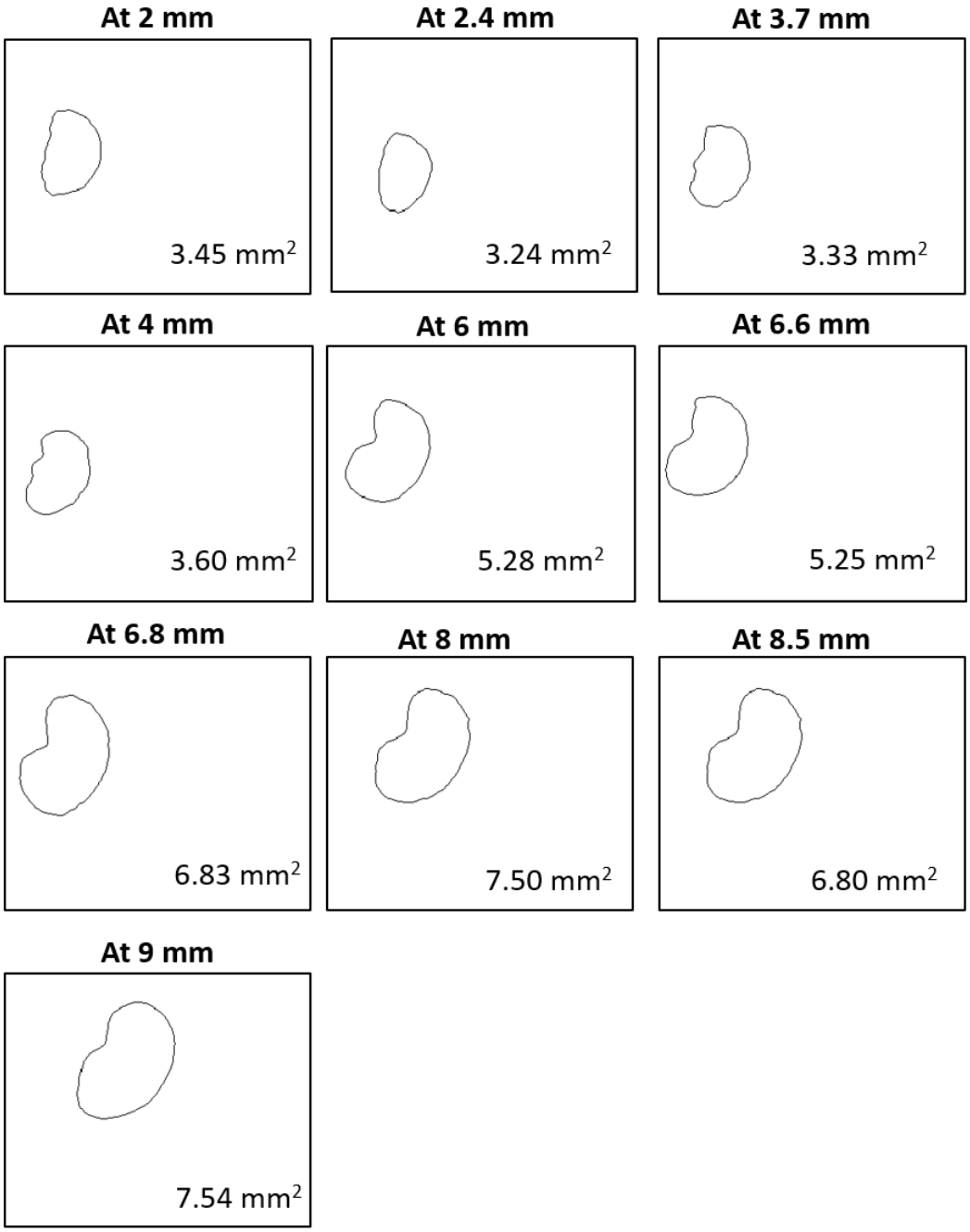

Figure A.1 Evolution of crack tip plastic zone for a crack which initiated at right edge of the hole on the front face of the un-expanded specimen, U3. The rectangular maps represent a sensor size of 320×256 pixels. The spatial resolution is 0.03 mm/pixel.

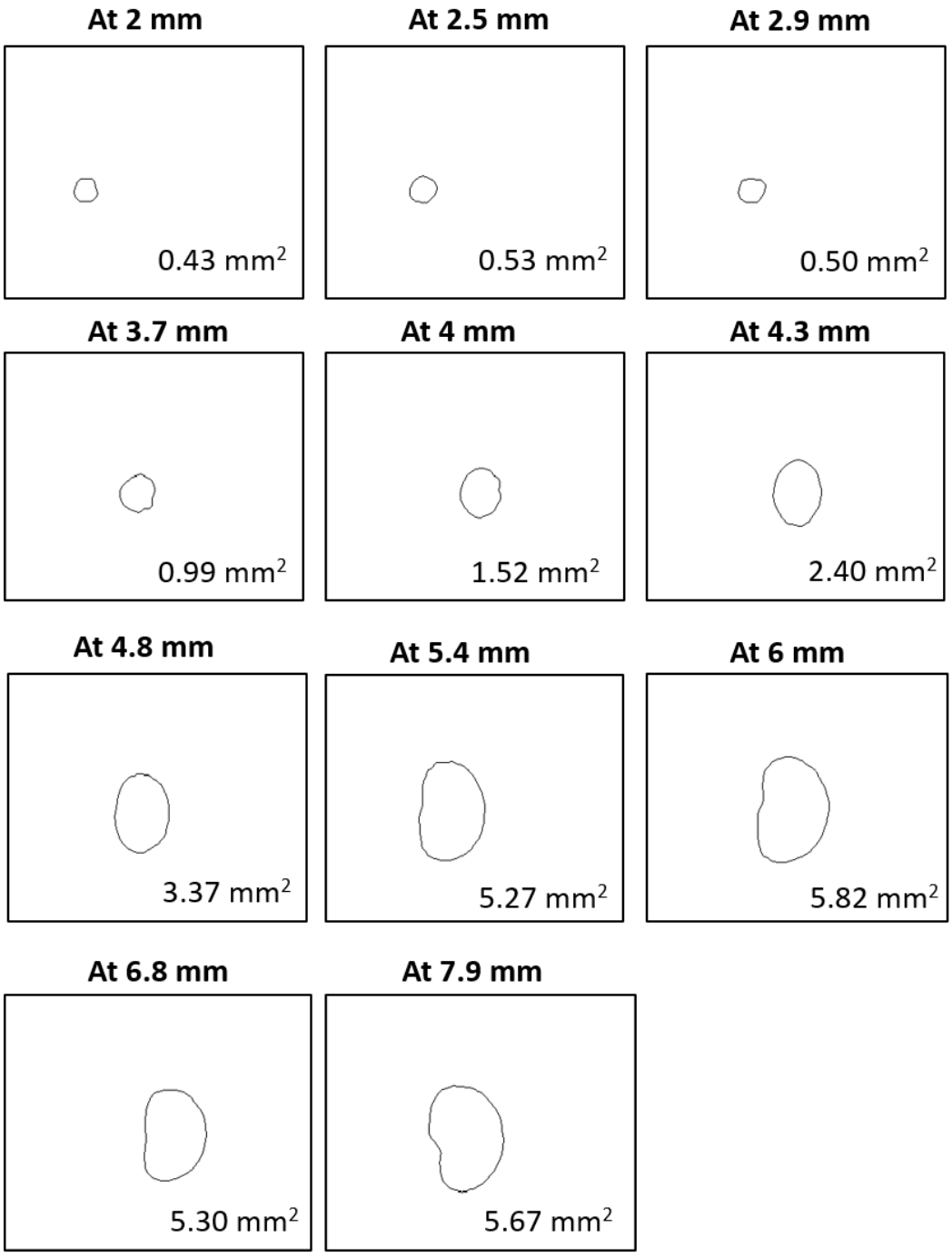

Figure A.2 Evolution of crack tip plastic zone for a crack which initiated at the right edge of the hole on the mandrel entry face of the cold-expanded specimen, C6 to which no initial compressive stress cycle was applied. The rectangular maps represent a sensor size of 320×256 pixels. The spatial resolution is 0.03 mm/pixel.

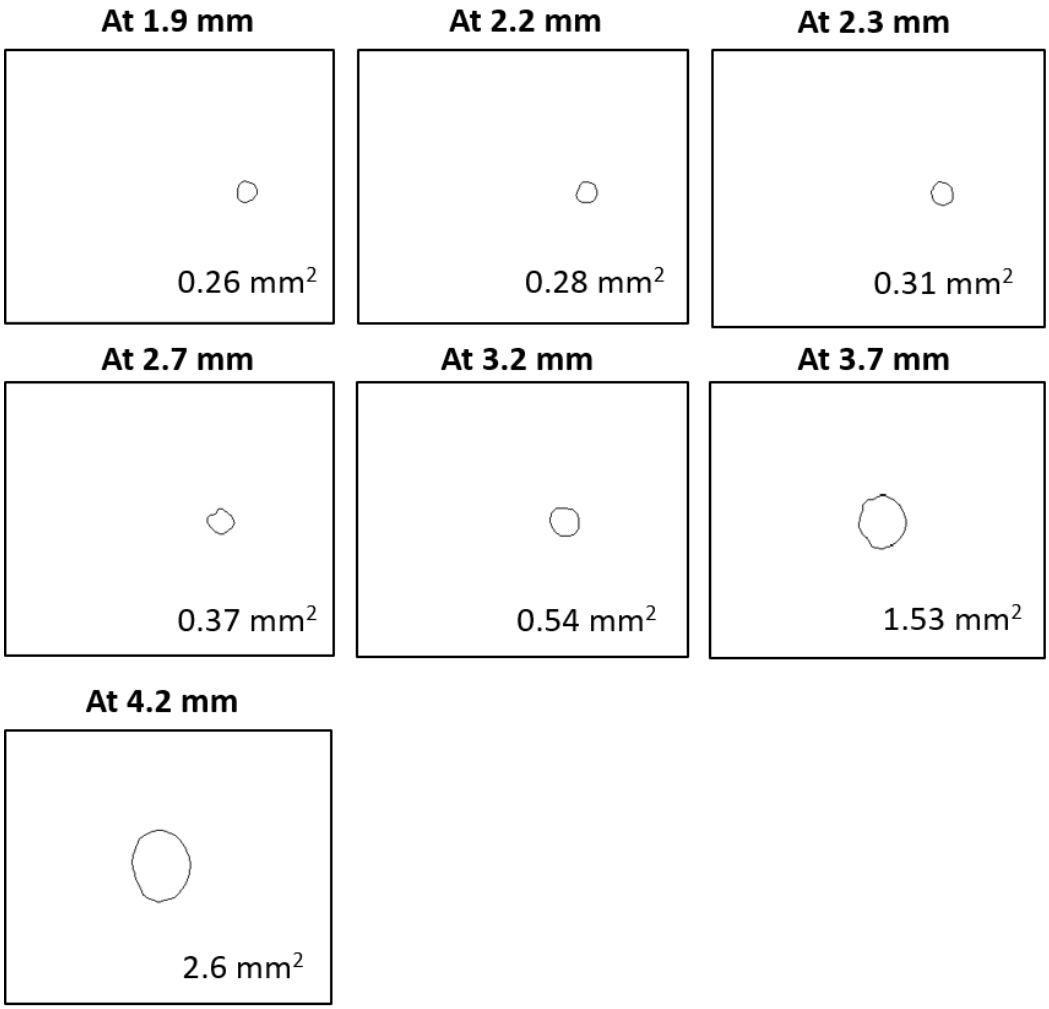

Figure A.3 Evolution of crack tip plastic zone for a crack which initiated from the left edge of the hole on the mandrel entry face of the cold-expanded specimen, C6 to which no initial compressive stress cycle was applied. The rectangular maps represent a sensor size of 320×256 pixels. The spatial resolution is 0.03 mm/pixel.

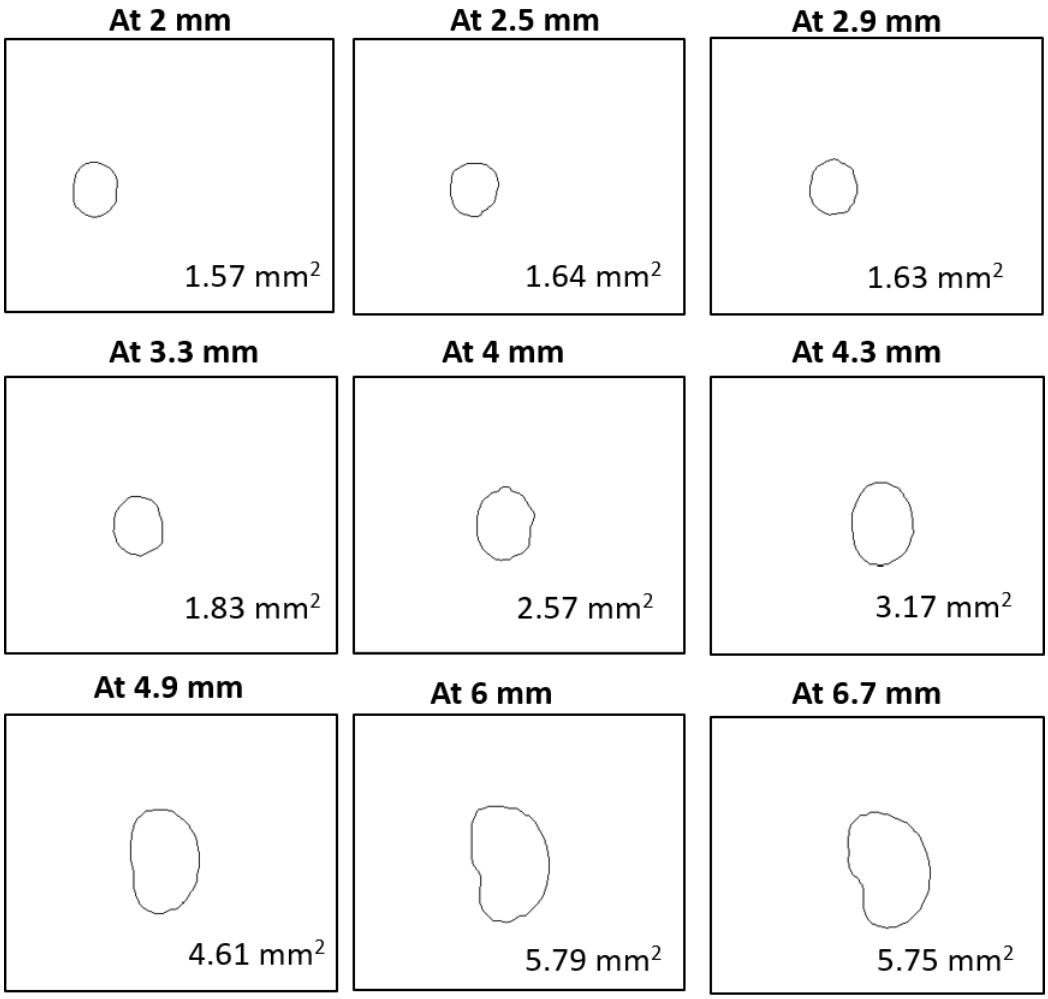

Figure A.4 Evolution of crack tip plastic zone for a crack which initiated at the right edge of the hole on the mandrel entry face of the cold-expanded specimen, C10 to which a single compressive stress cycle of -92.7 MPa was applied prior to fatigue loading. The rectangular maps represent a sensor size of 320×256 pixels. The spatial resolution is 0.03 mm/pixel.

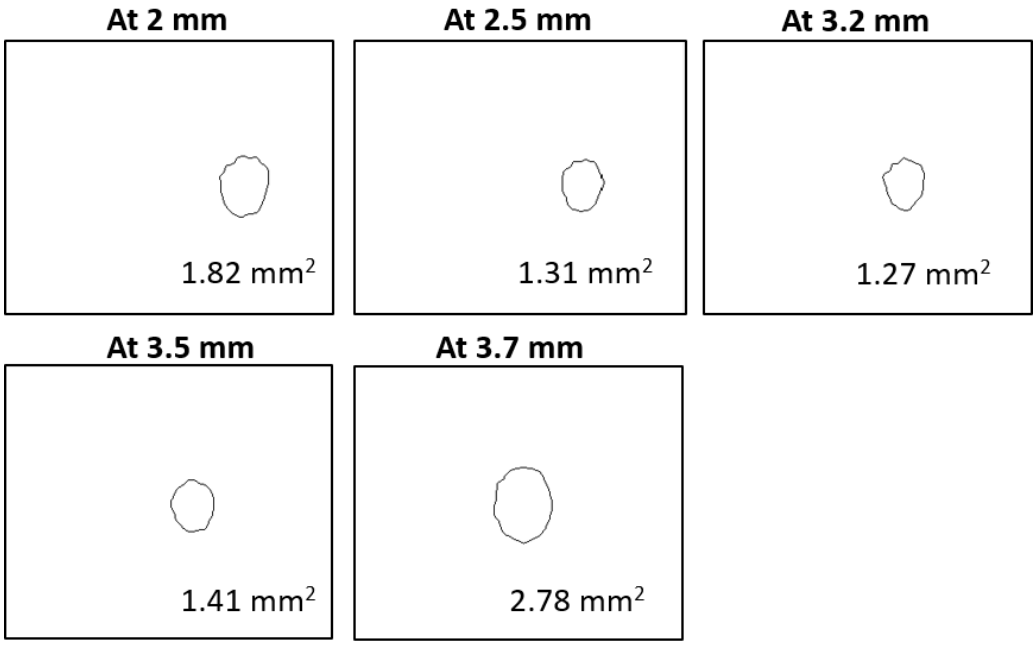

Figure A.5 Evolution of crack tip plastic zone for a crack which initiated at the left edge of the hole on the mandrel entry face of the cold-expanded specimen, C10 to which a single compressive stress cycle of -92 MPa was applied prior to fatigue loading. The rectangular maps represent a sensor size of 320×256 pixels. The spatial resolution is 0.03 mm/pixel.

APPENDIX B Fractographs

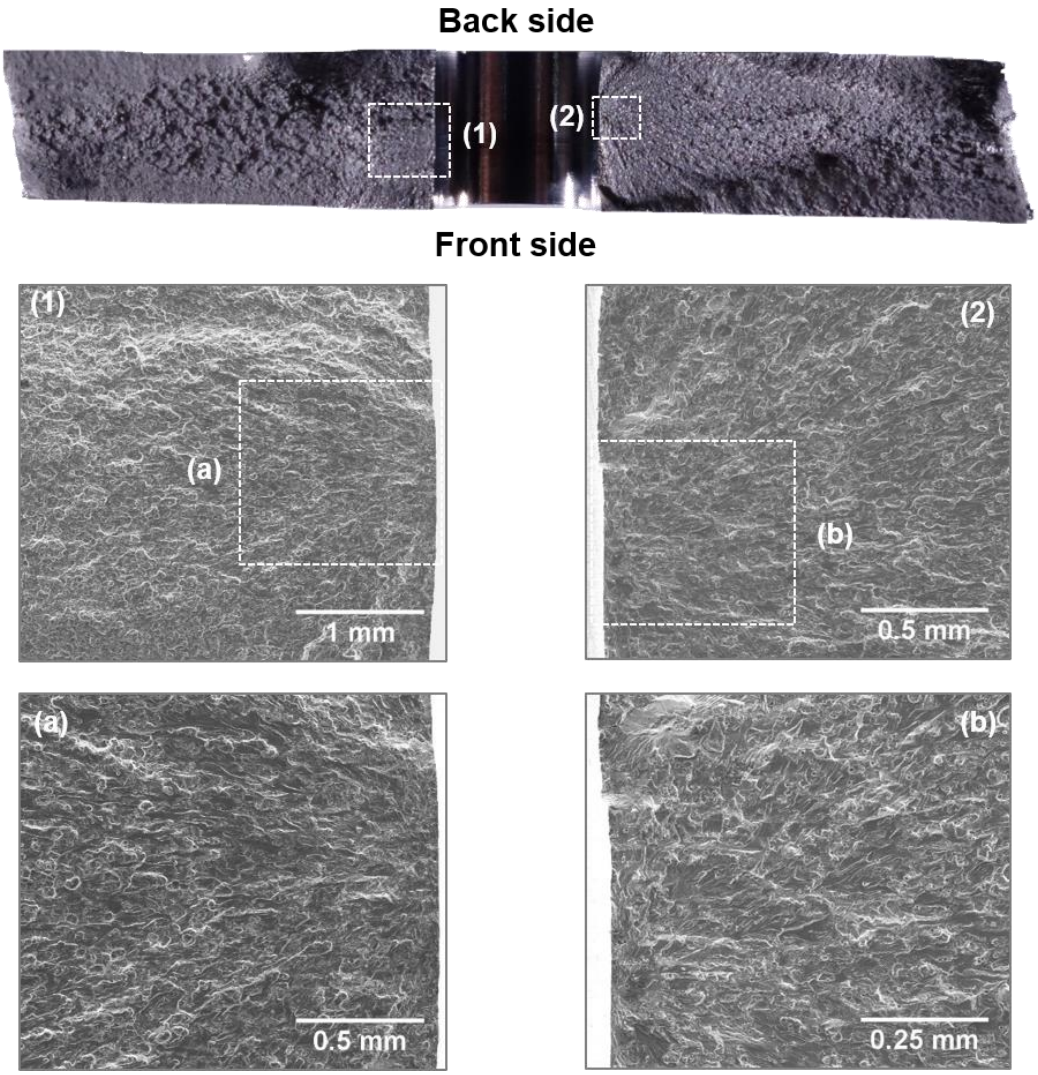

Figure B.1 Fracture surface morphology of the un-expanded specimen, U3. The optical micrograph on top shows the whole fracture surface. SEM images on the left and the right show the origin of fatigue cracks initiating from left and right edges of the hole, respectively. The fatigue crack initiated on the left, did not approach any of the specimen faces and remained sub-surface until specimen failure.

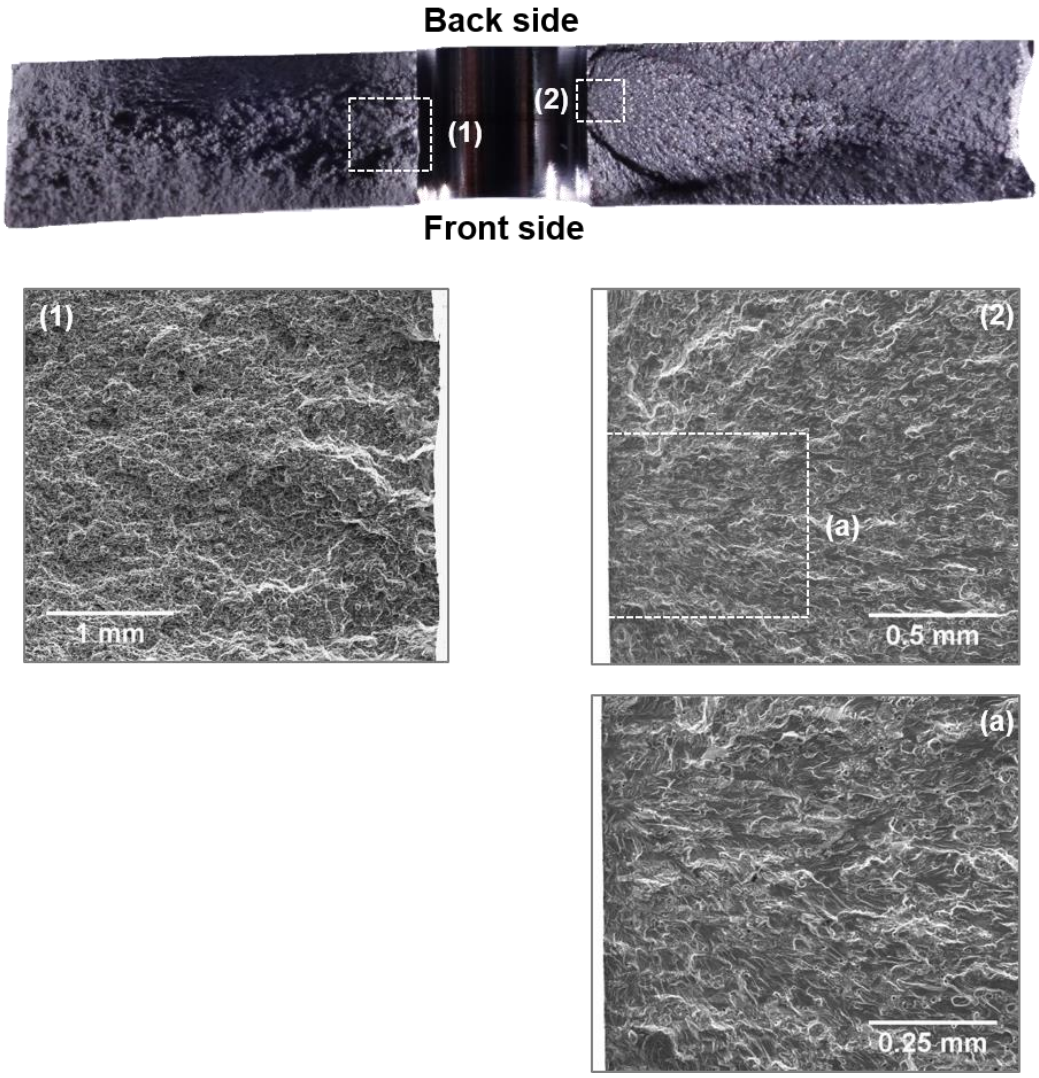

Figure B.2 Fracture surface morphology of the un-expanded specimen, U4. The optical micrograph on top shows the whole fracture surface. SEM images on the right show the origin of fatigue crack initiating from right edge of the hole. Image (a) shows the zoomed-in view of the crack initiation site in Image 2. SEM image on the left highlights the typical morphology which results from fast fracture.

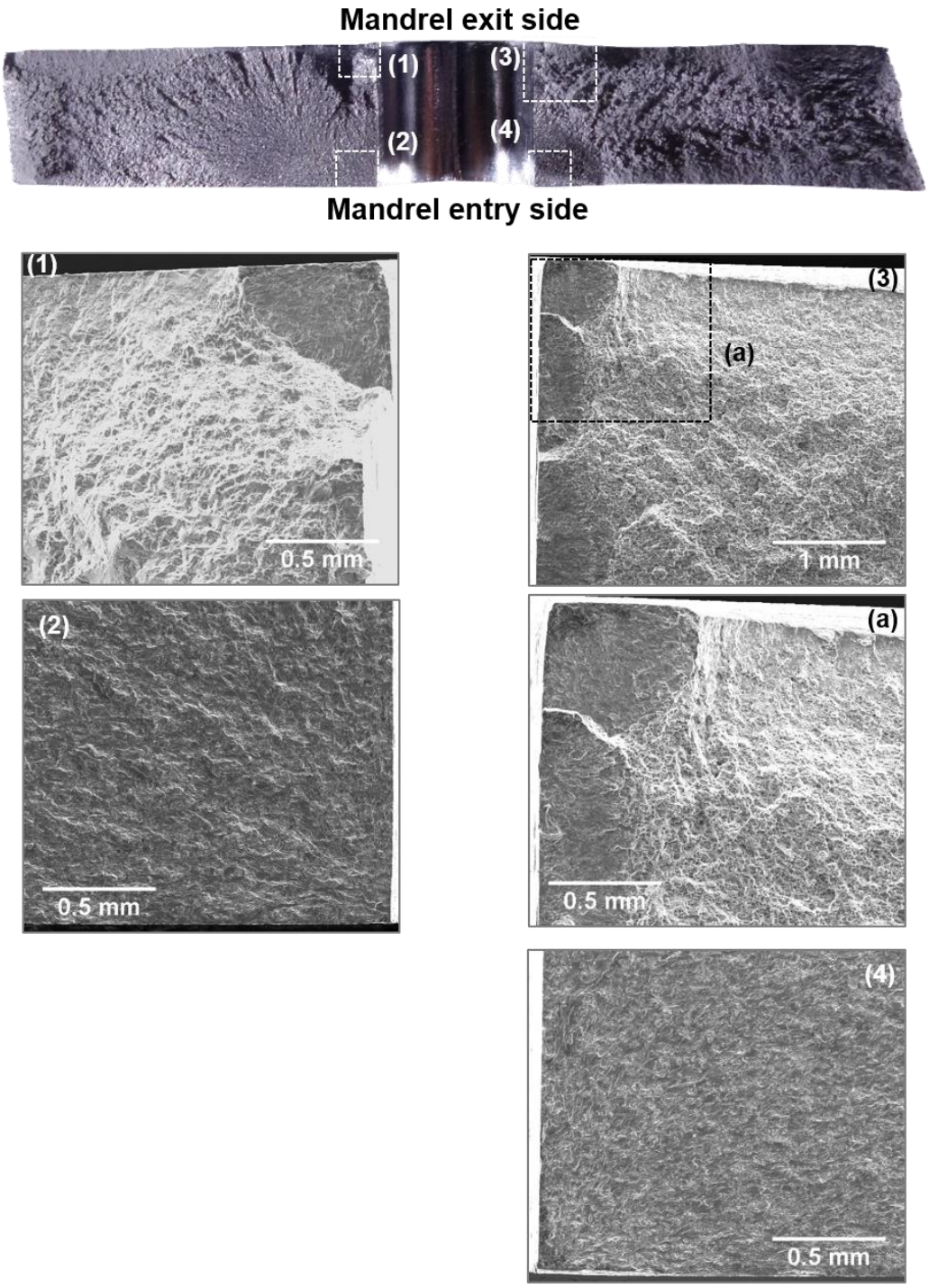

Figure B.3 Fracture surface morphology of the cold-expanded specimen, C4 with unmodified residual stress distribution. The optical micrograph on top shows the whole fracture surface. SEM images 1 and 3 show the origin of secondary fatigue cracks initiating from left and right corners on the mandrel exit side, respectively. Image (a) shows the zoomed-in view of the two crack initiation sites in Image 3. SEM images 2 and 4 show the origin of primary fatigue cracks initiating from left and right corners on the mandrel entry side, respectively.

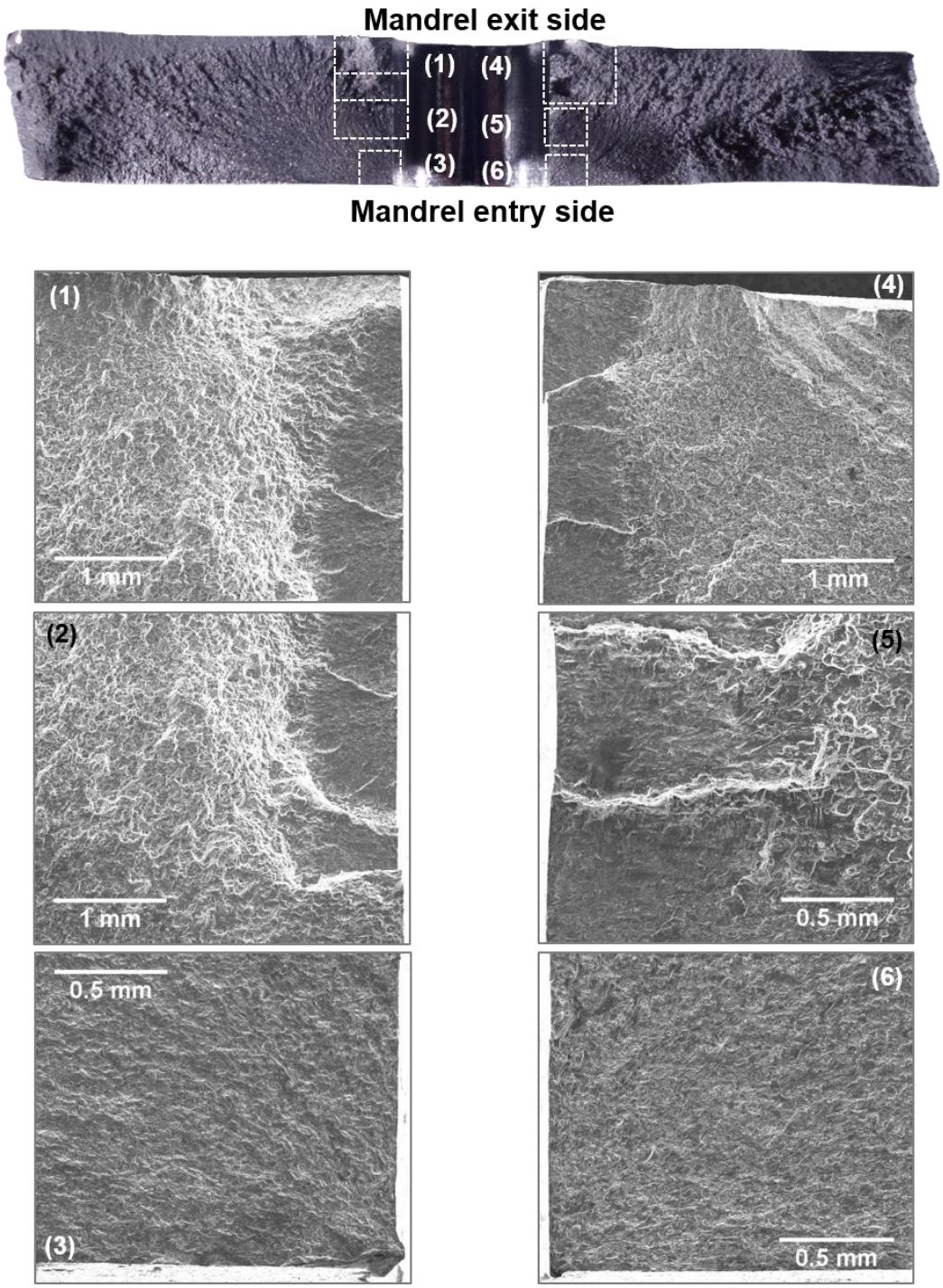

Figure B.4 Fracture surface morphology of the cold-expanded specimen, C5 with unmodified residual stress distribution. The optical micrograph on top shows the whole fracture surface. SEM images 1 & 2 and 4 & 5 show multiple secondary crack initiation sites along the left and right hole edges, respectively. SEM images 3 and 6 show the origin of primary fatigue cracks initiating from left and right corners on the mandrel entry side, respectively.

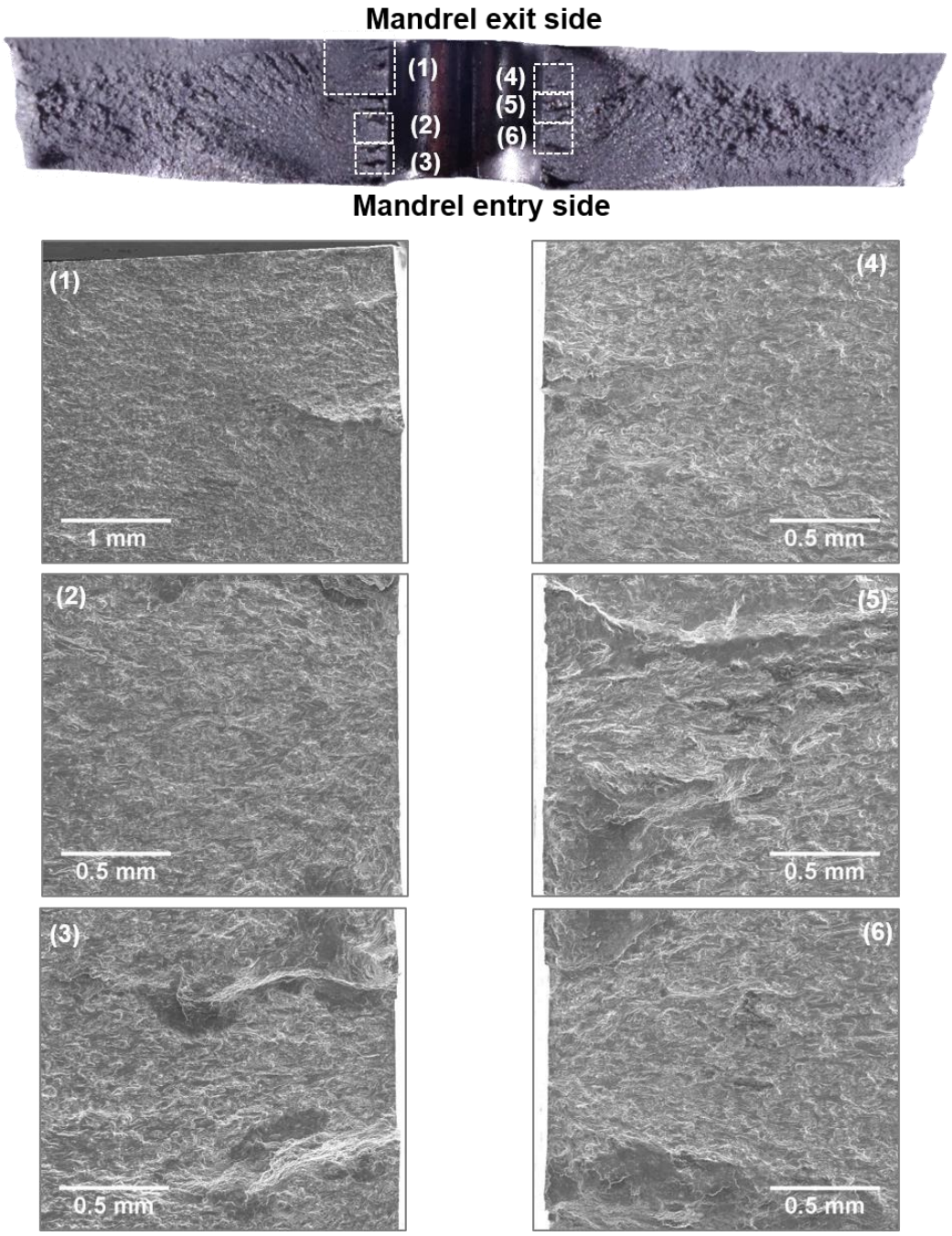

Figure B.5 Fracture surface morphology of the cold-expanded specimen, C11 with modified residual stress distribution after a single compressive stress cycle of -125 MPa was applied prior to fatigue loading. The optical micrograph on top shows the whole fracture surface. SEM images on the left and right highlight multiple crack initiation sites along the left and right edges of the hole, respectively.

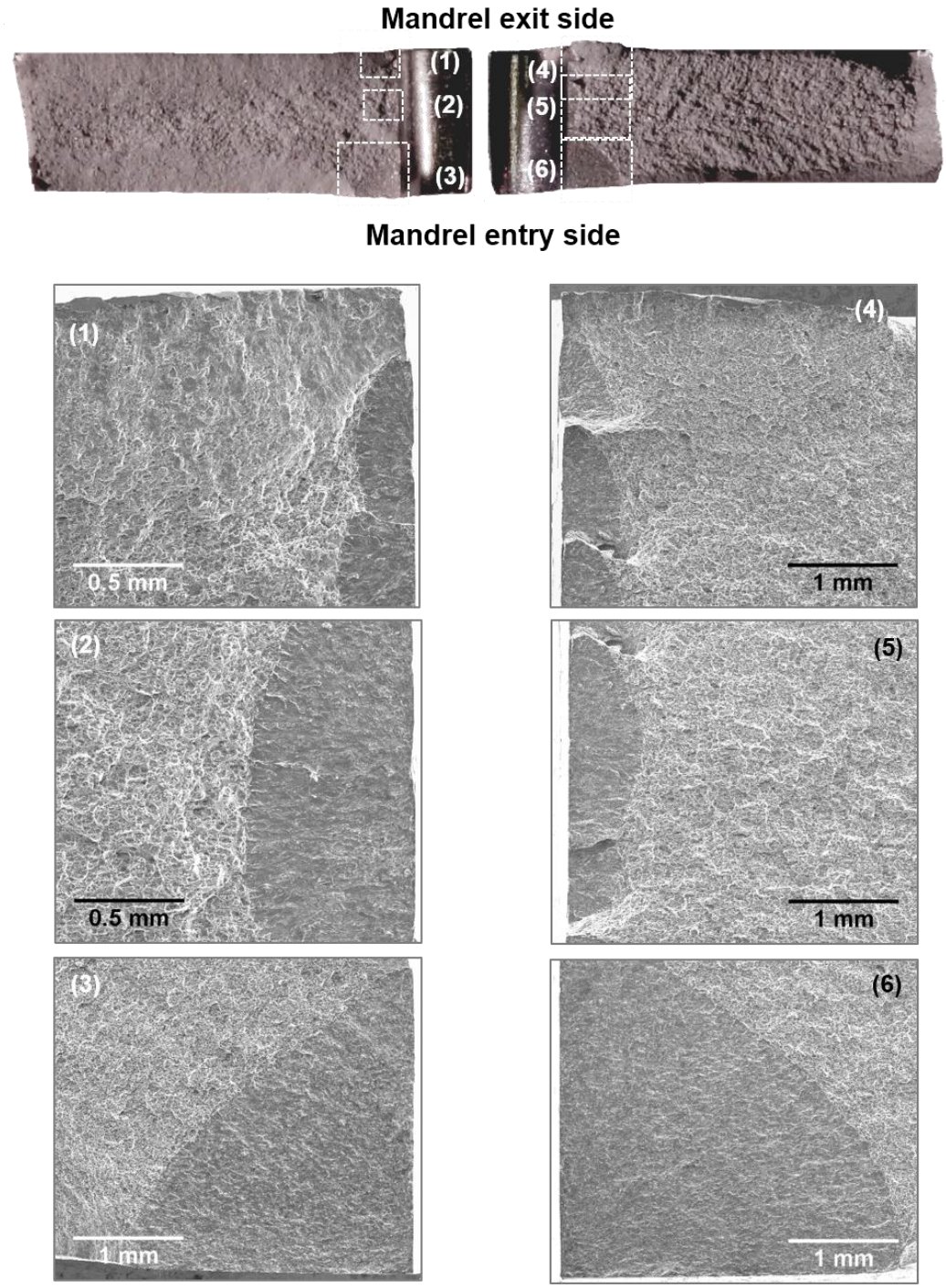

Figure B.6 Fracture surface morphology of the cold-expanded specimen, C8 which was failed by applying a tensile overload after 150k cycles of fatigue loading. The optical micrograph on top shows the whole fracture surface. SEM images 1 & 2 and 4 & 5 show multiple secondary crack initiation sites along the left and right hole edges, respectively. SEM images 3 and 6 show the origin of primary fatigue cracks initiating from left and right corners on the mandrel entry side, respectively.

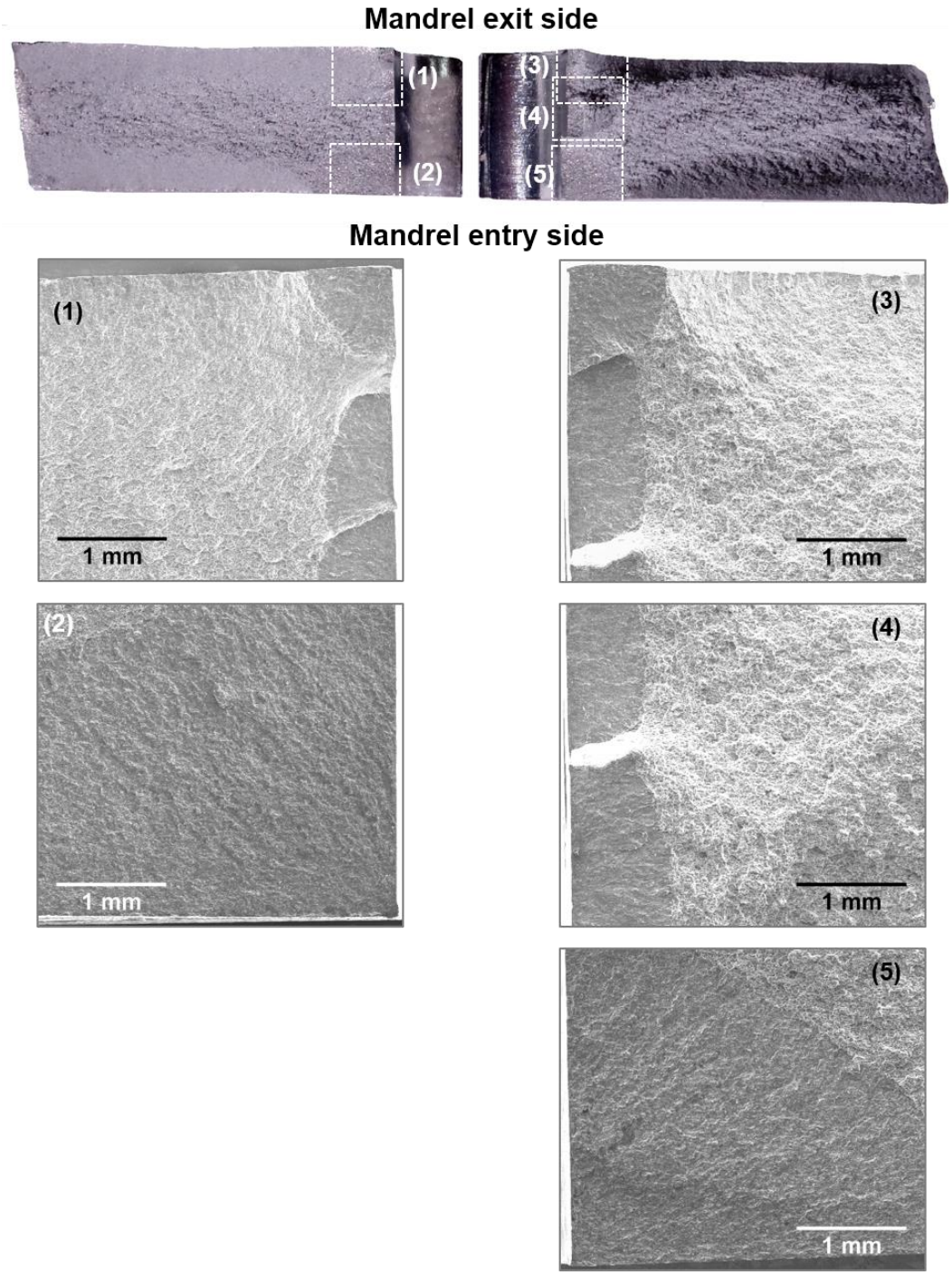

Figure B.7 Fracture surface morphology of the cold-expanded specimen, C9 which was failed by applying a tensile overload after 400k cycles of fatigue loading. The optical micrograph on top shows the whole fracture surface. SEM images 1 and 4 & 5 show multiple secondary crack initiation sites along the left and right hole edges, respectively. SEM images 2 and 6 show the origin of primary fatigue cracks initiating from left and right corners on the mandrel entry side, respectively.

APPENDIX C Residual elastic stress plots

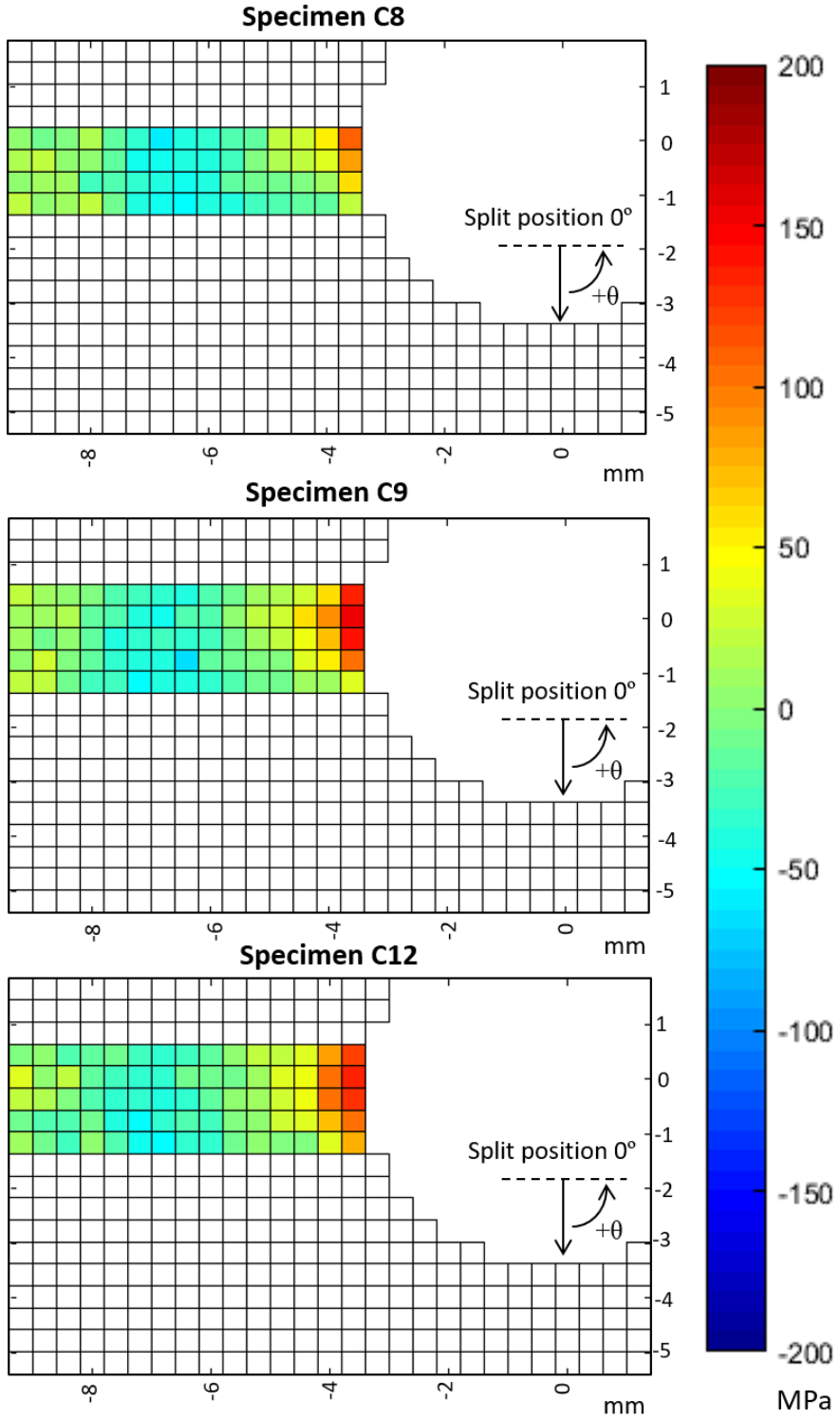

Figure C.1 Maps of X component of residual stresses close to the mandrel entry face for cold-expanded specimens, C8 with a 2.1mm crack (top), C9 with a 3.8 mm crack (middle) and C12 to which no loads were applied (bottom).

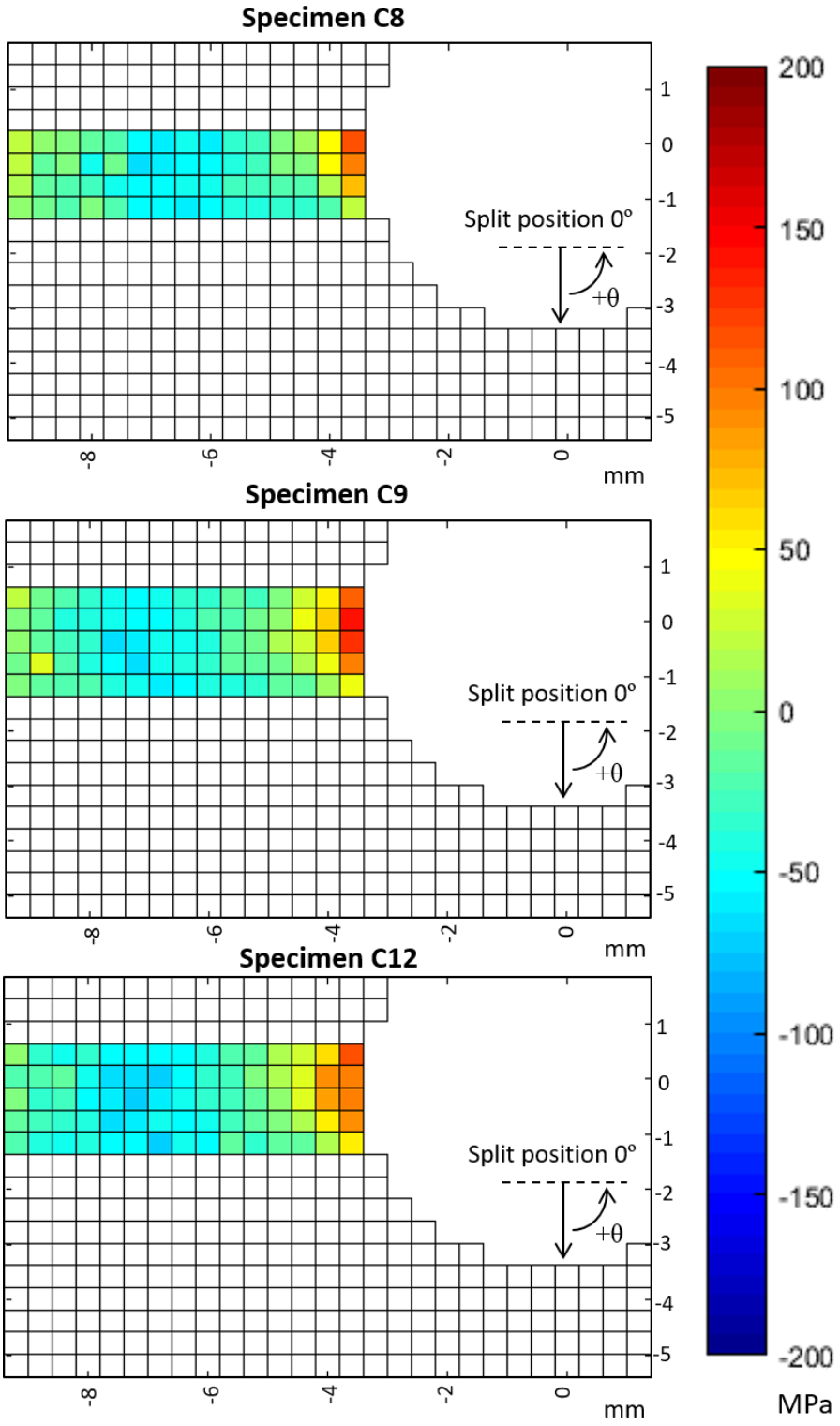

Figure C.2 Maps of X component of residual stresses close to the mandrel exit face for cold-expanded specimens, C8 with a 2.1mm crack (top), C9 with a 3.8 mm crack (middle) and C12 to which no loads were applied (bottom).

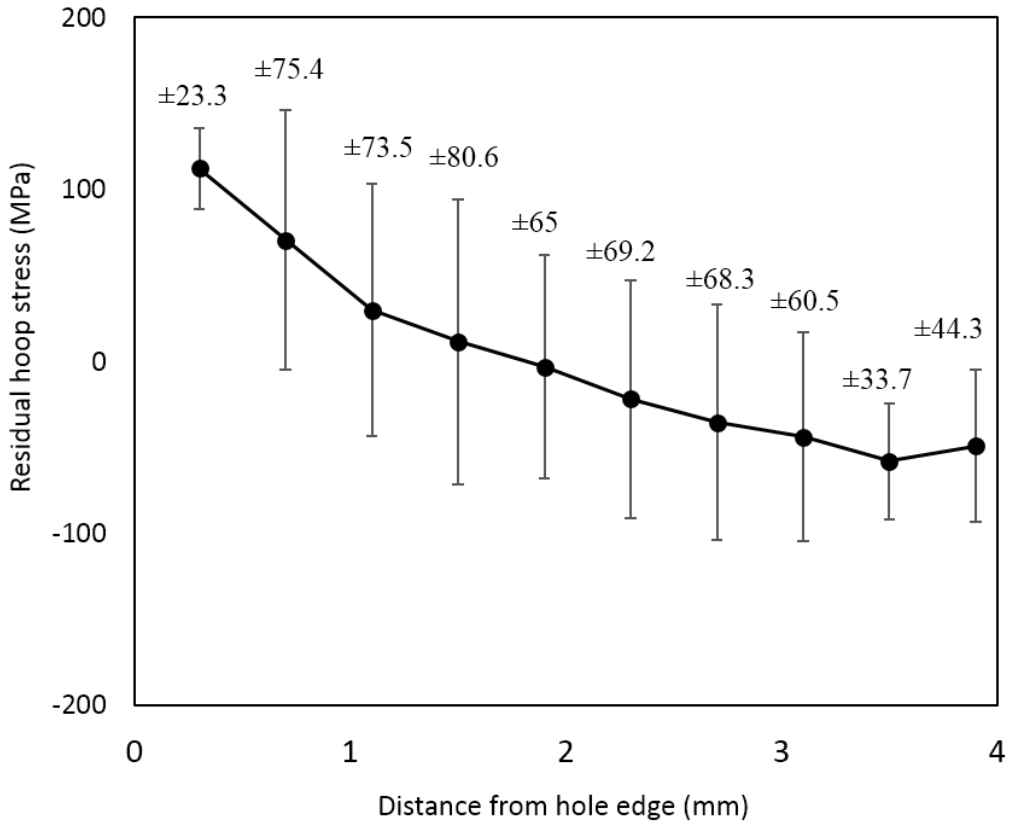

Figure C.3 Average residual radial stress profile, close to the mandrel exit face, for cold-expanded specimens, C12-C17 to which no loads were applied.

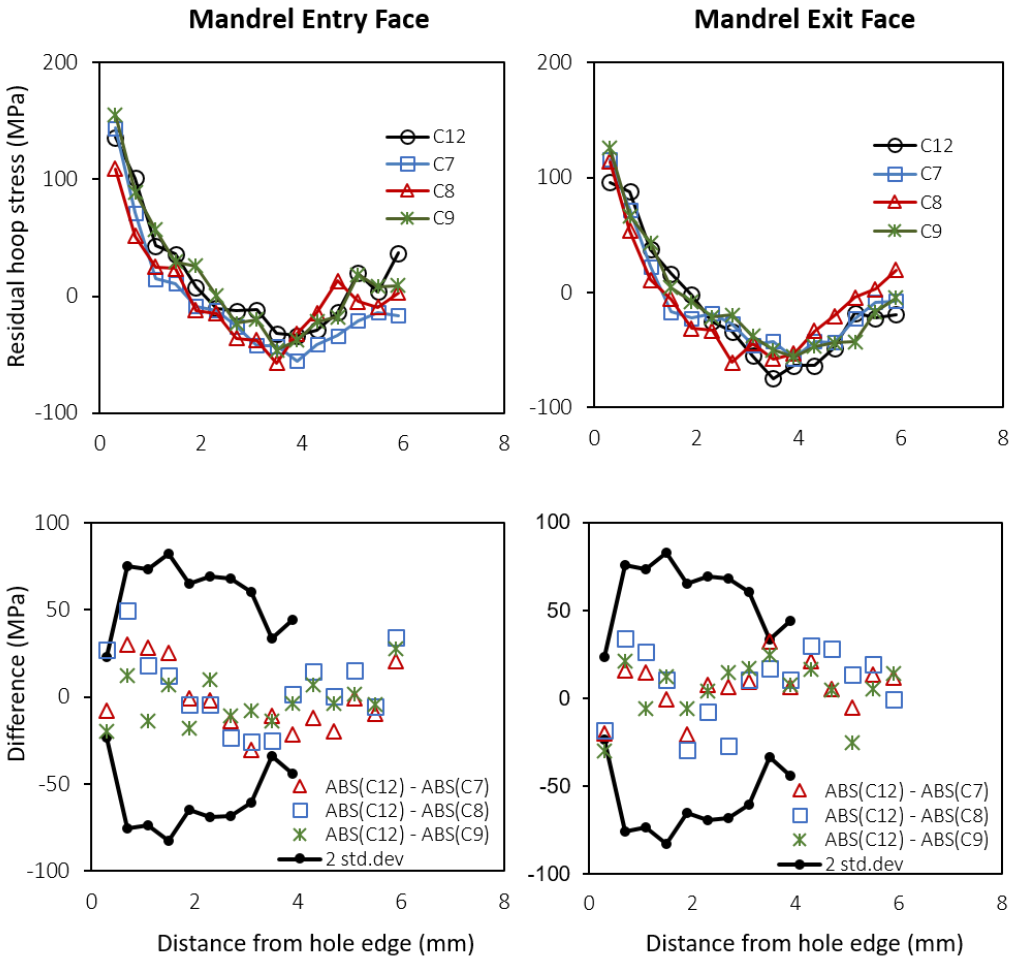

Figure C.4 Plots of residual radial stress profiles (top) and difference in their magnitudes (bottom) close to the mandrel entry (left) and exit (right) faces for cold-expanded specimens, C7 to which 50k cycles of fatigue loading was applied with no cracks observed during loading, C8 with a 2.1 mm crack, C9 with a 3.8 mm crack and C12 to which no loads were applied.

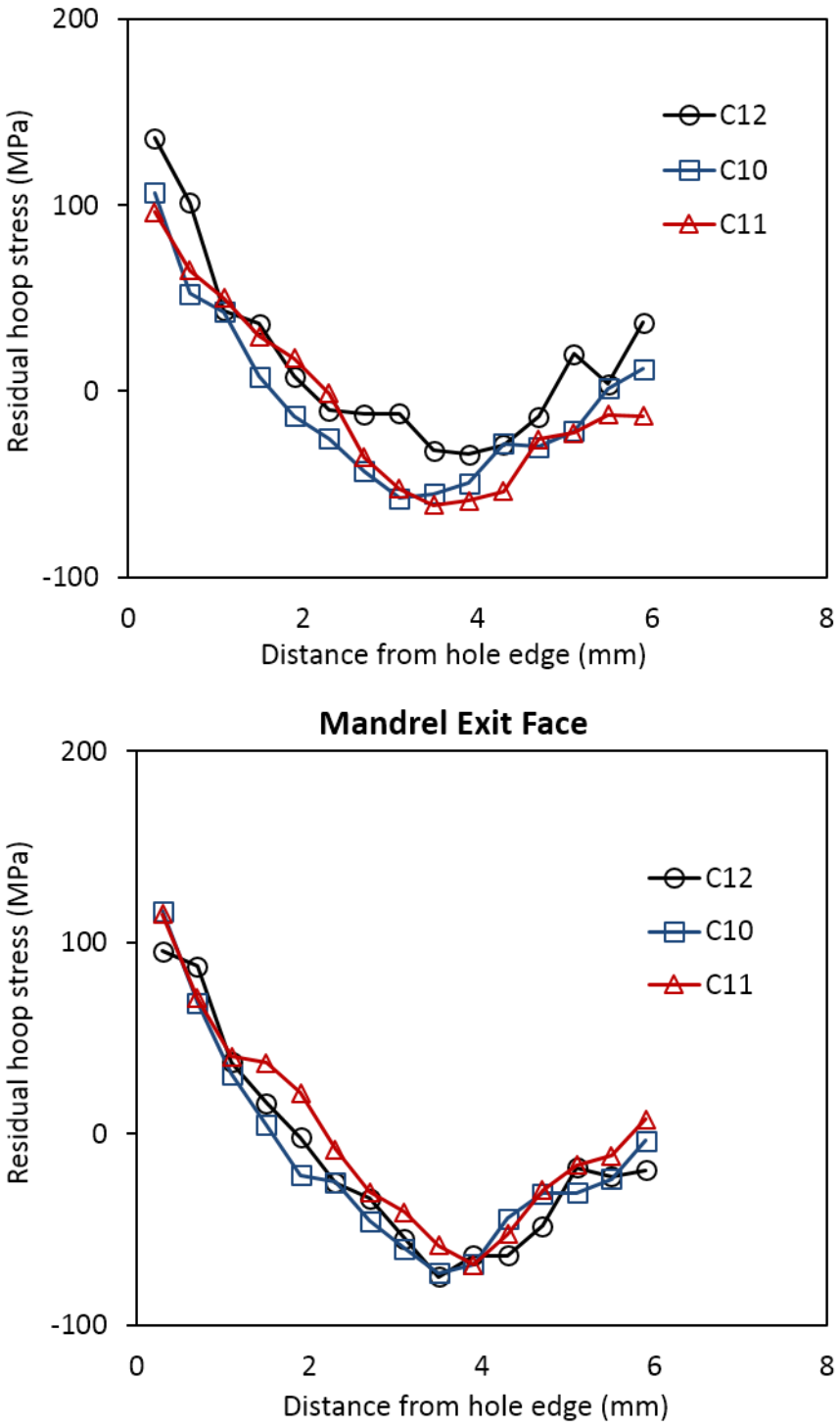

Figure C.5 Plots of residual radial stress profiles close to the mandrel entry (top) and exit (bottom) faces for cold-expanded specimens, C10 to which single compressive stress cycle of -92.7 MPa was applied, C11 to which single compressive stress cycle of -125 MPa was applied and C12 to which no loads were applied.